

Metal Mirror
Optics 523 Final Design Report
15 May, 2009
Federico Pennacchini

Table of Contents

1. Statement of Work.....	3
2. Optical Requirements.....	4
3. Mechanical Requirements.....	5
4. Environmental Requirements.....	6
5. The Design.....	7
6. The Interface.....	12
7. Lessons Learned.....	13
8. Appendix A. Analysis.....	14
9. Appendix B. Drawings.....	18
10. Appendix C. Purchased Parts.....	23
11. Appendix D. Supplemental Technical Papers on Single Diamond Point Turning.....	28

1. Statement of Work

A 188.5 mm f/1.5 primary mirror is to be designed for a Ritchey-Crétien telescope is to be designed to operate in the TIR for military and law enforcement remote sensing.. This telescope system is to be designed to be light-weight for mounting in a surveillance helicopter, plane, or UAV. In order to maximize stiffness while minimizing weight, a metal mirror was chosen as the optimal solution. Large metallic mirrors lend them selves naturally to fabrication by Single Point Diamond Turning (SPDT) as the mirror substrate can be machined on a CNC mill while the optical and datum surfaces can be precision machined to optical tolerances with the SPDT process. Given the sub-micron tolerances that the SPDT can achieve, the entire telescope can be machined to assemble in a plug-and-play manner negating the need to alignment, saving both time and expensive labor. Also, exotic aspheric and off-axis optical surfaces are no more difficult to fabricate due to the CNC nature of the SPDT process. Given these advantages weighed against slightly higher component fabrication costs that are almost balanced by reduced assembly labor costs and overcome for volume production because of the removal of the need for an alignment step in the assembly process and its associated labor and instrument costs makes Single Point Diamond Turning of a metal substrate mirror the preferred method for the design of this camera mirror.

2. Optical Requirements

Clear Aperture	188.5 mm
EFL	285.75 mm
Surface Roughness	100 Å
Operating Range	8-12 μm
Reflectance	> 90%
Surface	1/12λ RMS @ 8 μm

3. Mechanical Requirements

Elevation Travel	0-90°
Azumthul Travel	0-360°
Mass	5 kg
Resonance Frequency	100 Hz

4. Environmental Requirements

Operating Temperature Range	-20--35 °C
Operating Pressure Range	270-760 mmHg
Operating Humidity Range	0-100%
Operating Altitude	0-25,000 feet

5. The Design

The design is a hyperbolic reflective surface Single Point Diamond Turned (SPDT) into a machined aluminum 6061-T6 mirror supported by three flexure tabs. The mirror will be coated with an overcoat of pure aluminum to prevent thermal mis-match when the mirror gets cold at altitude. On top of the 120 μm thick pure aluminum coating will be a reflective gold layer to have reflectance above 90% for the entire operating range of 8-12 μm . The mass of this mirror is 1.5kg, well below the 5 kg requirement. The lowest resonance frequency (1st mode) was analyzed by FEA and was found to be 899 Hz, well above the 100 Hz requirement. Self-weight deflection was analyzed with FEA; the worst case was for the mirror pointed at the horizon. The RMS wavefront error point at horizon was found to be .37 μm , or better than $1/20\lambda$ at 8 μm , well within the $1/12\lambda$ requirement. Since the optical surface is pure aluminum on an aluminum surface, this mirror is athermalized by material, therefore it will retain it's figure over the entire operational temperature range. A 1mm x 1mm precession scallop is machined along the edge of the mirror surface for use as an alignment and datum feature.

A cross section of the mirror design is shown in figure 1 below.

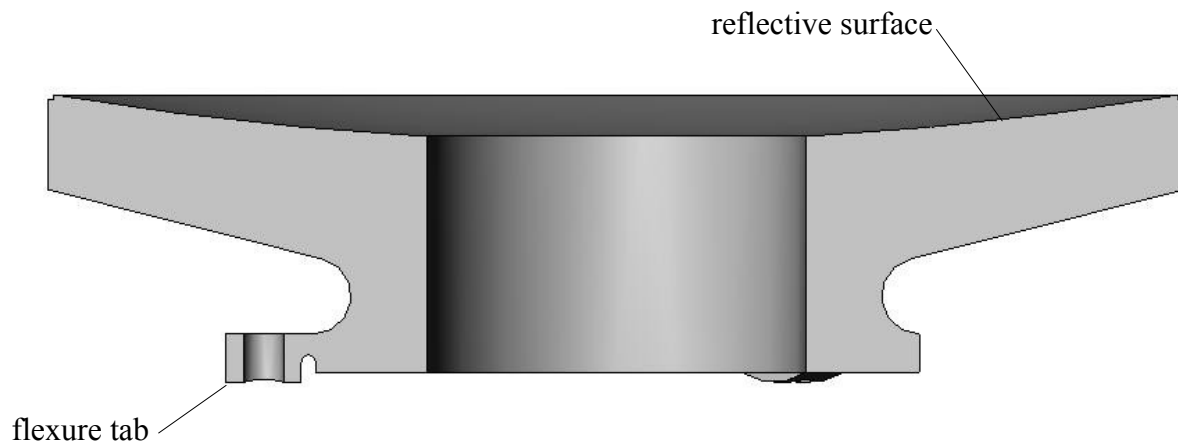


Figure 1. Cross section of mirror

An isometric view of the reflective side of the mirror is shown for clarity in figure 2 below and an isometric view of the mounting side of the mirror is shown in figure 3 below.

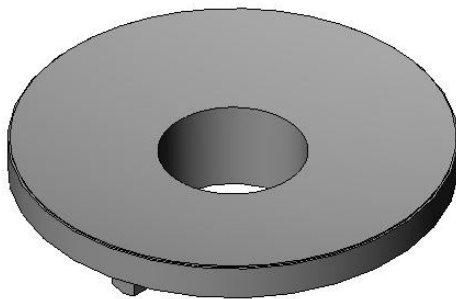


Figure 2.

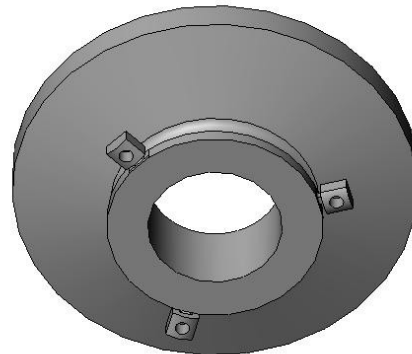


Figure 3.

The mirror is kinematically mounted via three cylindrical surface flexure tabs to three radial V-grooves spaced 120° apart. The entire assembly is held together with three through bolts fastened to three nuts and staked with 3M 2216 epoxy. Flat washers are used on the detector side under the bolt heads while spherical washers under the nuts are used to accommodate any non planarity caused by the flexure tabs. A cutaway of the mounting scheme is shown in figure 4 below.

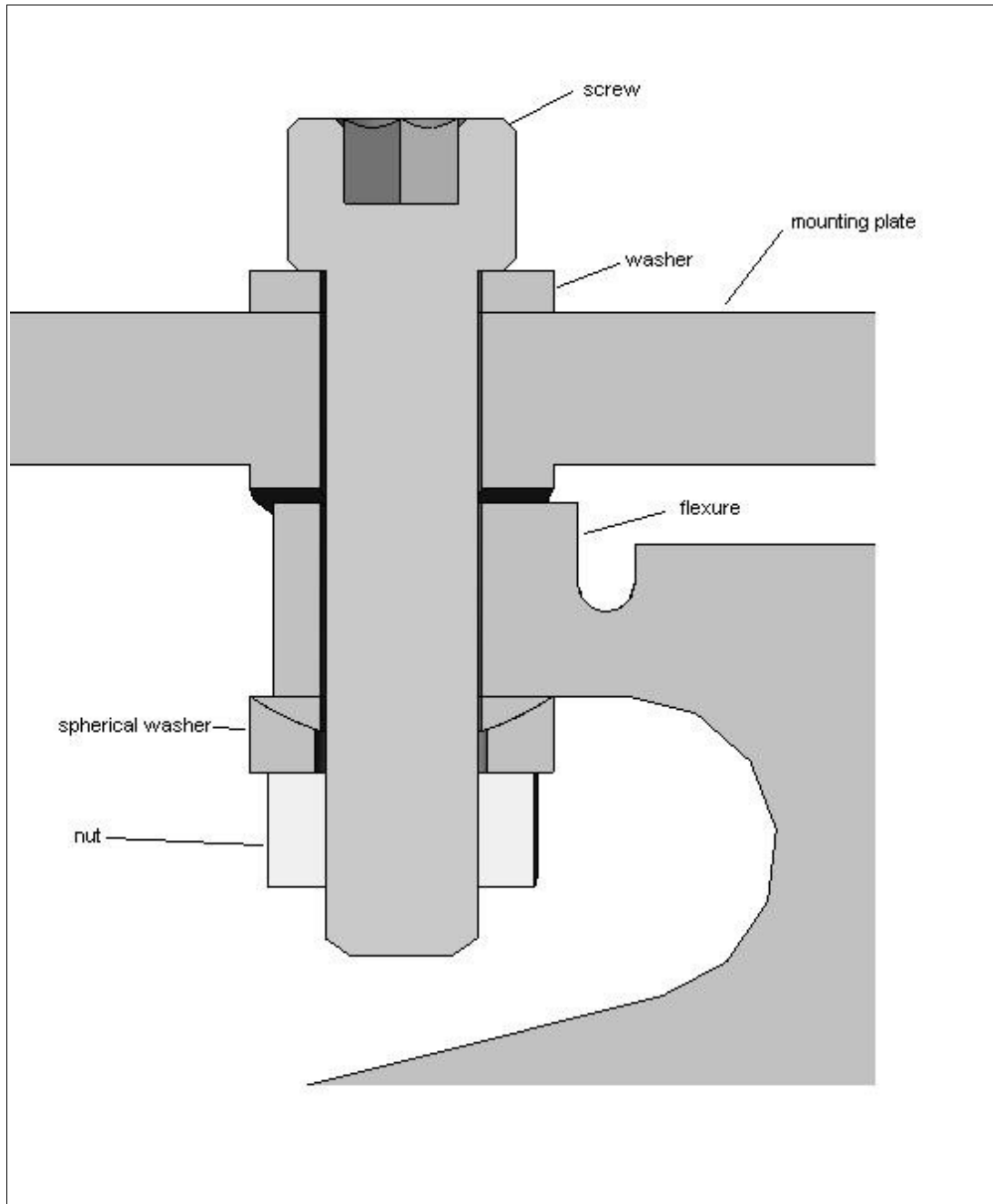


Figure 4. Mounting Scheme

A rendering of the kinematic mounting scheme is shown in figure 5 below. The three cylindrical interfacing surfaces ride in radial V-grooves providing precision alignment and repeatability around .001”.

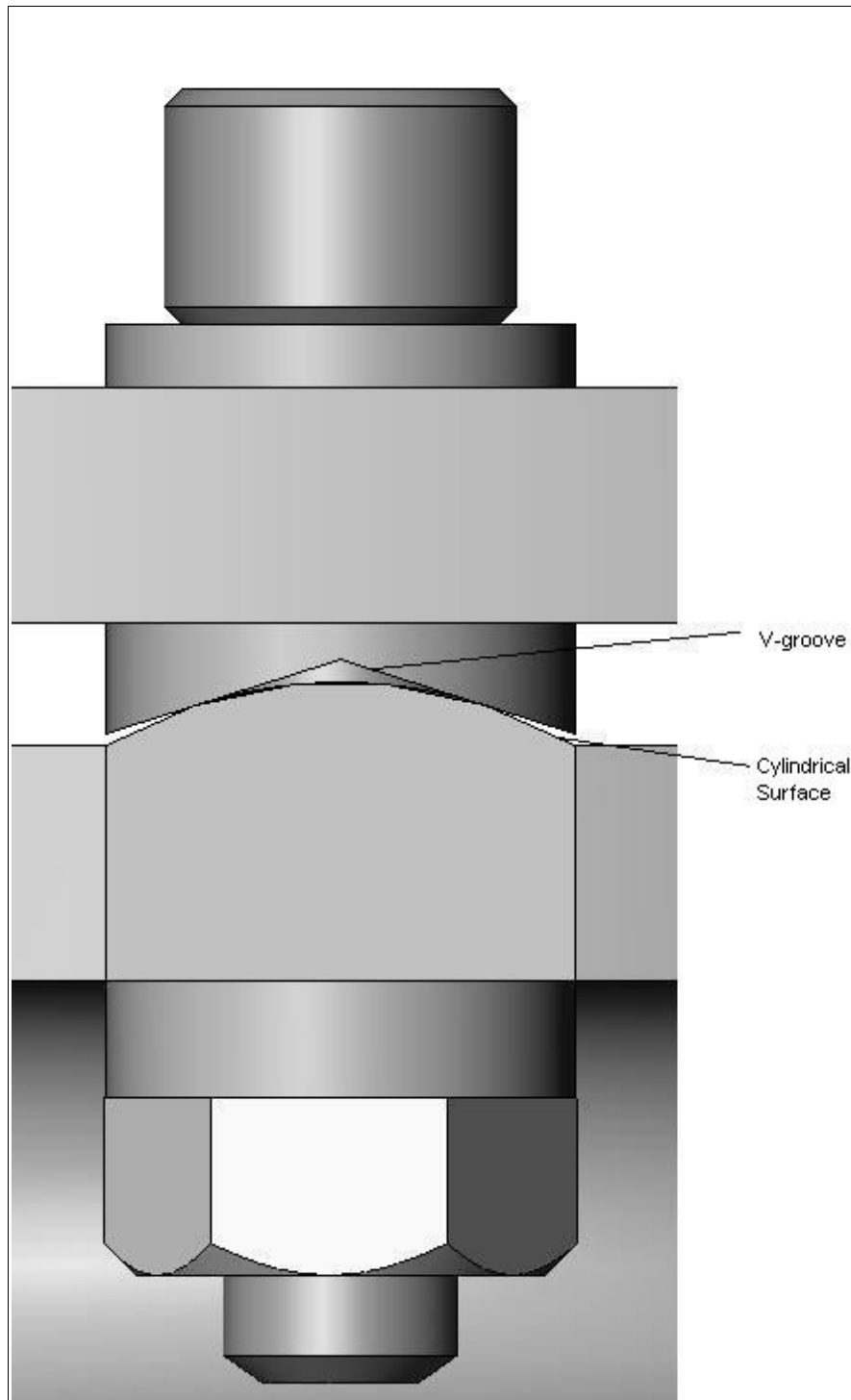


Figure 5. Kinematic Mount

In order to guarantee a precision optical surface, the mirror will need to be stress relieved several times to remove the internal stresses present in the aluminum. The stress relief process is relatively simple. The mirror is first placed in liquid nitrogen and left there until the temperature of the entire part has reached equilibrium with the LN_2 . Then the part is transferred to a vat of boiling water (while the mirror is still frozen at the LN_2 temperature). The process is repeated four more times. This process is referred to as uphill quenching. The part is uphill quenched after rough machining (all dimensions + 0.7 mm), then before after finish machining, before the $120\ \mu\text{m}$ pure aluminum coating is applied that the optical surface is finish machined into. Reflectance data for pure gold in the operational wavelength range is given in figure 6 below.

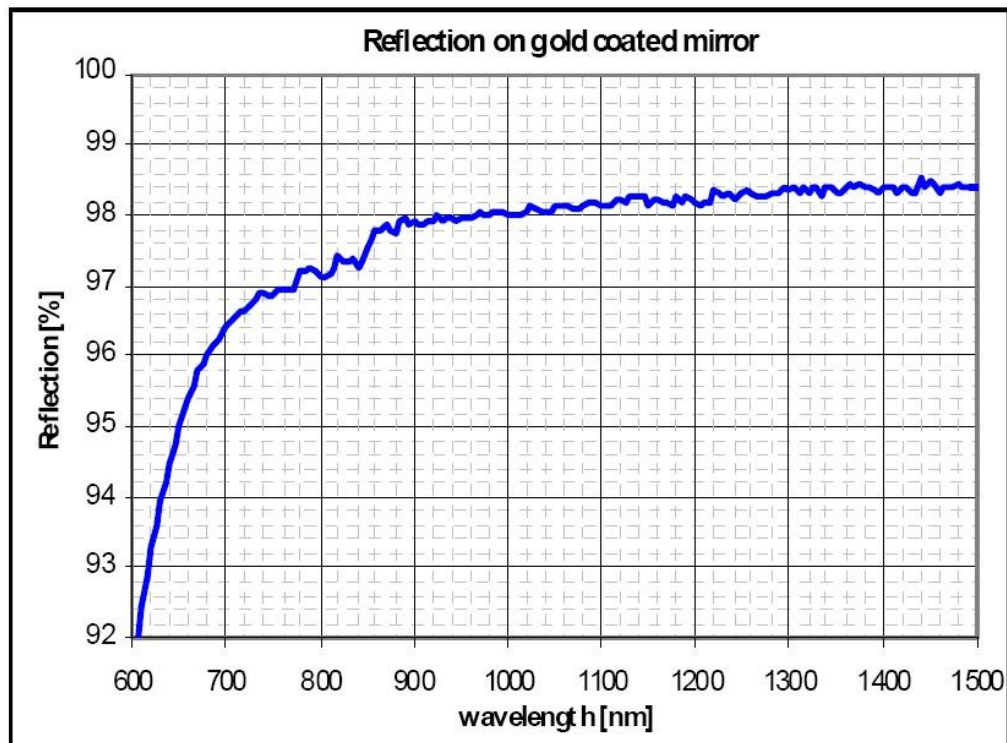


Figure 6. Gold Coating Reflective Performance

The flexure tabs that hold the mirror to the mounting plate are designed as flexures to accommodate any machine tolerance stack-up between the radial mounting V-grooves and the flexure tabs. The flexures are designed to be flexible in two degrees of freedom to accommodate any alignment errors with the V-grooves caused by machine tolerance stack-ups. Renderings of the flexures are shown in figures 7 and 8 below.

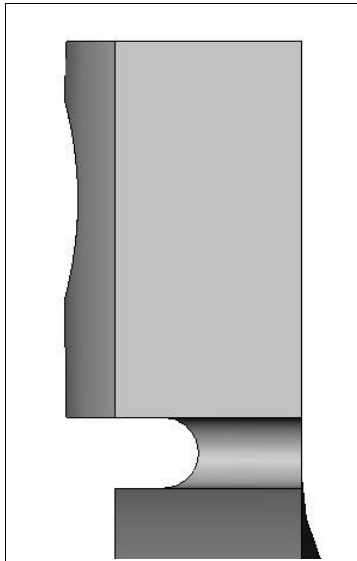


Figure 7

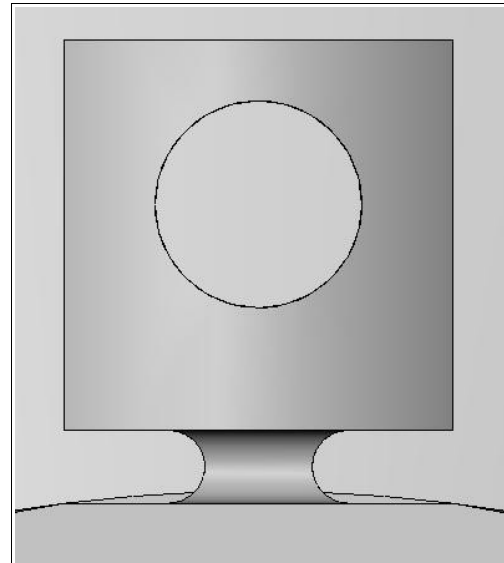


Figure 8

6. The Interface

The mirror interfaces with its mounting surface via three cylindrical surfaces on the mounting side of the flexure tabs. The flexure tabs on the mirror and the radial V-grooves on the mounting plate are spaced 120° apart. The mirror is attached to the mounting plate via through bolts running through the detector side of the mounting plate and are fastened with nuts on the flat surfaces (toward the reflective surface) of the flexure tabs. Renderings of the flexure tab and V-groove interface are shown in figures 9 and 10 below.

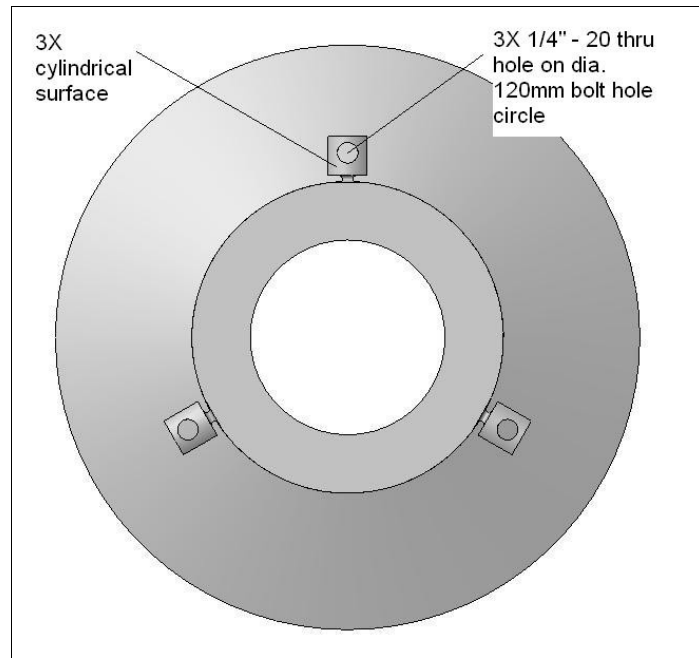


Figure 9. Mirror Interface

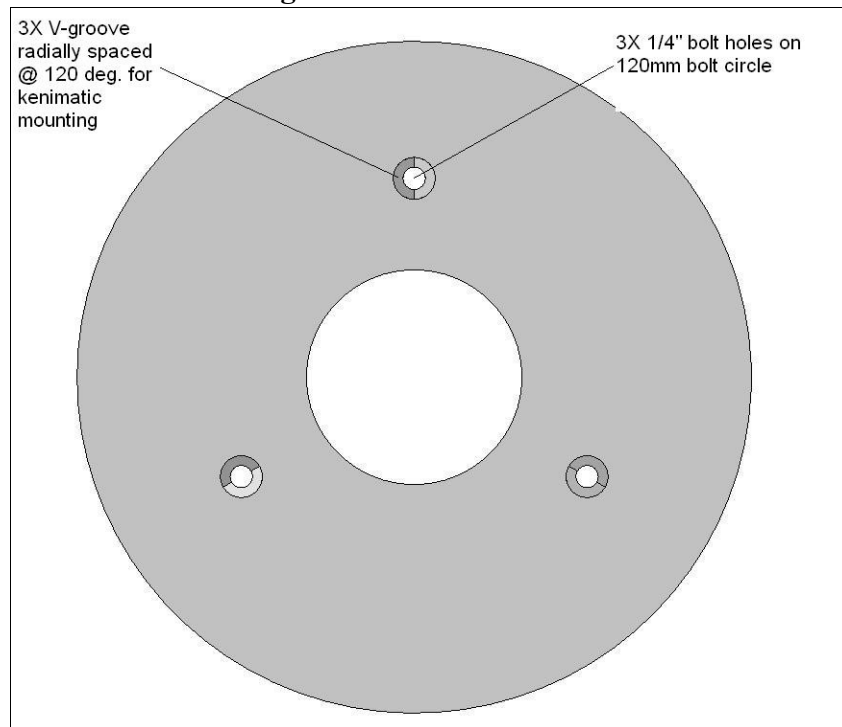


Figure 10. Mounting Interface

7. Lessons Learned

Metal mirrors have several fantastic attributes. The fact that flexure mounts can be machined into the mirror and with SPDT the mirror can be machined to tight enough tolerances to negate the need for assembly is amazing. The fact that the optical surface can be machined directly into the metal for IR imaging systems and even for visible systems with some care without the need to polish the metal surface is amazing. For UV reflective systems, the figure of the reflecting surface can be machined directly into electroless nickel that can then be polished out to a UV acceptable surface smoothness is also incredible. The most useful application I think for this process though is the fact that aspheric and non axi-symmetric surfaces can be SPDT almost as easily as a spherical surface. That is incredible for off-axis and high performance systems. I know from two years personal experience as an optical technician grinding and polishing large astronomical telescope mirrors that spherical and flat surfaces are easy to grind and polish. Aspheric surfaces are extremely difficult to polish into a mirror surface and it's easy to make mistakes when aspherizing a mirror surface. Off-axis systems are also extremely difficult. The company I worked as an optical technician for was bankrupted by the labor costs of re-figuring an off-axis system we designed and built. I see this as a fantastic technology that I hope matures further driving costs down to make this a viable manufacturing technology for consumer volume optics. I would love to see a renaissance of ultra-high performance consumer optics with the decreased aberrations and complexity (less required surfaces to cancel out aberrations) that aspheric surfaces provide.

Appendix A – Analysis

Weight: The mass of the mirror was calculated in SolidWorks. It was found to be 1.5kg.

Resonance Frequency: The resonance frequency was analyzed using CosmosWorks. The resonance frequencies for all five modes are listed in table 11 below. Images of the five resonance modes are shown in figures 12-16.

	A	B	C	D
1	05:52:00 PM	Tuesday	04/28/09	2009
2	Study name: Resonance Frequency			
3	Mode No.	Frequency(Rad/sec)	Frequency(Hertz)	Period(Seconds)
4	1	5646	898.58	0
5	2	5655.3	900.08	0
6	3	8694.1	1383.7	0
7	4	8756.2	1393.6	0
8	5	14212	2262	0

Figure 11. Resonance Modes and Resonance Frequencies

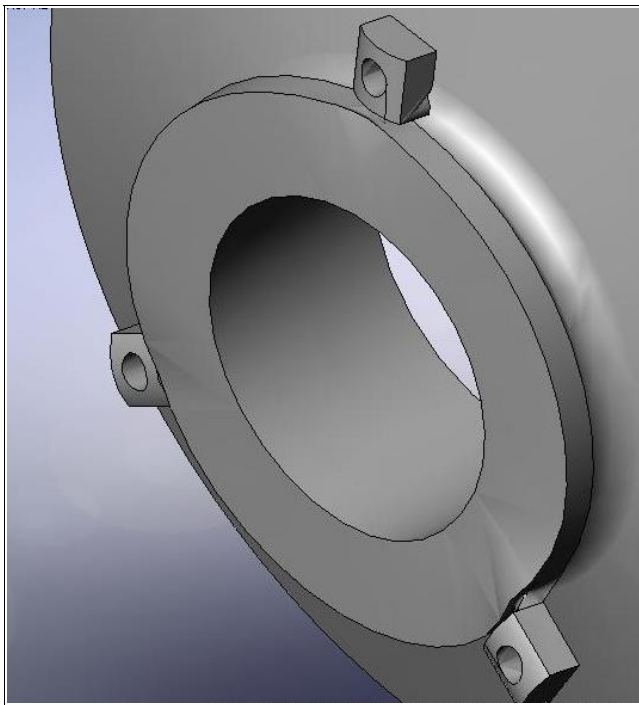


Figure 12. Resonance Mode 1

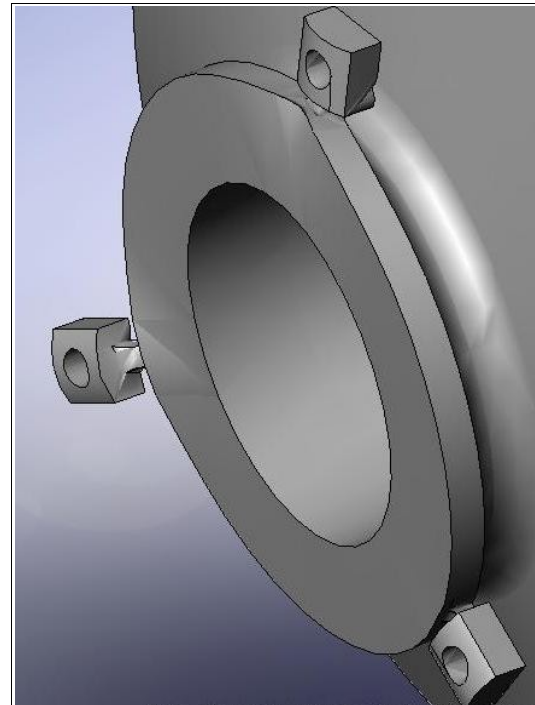


Figure 13. Resonance Mode 2

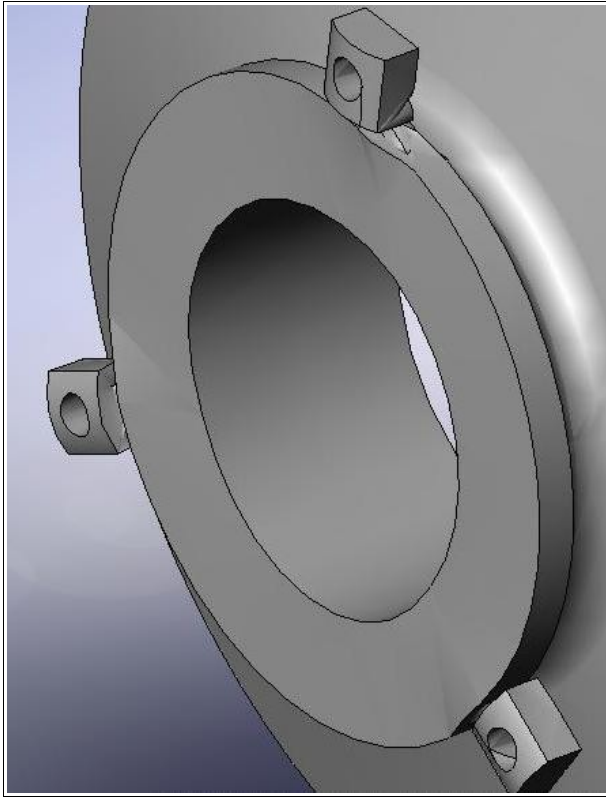


Figure 14. Resonance Mode 3

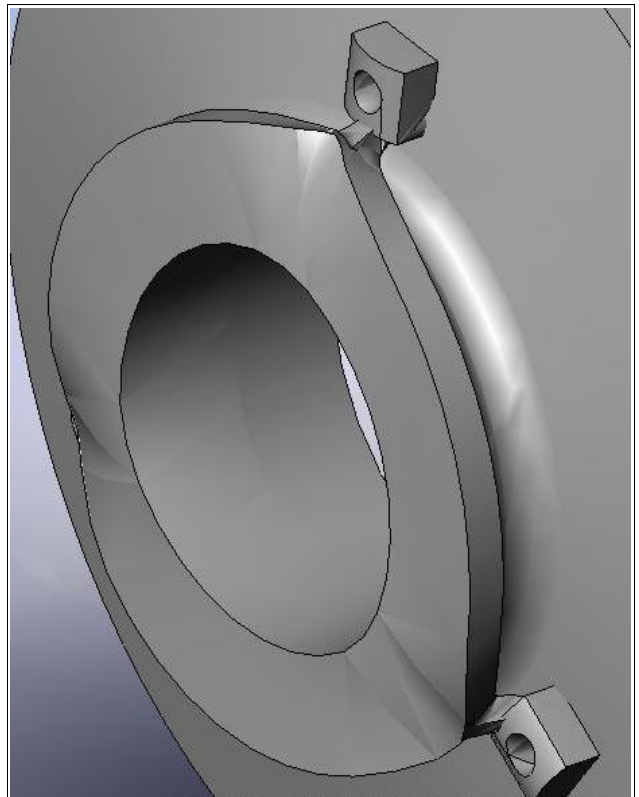


Figure 15. Resonance Mode 4

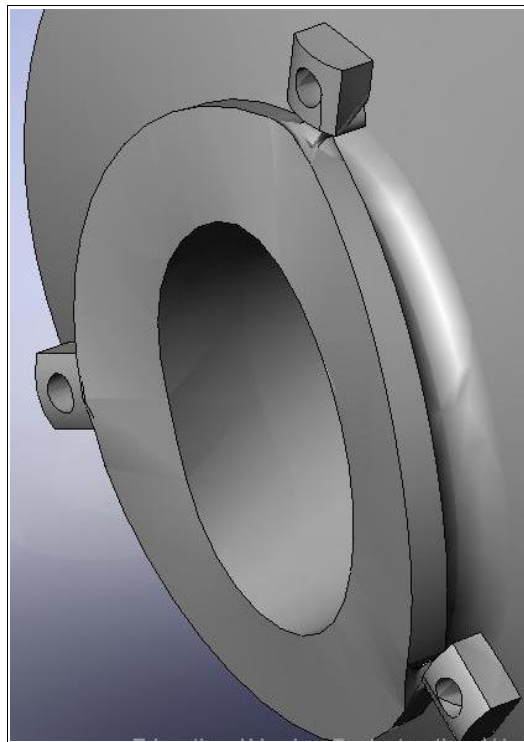


Figure 16. Resonance Mode 5

RMS Wavefront Error:

The RMS wavefront error due to self weight deflection was analyzed in CosmosWorks for the mirror pointing straight down, looking at the ground, at a 45° angle below the horizon, and at the horizon. The RMS wavefront error for those three conditions are listed in table 17 below.

Mirror Pointing Direction	RMS Wavefront Error (μm)
Vertical (straight down)	.07
45° (halfway between vertical and horizontal)	.25
Horizontal (at the horizon)	.37

Table 17. RMS Wavefront Error

Figure 18 below shows the displacement plot from CosmosWORKS for the mirror in the vertical configuration. Figure 19 below shows the displacement plot for the mirror at 45° while figure 20 shows the displacement for the mirror looking at the horizon.

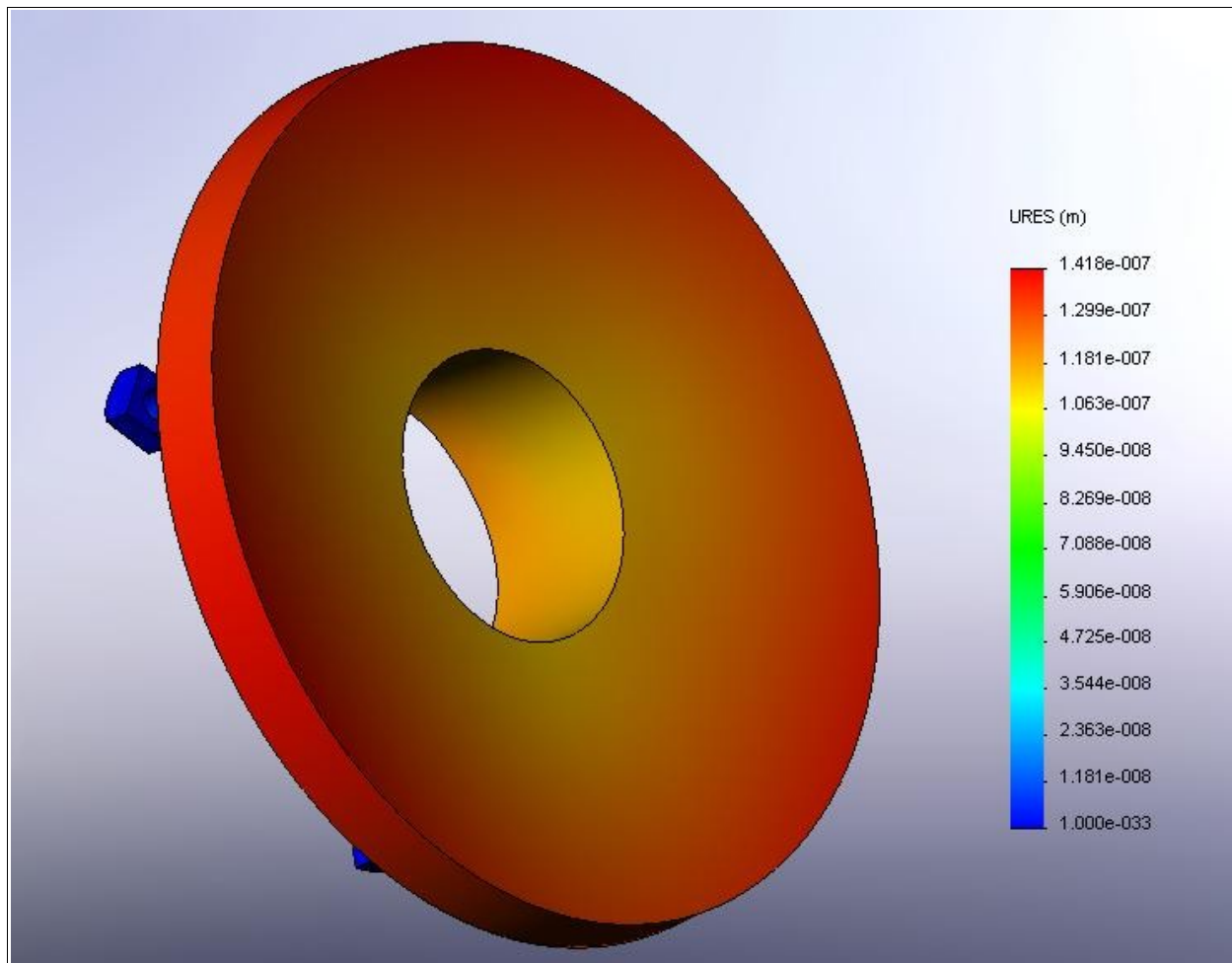


Figure 18. Displacement for vertical mirror

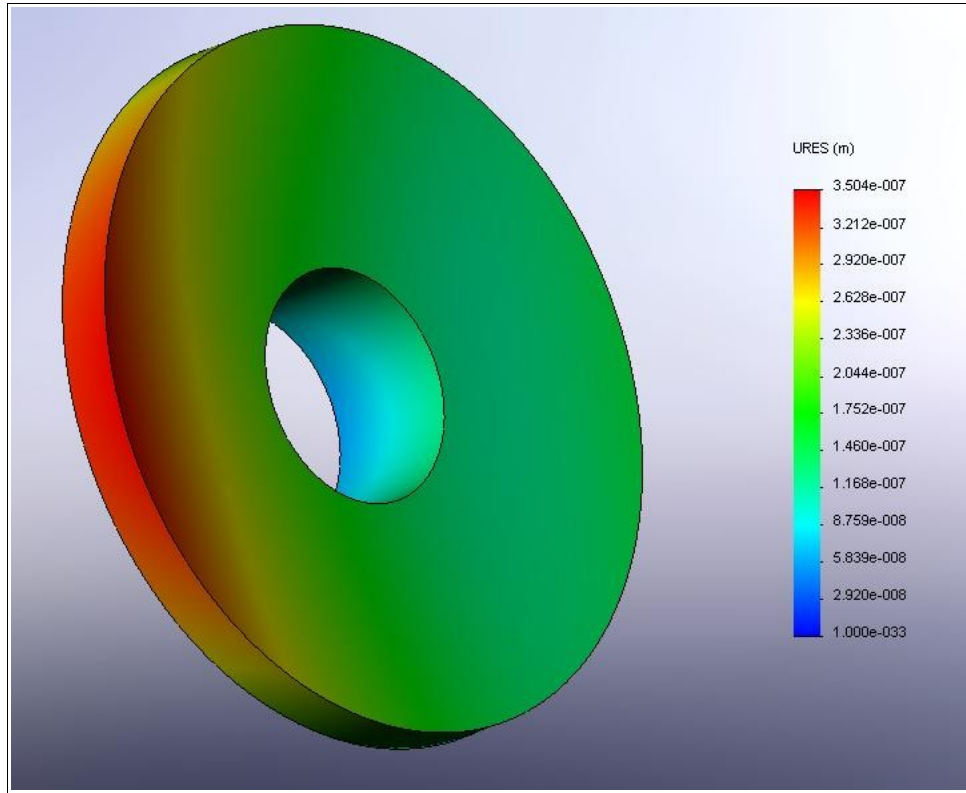


Figure 19. Displacement for mirror at 45°

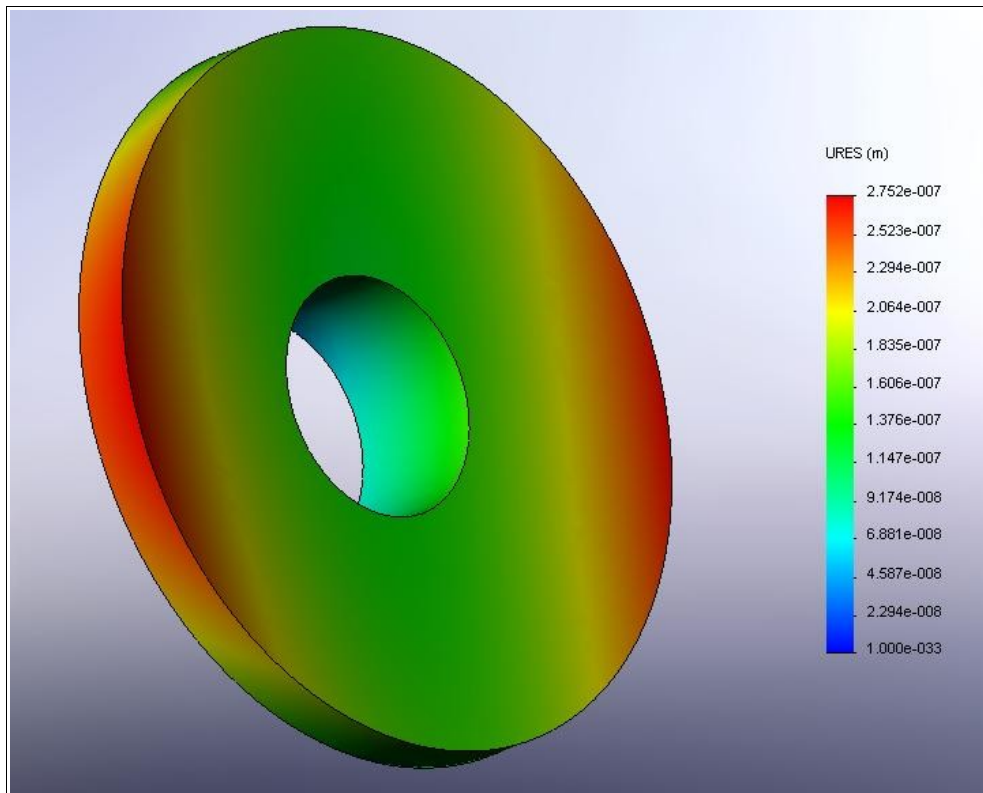


Figure 20. Displacement for mirror pointing at horizon

Appendix B - Drawings

8 7 6 5 4 3 2 1

D

C

B

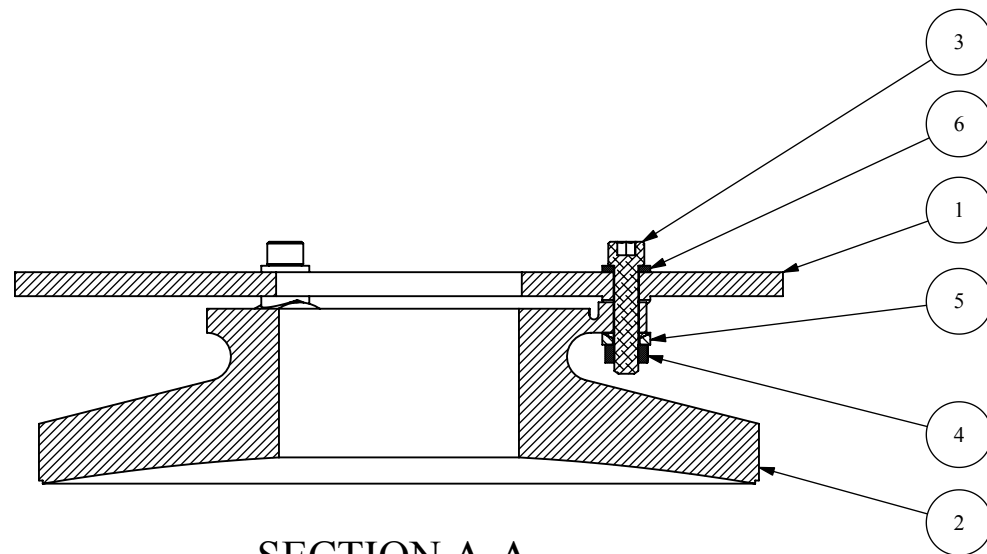
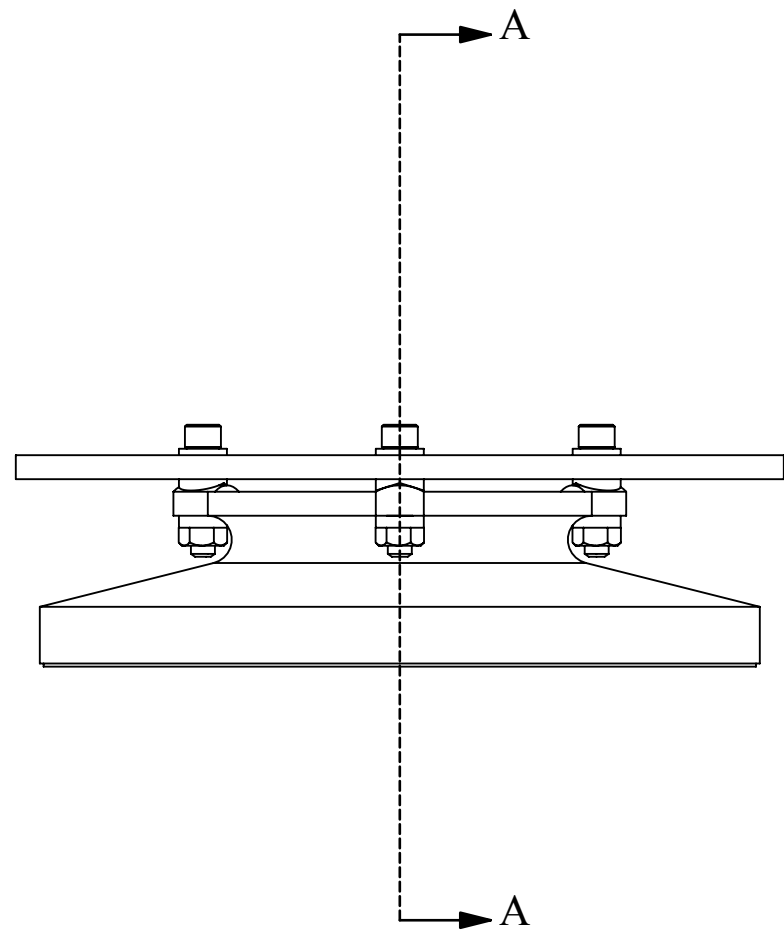
A

D

C

B

A



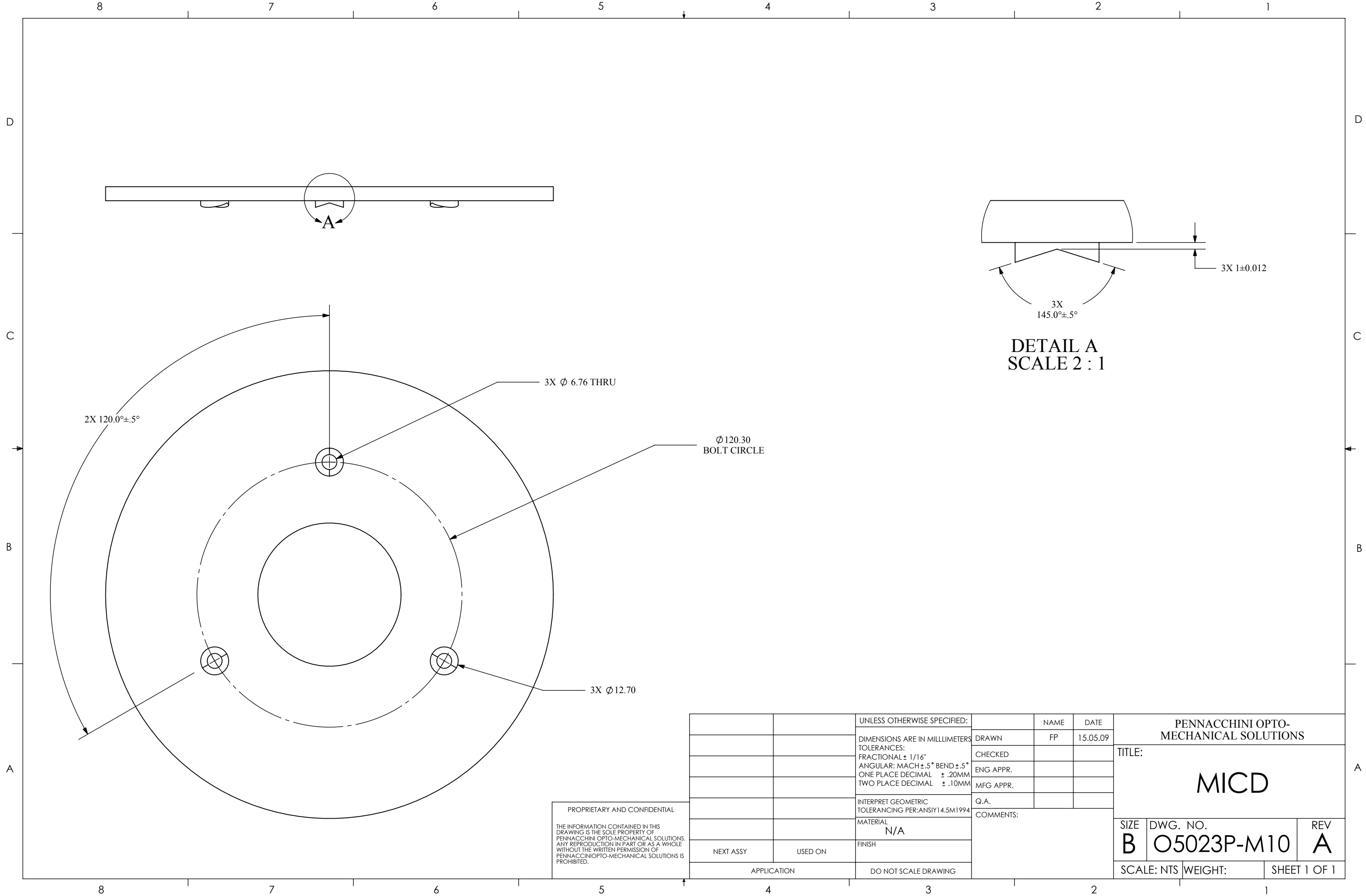
SECTION A-A
SCALE 1 : 2

ITEM NO.	PART NUMBER	DESCRIPTION	QTY.
1	O5023P-M10	MIRROR MOUNTING PLATE	1
2	O523P-O10	MIRROR	1
3	92196A543	1/4" - 20 X 1-1/8" CRES SHCS	3
4	91841A029	1/4" - 20 CRES NUT	3
5	MMCR 91944A028	1/4" CRES SPHERICAL WASHER	3
6	MMCR 98017A660	1/4" CRES WASHER	3

PROPRIETARY AND CONFIDENTIAL
THE INFORMATION CONTAINED IN THIS DRAWING IS THE SOLE PROPERTY OF PENNACCHINI OPTO-MECHANICAL SOLUTIONS. ANY REPRODUCTION IN PART OR AS A WHOLE WITHOUT THE WRITTEN PERMISSION OF PENNACCHINI OPTO-MECHANICAL SOLUTIONS IS PROHIBITED.

		UNLESS OTHERWISE SPECIFIED:		NAME	DATE	PENNACCHINI OPTO-MECHANICAL SOLUTIONS				
		DIMENSIONS ARE IN MILLIMETERS		DRAWN	FP	15.05.09				
		TOLERANCES:		CHECKED		TITLE:				
		FRACTIONAL ± 1/16"		ENG APPR.		MIRROR MOUNT ASSEMBLY				
		ANGULAR: MACH ± .5° BEND ± .5°		MFG APPR.						
		ONE PLACE DECIMAL ± .20MM		Q.A.		SIZE	DWG. NO.	REV		
		TWO PLACE DECIMAL ± .10MM		COMMENTS:		B	O523P-M01	A		
		INTERPRET GEOMETRIC TOLERANCING PER:ANSI Y14.5M1994						SCALE: NTS	WEIGHT:	SHEET 1 OF 1
		MATERIAL								
		N/A								
		FINISH								
NEXT ASSY	USED ON									
APPLICATION		DO NOT SCALE DRAWING								

8 7 6 5 4 3 2 1



**DETAIL A
SCALE 2 : 1**

2X 120.0±.5°

3X Ø 6.76 THRU

Ø 120.30
BOLT CIRCLE

3X Ø 12.70

PROPRIETARY AND CONFIDENTIAL
THE INFORMATION CONTAINED IN THIS DRAWING IS THE SOLE PROPERTY OF PENNACCHINI OPTO-MECHANICAL SOLUTIONS. ANY REPRODUCTION IN PART OR AS A WHOLE WITHOUT THE WRITTEN PERMISSION OF PENNACCHINI OPTO-MECHANICAL SOLUTIONS IS PROHIBITED.

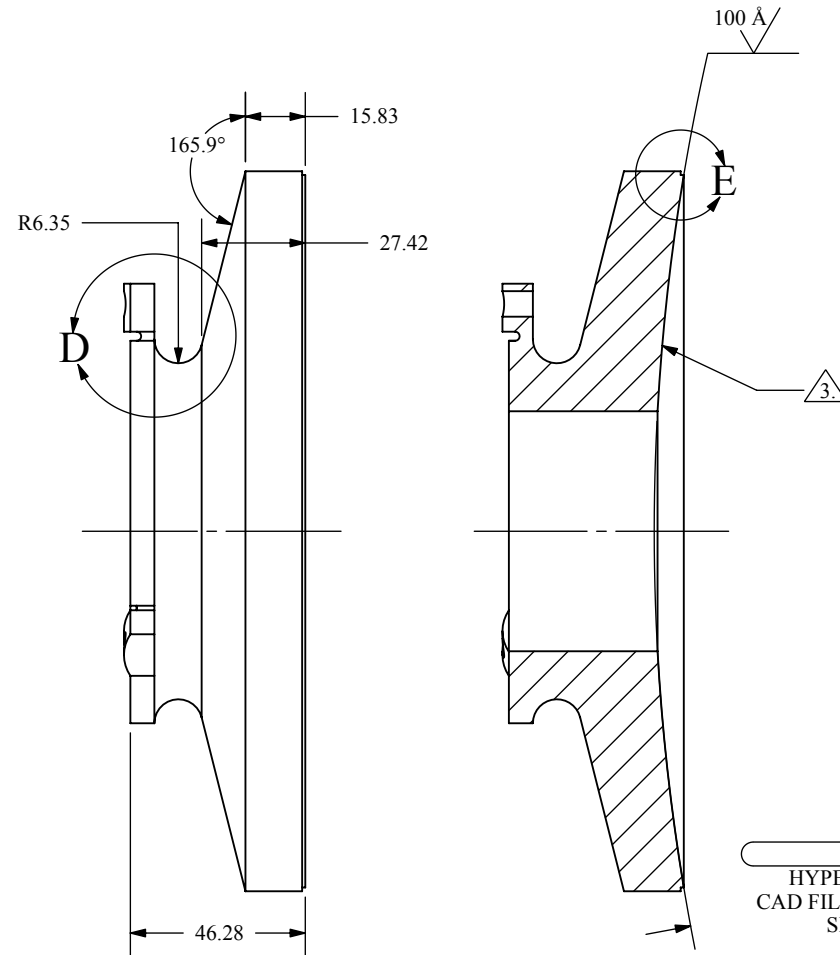
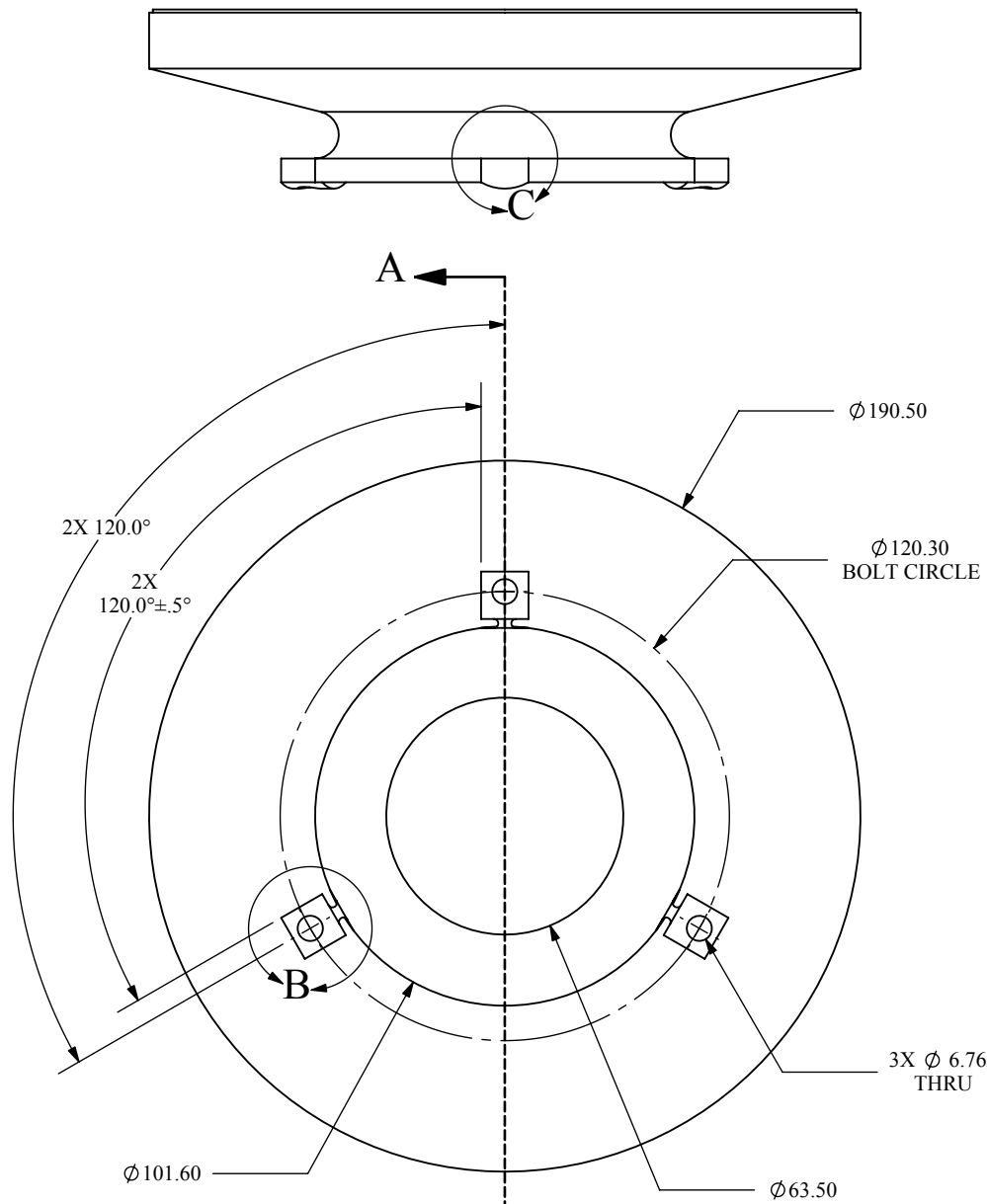
		UNLESS OTHERWISE SPECIFIED:		NAME	DATE	PENNACCHINI OPTO-MECHANICAL SOLUTIONS	
		DIMENSIONS ARE IN MILLIMETERS		DRAWN	FP	TITLE:	
		TOLERANCES:		CHECKED		MICD	
		FRACTIONAL ± 1/16"		ENG APPR.			
		ANGULAR: MACH ± .5° BEND ± .5°		MFG APPR.			
		ONE PLACE DECIMAL ± .20MM		Q.A.		SIZE	DWG. NO.
		TWO PLACE DECIMAL ± .10MM		COMMENTS:		B	O5023P-M10
		INTERPRET GEOMETRIC TOLERANCING PER:ANSI Y14.5M1994				SCALE: NTS	WEIGHT:
		MATERIAL					SHEET 1 OF 1
		N/A					
		FINISH					
NEXT ASSY	USED ON	DO NOT SCALE DRAWING					
APPLICATION							

REV **A**

NOTES:

1. DRAWING CONTAINS KEY DIMENSIONS FOR QUOTING AND INSPECTION. FABRICATE TO CAD FILE O5230-010.STEP
2. ROUGH MACHINE (DIMENSION + 0.7 mm) AND STRESS RELIEVE PER LMA EPS10321, REV D, METHIOD II. THIS IS A LIQUID NITROGEN DIP, THEN BOILING WATER DIP. ALL EDGES MAY BE LEFT SHARP FOR THIS STEP. REPEAT AFTER FINISH MACHINING.
3. AFTER FINISH MACHINING, COAT WITH PURE ALUMINUM, 150 μm THICK, HOLDING ALL POSITIONAL TOLERANCES AND SURFACE FINISHES. THEN APPLY OPTICAL REFLECTIVE SURFACE OF PURE GOLD, REFLECTIVITY > 90% FOR 8-12 μm.
4. CAD WEIGHT: 1.5 Kg.

D
C
B
A



SECTION A-A

PROPRIETARY AND CONFIDENTIAL
THE INFORMATION CONTAINED IN THIS DRAWING IS THE SOLE PROPERTY OF PENNACCHINI OPTO-MECHANICAL SOLUTIONS. ANY REPRODUCTION IN PART OR AS A WHOLE WITHOUT THE WRITTEN PERMISSION OF PENNACCHINI OPTO-MECHANICAL SOLUTIONS IS PROHIBITED.

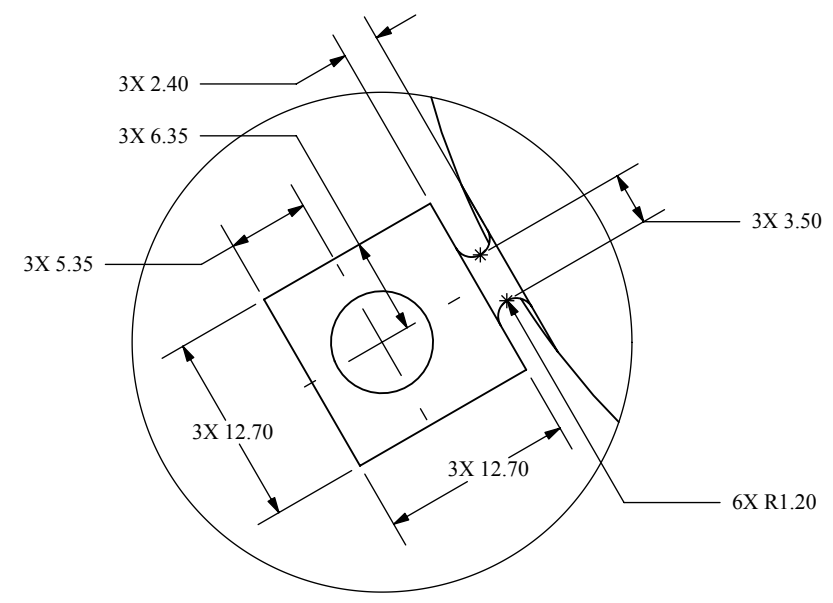
		UNLESS OTHERWISE SPECIFIED:		NAME	DATE	PENNACCHINI OPTO-MECHANICAL SOLUTIONS	
		DIMENSIONS ARE IN MILLIMETERS		DRAWN	FP	13.05.09	
		TOLERANCES:		CHECKED		TITLE:	
		FRACTIONAL ± 1/16"		ENG APPR.		MIRROR	
		ANGULAR: MACH ± .5° BEND ± .5°		MFG APPR.			
		ONE PLACE DECIMAL ± .20MM		Q.A.		SIZE	
		TWO PLACE DECIMAL ± .10MM		COMMENTS:		DWG. NO.	
		INTERPRET GEOMETRIC TOLERANCING PER:ANSI Y14.5M1994				O523P-O10	
		MATERIAL				REV	
		AL 6061-T6				A	
NEXT ASSY		USED ON				SCALE: NTS	
APPLICATION		DO NOT SCALE DRAWING				WEIGHT:	
						SHEET 1 OF 2	

8 7 6 5 4 3 2 1

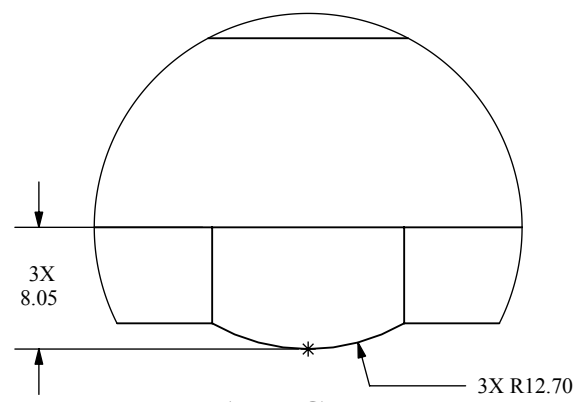
8 7 6 5 4 3 2 1

D
C
B
A

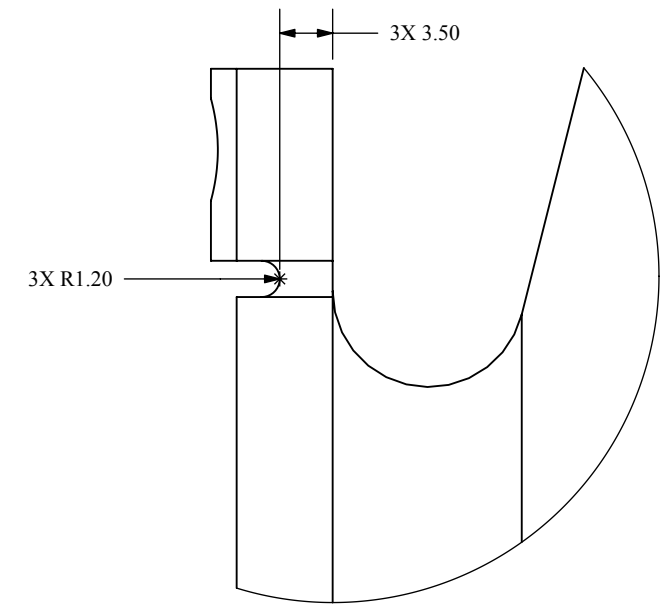
D
C
B
A



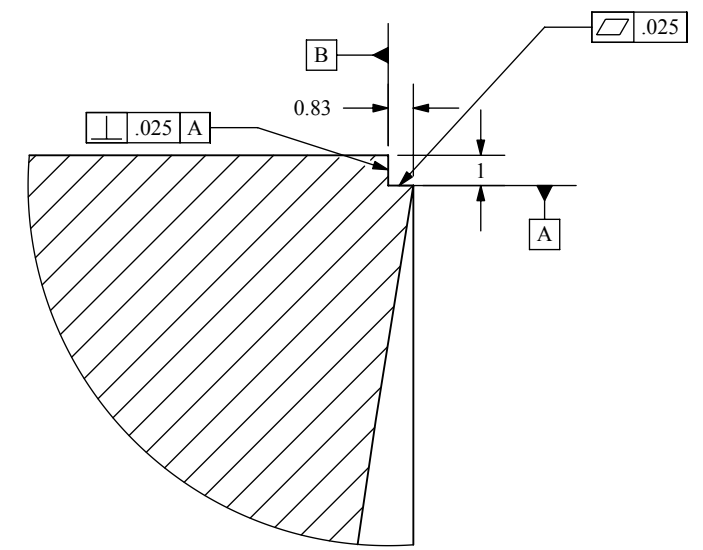
DETAIL B
SCALE 2 : 1



DETAIL C
SCALE 2 : 1



DETAIL D
SCALE 2 : 1

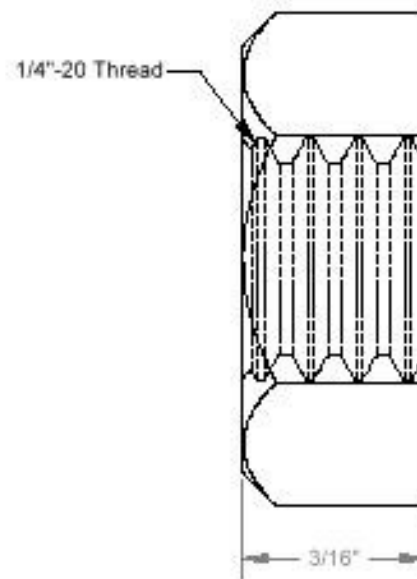
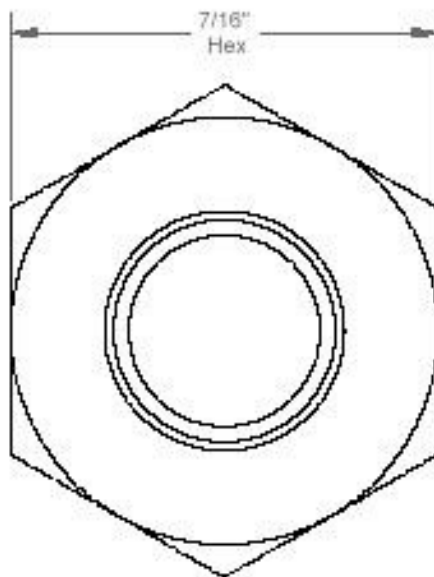
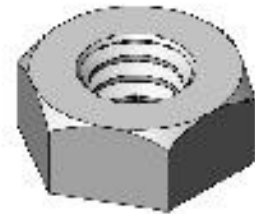


DETAIL E
SCALE 4 : 1

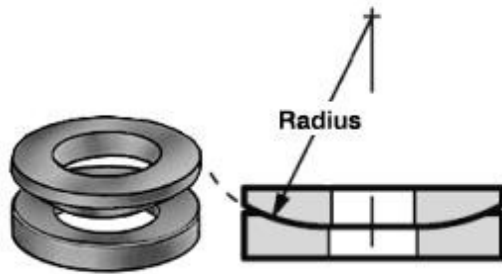
8 7 6 5 4 3 2 1

SIZE	DWG. NO.	REV
B	O523P-O10	A
SCALE: 1:2	WEIGHT:	SHEET 2 OF 2

Appendix C – Purchased Parts

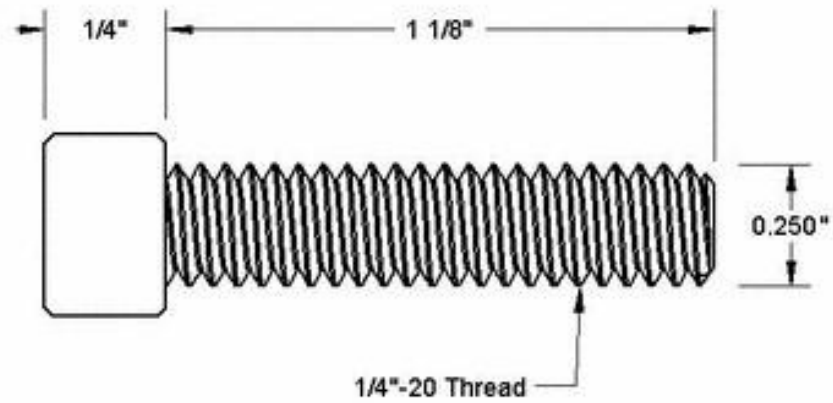
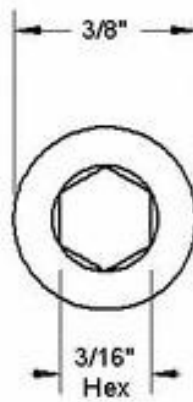


McMASTER-CARR <small>ESTD 1920</small>	PART NUMBER 91841A029
http://www.mcmaster.com (c) 2003 McMaster-Carr Supply Company	18-8 Stainless Steel Machine Screw Nut
<small>Unless otherwise specified, dimensions are in inches. Information in this drawing is provided for reference only.</small>	



Part Number: 91944A028

Shape	Spherical
For Screw Size	1/4"
Material Type	Stainless Steel
Finish	Plain
Stainless Steel Type	18-8 Stainless Steel
Spherical Piece	Set
Radius	7/64"
Male Inside Diameter	.266" (17/64")
Female Inside Diameter	.281" (9/32")
Outside Diameter	.5" (1/2")
Minimum Thickness	.25" (1/4")
Maximum Thickness	.281" (9/32")
Rockwell Hardness	B84
Specifications Met	Not Rated



McMASTER-CARR 	PART NUMBER	92196A543
	18-8 Stainless Steel Socket Head Cap Screw	

Unless otherwise specified, dimensions are in inches. Information in this drawing is provided for reference only.



Part Number: 98017A660

\$5.81 per Pack of 100

Shape	Round Hole
For Screw Size	1/4"
Material Type	Stainless Steel
Finish	Plain
Stainless Steel Type	18-8 Stainless Steel
Inside Diameter	.265"
Outside Diameter	.5" (1/2")
Minimum Thickness	.059"
Maximum Thickness	.067"
Rockwell Hardness	B70
Specifications Met	Aeronautics Specification (AN), Federal Specifications (FED), National Aerospace Standards (NAS)
AN Specification	AN 960
FED Specification	FF-W-92
NAS Specification	NAS 1149
NAS 1149 Dash#	C416
AN 960 Dash #	C416

Appendix D – Supplemental Papers on Single Point Diamond Turning



Moore Nanotechnology Systems, LLC
426A Winchester St., P.O. Box 605
Keene, NH 03431-0605 USA
Tel (603) 352-3030
Fax (603) 352-3363
www.nanotechsys.com

Nanotechnology Systems

Advantages of Hydrostatic Oil Bearing Spindles for Ultra Precision Grinding Applications:

- Hydrostatic and Aerostatic spindles have similar theoretical rotational accuracy.
- Because the stiffness of the bearing (both hydrostatic and aerostatic) is proportional to supply pressure, and film compressibility, hydrostatic bearings have much higher static stiffness (assuming common geometries)
- The overwhelming advantage of oil hydrostatic bearings is their extremely high damping ratio. The damping ratio of a hydrostatic bearing is several hundred times greater than that of an aerostatic bearing. This is due to the difference in fluid viscosity and compressibility between oil and air. Hydrostatic bearings are the only type of bearings that effectively combine Ultra High Accuracy, Very High Stiffness, and Ultra High Damping Ratio (a.k.a. – Vibroresistence).
- Damping Ratio is extremely important when hard and brittle materials are machined, regardless of process (grinding, turning, or milling). This is one of the reasons slides for Ultra Precision equipment have evolved from aerostatic bearing technology to oil hydrostatic bearing technology. Even when cutting forces are very small (finish grinding for example) a high damping ratio allows you to achieve better surface finishes (particularly with interrupted cuts) which essentially leads to increased machining productivity.
- Typically, high speed spindles utilize an integrated (or integral) motor. Electromagnetic forces between the stator and rotor have radial component influences that can ultimately affect the shaft's rotational accuracy. Hydrostatic oil bearings dramatically reduce the rotational inaccuracies caused by motor influence.
- Generally, when an AC integral motor is used the rotor can reach higher temperatures, which will ultimately transfer through to the spindle shaft. Hence, we have designed internal cooling into our motor cavities (utilizing chilled oil) to control thermal expansion and maintain long-term stability.

Other Unique Advantages of Nanotech Ultra-Precision Machining Systems

Nanotech Machines incorporate the latest precision engineered state-of-the-art designs, providing significantly advanced features not offered by our competitors. Even with these unique advantages, our prices and deliveries are still very competitive.

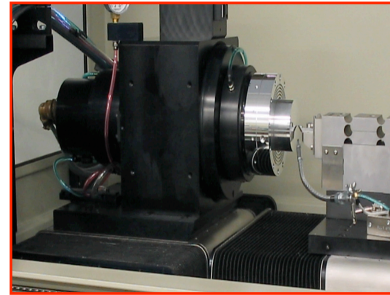
- Liquid-cooled, temperature controlled, Professional Instruments groove-compensated air bearing workspindles for long-term stability and unparalleled accuracy. Thermal stability is extremely important for your workholding spindle. If you have spindle growth from thermal expansion, it can result in tilt motion or transfer of heat to the slideways, both of which will adversely affect performance.
- Windows NT based CNC front-end with operating screens and control panels that resemble a Fanuc CNC (for ease of training and operation).
- Athermalized scale mounting devices & spindle housings for enhanced thermal stability.
- Hydrostatic oil bearing grinding spindles which provide unmatched stiffness and damping characteristics (critical to sustainable deterministic microgrinding of optical components).
- On-machine Workpiece Measurement & Error Compensation System with unique aspheric algorithm correction that is unequalled in accuracy and repeatability.
- A host of unique accessories including fully automated LVDT and Optical Tool Set Stations with on-screen viewing, and a parallel motion Micro Height Adjust Tool Holder with unprecedented stiffness at the cutting tool.

Application Report

Aluminum (Al)



Moore Nanotech® 250UPL



Objective: To quantify surface finish and form results obtainable on Aluminum using the Nanotech 250UPL.

Process:

- 2-Axis Single Point Diamond Turning

Part Configuration:

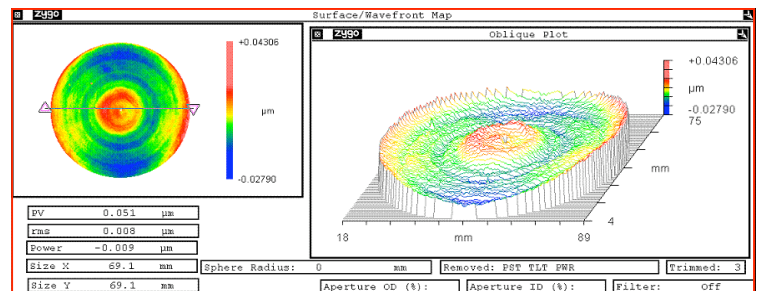
- **Material:** Aluminum
- **Diameter:** 75 mm
- **Radius:** 250 mm
- **Surface Type:** CX Spherical

Machining Parameters:

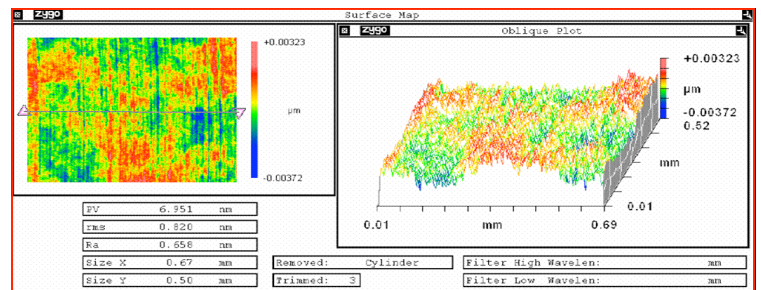
- **Spindle RPM:** 2000
- **Finish Feedrate:** 7.5 mm/min
- **Finish Depth of Cut:** 2 μm
- **Coolant:** Odorless Mineral Spirits

Tool Configuration:

- **Radius:** 0.75 mm
- **Top Rake:** 0 Degree



Form Accuracy: PV = 0.051 μm



Surface Finish: Ra = 0.658 nm



Moore Nanotech® 250UPL

Application Report

Calcium Fluoride (CaF₂)



Objective: To quantify surface finish and form results obtainable on CaF₂ using the Nanotech 250UPL.

Process:

- 2-Axis Single Point Diamond Turning

Part Configuration:

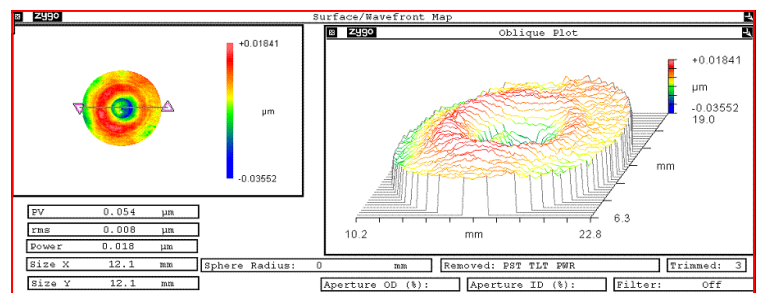
- **Material:** CaF₂
- **Diameter:** 24 mm
- **Radius:** 200 mm
- **Surface Type:** CX Sphere

Machining Parameters:

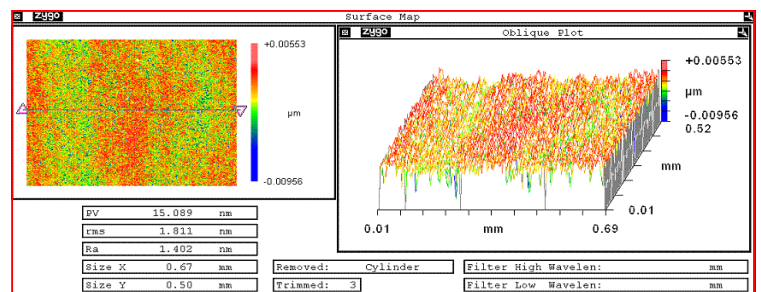
- **Spindle RPM:** 2000
- **Finish Feedrate:** 2.5 mm/min
- **Finish Depth of Cut:** 1 μm
- **Coolant:** Odorless Mineral Spirits

Tool Configuration:

- **Radius:** 0.635 mm
- **Top Rake:** - 25 Degree



Form Accuracy: PV = 0.054 μm



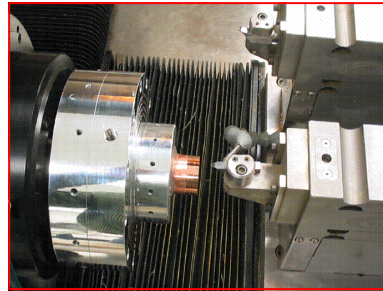
Surface Finish: Ra = 1.402 nm



Moore Nanotech® 250UPL

Application Report

Copper (Cu)



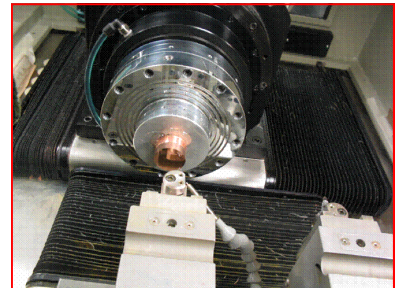
Objective: To quantify surface finish and form results obtainable on OFHC Copper using the Nanotech 250UPL.

Process:

- 2-Axis Single Point Diamond Turning

Part Configuration:

- **Material:** OFHC Copper
- **Diameter:** 30 mm
- **Radius:** 200 mm
- **Surface Type:** CX Spherical

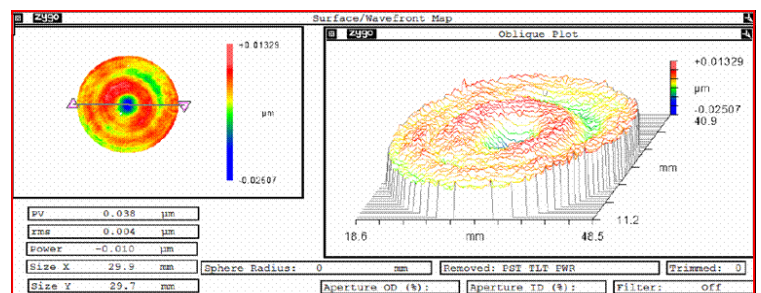


Machining Parameters:

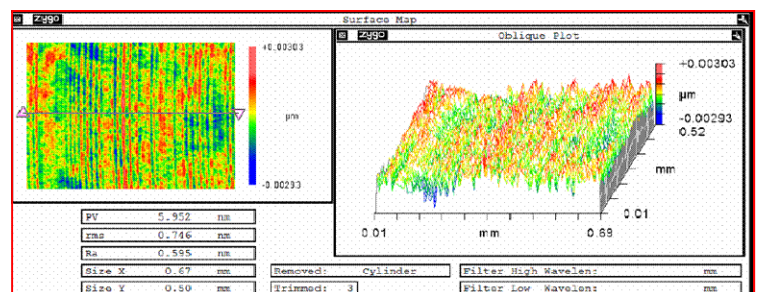
- **Spindle RPM:** 4000
- **Finish Feedrate:** 5 mm/min
- **Finish Depth of Cut:** 0.5 μm
- **Coolant:** Odorless Mineral Spirits

Tool Configuration:

- **Radius:** 1.5 mm
- **Top Rake:** 0 Degree



Form Accuracy: PV = 0.038 μm



Surface Finish: Ra = 0.595 nm



Moore Nanotech® 250UPL
With Shear Damped Air Isolation System

Application Report

Electroless Nickel (EINi) (Plated on Steel Substrate)



Objective: To quantify “champion” surface finish and form accuracy obtainable in electroless nickel plating using the Nanotech 250UPL.

Process:

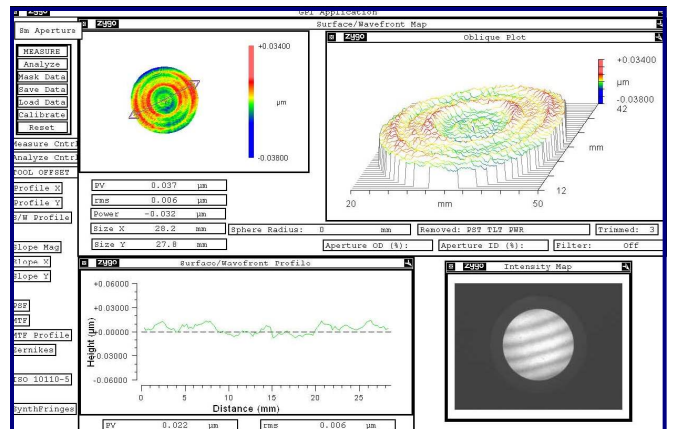
- 3-Axis Tool Normal Diamond Turning (XZB)

Advanced Optional Accessory:

- Shear Damped Air Isolation System

Part Configuration:

- **Material:** Electroless Nickel
- **Diameter:** 30 mm
- **Radius:** 30 mm



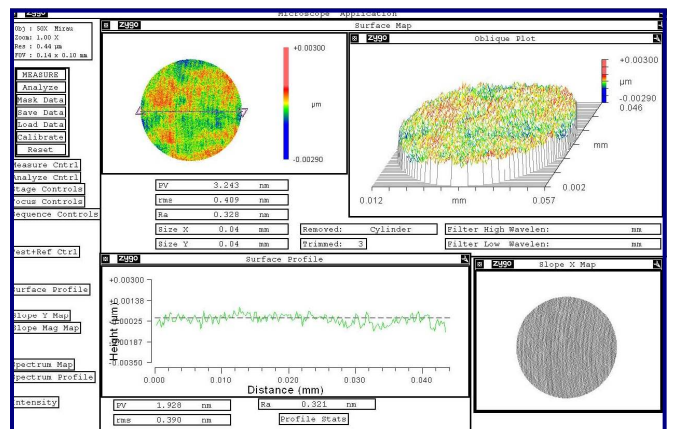
Form Accuracy: PV = 0.037 µm

Machining Parameters:

- **Spindle RPM:** 1550
- **Finish Feedrate:** 1.0 mm/min
- **Finish Depth of Cut:** 3 µm
- **Coolant:** Odorless Mineral Spirits

Tool Configuration:

- **Radius:** 0.76 mm
- **Top Rake:** 0 Degree



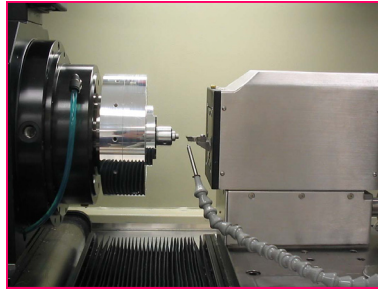
Surface Finish: Ra = 0.328 nm
PV = 3.243 nm



Moore Nanotech® 250UPL

Application Report

Electroless Ni (EINi)



Objective: To quantify surface finish and form results obtainable on EINi using the NFTS-6000 Fast Tool Servo on the Nanotech 250UPL.

Process:

- Nanotech NFTS-6000 Machining

Part Configuration:

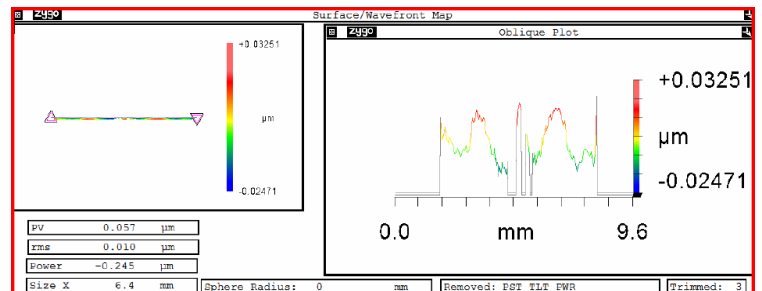
- **Material:** Electroless Nickel Plating
- **Diameter:** 6 mm
- **Radius:** 8.6 mm / 13 mm CX
- **Surface Type:** Toric

Machining Parameters:

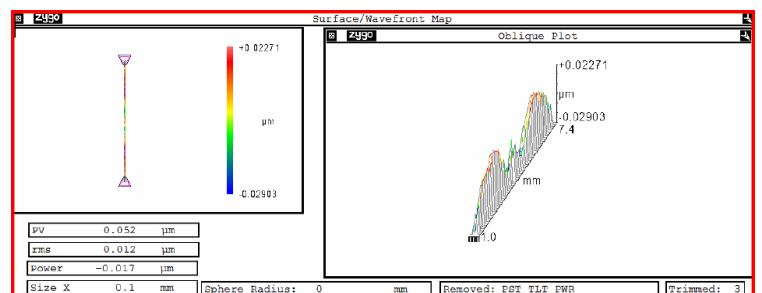
- **Spindle RPM:** 1000
- **Finish Feedrate:** 2 mm/min
- **Finish Depth of Cut:** 2 μm
- **Coolant:** Odorless Mineral Spirits

Tool Configuration:

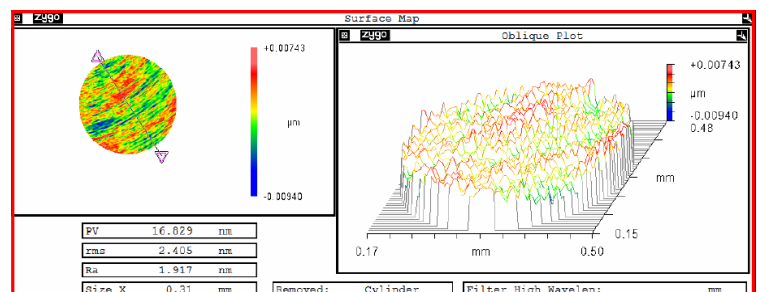
- **Radius:** 0.257 mm
- **Top Rake:** 0 degree



Form Accuracy: PV = 0.057 μm , 8.6mm Rad



Form Accuracy: PV = 0.052 μm , 13mm Rad



Surface Finish: Ra = 1.917 nm

Application Report

Germanium (Ge)



Moore Nanotech® 250UPL

Objective: To characterize absolute machine performance in terms of surface finish and form accuracy using Ge

Process:

- 2-Axis Single Point Diamond Turning

Part Configuration:

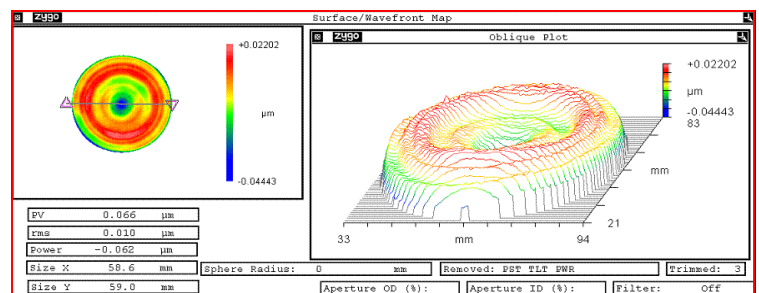
- Material: Ge
- Diameter: 60 mm
- Radius: 250 mm
- Surface Type: CX Sphere

Machining Parameters:

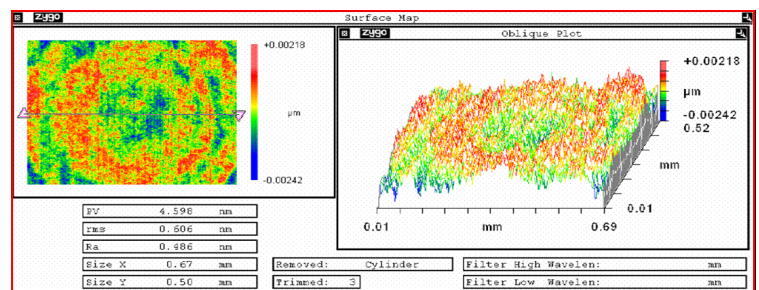
- Spindle RPM: 2500
- Finish Feedrate: 2 mm/min
- Finish Depth of Cut: 2 μm
- Coolant: Odorless Mineral Spirits

Tool Configuration:

- Radius: 0.635mm
- Top Rake: - 25 Degree



Form Accuracy: PV = 0.066 μm



Surface Finish: Ra = 0.486 nm



Moore Nanotech® 250UPL

Application Report

Zinc Selenide (ZnSe)



Objective: To quantify surface finish and form results obtainable on ZnSe using the Nanotech 250UPL.

Process:

- 2-Axis Single Point Diamond Turning

Part Configuration:

- **Material:** ZnSe
- **Diameter:** 50 mm
- **Radius:** 267 mm
- **Surface Type:** CX Sphere

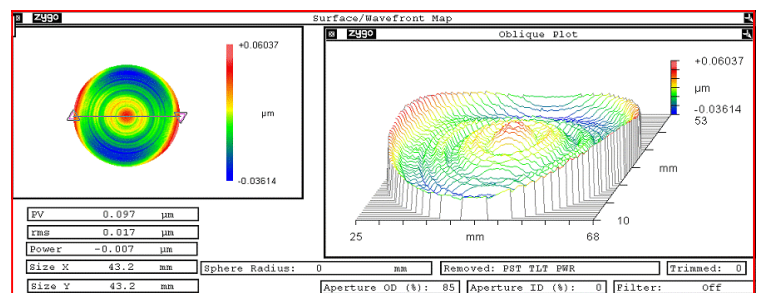


Machining Parameters:

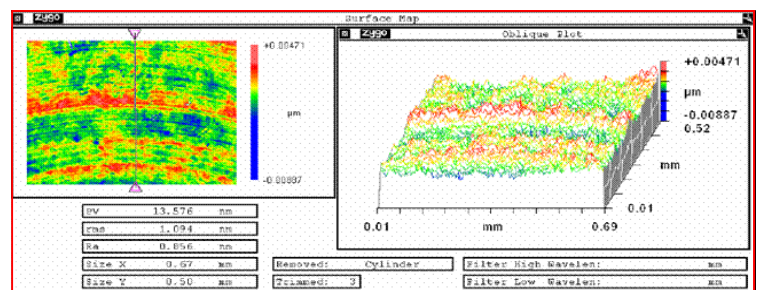
- **Spindle RPM:** 2500
- **Finish Feedrate:** 2 mm/min
- **Finish Depth of Cut:** 4 μm
- **Coolant:** Odorless Mineral Spirits

Tool Configuration:

- **Radius:** 0.635 mm
- **Top Rake:** - 25 degree



Form Accuracy: PV = 0.097 μm



Surface Finish: Ra = 0.856 nm

16 September 2004

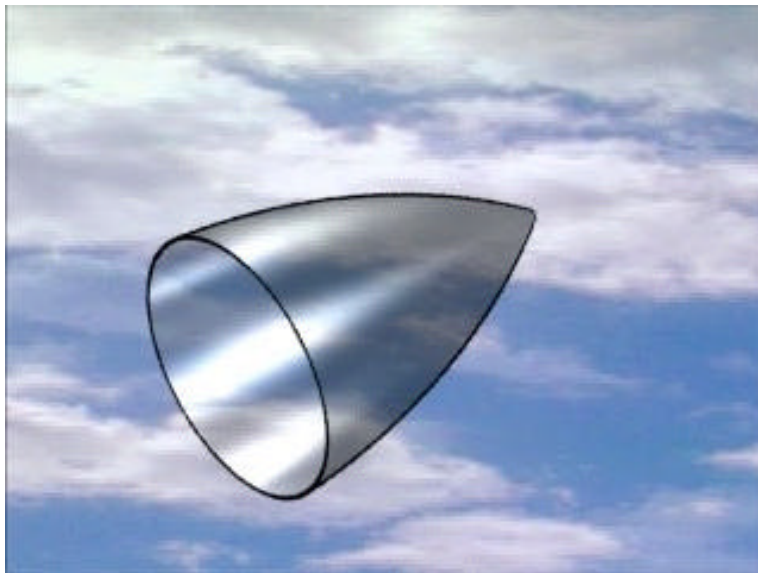
TECHNOLOGY DEMONSTRATION BRIEF

CONFORMAL OGIVE ALON™ DOME FABRICATION

Keywords:

Conformal, freeform, optics, ogive, ALON , domes, near-net-shape castings, infrared transmitting ceramics

This brief will describe a successful project at the Center for Optics Manufacturing (COM) to demonstrate a conformal optics manufacturing process to deterministically microgrind a freeform ogive missile dome of ALON ceramic from a near-net-shape cast blank. The dome is 6.45 inches tall and 4.7 inches wide at the base. The concave surface was an off axis sphere, and the convex surface was an asphere. Both surfaces transitioned to a sphere at their apex.



Contact:

John Schoen
Acting Director
Tel: 585-275-8296
Email: schoen@LLE.rochester.edu

Fabrication Processes:

A near net shape molded dome of ALON was provided in an oversized condition. The dome's shapes were then deterministically contour microground with toric shaped grinding wheels on the convex surface, and ball shaped grinding wheels on the concave surface. For added stiffness and positional accuracy during grinding, COM leveraged and applied the technology the Moore Nanotech 500FG multi-axis freeform machining platform developed in the DARPA Precision Conformal Optics Technology program.

The following presents the steps used to fabricate the dome.

- The dome blank was received molded oversized to the final shape, per Figure 1



Figure 1: ALON dome as near net shape

- The first step was to block the blank into a conforming fixture using UV adhesive for processing the concave surface (see figure 2). The first grinding step was to grind a flat on the base, and bring the dome to the correct height.

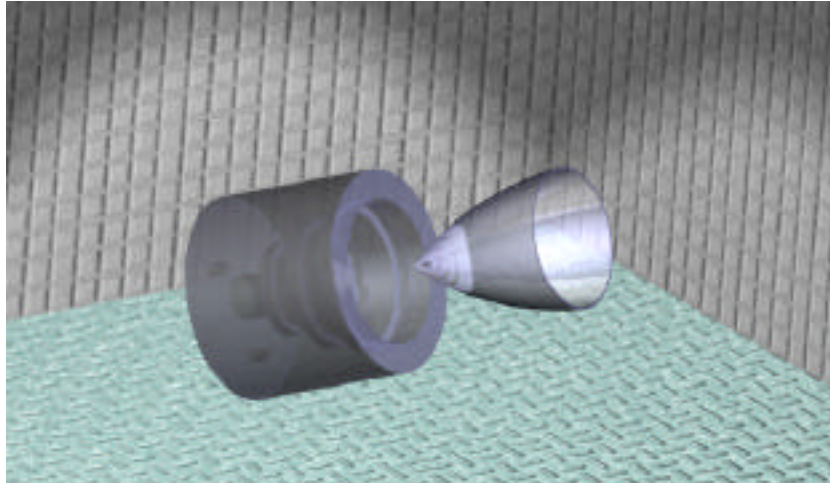


Figure 2: Computer model of ALON dome and fixture for concave side processing.

- The second step was to grind (FG500) the concave surface using ball tools. The surface would be referenced to the flat base that was ground in the previous step. To accomplish this task, a series of different size ball tools were used to reduce tool wear during the grinding cycle, and to maximize grinding efficiency.



Figure 3: Examples of ball tools grinding ALON dome, and various ball tool configurations.

- The final step for the concave surface was to develop a hybrid conventional polishing process it before deblocking. A tool was designed and made by a rapid prototype machine located at COM's facility. The tool was made with a shorter radius to accommodate the thickness of double-sided foam tape, and a polyurethane pad with a diamond slurry worked the best to remove the sub-surface damage and "shine" the surface. Figure 4 shows this process.

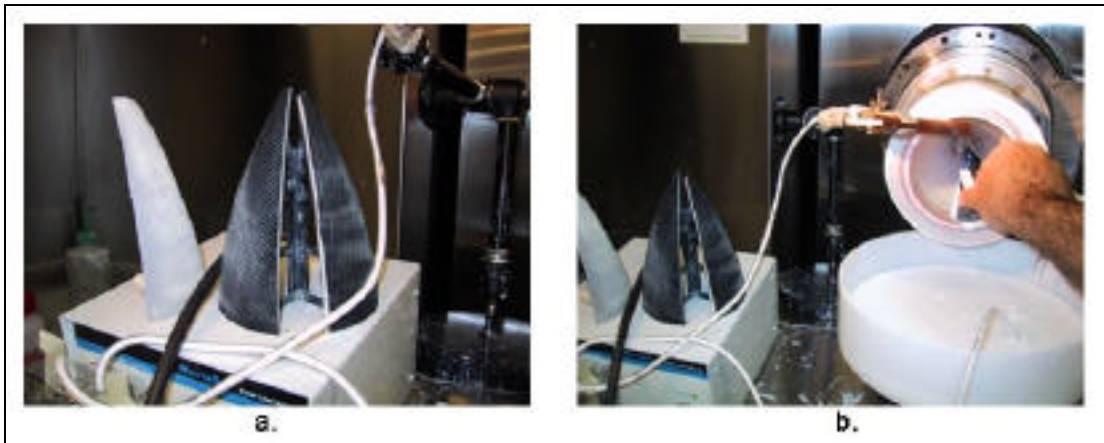


Figure 4: a.) Polishing tools with various polyurethane pads attached. b.) Polishing tool was hand held during polishing operation.

- Once the concave side was complete, the dome was deblocked and inverted to grind the convex surface. The fixture for the convex surface held the dome by the concave curve with the adhesive, and was referenced by optical contact with the base to try and obtain the best tilt accuracy. Figure 5 shows this process.

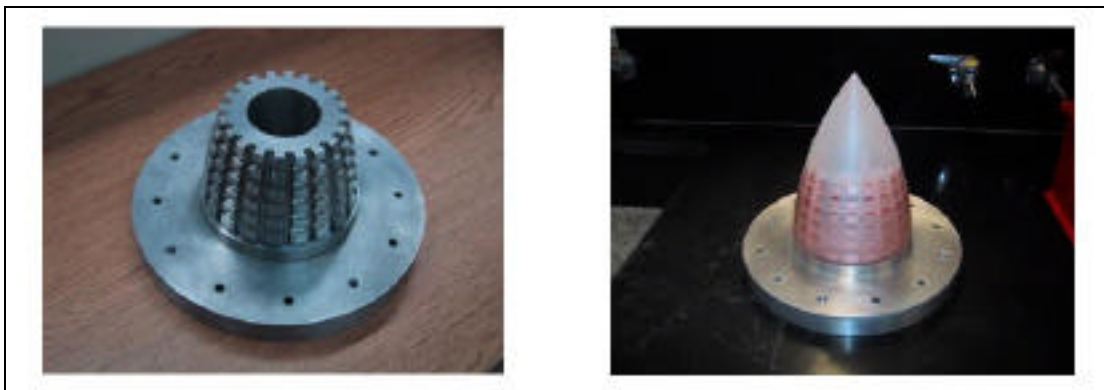


Figure 5: Blocking fixture for the convex surface processing, and dome mounted to fixture.

- The dome's convex surface was then ground to final shape with two torrid shaped contour grinding wheels using a 3-axis motion (X, Z and B). Figure 6 depicts this process on the Moore FG500 freeform machine platform.

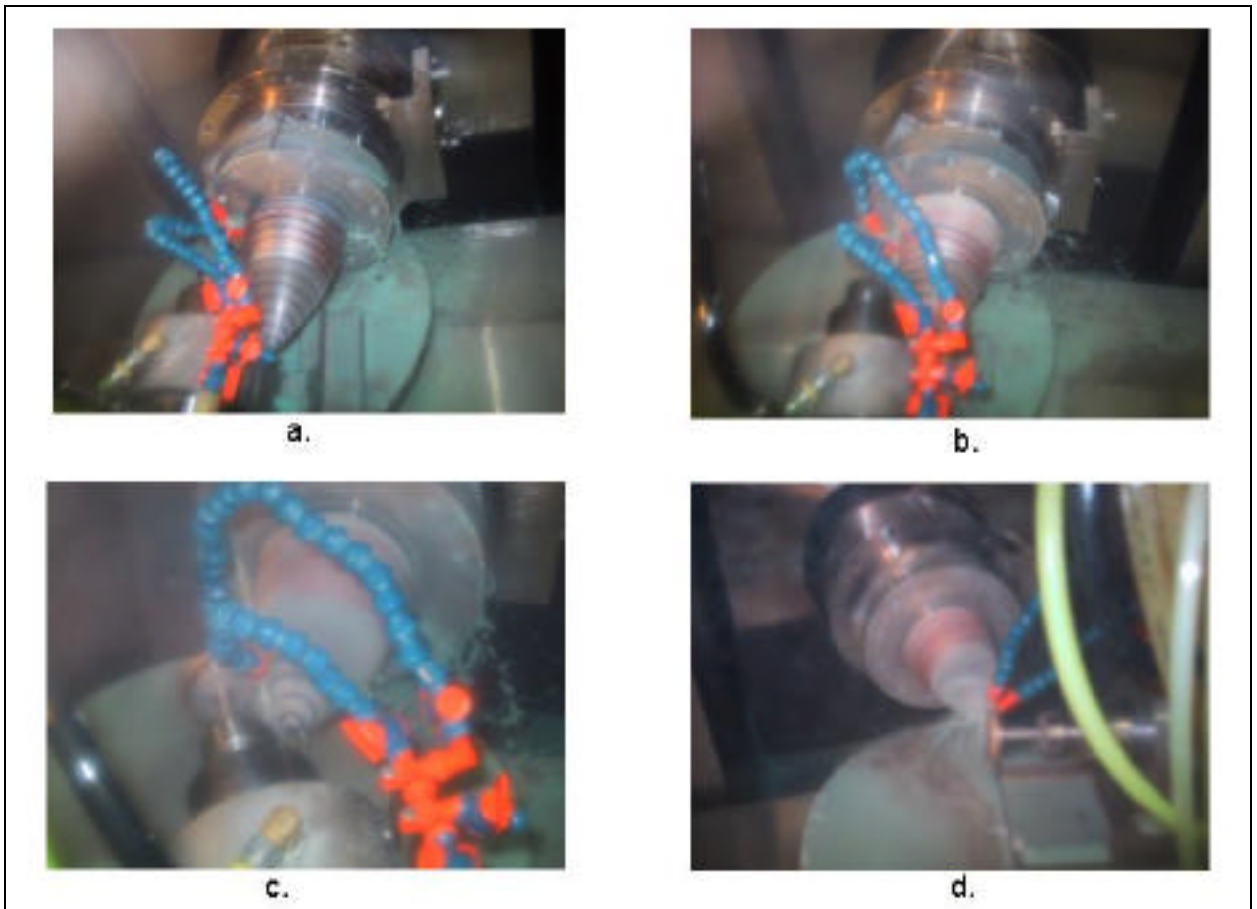


Figure 6: Progression of grinding wheel for contour grinding the convex surface of the ALON dome.

- Once the convex surface of the dome was ground to final specifications, it was hand polished to remove the residual sub-surface damage. The dome was left blocked on its fixture, and placed on a single spindle polisher. There, the same process was used as described in step 3. Figure 7 shows the finalized dome.



Figure 7: Finished ALON dome on mounting fixture.

Current Development Efforts (2004):

COM's next focus has been to follow the successful grinding effort and to explore, develop and refine affordable and deterministic finishing/polishing processes for these conformal ogive shapes and the diverse range of IR ceramics such as ALON , Spinel, Zinc Sulfide and/or nanograined alumina. These materials have relevance to DoD joint services and programs in the areas of transparent armor and missile systems.

A new compliant sub-aperture optical finishing technique is being investigated for the removal of mid-spatial frequency artifacts and smoothing of hard polycrystalline infrared ceramics for aspheric applications and conformal shaped optics. The Ultra-Form concept was developed by Optipro Systems, Ontario, NY, and is a joint process development effort with the Center for Optics Manufacturing (COM).

[Optipro Systems, Ontario, NY has been involved with deterministic processing programs since the inception of COM and was one of the first companies to commercialize the revolutionary Opticam series of optical grinding platforms. Optipro has also provided significant in-kind support to this new effort in equipment, metrology and engineering support.]

Developmental Superfine Platform (In-kind loan from Optipro Systems)



The Ultra-Form tool is a pressurized, elastomeric bladder in the shape of a toroid. Finishing pads are attached to the periphery, allowing the use of a wide variety of pad materials and abrasive selections.

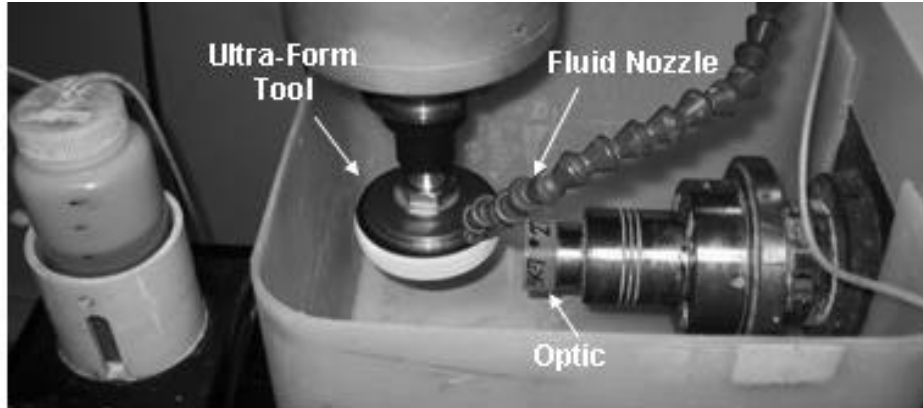
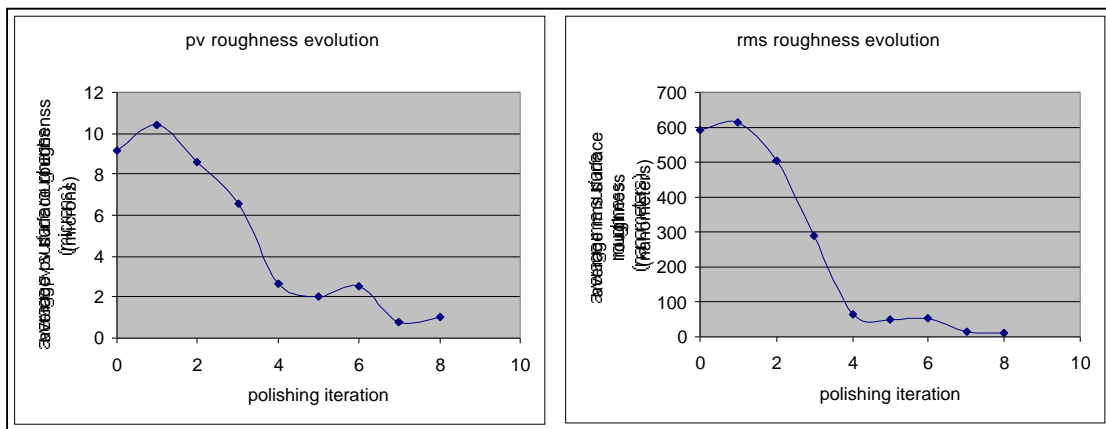


Figure 1: Ultra-Form process

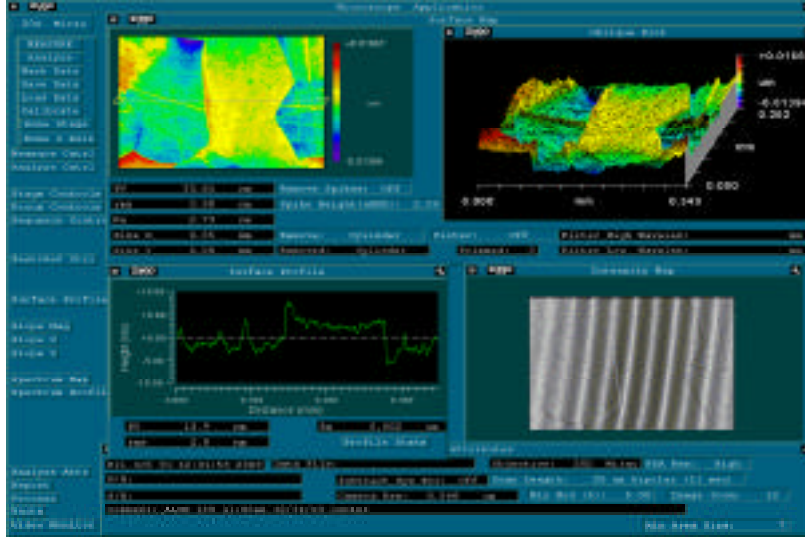
Initial development emphasis has been placed on demonstrating the reduction of surface roughness, removal of mid-spatial artifacts and understanding the material removal function and associated parameters.

For ALON™ (from Surmet Corporation), which is a hard polycrystalline ceramic material, a diamond developmental pad was found that performed extremely well. With this pad we were able to remove sub-surface damage from ALON™, reduce the rms surface roughness below 10 nanometers and not induce any grain highlighting.



Roughness evolution of ALON™ using the Ultra-Form tool. Measurements are an average of 5 data points taken across the surface on a Zygo NewView 5000.

Promising ALON Results on Optipro CpX125 with 3M diamond pad



COM is currently conducting experimentation and materials process development for:

- ALON (Surmet, previously Raytheon),
- Spinel (Surmet and Technology Assessment and Transfer)
- Nano-grained alumina (CeraNova)

Future Frontiers and Peril in 2005

COM's future objectives remain directed to developing and implementing affordable processes for the manufacture of precision optical shapes with an emphasis on emerging IR ceramics.

These efforts involve leveraging a core competency of material science and the relationship to fabrication, finishing solutions employing new and novel approaches such as the above Ultra-Form process and Jet-Magnetorheological finishing.

Support is essential to continue these efforts with our industrial partners and leverage COM's assets of fabrication expertise and the resources of the University of Rochester.

The future of COM is in jeopardy and will close in early 2005 without further support and funding for these efforts. Information regarding COM is attached.

Contact:

John M. Schoen, Acting Director

Tel: (585) 275-8296 • Fax: (585) 275-7225 • Email: schoen@LLE.rochester.edu

Overview of the Center for Optics Manufacturing

The University of Rochester's Center for Optics Manufacturing (COM), established in 1990, is a nationally supported, award-winning university-industry-DoD research and development alliance that is modernizing precision optics manufacturing technology. The Army has funded COM, a DoD Center of Excellence for Optics, on a yearly basis since its inception. Part of the Army's Manufacturing Science and Technology (ManTech) program, COM is an important element of the DoD strategy to develop and acquire affordable equipment for the warfighter, and to do so with dramatically reduced cycle time using commercial processes. COM fulfills this objective by systematically identifying and attacking manufacturing cost drivers and technology shortfalls that prevent the application of advanced optical shapes in next-generation optical systems. COM's resources are its skilled staff, a large pool of University faculty and students, and industrial collaborators in small and large companies throughout the US.

Awards and Accomplishments

- DoD Manufacturing Technology Achievement Award in both 1992 and 2000
- Photonics Circle of Excellence Award in 1993 and 2000
- Laser Focus Commercial Technology Award in 1993 and 2000
- R&D 100 Award in 2001 for breakthrough optics manufacturing technology developments
- Over 150 COM-developed machines in commercial use on factory floors throughout the US

Facilities and Research Programs

COM occupies 10,000 ft² at the Center for Optoelectronics and Imaging on the University's South Campus. Experimental and commercial CNC precision grinding and polishing machines are located in an open "shop floor" area. Here, teams study the manufacturing processes for finishing spheres, aspherics and conformal optics from an array of glasses, crystals and polycrystalline materials. Fundamental to this research is the development of scientific rule-based methods for the achievement of low subsurface damage in rapid grinding to shape, followed by rapid polishing to sub-nanometer roughness levels with surface figure errors at or below 0.1 micron. Optics metrology is carried out in a separate area equipped with an array of state-of-the-art instruments for evaluating surface form and roughness. A third lab is devoted to slurry fluid chemistry issues in the Magnetorheological Finishing (MRF) process that was invented at COM in the mid-1990's. COM's current emphasis is on process improvements for the manufacture of optics from hard, polycrystalline ceramics that offer multi-spectral imaging capability to viewing systems in tanks and aircraft.

DYNAMIC MODELING AND ANALYSIS OF MOTORIZED MILLING SPINDLES FOR OPTIMIZING THE SPINDLE CUTTING PERFORMANCE

Dr. Sinan Badrawy, Engineering Manager
Moore Nanotechnology Systems, LLC

ABSTRACT

Future machine tools have to be highly dynamic systems to sustain the required productivity, accuracy and reliability. Both the machine tool system and the spindle system (Spindle/Tool-holder/Tool) are necessary to be optimized for their usability or cutting performance to meet the productivity and availability requirements of the end user. However, in industrial practice, the availability of a machine system is significantly influenced by the spindle cutting performance and its reliability. The focus of this paper is to show a design methodology for optimizing the dynamic cutting performance of spindles by establishing the relationship between the required cutting parameters and the basic design principles of a spindle/tool-holder/tool system. In addition, the influence of the spindle cutting performance, which is determined by the tooling parameters (such as spindle/tool holder interface, tool holder mass, etc.) will be shown in this paper.

NOMENCLATURE

b_{cr}	[mm]	Critical axial depth of cut
c	[Ns/mm]	Viscose damping
c_M	[cm ³ /min/kW]	Material cutting factor
D_{Tool}	[mm]	Tool diameter
F	[N]	Force
f_n	[Hz]	Natural frequency
f_R	[Hz]	Resonance frequency
f_z	[mm/rev]	Chip per tooth
$G(j\omega)$	[mm/N]	Dynamic transfer function
k	[N/mm]	Stiffness
k_{cb}	[N/mm ²]	Specific dynamic cutting coefficient
MRR_{cr}	[cm ³ /min]	Critical material removal rate
n_{Base}	[rpm]	Spindle base speed
P_{cr}	[kW]	Critical machining power
P_{S1}	[kW]	Continuous spindle power
S_{pe}	--	Spindle cutting performance factor
Y	[mm]	Displacement response
Z	--	Number of teeth
Z_{avg}	--	Average number of teeth in cut
ξ	--	Damping ratio
μ	--	Machining overlapping factor (for milling $\mu = 1$)

INTRODUCTION

Two common test methods for evaluating the cutting performance of spindles and machine tool systems are being applied in industry today [1, 2, 3, 4]. The first method determines the availability of the specified continuous P_{S1} rated spindle power over a given speed range through performing horsepower cuts. The second method is to predict or perform a variety of test cuts with a defined tool and workpiece material to determine the chatter free cutting speed zones (lubing diagrams) and their critical axial depth of cut [5, 6, 7, 8]. However, both of these methods are influenced by a variety of cutting parameters, such as tool wear conditions, tool geometry, etc. Neither of these methodologies can establish a direct comparison of the cutting performance between different spindle designs nor can they be applied in the conceptual design phase of the machine tool and/or the spindle system.

In order to compare different milling spindle designs or concepts independently from their application requirements as well as their power and speed characteristics, a methodology has to be established which allows defining the amount of the available spindle power that can be utilized for chip removal under no chatter conditions at any given spindle speed. In other words, the spindle cutting performance S_{pe} can be defined as the ratio between the critical machining power P_{cr} which can be utilized for chip removal, chatter free, at the spindle base speed n_{Base} for a given workpiece material, and the available continuous spindle power P_{S1} :

$$S_{pe} = \frac{P_{cr}}{P_{S1}} \quad (1)$$

The critical machining power P_{cr} is determined with:

$$P_{cr} = MRR_{cr} \cdot c_M \quad (2)$$

while the Critical Material Removal Rate (MRR_{cr}) is:

$$MRR_{cr} = b_{cr} \cdot f_z \cdot z \cdot n_{Base} \cdot D_{Tool} \quad (3)$$

Table 1 shows the values for some material cutting factors c_M which are commonly machined.

Material	c_M [cm ³ /min/kW]	k_{cb} [N/mm ²]
Aluminum	70	83
Gray Cast Iron	40	200
Alloy Steel	30	355
Titanium	25	387

Table 1: Examples for c_M and k_{cb} values for commonly machined materials

The critical axial depth of cut value b_{cr} is determined through the maximum negative real part $Re_{\max}\{G(j\omega)\}_{neg}$ of the dynamic transfer function of a spindle/tool-holder/tool system (Figure 1) [5]. This value reflects a chatter free cutting condition across the entire spindle speed range of a spindle/tool-holder/tool system. The well known stability lobe diagram, which predicts the

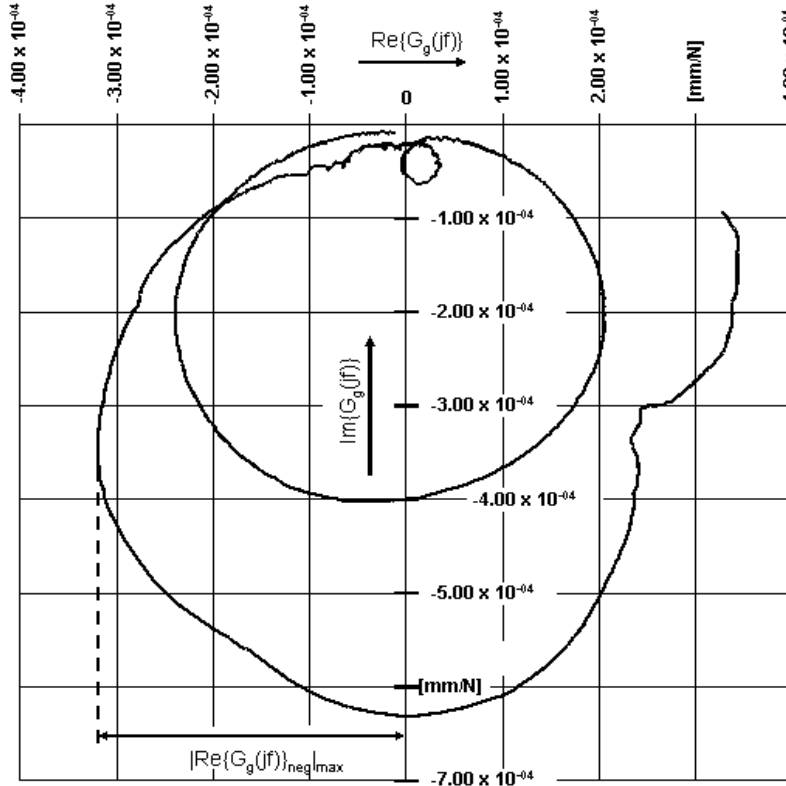


Figure 1: Example of the maximum negative real part of a dynamic transfer function for a spindle/tool-holder/tool system

stability of the spindle/tool-holder/tool system as a function of the spindle speed shows this value (See [Figure 2](#)) [9, 10, 11]. Chatter and chatter free regions are seen depending on the selected spindle speed range. However, by selecting an axial depth of cut equal to or less than the critical axial depth of cut, a chatter free cutting condition can be achieved. This value is determined for a slotting cut through the relationship:

$$b_{cr} = \frac{1}{(1 + \mu) \cdot k_{cb} \cdot z_{avg} \cdot |\text{Re}\{G(j\omega)\}_{neg|max}} \quad (4)$$

Table 1 shows values for the specific dynamic cutting coefficient k_{cb} for commonly machined materials.

The spindle cutting performance value S_{pe} determines the amount of the available spindle power, which can be utilized for chip removal. If S_{pe} is less than 1, the available continuous spindle power P_{S1} can only be utilized partially for chip removal. The spindle/tool-holder/tool system will chatter before reaching its maximum continuous spindle power P_{S1} . If S_{pe} is equal to/or greater than 1, the maximum continuous spindle power can be utilized completely for chip removal under no chatter conditions.

As shown in the above equations, the spindle cutting performance S_{pe} is not only influenced by the characteristics of spindle design and the spindle/tool-holder/tool system configuration ($|\text{Re}\{G(j\omega)\}_{neg|max}$), but also by the selected cutting parameters such as the chip per tooth, spindle speed and the material properties of the workpiece. To optimize the spindle cutting performance

all of the above influencing parameters have to be taken into consideration. For example, the cutting performance of a given spindle/tool-holder/tool system can be increased from $S_{pe} = 0.7$ to $S_{pe} = 1$ by simply increasing the chip per tooth from 0.13 mm/rev to 0.18 mm/rev.

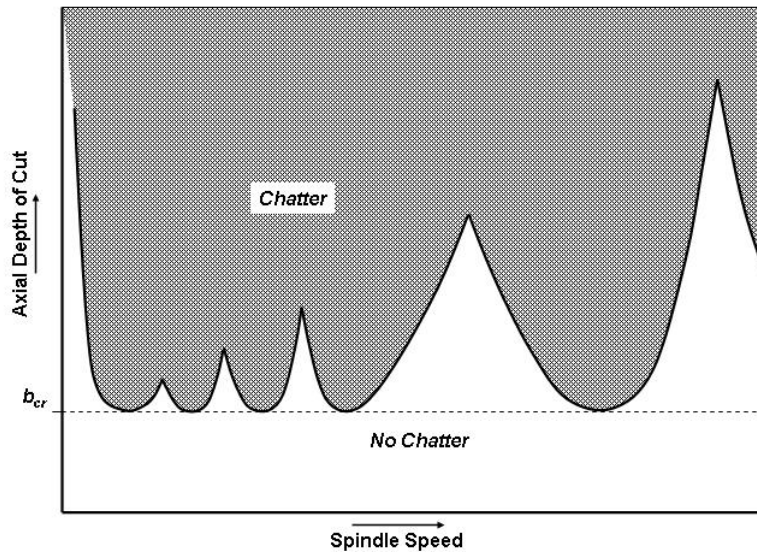


Figure 2: Example of a stability lobe diagram

However, besides changing the technological cutting parameters to increase the cutting performance of a given spindle/tool-holder/tool system, this paper will discuss the influences regarding the conceptual design of milling spindles as well as the configuration of the spindle/tool-holder/tool system to the overall spindle cutting performances. This is demonstrated on an example of a motorized high speed milling spindle which can be configured with different spindle/tool-holder interfaces as well as different types of bearing stiffness.

DYNAMIC MODELING OF MOTORIZED HIGH SPEED MILLING SPINDLES

In order to define the influence of the spindle/tool-holder/tool system configuration of the spindle cutting performance, a Finite Element Model of a motorized 24,000 rpm / $P_{SI}=30$ kW high speed spindle was modeled by using the FEM-Software ADAMS. Figure 3 shows the conceptual design of the analyzed spindle.

This spindle can be equipped with different configurations depending on the required maximum spindle speed and power. Such configurations are the spindle/tool-holder interfaces, the continuous spindle power, the bearing types (steel-ball or hybrid ceramic bearings) as well as the spindle/machine tool interface.

In general, the modeled spindle is designed with two 70 mm inner-race diameter front bearings mounted back to front, and one 65 mm inner-race diameter tail bearings mounted in floating bushing which is spring loaded against the two front bearings. Additionally, to increase the

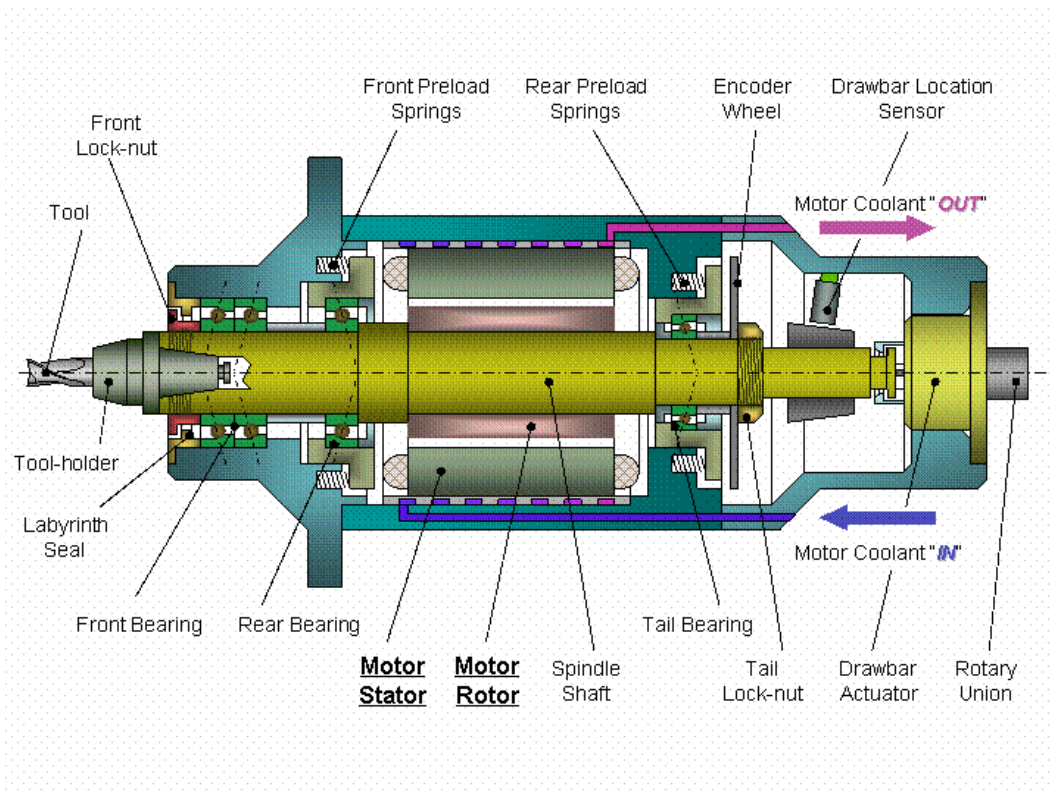


Figure 3: Schematic layout of the analyzed 24,000 rpm, 30 kW high speed spindle.

overall radial spindle shaft stiffness as well as the front bearing axial preload, a rear bearing has been implemented in the front, which is spring loaded against the two front bearings as well. The total axial spindle bearing preload is set at 1800 N. The rotor of an induction-type motor is mounted on the spindle shaft. The continuous power limit P_{S1} is dependent on the heat, which is generated in the stator and rotor. While the generated heat in the stator can be most removed through the water jacket, the heat of the rotor has to pass through the bearings. Due to the temperature limitation of the phenolic ball-cages as well as the required strength of the spindle shaft/rotor interference fit, a maximum continuous spindle power of 30 kW from 5000 to 24,000 rpm cannot be exceeded.

DYNAMIC SPINDLE MODELING WITH FEA

Based on the mechanical model of the spindle design, shown in Figure 3, an FEA model of the spindle shaft was developed using ADAMS software (see Figure 4). The shaft was discretized by multiple beam elements with different cross section geometries. The angular contact bearings were represented by radial and axial linear spring elements with a proper stiffness and damping. The spindle/tool-holder interface was abstracted by two springs at the front and rear of the contact surface as well as by one axial spring element between the spindle and tool-holder, representing the drawbar gripper. Spindle parts, which do not contribute to the spindle stiffness, were simplified as point masses and added onto the shaft to their centers of gravity. Taking advantage of ADAMS, local damping in the springs and the finite elements can be easily counted

and changed. Through applying a virtual impulse force at the modeled tool tip, necessary data for calculating the dynamic compliance of the spindle/tool-holder/tool system can be determined.

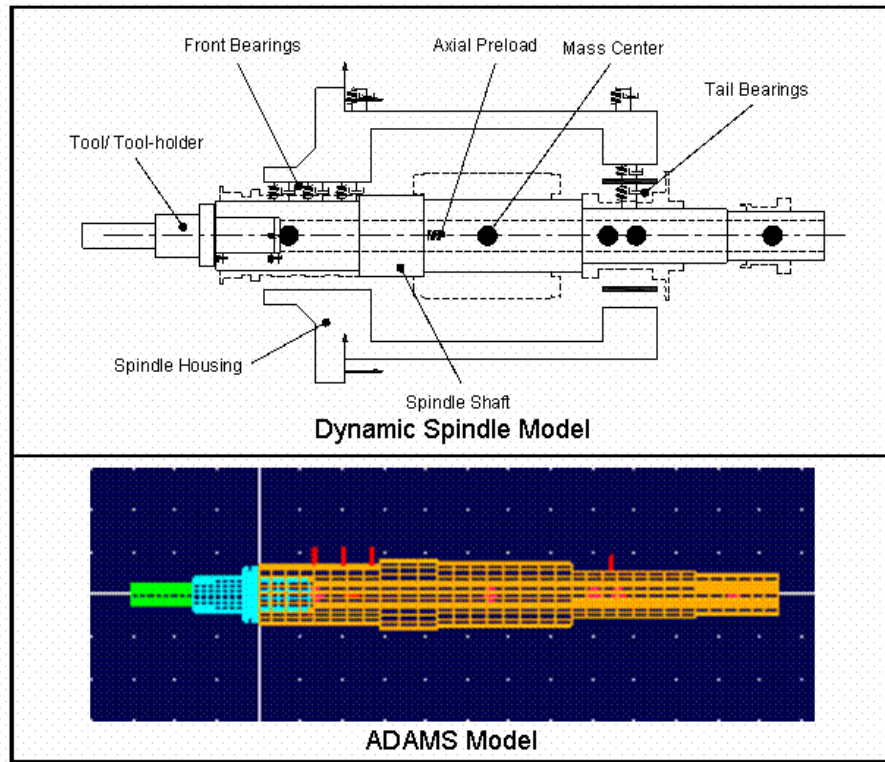


Figure 4: FEA model of the spindle.

DETERMINING THE SPINDLE/TOOL-HOLDER/TOOL SYSTEM DAMPING

Every spindle/tool-holder/tool system consists of multiple mechanical components, which are coupled together and can be represented in a dynamic model as mass, spring and damping elements. While the mass and the spring stiffness determine the natural frequency f_n of the system, the damping element, represented by the damping ratio ξ , governs the resonance increase of the vibration amplitude and with it, the dynamic system stiffness. Therefore, a determination of the local damping ratio ξ or the local viscose damping value c of the spindle/tool-holder/tool system, has paramount importance for modeling the overall dynamic stiffness of a spindle.

Generally, the damping ratio ξ of a dynamic system can be determined by the so-called $\sqrt{2}$ -method from the dynamic compliance curve of the spindle/tool-holder/tool system (see Figure 5) [4]. By determining the maximum compliance of the analyzed mode shape $|1/k|_{\text{R}}$ and its multiplication with $1/\sqrt{2}$ the two frequencies f_1 and f_2 can be obtained. With

$$\xi = \frac{f_2 - f_1}{2 \cdot f_R} \quad (5)$$

the damping ratio of the analyzed mode can be determined.

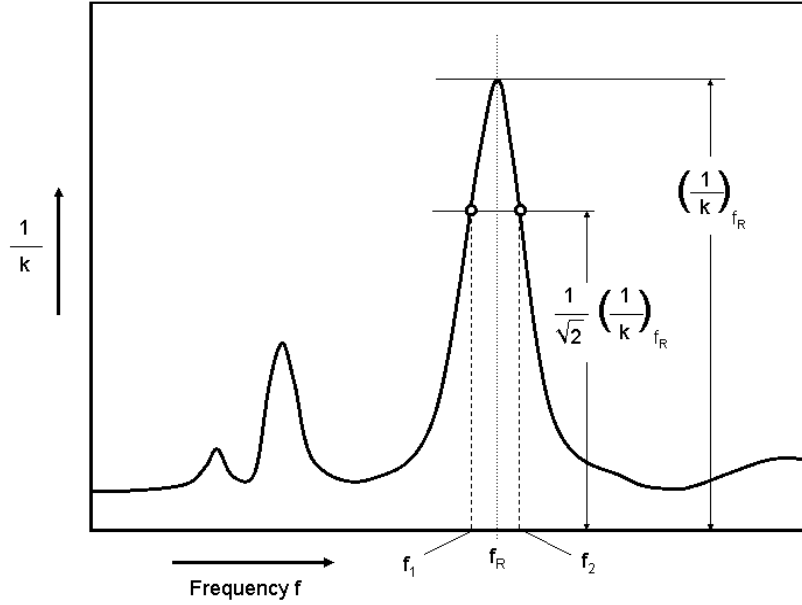


Figure 5: $\sqrt{2}$ -method for determining the damping ratio ξ

Like most FEA modeling software, ADAMS requires the viscose damping c , as a model input value. By knowing the damping ratio ξ as well as the natural frequency f_n of the analyzed mode (Real part of the FRF equal 0), the viscose damping value c can be calculated with:

$$c = 2 \cdot \xi \cdot \frac{k}{f_n} \quad (6)$$

This methodology can normally be used for every resonance increase of a measured dynamic compliance curve. For a boundary condition, a judgment must be made as to whether the compliance of the position being examined is, in addition, materially affected by neighboring resonance points. The frequency difference necessary between neighboring resonance frequencies decreases as the damping ratio reduces, i.e. with a narrower spread of the resonance increase.

The determination of the damping ratio ξ for a spindle/tool-holder/tool system from its dynamic compliance curve using the $\sqrt{2}$ -method is only possible for pronounced conditions of single-mass vibrators, i.e. only when the single resonance peaks are occurring far from each other. To determine the damping ratio between the spindle/tool-holder interface, a spreading of the two resonance peaks of the tool-holder/tool assembly and the spindle/tool-holder/tool system has to be established. As a tool/tool-holder assembly, a solid 2-fluted carbide end-mill with a tool diameter of 25.4 mm was implemented into a CAT #40-taper shrink-fit type tool-holder with an overhang of 76 mm ($L/D = 3:1$). This tool/tool-holder interface has a low dynamic damping ratio and a higher stiffness in comparison to the collet-chuck type tool-holder. Additionally, the total mass of this tool/tool-holder assembly is about 20% less than a collet-chuck type tool-holder assembly, which leads to an additional resonance frequency shift of the tool/tool-holder mode away from the spindle/tool-holder/tool resonance frequency mode. The dynamic compliance function was obtained through measuring the real part ($\text{Re}\{G(j\omega)\}$) and the imaginary part

($\text{Im}\{G(j\omega)\}$) of the FRF (frequency response function) using impact excitation at the tip of the tool and applying the equation

$$\frac{1}{k(\omega)} = \sqrt{(\text{Re}\{G(j\omega)\})^2 + (\text{Im}\{G(j\omega)\})^2} \quad (7)$$

to the measured values. The results of these measurements can be seen in [Figure 6](#).

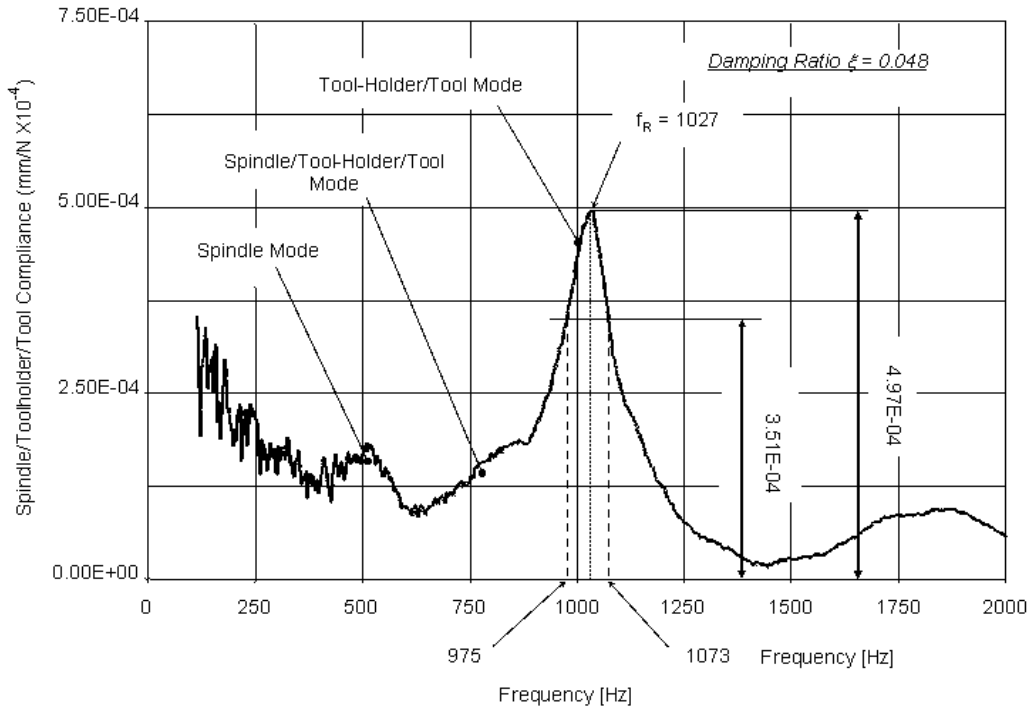


[Figure 6](#): Determining the damping ratio ξ from of the dynamic compliance curve by applying the $\sqrt{2}$ -method

Several prominent modes can be here seen. Analyses through the finite element computation shows that the mode around 512 Hz is the spindle bending mode, referred to in this paper as the spindle/tool-holder/tool mode. The next highest mode at 1027 involves the tool/tool-holder assembly and is referred to as the tool-holder/tool mode. Based on the FRF measurements and the above shown $\sqrt{2}$ -methodology, the damping ratio ξ for the spindle/tool-holder interface can be computed as 0.048.

DETERMINING THE DYNAMIC COMPLIANCES

Modal testing theory has been successfully used for calculating the frequency spectrum of machine tool structures [12]. A frequency spectrum includes the amplitude-frequency characteristic (dynamic compliance) and the phase-frequency characteristic of a system. Frequency characteristic analysis is important to gain an understanding of the dynamic performance of a spindle/tool-holder/tool system especially when the spindle speed has a wide operating range. The dynamic response function can further be used to calculate the stability lobe

diagram to evaluate the dynamic spindle performance. Mathematically, suppose that if the impact force acting on the tool is $F(t)$, the displacement response of the tool tip is $Y(t)$, then the dynamic compliance $G(j\omega)$ of the spindle is defined as

$$G(j\omega) = \frac{\int_0^T Y(t)e^{-j\omega t} dt}{\int_0^T F(t)e^{-j\omega t} dt} = \frac{E_Y(j\omega)}{E_F(j\omega)} \quad (8)$$

where $E_F(j\omega)$ and $E_Y(j\omega)$ are complex energy spectrums of the input force and output displacement. The integrations are the Fourier transform expressions and can be calculated by FFT algorithm [13]. Dividing the complex energy spectrum by the integration time T , we obtain the complex power spectra:

$$\begin{aligned} S_F(j\omega) &= \frac{1}{T} E_F(j\omega) \\ S_Y(j\omega) &= \frac{1}{T} E_Y(j\omega) \end{aligned} \quad (9)$$

After expansion with the complex conjugate, the dynamic compliance can be expressed as

$$\begin{aligned} G(j\omega) &= \frac{S_Y(j\omega)}{S_F(j\omega)} = \frac{S_Y(j\omega) \cdot S_F^*(j\omega)}{S_F(j\omega) \cdot S_F^*(j\omega)} = \frac{S_{YF}(j\omega)}{S_{FF}(\omega)} \\ &= \frac{\text{Re}\{S_{YF}(j\omega)\} + j\text{Im}\{S_{YF}(j\omega)\}}{S_{FF}(\omega)} \end{aligned} \quad (10)$$

where $S_F^*(j\omega)$ is the complex conjugate of $S_F(j\omega)$, $S_{FF}(j\omega)$ is the auto-power spectrum (real), $S_{YF}(j\omega)$ is the cross-power spectrum (complex). The magnitude of $G(j\omega)$ is the dynamic compliance.

MODEL EVALUATION

To evaluate the FEA spindle/tool-holder/tool system model, measurements using impact excitation at the tool tip were performed. [Figure 7](#) shows the dynamic transfer function (real and imaginary part) of the analyzed spindle and the simulation FEA model. About 10 to 20% difference exists due to the omitting of detailed geometry modeling. The purpose of FEA modeling and simulation is not only to define the tendency but also to influence the design parameters (bearing stiffness, spindle/tool-holder interface stiffness and damping, tool geometry, etc.) on the cutting performance; the existing small deviations of the FEA model are insignificant and will not degrade the analytical results.

RESULTS AND DISCUSSION

Generally, the finite element analyses computation of the spindle/tool-holder/tool system shows three dominant mode shapes, which are illustrated in [Figure 8](#). With the given model boundary conditions (stiffness, mass and viscose damping distribution) the first mode, spindle mode,

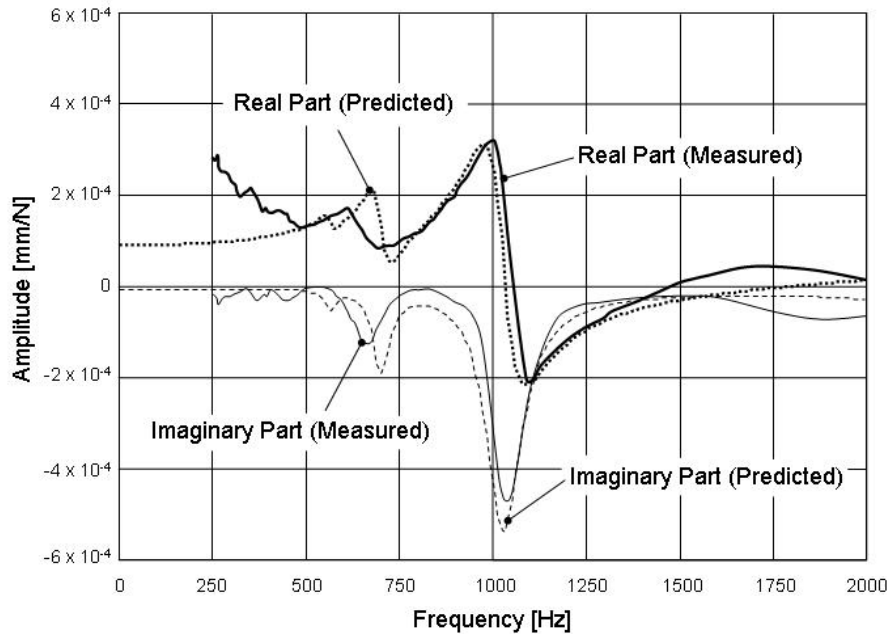


Figure 7: Comparison of the dynamic transfer function between the tap test result and the FEM model simulation

occurred at a resonance frequency of 581 Hz, the second mode, spindle/tool-holder/tool mode, at 720 Hz and the third mode, tool-holder/tool mode, at 1005 Hz. These results were based on a shrink-fit type CAT #40 tool-holder with a 25.4 mm diameter, solid carbide, 2-fluted end mill. The applied stiffness values for the bearings were obtained from the bearing manufacturer, and the stiffness values of the spindle/tool-holder interfaces (CAT #40 HSK 63A and HSK 80F) are based on literature reviews [14, 15, 16, 17 and 18]. The selected stiffness and viscous damping values for this case are given in [Table 2](#).

As discussed earlier, the spindle cutting performance is not only determined by the spindle design but also by tool geometry. [Figure 9](#) shows the computed dynamic compliances of the spindle/tool-holder/tool system for a 25.4 and a 19 mm diameter tool with the same overhang of 76 mm. In both cases, the tool-holder/tool mode shape showed the highest dynamic compliance. The transition from a larger to a smaller tool diameter increased the resonance frequency from 1005 to 1087 Hz and its compliance amplitude. Due to the increase of the resonance frequency and the constant damping ratio of the spindle/tool-holder interface ($\xi=0.048$), the overall width of the resonance peak increases as well.

These results show that the tool diameter has a significant influence on the overall system compliance and the spindle cutting performance. By applying the equations (1 to 4), the spindle cutting performance S_{pe} is for the 19 mm tool diameter 0.39 and for the 25.4 mm tool diameter 0.46. These calculations have been performed for machining aluminum, with a chip load $f_z = 0.25\text{mm/rev}$. Even the predicted maximum negative real part of the FRF for the larger tool was greater than the 19 mm tool diameter ($-2 \times 10^{-4} \text{ mm/N}$ for the 25.4 mm tool and $-1.73 \times 10^{-4} \text{ mm/N}$ for the 19 mm tool), which results in a shallower critical axial depth of cut, the overall material removal rate is higher due to the larger tool diameter. This example shows clearly that

the spindle cutting performance is not only influenced by the spindle design but also by the spindle, tool-holder and tool configuration.

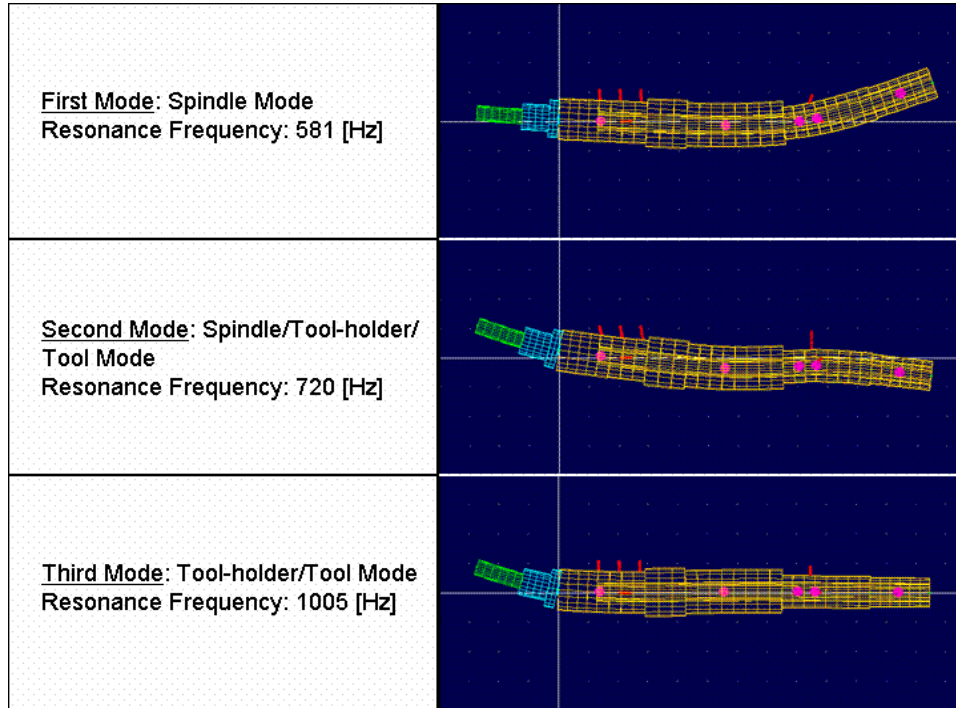


Figure 8: Most dominant mode shapes of the analyzed spindle/tool-holder/tool system

System Component	Stiffness k [N/mm]	Viscose Damping c [Ns/mm]
Spindle/Tool-Holder Interface	Front: 24.0×10^5 Rear: 21.6×10^5	Front: 0.154 Rear: 0.154
Front Bearing	7.75×10^5	0.025
Rear Bearing	7.75×10^5	0.025
Tail Bearing	4.1×10^5	0.025

Table 2: Stiffness and viscose damping coefficients

The influence of the tool-holder type to the spindle cutting performance has been analyzed through modeling three different spindle/tool-holder interfaces (CAT #40, HSK-63A and HSK-80F) on the above described spindle. All these analyzed interfaces can be implemented on a spindle with a 70 mm inner diameter front bearing. The results of these analyses are shown in Figure 10. As evidenced above, the spindle/tool-holder interface stiffness has a major impact on the compliance of the spindle/tool-holder/tool system. The interface type not only effects the dynamic compliance of the most dominant mode but also all the other modes. Further, the HSK-63A as well as the HSK 80F interface shifts the natural frequency of the tool-holder/tool mode to

a higher frequency due to the increase in the interface stiffness, while the natural frequency of the second mode (spindle/tool-holder/tool mode) remains the same.

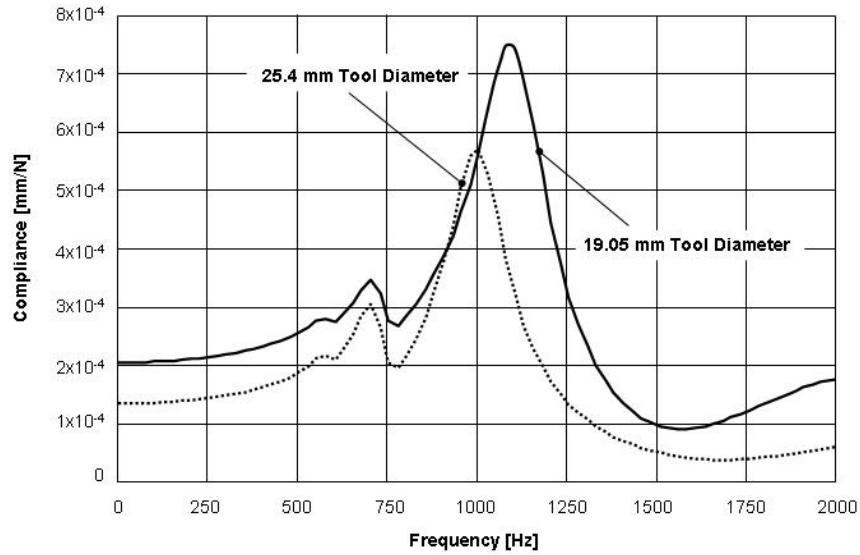


Figure 9: Dynamic compliances of the spindle/tool-holder/tool system for two different tool diameters

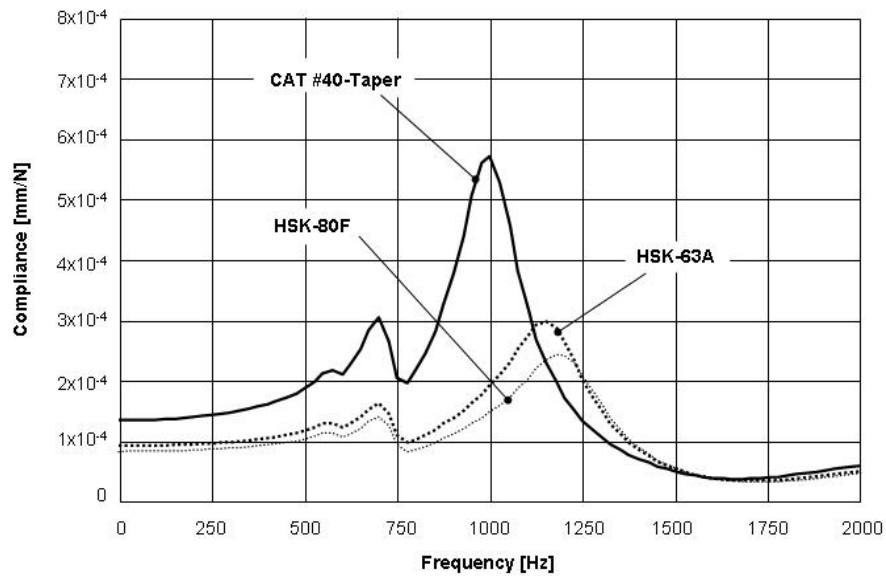
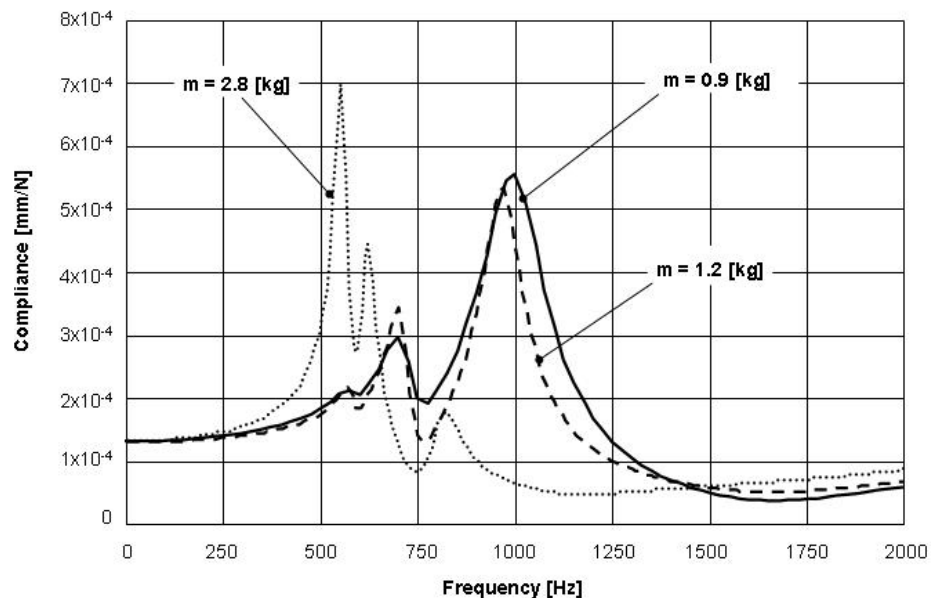


Figure 10: Dynamic compliances of the spindle/tool-holder/tool system for a spindle with CAT #40, HSK 63A and HSK 80F for spindle/tool-holder interface

It is anticipated that by choosing a HSK 63A or HSK 80F interface, a lower dynamic compliance of the tool-holder/tool mode will be seen. Further, the dynamic cutting performance for the above modeled spindle/tool-holder/tool system will increase by 180 % for an HSK 63A interface, due to the smaller predicted maximum negative real part of the FRF (-7.1×10^{-5}). This improvement in the dynamic cutting performances as well as the dynamic stiffness of the tool and tool-holder is mainly caused by the simultaneous fit of the tool-holder flange and the taper to the spindle interface. Additionally, this simultaneous fit also gives the HSK type interface a higher bending moment capability.

Besides the influence of the spindle/tool-holder interface, dynamic FEA computations for determining the influence of the tool-holder mass to the overall dynamic characteristics of the spindle/tool-holder/tool system were performed as well. These analyses were based on three identical CAT #40 type tool-holders with different masses. The first tool-holder represented a shrink-fit type, the second, a collet type (0.3 kg more than the shrink-fit), and the third a hydraulic-chuck type (1.9 kg more than the shrink-fit). All of the analyzed tool-holders were modeled with a 25.4 mm end-mill, which had a tool length (tool tip to tool-holder) of 76 mm. In all three cases the joint stiffness as well as the damping ratio between the tool and tool-holders has been assumed to be the same. The results of these analyses are illustrated in [Figure 11](#). As is evidenced, by increasing the tool-holder mass, the resonance frequency decreases. Especially in the case of the hydraulic-chuck type tool-holder a dramatic frequency shift can be observed. The tool-holder/tool mode shifted from 1005 Hz to 552 Hz, which is below the spindle mode (first mode). In addition, the overall compliance of all modes increased with the tool-holder mass.



[Figure 11](#): Dynamic compliances of the spindle/tool-holder/tool system for three different tool-holder masses

However, the increase of the tool-holder mass has only a minor influence on the spindle cutting performance. [Figure 12](#) shows the real and imaginary parts of the computed dynamic transfer

functions for the shrink-fit and the hydraulic type tool-holders. In the case of the shrink-fit type tool-holder, the third mode (tool-holder/tool mode) dominated the spindle cutting performance (maximum negative real part of the FRF) by increasing the tool-holder mass, while the second mode increases and dominates the overall spindle cutting performance. In both cases, the spindle cutting performance for the analyzed spindle has been determined as $S_{pe} \approx 0.46$.

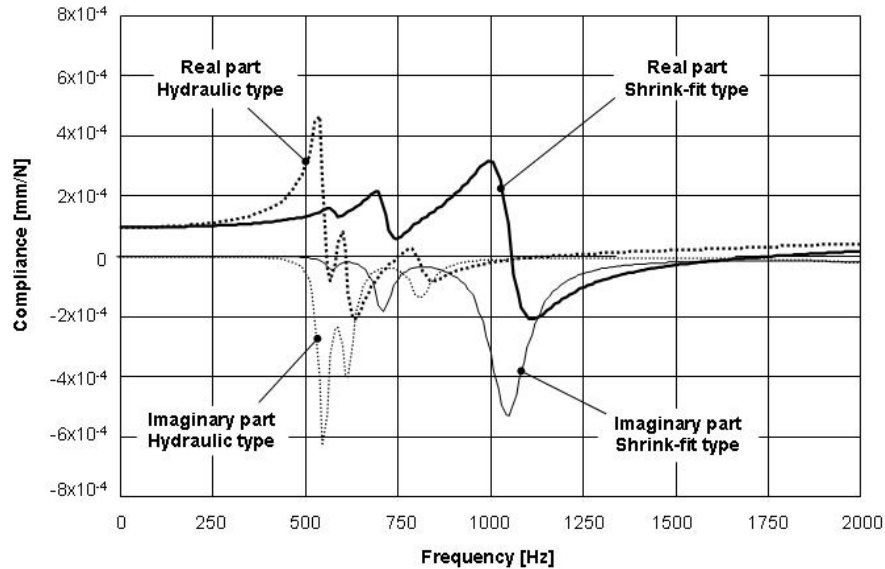


Figure 12: Real and imaginary parts of the computed dynamic transfer functions for a shrink-fit and a hydraulic-chuck type tool-holder

The dynamic mode shape analyses shows that by increasing the tool-holder mass, an amplification of the spindle mode due to the cantilever effect occurs (Figure 13). Additionally, the pronounced vibration conditions of a single-mass or a single spindle component, as it is shown in Figure 7, are no longer effective. The vibrations of the tool-holder/tool mode effect the vibration of the spindle tail and vice-versa. This effect occurs when both resonance frequencies of the tool-holder/tool mode and the spindle mode are approaching each other. As indicated earlier, an increase of the tool-holder mass does not effect the spindle cutting performance but could effect the spindle reliability due to the increased vibration amplitudes of the spindle tail. To avoid machining under chatter conditions, the tooth passing frequency has to approach the most dominant frequency of the spindle/tool-holder/tool system. However, machining under these frequencies will increase the vibration of the spindle tail which can lead to fretting corrosion and/or contact between stationary and rotational spindle parts (encoder wheel, labyrinth seals etc.). The magnitude of these vibrations (spindle tail) can only be determined through the cross transfer function of the spindle/tool-holder/tool system (see Figure 14). In general, it is recommended that to increase spindle reliability, the spindle tail vibration should be lessened through lighter tool/tool-holder masses.

To determine the influence of the spindle bearing stiffness to the overall dynamic behavior of the spindle/tool-holder/tool system, analyses have been performed with the example of two different

angular contact bearing types. The first bearing type was steel ball bearings and the second type, hybrid ceramic. In both cases, the bearing location and the bearing orientation were identical. The applied stiffness values as well as the dynamic compliances are shown in [Figure 15](#). As indicated in the shown figure, a change in the bearing stiffness has only a minor influence on the

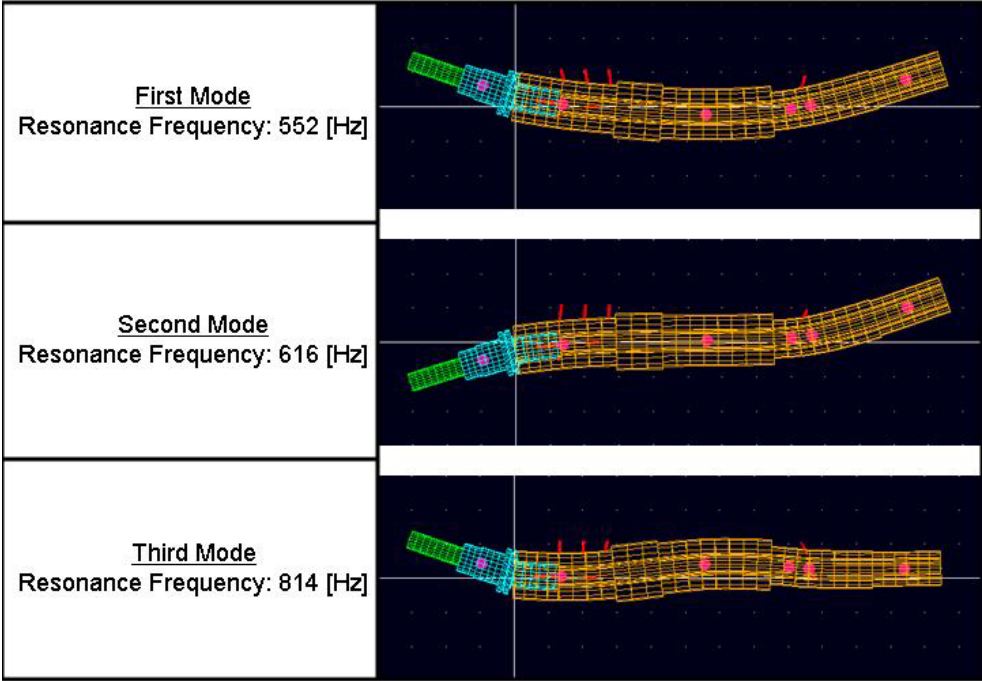


Figure 13: Spindle/tool-holder/tool modes for a hydraulic-chuck type tool-holder

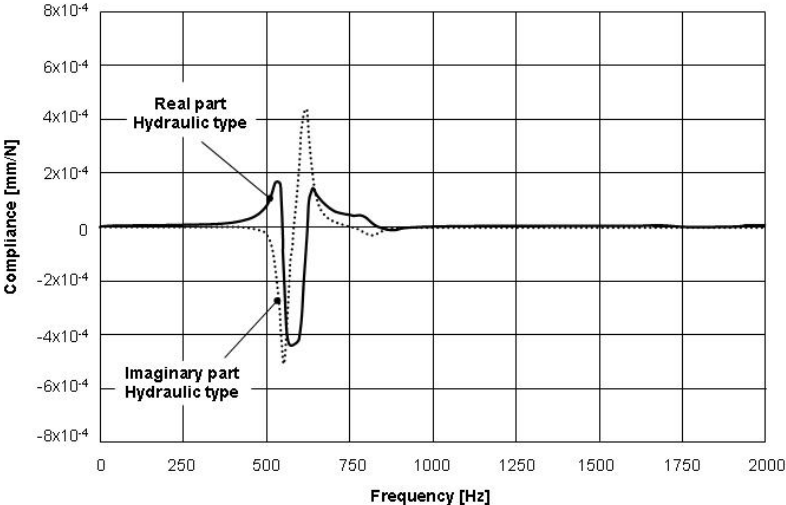


Figure 14: Real and imaginary parts of the cross transfer function of the analyzed spindle with the hydraulic-chuck type tool-holder

overall system compliance and its cutting performance. The resonance frequency of the spindle/tool-holder/tool mode as well its compliance, increases. Moreover, the most dominant mode (tool-holder/tool mode) is not significantly influenced by the spindle bearing stiffness, therefore, in both cases; the spindle cutting performance remained the same ($S_{pe} = 0.46$ and 0.47).

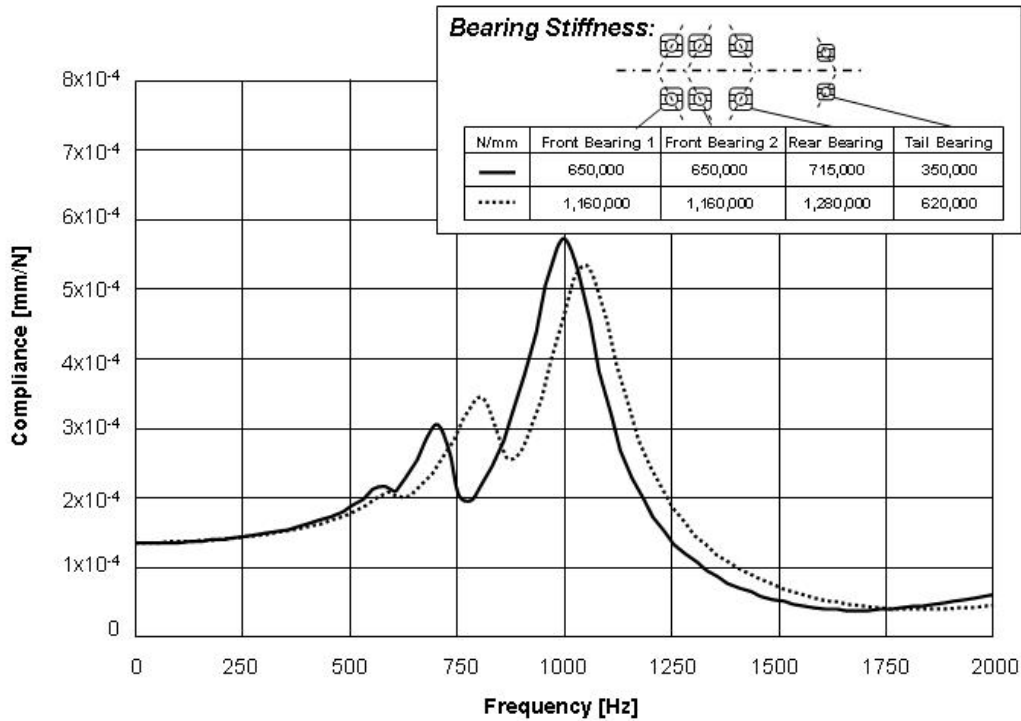


Figure 15: Dynamic compliances of the spindle/tool-holder/tool system for two different bearing types

CONCLUSIONS

A methodology has been established which allows to define the spindle cutting performance for different spindle designs or concepts independently from their application requirements as well as their power and speed characteristics. This methodology was applied on an example of a high speed milling spindle to evaluate the different spindle/tool-holder/tool configurations as well as to determine the influence of the tool-holder and the spindle bearing stiffness to the overall cutting performance. Through a dynamic FEA model of the analyzed spindle the influences of the spindle cutting performance were reached. An analytical approach determined the dynamic compliances as a function of the frequency spectrum. Experimental FRF measurements of this spindle provided the input parameters for this model as well as for model verification. Simulations of different spindle/tool-holder interfaces were explored which showed that the interface stiffness has a dramatic impact on the spindle cutting performance. Additional simulations by varying the tool-holder mass were established as well. Increasing the tool-holder mass allows higher compliance of the tool and the spindle mode. Decreasing the spindle tail

vibration by using lighter tool/tool-holder assembly will increase spindle reliability. Further, the simulations showed that increasing the bearing stiffness has only a minor influence of the spindle cutting performance for the analyzed spindle concept with two front bearing, one rear bearing and one tail bearing arrangement.

REFERENCES

- [1] Tlusty, J.; Koenigsberger, F. In *Specifications and Test of Metal-Cutting Machine Tools*, Proceedings of the Conference 19th and 20th, University of Manchester, Institute of Science and Technology (UMIST), Feb 19-20, 1970; Revell and George Limited: Manchester; Vol. 1.
- [2] *Cutting tests for determining the dynamic machine tool behavior*, BAS-Standard, Sweden, 1970, AB BORFORS; ALFA-LAVAL AB; ASEA; SAAB-SCANIA.
- [3] *Machine Test Book-Records of Spindle Test*, 1998, CINCINNATI MACHINE.
- [4] Weck, M. Dynamisches Verhalten von Werkzeugmaschinen. In *Werkzeugmaschinen, Fertigungssysteme, Messtechnische Untersuchung und Beurteilung*; VDI-Verlag GmbH: Dueselldorf, 1992; Vol. 4, 269-282.
- [5] Weck, M.; Teipel, K. In *Dynamisches Verhalten spanender Werkzeugmaschinen*; Springer-Verlag: Berlin, Heidelberg, New York, 1977.
- [6] Tlusty, J.; Smith, S.; Zamudio, C. In *Evaluation of Cutting Performance of Machining Centers*, Annals of the CIRP **1991**, 40/1, 405-410.
- [7] Smith, S.; Winfough, W.; Young, K.; Hally, J. In *The Effect of Dynamic Consistency in Spindles on Cutting Performance*, Proceeding of the ASME Manufacturing Engineering Division 2000, MED-Vol. 11, 927-933.
- [8] Tlusty, J. Handbook of High Speed Machining Technology, In *Machine Dynamics*; R.I. King, ed., Chapman and Hall, New York.
- [9] Altintas, Y.; Budak, E. In *Analytical Prediction of Stability Lobes in Milling*, Annals of the CIRP 1995, 44/1, 357-362.
- [10] Smith, S.; Tlusty, J. In *Update on High-Speed Milling Dynamics*, Transaction of the ASME Journal of Engineering for Industry 1990, 112, 142-149.
- [11] Tlusty, J.; Zaton, W.; Ismail, F. In *Stability Lobes in Milling*, Annals of the CIRP 1983, 32/1, 309-313.
- [12] Ewins, D.J. Theory and Practice, In *Modal Testing*; John Wiley & Sons, Inc.: New York, 1984.
- [13] Brigham, E.O. In *The Fast Fourier Transform and its Applications*; Prentice Hall Inc.: Englewood Cliffs, NJ, 1988.
- [14] Erstellung einer technischen Richtlinie fuer Holschaftkegel-Werkzeuge, Report of the 6th committee meeting, WZL, Sep 2001; RWTH-Aachen, Germany.
- [15] Agapiou, J.; Rivin, E.; Xie, C. In *Toolholder/Spindle Interfaces for CNC Machine Tools*, Annals of CIRP 1995, 44/1, 383-387.

- [16] Weck, M.; Schubert, I. In *New Interface Machine/Tool: Hollow Shank*, Annals of the CIRP 1994, 43/1, 345-348.
- [17] Schmitz, T. In *Predicting High-Speed Machining Dynamics by Substructure Analysis*, Annals of the CIRP 2000, 49/1, 303-308.
- [18] Ferreira, J.; Ewins, D. In *Nonlinear Reacceptance Coupling Approach Based on Describing Functions*, Proceeding of the 14th International Modal Analysis Conference, 1995, Dearborn, MI, 1034-1040.

Freeform Cubic Phase Plate

K. Bryant, U.S. Army Night Vision and Electronic Directorate, Ft. Belvoir, VA
R. Cassin, L. Chaloux, Y. Tohme, Moore Nanotechnology Systems, Keene, NH
D. Puczek, G. Dunn, H. Takeuchi, Panasonic Factory Automation, Elgin, IL

In the March 2004 edition of *Convergence*, graduate student Wanli Chi and Professor Nicholas George at the University of Rochester's Institute of Optics, presented a fabrication process utilizing deterministic microgrinding (DMG) and magnetorheological finishing (MRF) for a **logarithmic asphere** of BK7 glass to achieve extended depth of field performance in an imaging system.

A parallel project was also on-going to extend the depth of field for a Long-Wave Infrared (LWIR) imaging system. A collaborative effort involving the U.S. Army Night Vision Lab, Moore Nanotechnology Systems and Panasonic Factory Automation demonstrated a successful freeform process for a **cubic phase plate** made of Zinc Sulfide (ZnS), which was the critical component for the imaging system. The resulting surface profile matched the formula to within $\pm 0.20\mu\text{m}$. This was deemed essentially perfect, because it corresponded to $\pm 0.02\lambda$ in the 8-12 μm region.

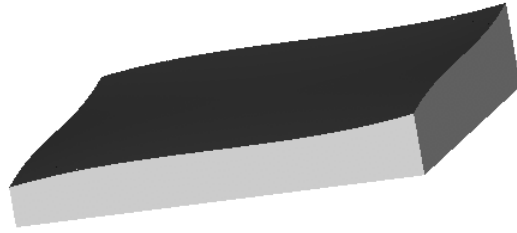
The following are abstracts of the design, manufacturing and metrology methods in this project.

Application and Design

(Kyle R. Bryant — k.bryant@nvl.army.mil)

By applying an optical distortion and digital restoration technique to digitally captured imagery, one can realize benefits such as extended depth of field, thermal focus shift invariance, loosened optical design tolerances, and more. The Night Vision and Electronic Directorate (NVESD) began investigating this imaging technique for Long-Wave Infrared (LWIR), low signal applications, since this is predominantly the environment that night vision technology is used. These applications call for fast, wide field of view optics with large depths of field that are covert to threats.

The cubic phase plate design and geometry is shown on the next page in exaggerated forms. The total peak-to-valley on the actual phase plate surface is 100-microns (shown in the formula) whose coefficients are given in millimeters. Note, the base window thickness is arbitrary, but is 3mm (*thi*) for this example. The total plate thickness is z , and the x/y origin is at the center of the part. The overall size of the part is 25mm x 25mm.



$$z = 0.025 \left(\left(\frac{x}{10} \right)^3 + \left(\frac{y}{10} \right)^3 \right) + thi$$

Figure 1: Phase Plate Form

Slow Slide Servo (S³) Machining Process
(Robert Cassin — cassin@nanotechsys.com)

In recent years, a significant amount of work has been accomplished in the area of freeform optical surface generation. Most of this work is driven by market demand for these types of surfaces, which currently includes eyewear, electro-optics, LED optics, defense, automotive, and others. Presently, there are several methods to manufacture such surfaces of which the most common ones are grinding and raster flycutting. Both grinding and raster flycutting rotate the tool and traverse either the tool and/or workpiece in three linear axes to cut the surface. Grinding and fly cutting can produce very accurate surfaces but require long machining cycles and are difficult to set-up. Another method of fabrication is the Fast Tool Servo (FTS), which is widely applied in the contact lens industry. However, most FTS systems have a maximum travel range of less than 1mm and therefore are limited to certain part geometries with small departures.

In this project Moore Nanotechnology Systems demonstrated how they perfected an alternative method of freeform optical surface fabrication, the Slow Slide Servo (S³). The S³ method is similar to the FTS in that, the part is mounted on the spindle and as the spindle rotates, the tool oscillates (Figure 3). Unlike the FTS method, the system does not use any additional axes for oscillating the tool; the Z-axis slide generates the oscillations. Another difference is the spindle position control (or C-axis). In a FTS setup, the spindle has an encoder that feeds the position to the FTS unit without putting the spindle in position control. In the S³ all axes are under fully coordinated position control. The S³ can oscillate at ranges up to 25mm, is easy to set-up, inexpensive and allows the manufacturing of highly accurate parts.

Since the material for this application is Zinc Sulfide, a negative rake diamond cutting tool was used. The sag of the surface is 100µm Peak to Valley (PV). The form results shown in Figure 5 demonstrate the PV error is 0.26µm and the surface finish shown in Figure 6 has a roughness of 4.6nm Ra.



Figure 2: Moore Nanotech 350UPL

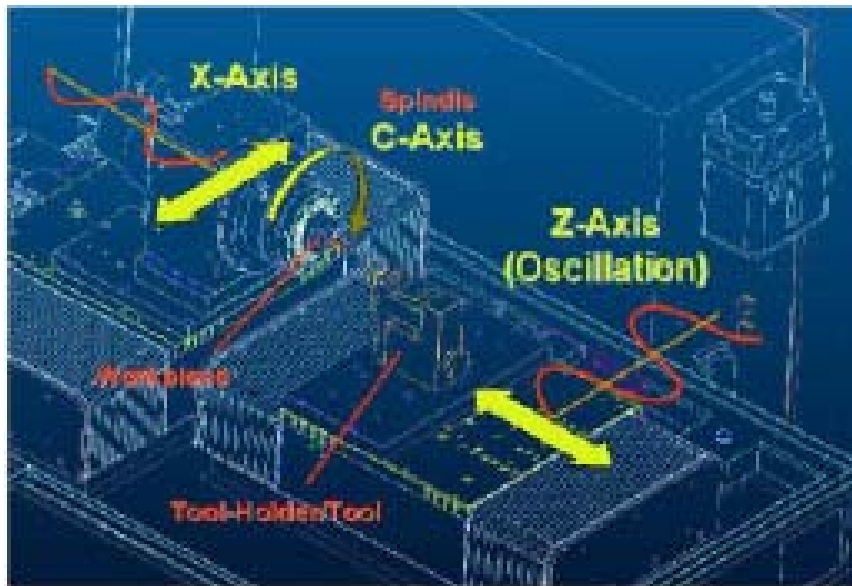


Figure 3: Set up with machining for Slow Slide Servo (S^3)

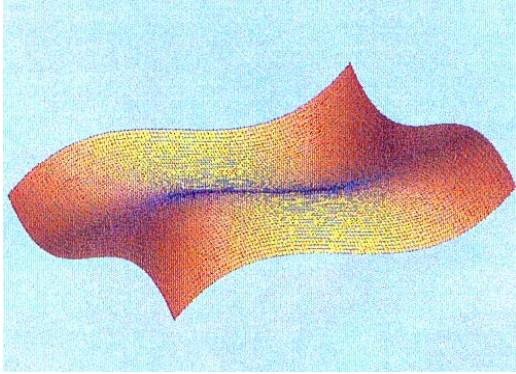


Figure 4. Surface of cubic phase plate.
Material: Zinc Sulfide 27mm X 27mm

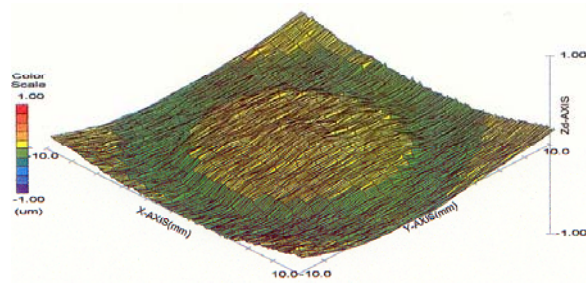


Figure 5. Phase plate form accuracy results
Form results (Panasonic UA3P)
0.263 μ m PV 0.055 μ m Rms

Finish results (Zygo NewView)
4.569nm Ra 6.077nm Rms

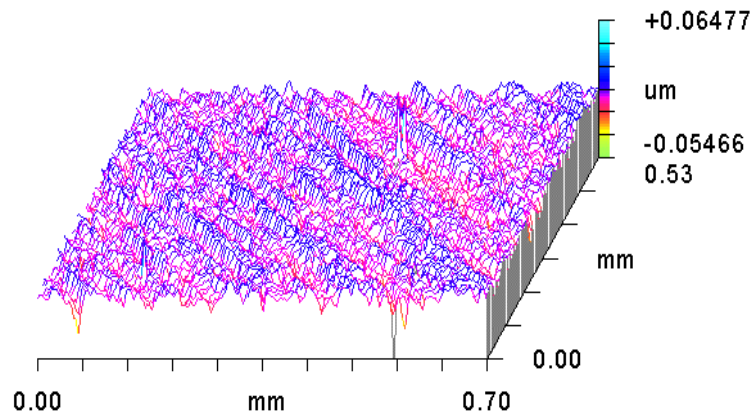


Figure 6. Phase plate surface finish results.

The machining tests performed with the S³ indicate that it is a very viable method for producing freeform optical surfaces. Surface finish and form accuracy results are comparable to axisymmetric diamond turning results. In addition, this method is inexpensive, does not have sag limitations, is very accurate, reduces cycle times and is easy to set-up.

Metrology : UA3P, Ultrahigh Accurate 3-D Profilometer
(David Puczek — puczek@panasonic.com)

Panasonic's applications laboratory in Elgin, Illinois joined the effort to provide a full aperture (20mm x 20mm) map of the surface.

The Ultrahigh Accurate 3-D Profilometer (UA3P) offers the capability to measure surfaces up to 60° slope angle, exceeding the capability of COM's interferometers and optical probe-measuring tools. The UA3P combines 3-D measurement capabilities, an interferometer function, atomic force microscopy and roughness measurement in one machine that allows measurements to be taken from objects as small as 2µm to large objects up to 400 mm.

A 2µm diamond stylus was used and a user-defined equation was set up. This set up, using the customer's 3rd order polynomial equation for the object's surface, provided information for the UA3P to compare the measured results to the actual surface topography. The measurement type was a standard X rectangle scan for the UA3P, measuring +/- 10 mm in the X and Y from the center of the object moving at 3 mm/sec. Approximately 7400 data points were collected, but changing the speed and data sampling pitch can collect more data points if needed. After the data collection, the editing features on the UA3P were used to eliminate any noise from the data, such as dust on the surface of the object. When editing was completed, the data was plotted directly from the UA3P in various forms, such as Zd compared to X, Y. (see Figure 5)

Future Efforts: COM is exploring finishing optimization processes for improved surface finishes on polycrystalline IR materials such as ZnS. These efforts will be reported in upcoming editions.

Machining of Freeform Optical Surfaces by Slow Slide Servo Method

Yazid E. Tohme and Jeff A. Lowe
Moore Nanotechnology Systems LLC
426A Winchester St. Keene, NH



Motivation

- Provide a simple cost effective method to produce freeform optical surfaces
 - Minimize the amount of axes and equipment
 - Simple tool set-up
 - Simple part set-up
 - Simple CNC programming
 - Improve surface finish
 - Improve form accuracy
 - Reduce machining cycle time

Examples of Freeform Surfaces

Grinding Application



Automotive Heads-Up Displays
Finish Cycle: 50hrs. (Large lens)
Finish Cycle: 30hrs. (Small lens)
Courtesy: B-con Engineering

Fly Cutting Application
F-Theta Lenses
Finish Cycle: 20hrs



Manufacturing of Freeform Optics

➤ Grinding

- Slow machining cycle
- Un-deterministic process (Wheel Wear)

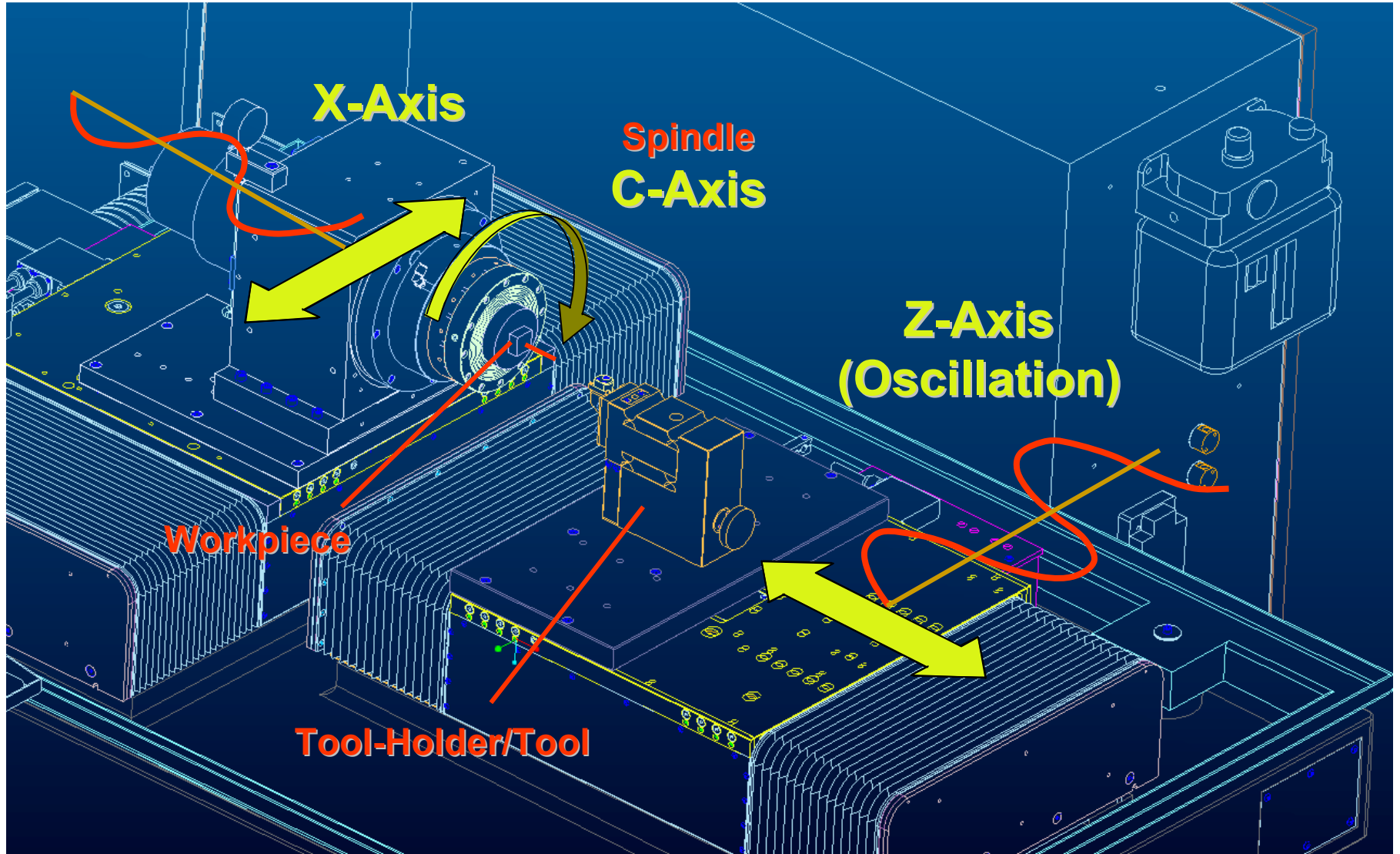
➤ Fly Cutting or Raster Cutting

- Slow machining cycle
- Difficult to set-up
- Limited by tool swing diameter

➤ Fast Tool Servo

- Fast machining cycle
- Limited travel

Slow Slide Servo



Key Requirements for Slow Slide

- Two linear axes X and Z
- Position controlled spindle or C-axis
- Direct drive motors on all axes
- Friction free bearings on all axes
- Low heat generation from motors and bearings (Air or liquid cooling)
- High resolution feedback systems
- High bandwidth closed position loops

- CNC requirements
 - High speed data processing
 - Look ahead capabilities
 - High order trajectory generation

Diamond Turning Lathe

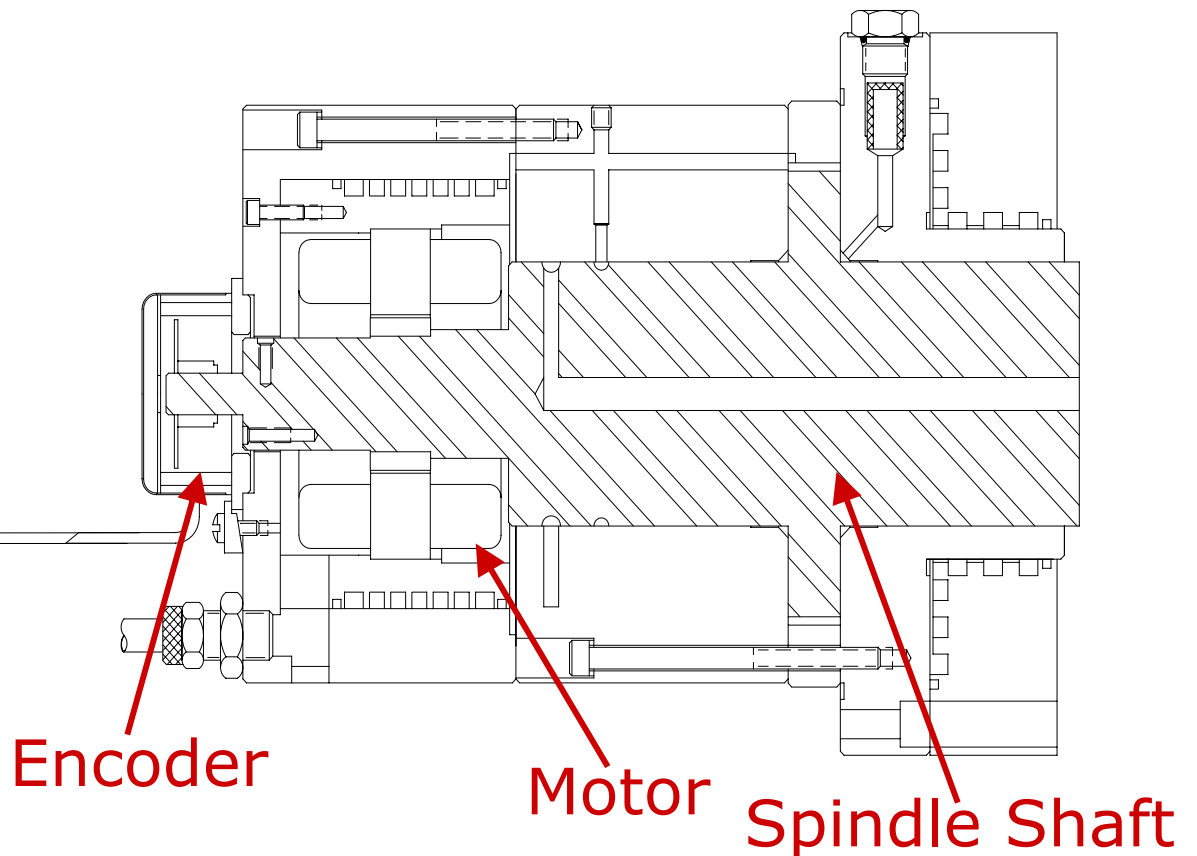
- Two Linear axes
 - Hydrostatic bearings
 - Air cooled linear motors
 - 8.6nm feedback resolution
 - 100 Hz position loop bandwidth
- Open Architecture CNC
 - Look ahead capabilities
 - High order trajectory generation
 - High speed servo loop
 - Unlimited file size



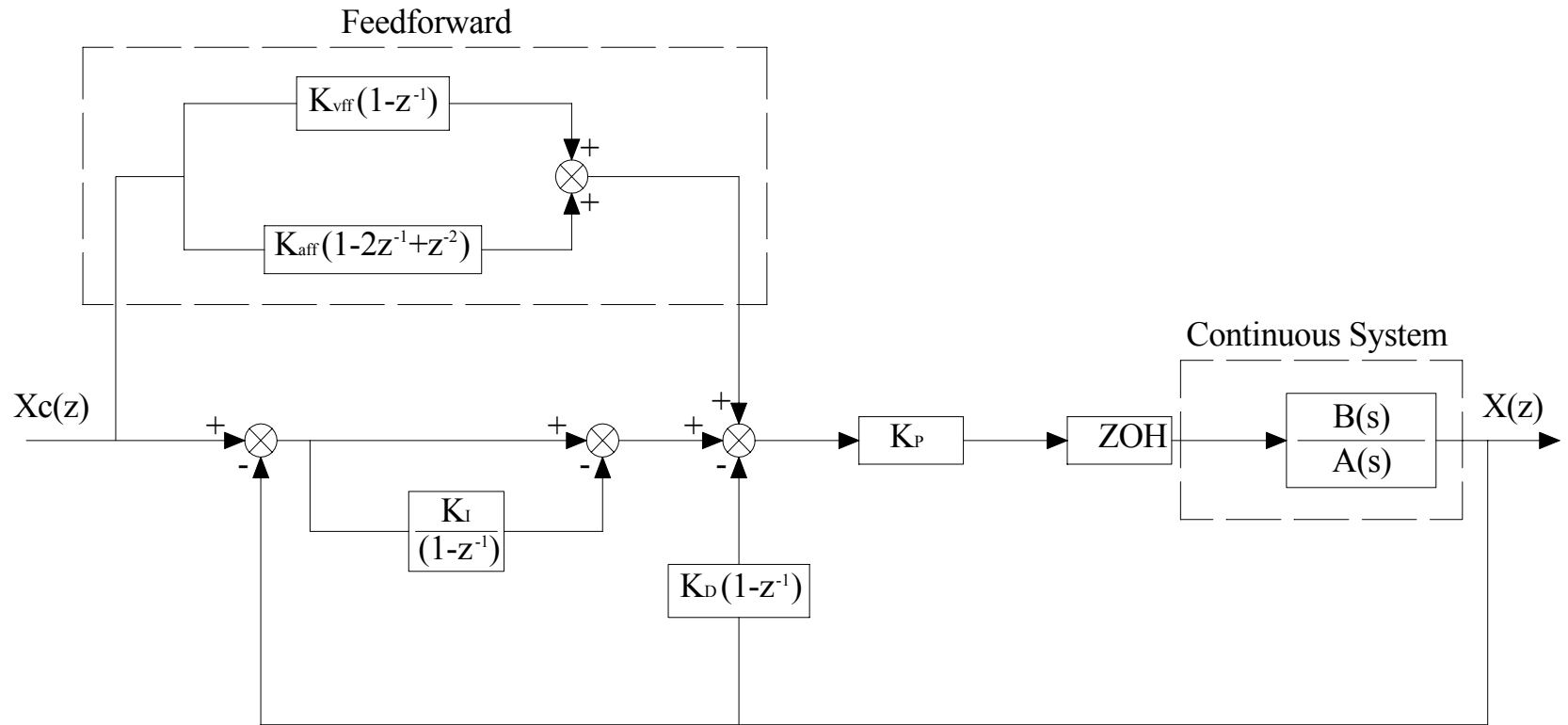
Spindle / C-axis

- Groove compensated air bearing (Liquid cooled)
- Integrated motor (Liquid cooled)
- Integrated encoder: 20,480,000 counts/rev (0.06 arc-sec)
- Max. speed in position mode 2000 RPM
- No structural dynamics between command and response below 1000 Hz

DSP Interpolator

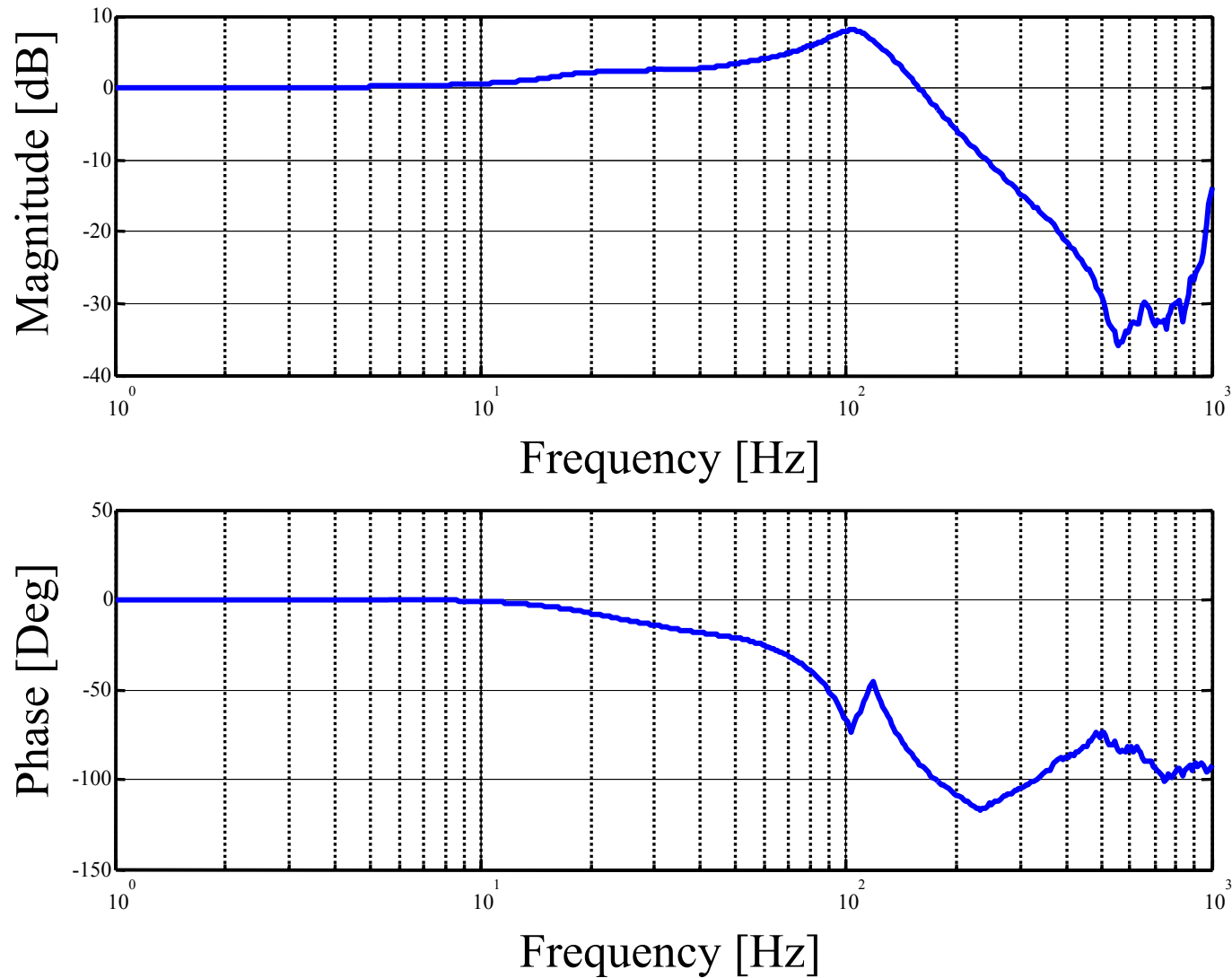


C-axis Block Diagram



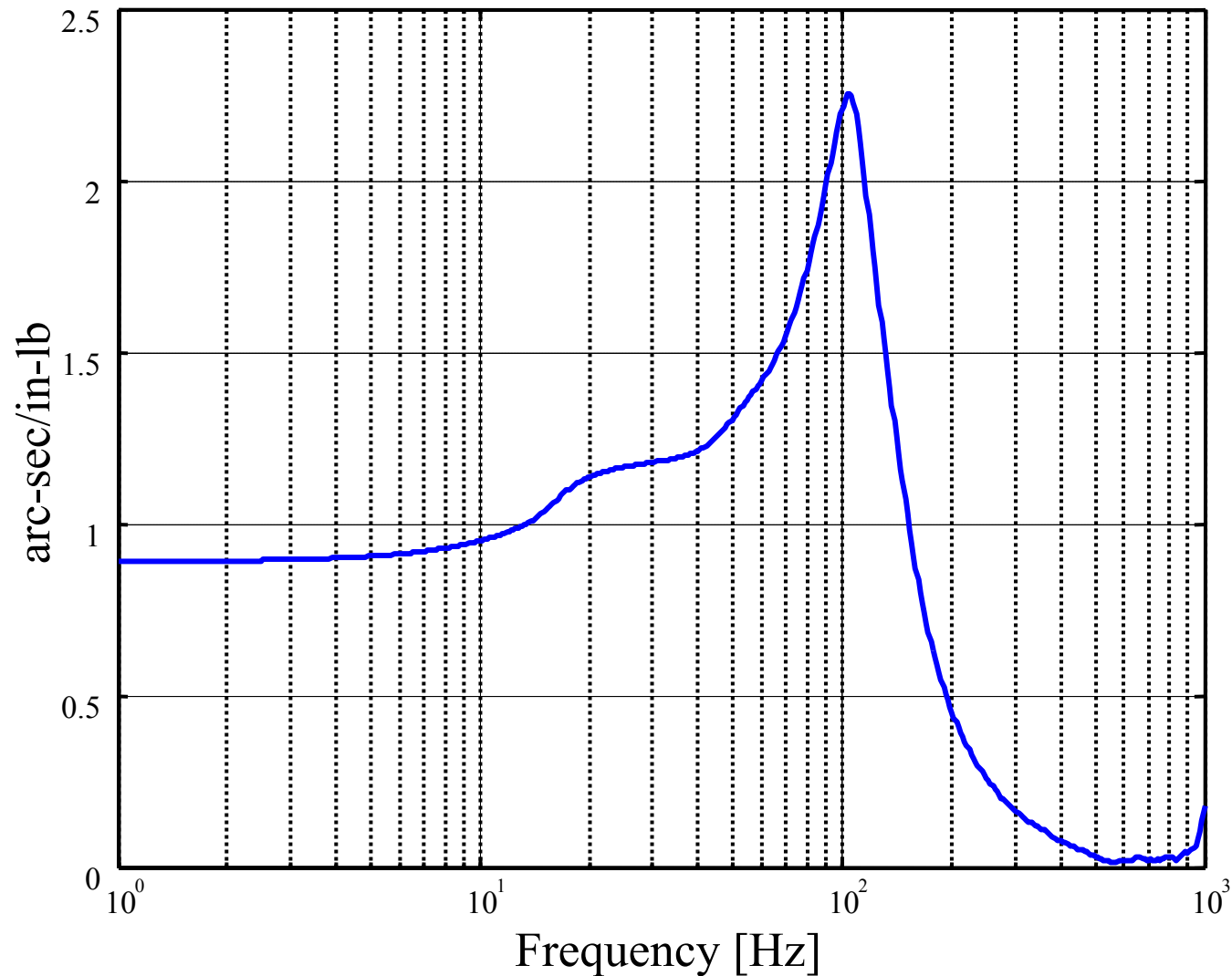
Where -- K_P : Proportional Gain K_{vff} : Velocity Feedforward Gain
 K_I : Integral Gain K_{aff} : Acceleration Feedforward Gain
 K_D : Derivative Gain ZOH: Zero-Order-Hold
 $B(s)/A(s)$: Open Loop Transfer Function

Closed Loop Transfer Function



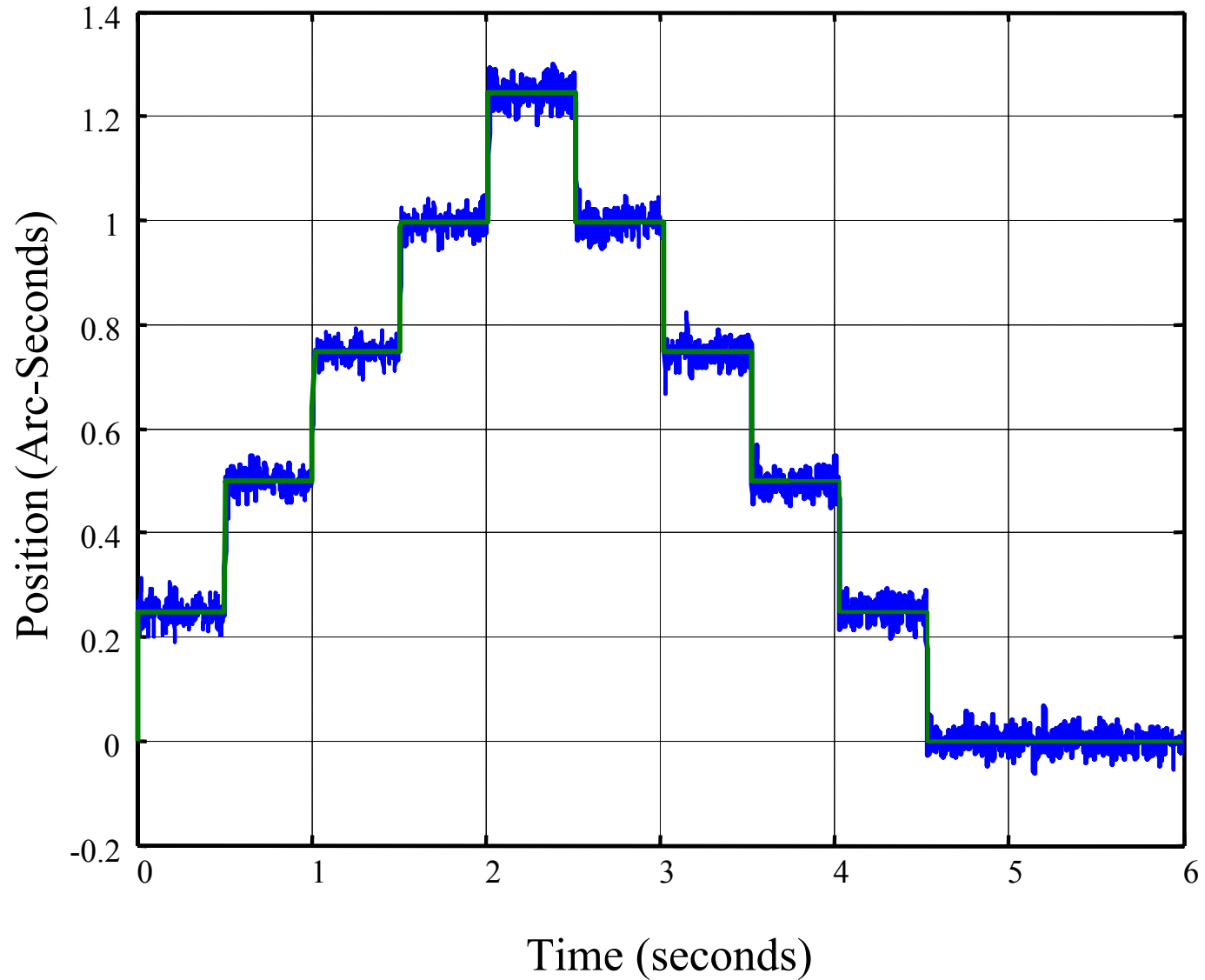
- 170 Hz Closed position loop bandwidth
- No phase shift up to 10Hz

C-axis Compliance



- 1 arc-sec/in-lb from 0 to 10 Hz
- 2.25 arc-sec/in-lb

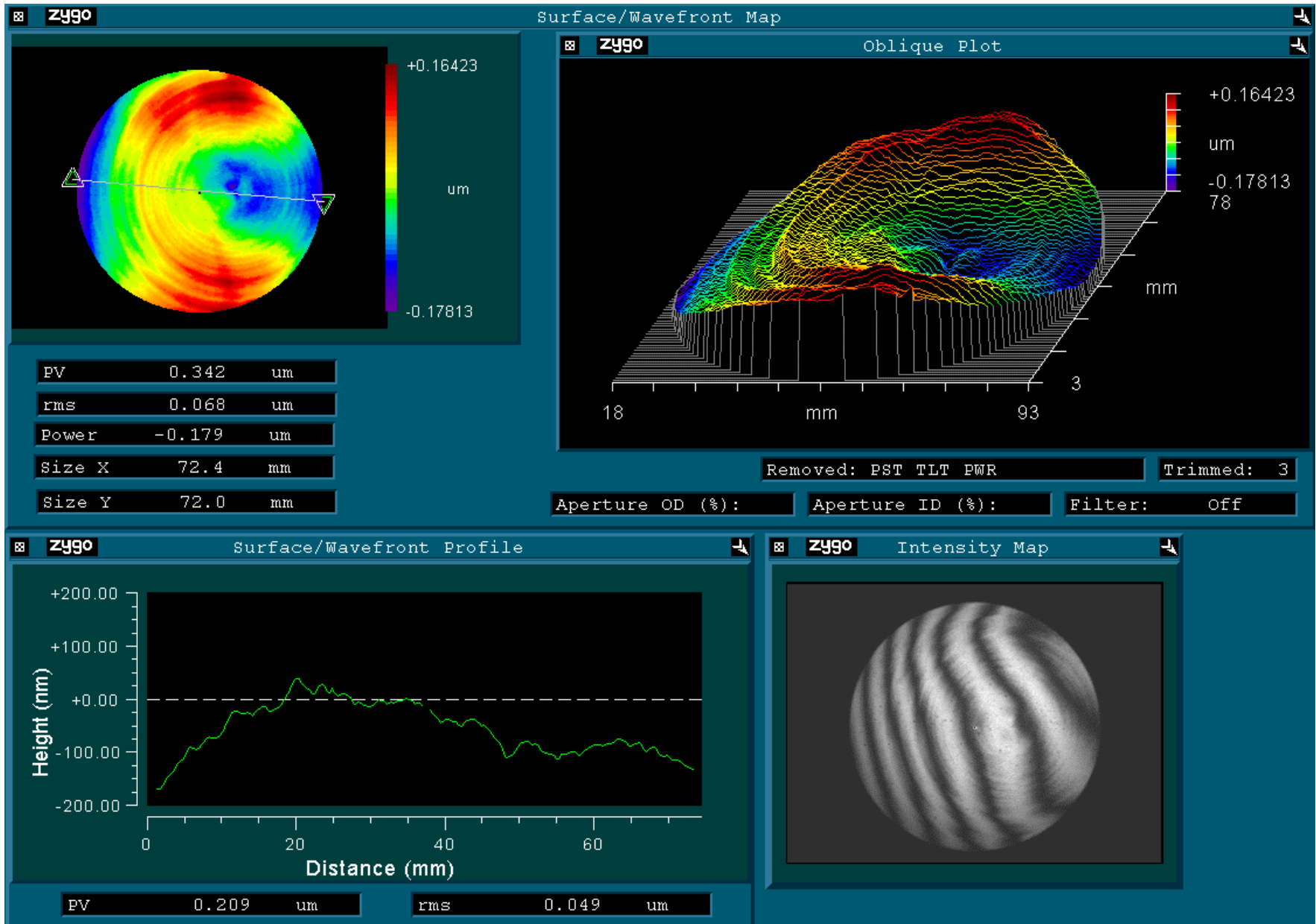
1/4 Arc-Second Step Moves



Cutting Tests

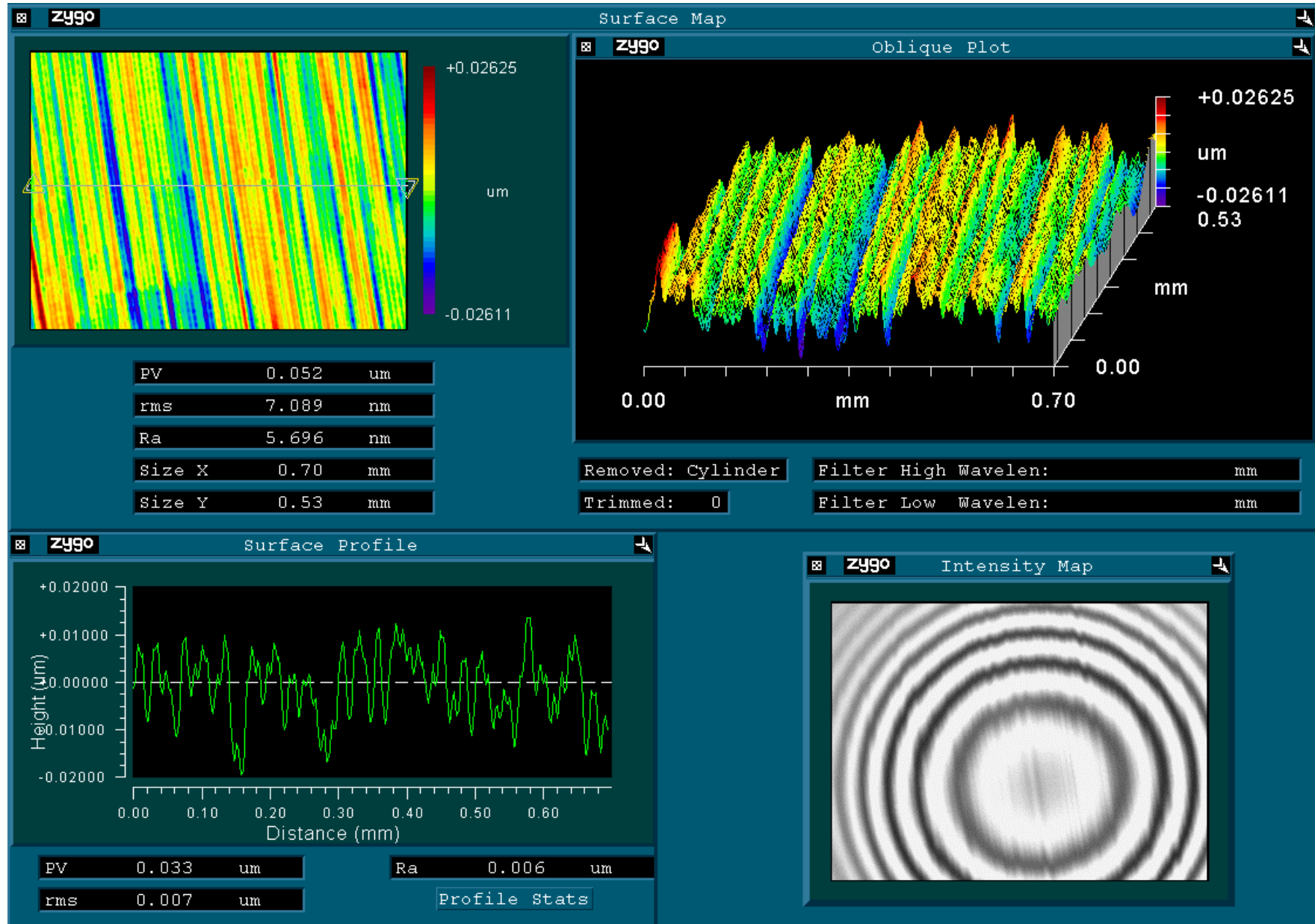
- De-Centered Concave Sphere (6061 Al)
 - Diameter: 75mm, Concave Radius: 75mm
 - Off-axis Distance: 19.4mm, Sag: 10mm PV
 - Finish Machining Cycle: 30 minutes
- On-axis Tilted Flat (6061 Al)
 - Diameter 50mm, Tilt Angle 2.25 Degrees
 - Sag: 2mm PV
 - Finish Machining Cycle: 30 minutes
- Cubic Phase Plate (ZnS)
 - Size: 20mm X 20mm
 - Sag: $\sim 100 \mu\text{m}$ PV
 - Finish Machining Cycle: 21 minutes

De-Centered Sphere -Form Results



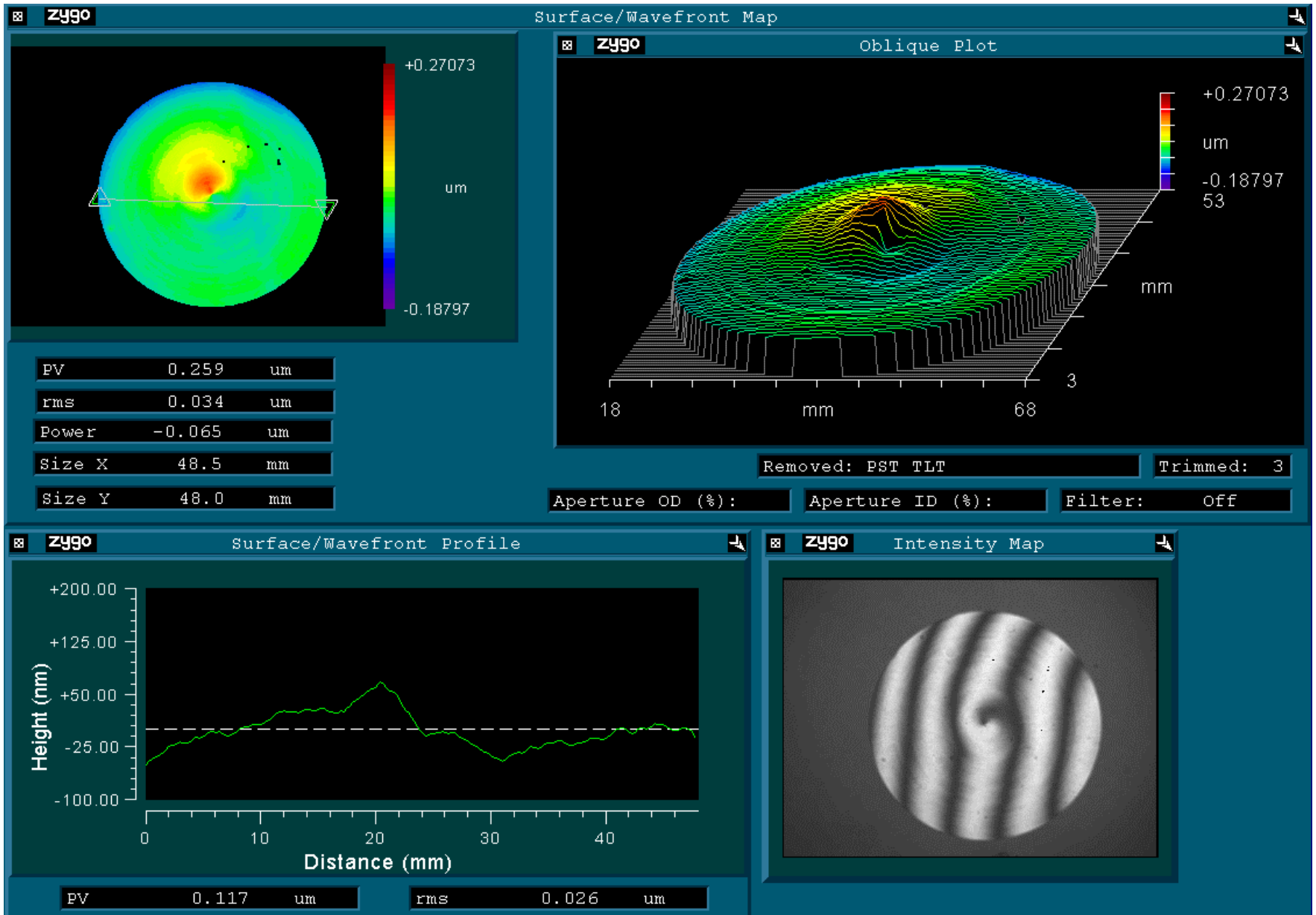
PV-error 0.342 μm

De-Centered Sphere -Finish Results



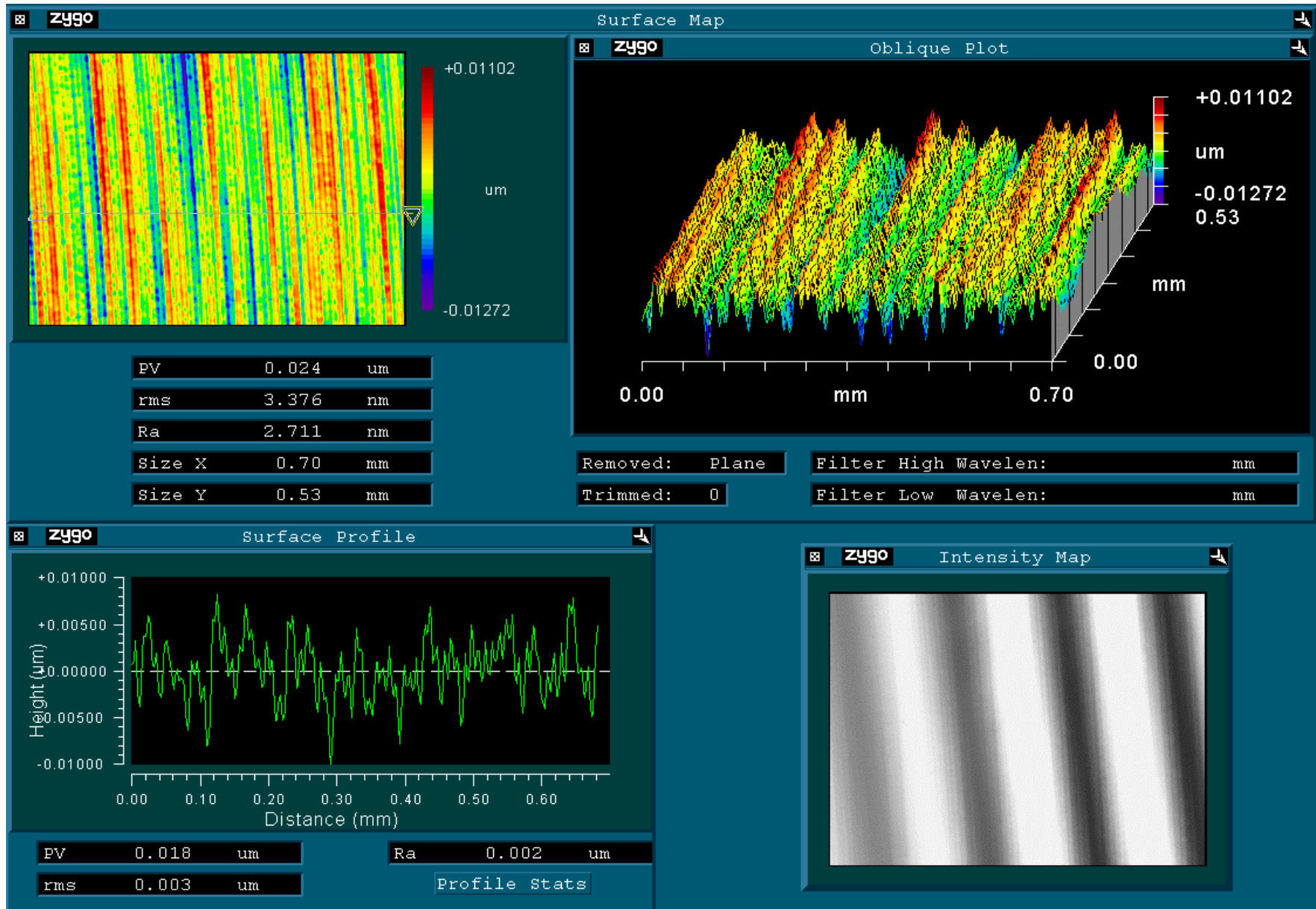
Actual Ra: 5.696nm, Theoretical Ra: 4.6nm

Tilted Flat -Form Results



PV-error 0.259 μm

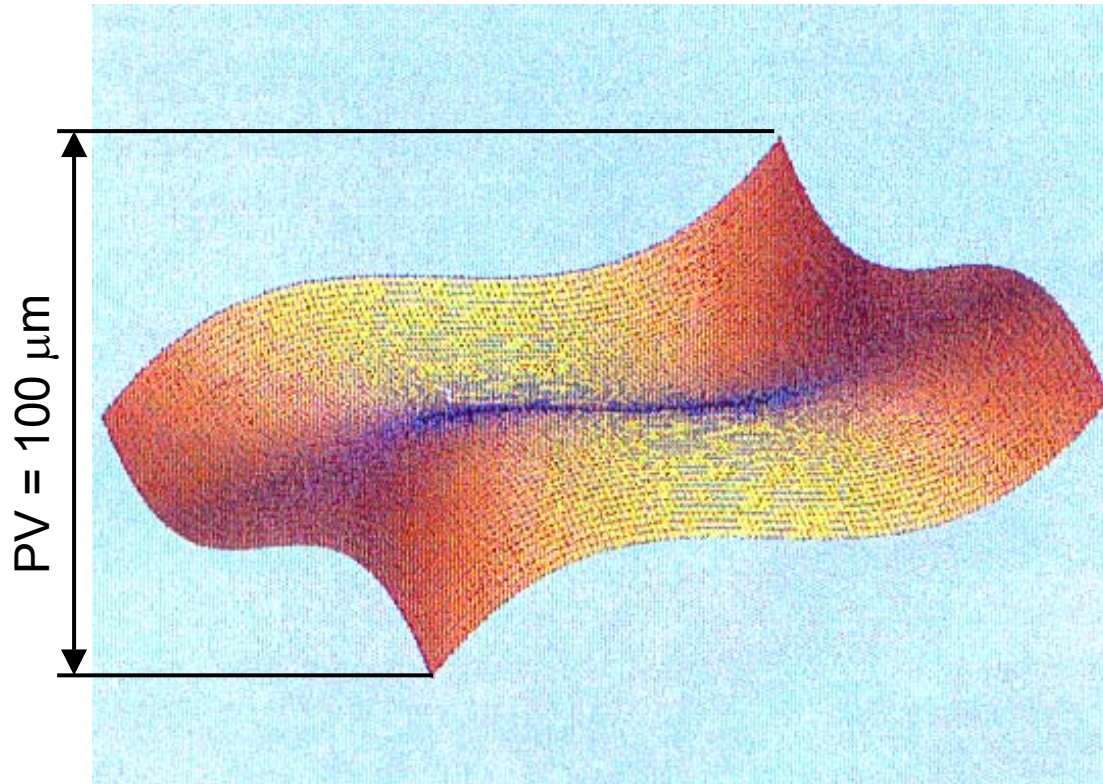
Tilted Flat -Finish Results



Actual Ra: 2.711nm, Theoretical Ra: 2.0nm

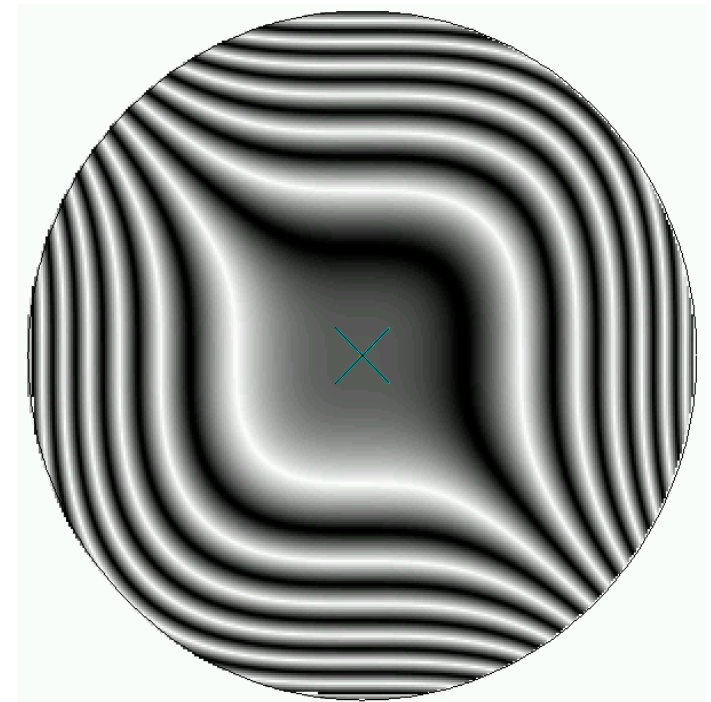
Cubic Phase Plate

Surface Equation: $Z=0.025 ((X/10)^3 + (Y/10)^3)$



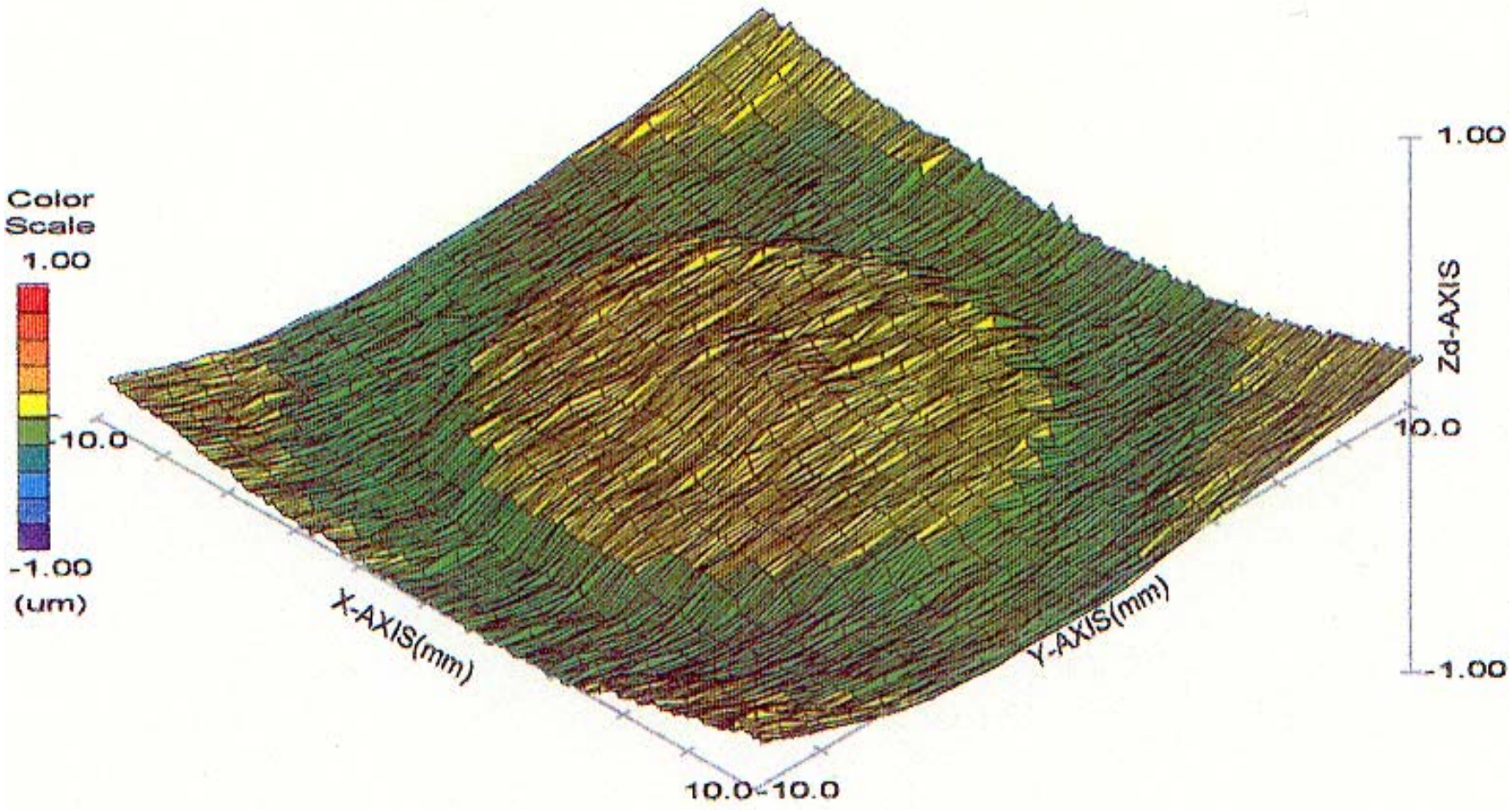
Mathematical Representation of the Cubic Phase Plate Surface

Material: ZnS (Zinc Sulfide)
Tool: . Material: Diamond
. Rake Angle: -25°
. Tool Radius: 0.6 mm
Feedrate: 7 μm/rev



Interferometric Representation of the Cubic Phase Plate Surface

Cubic Phase Plate -Form Results



nanotech

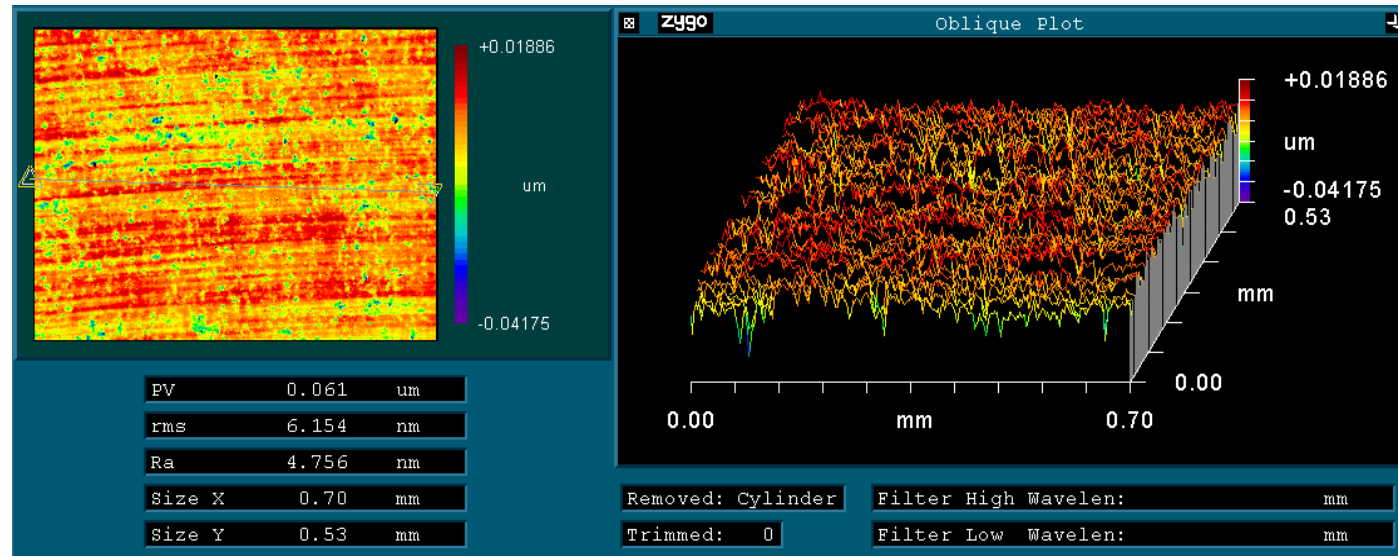
UA3P/Panasonic

Form Error: 0.263 μm

Cubic Phase Plate -Finish Results

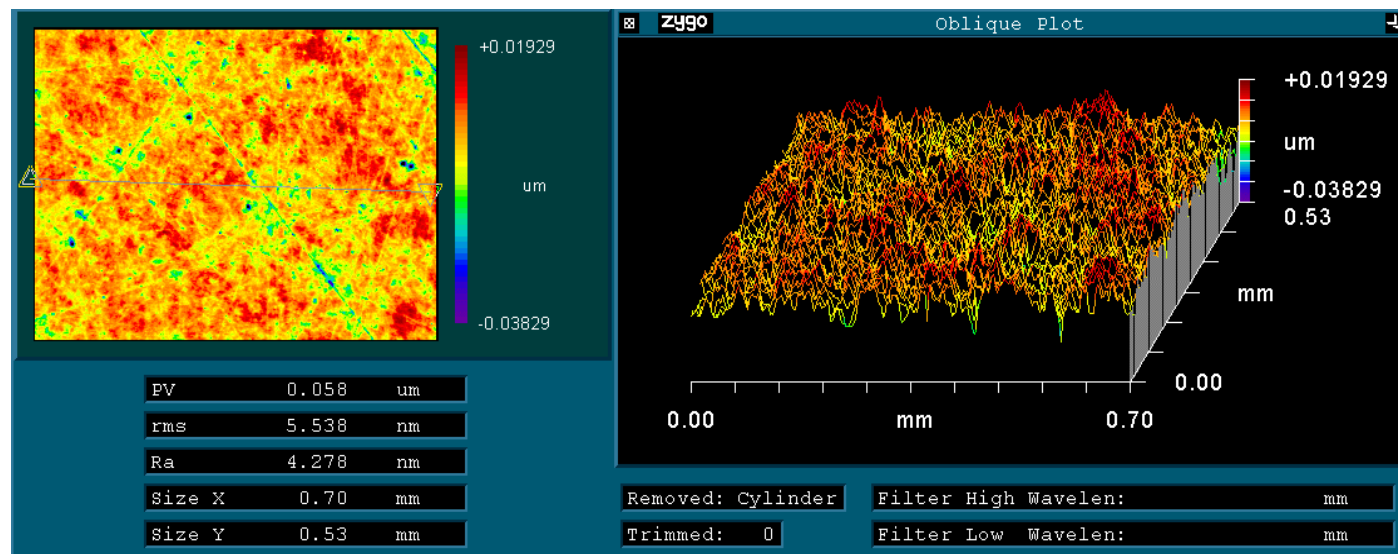
Slow Slide Servo Results

Ra: 4.756nm



Typical Polishing Results

Ra: 4.278nm



Future Work/Questions

- Improve form accuracy to less than $0.2 \mu\text{m}$
- Machine different surfaces
- Understand cutting mechanics

- Questions?

*Recent C & B Axis Developments from
Moore Nanotechnology Systems, LLC*

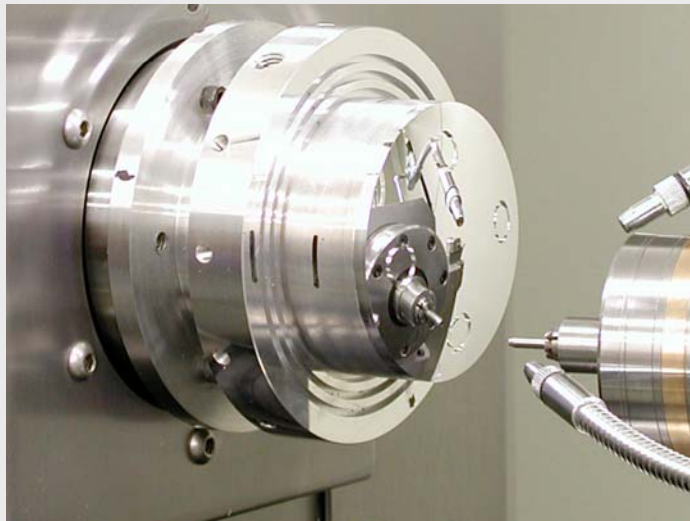
Bob Cassin

Moore Nanotechnology Systems, LLC

Keene, New Hampshire 03431 USA

www.nanotechsys.com

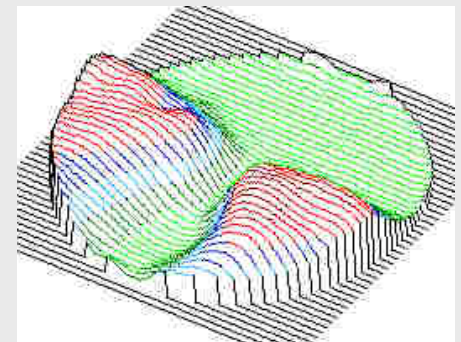
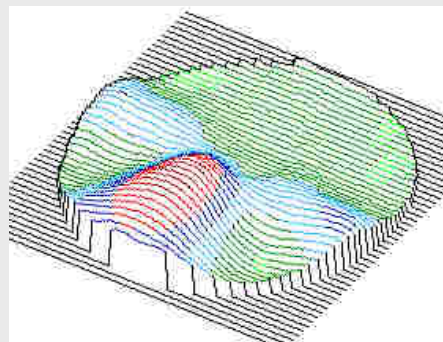
Applications for B-Axis and C-Axis Machining



Micro-Milled with
C, Z, & X-Axis



B-Axis Hemisphere Turning



C-Axis Progressive Lens Molds

Nanotech[®] 350UPL with B & C-Axis



Nanotech 350UPL Ultra-Precision
4 - Axis Ultra-Precision Lathe

- Based on the highly successful Nanotech 350UPL platform
- Granite spindle riser allows a 200mm swing diameter over the B-Axis
- Independent oil hydrostatic slideways (X & Z) with DC linear motors provide stiff, and well damped linear motions
- Liquid-cooled, PI cartridge type air bearing work spindle with < 50 nm axial and radial motion error (50 - 6,000 rpm)
- Delta Tau PC based CNC motion controller with Windows 2000 front end

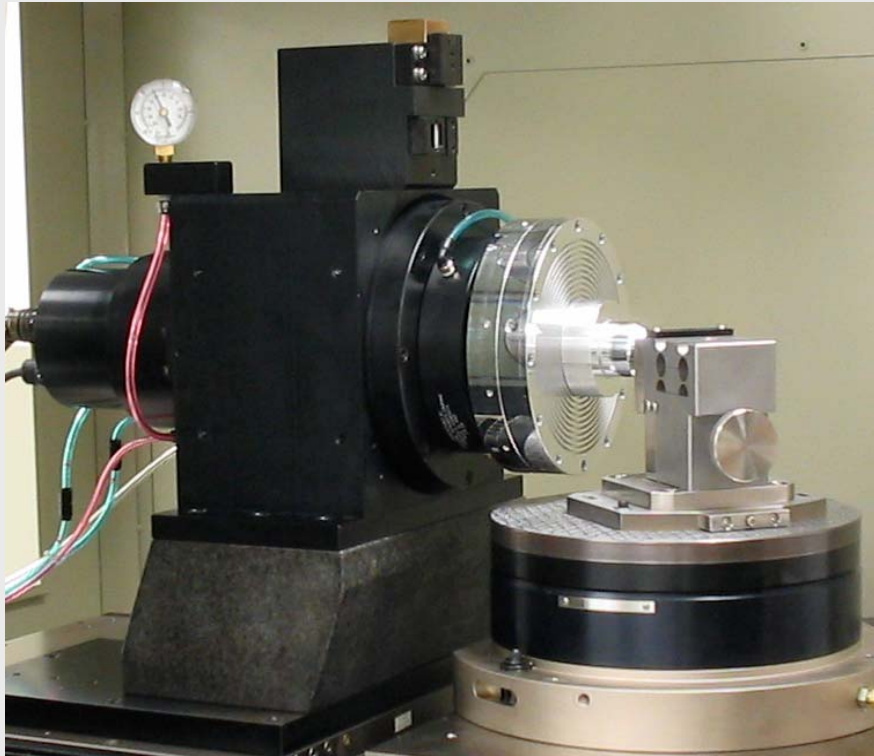
Nanotech[®] 350FG 5 - Axis FreeForm Generator



Nanotech 350FG with Micro Milling Option

- Box-way hydrostatic oil bearing slide design on X, Z, & Y axes
- Hydrostatic oil bearing rotary B-Axis
- Programmable C-Axis / Workspindle imbedded into the Y-axis carriage to improve loop stiffness, reduce Abbe errors, and maintain symmetry
- High speed air bearing micro-milling spindle
- Optional observation camera with monitor

Nanotech[®] Oil Hydrostatic Rotary B-Axis



- Oil hydrostatic bearing
- Positioning accuracy is ≤ 2.0 arc sec (compensated)
- Axial and Radial Error Motion $\leq 4\mu$ "
- Maximum speed 50 rpm
- Low profile compact design
- Micro-height adjust toolholder with X & Z adjustment plate

Oil Hydrostatic Rotary B-Axis

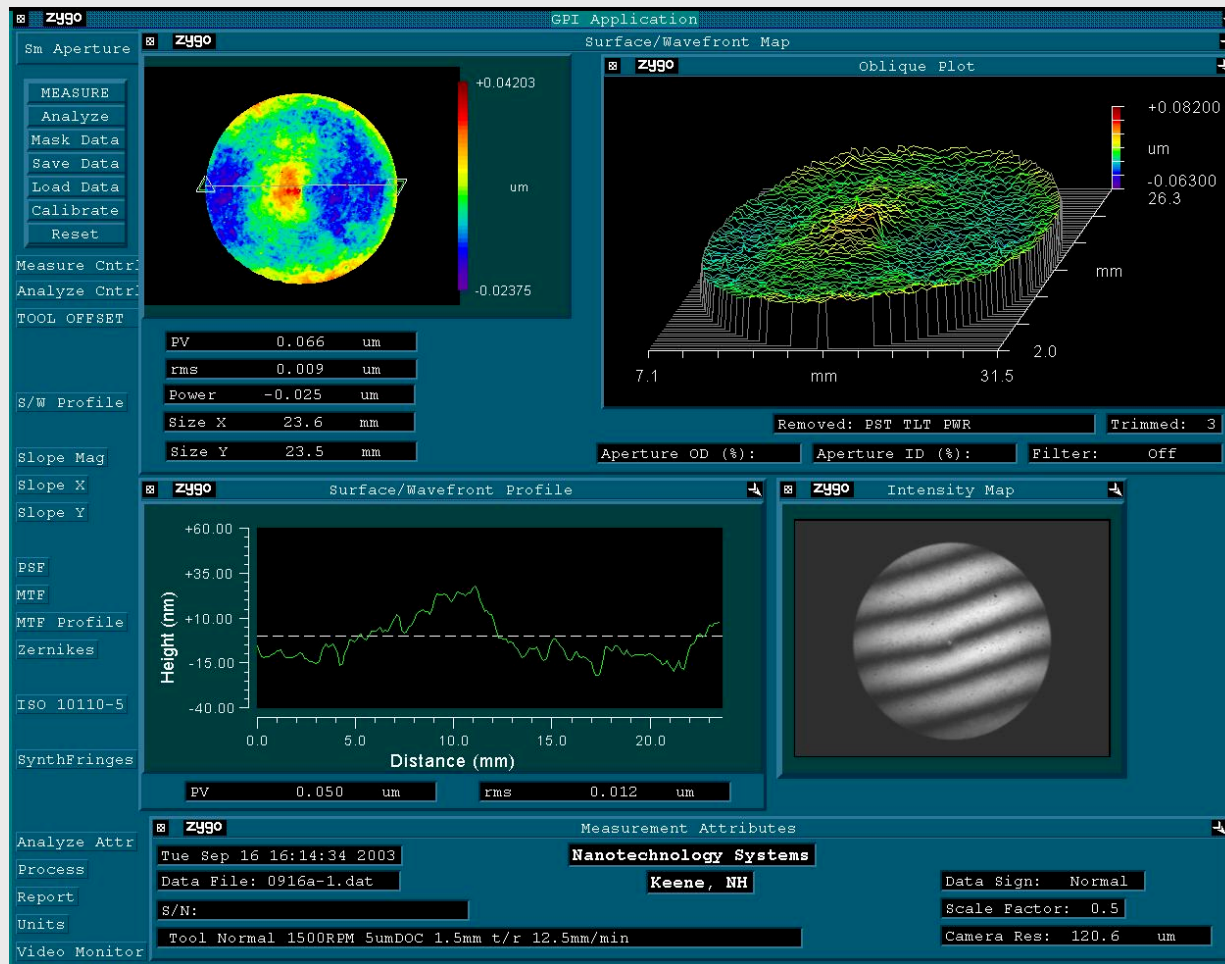
B - Axis Contouring Results

(Form Accuracy - Aluminum)



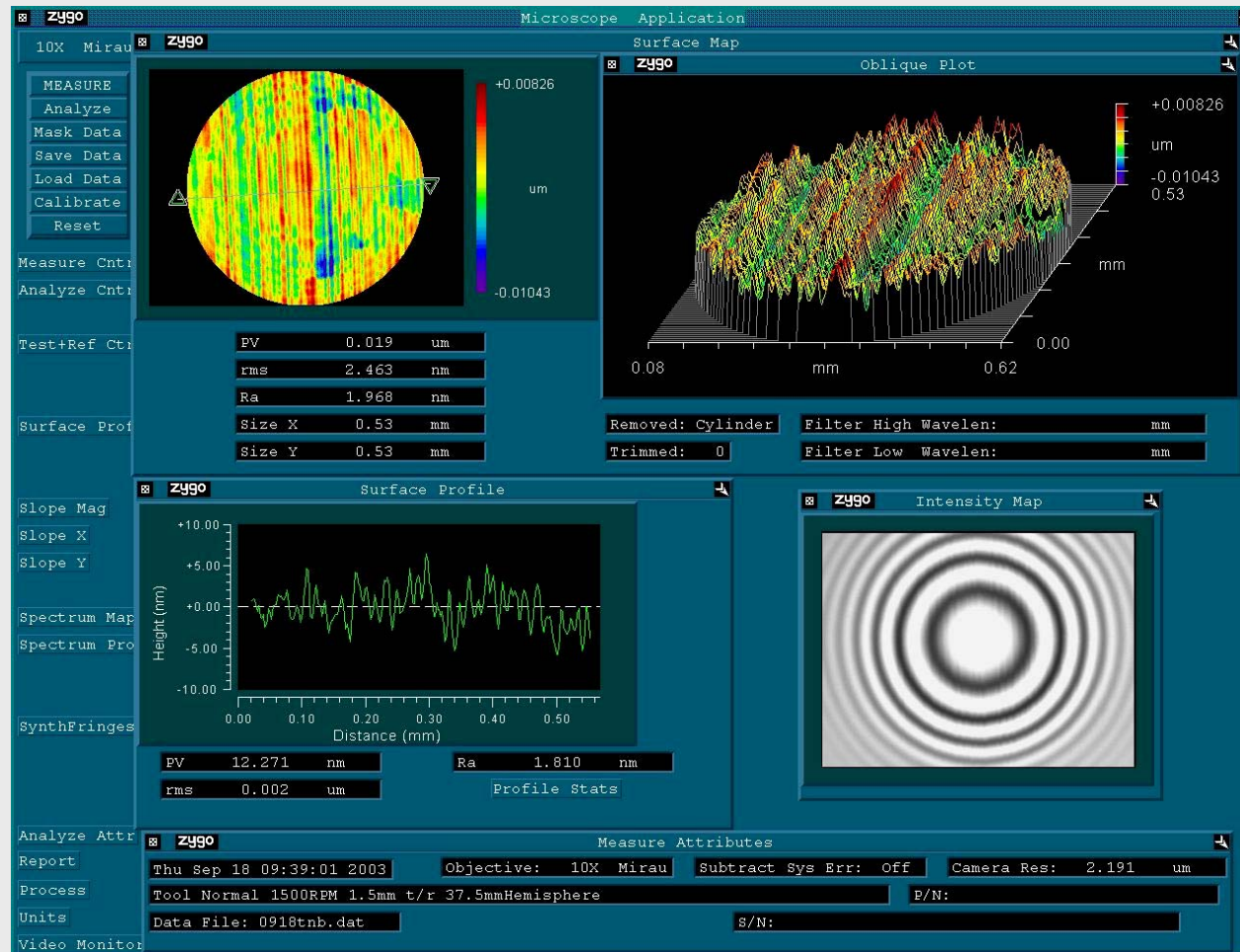
0.066 μ m P-V
(37.5mm CX
Hemisphere)

1500rpm,
12.5mm/min.



B-Axis Contouring Results

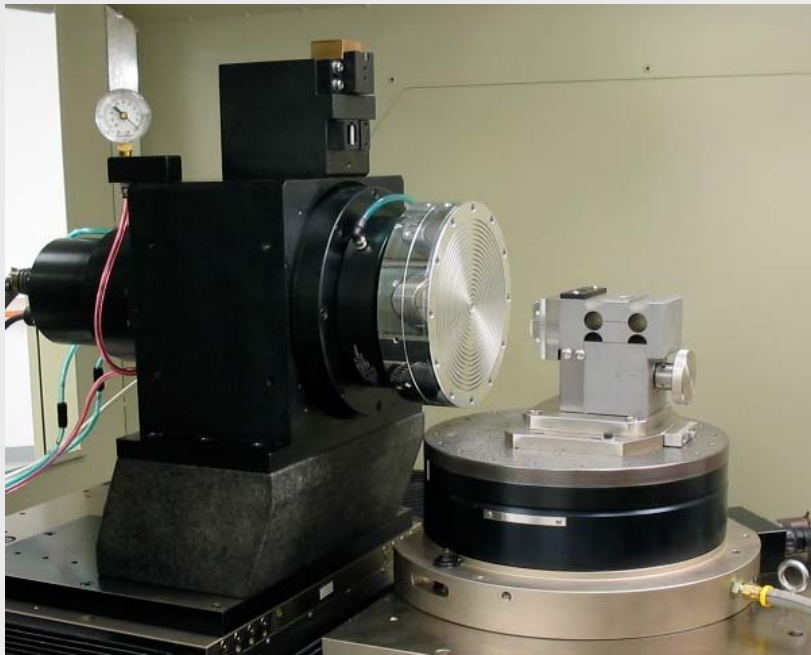
(Surface Finish - Aluminum)



1.96nm Ra
(37.5mm CX
Hemisphere)

1500rpm,
12.5mm/min.

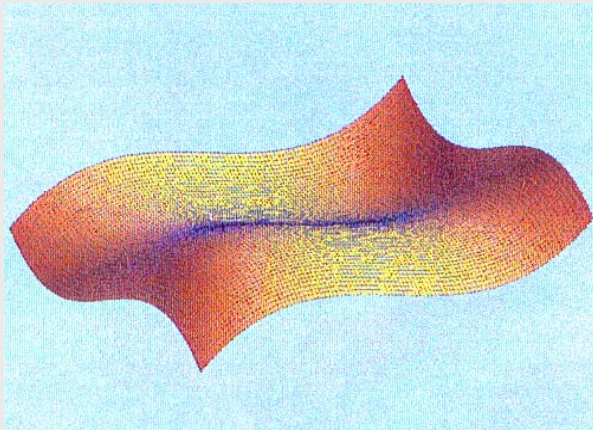
Liquid-Cooled Programmable Air Bearing Rotary C-Axis



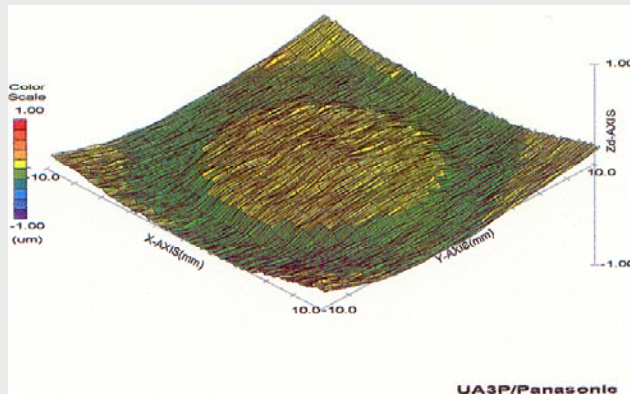
Specially designed Professional Instruments groove-compensated air bearing workspindle

- Resolution of the encoder and its electronics is 0.063 arc-seconds
- Positioning accuracy is +/- 2 arc seconds
- C-Axis can operate at a maximum speed of 2,000 RPM
- < 50nm axial & radial motion error
- 120lb. (55kg.) load capacity
>1,000,000 lbs. / in. axial stiffness
>500,000 lbs. / in. radial stiffness
- Liquid-cooled motor and bearing journals
- Closed-loop chiller maintains temperature control to $\pm 0.5^{\circ}\text{F}$

3-Axis Contour Machining With Rotary C-Axis & X & Z linear axes



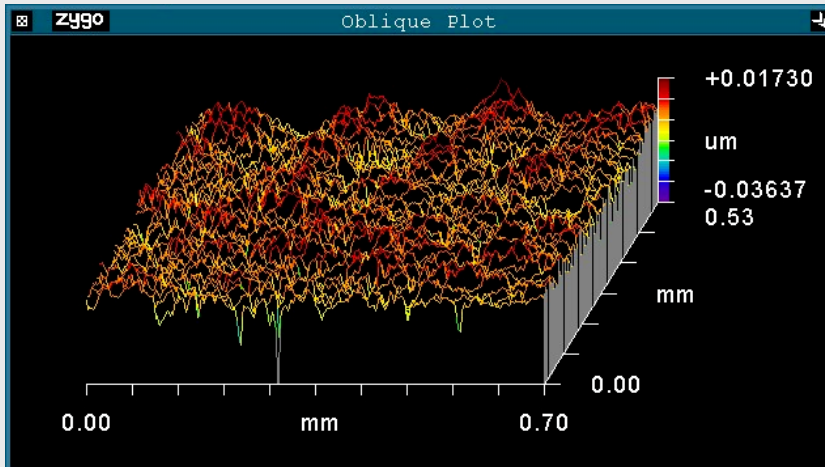
Surface of cubic phase plate



Phase plate form accuracy results

- Cubic Phase Plate Machined on the Nanotech 350UPL with C-Axis using our Slow Slide Servo (S³) technique
- Material: Zinc Sulfide 27mm X 27mm
- Form results **0.263 μm PV** (Panasonic UA3P)
- Utilizes coordinated simultaneous motion of X & Z linear axes; and C (spindle positioning) axis

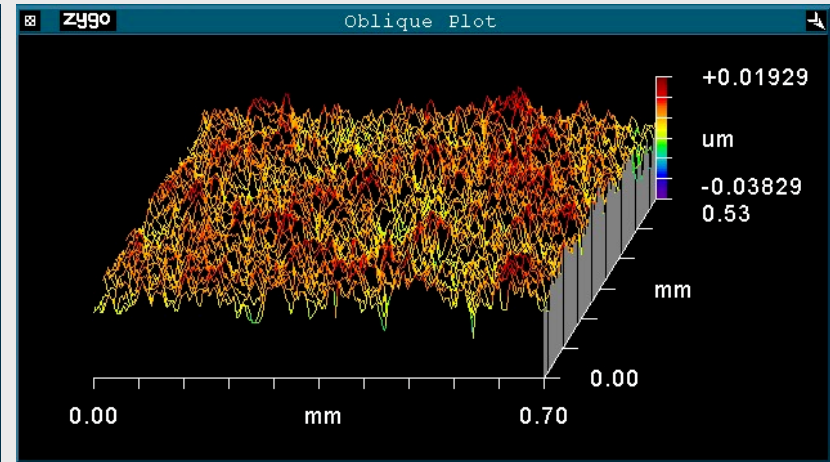
3-Axis Contour Machining With Rotary C-Axis & X & Z linear axes



Surface roughness of cubic phase plate as mached on the Nanotech 350UPL

PV	0.054	um
rms	5.319	nm
Ra	4.112	nm

Material: Zinc Sulfide 27mm X 27mm
4.112nm Ra 5.316nm Rms
(Zygo NuView)

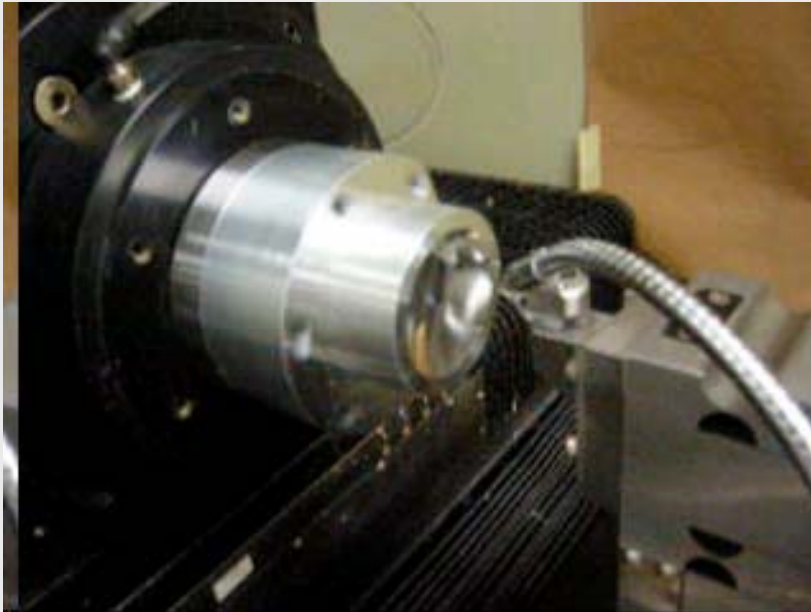


Surface roughness of cubic phase plate Polished side

PV	0.058	um
rms	5.538	nm
Ra	4.278	nm

Material: Zinc Sulfide 27mm X 27mm
4.278nm Ra 5.538nm Rms
(Zygo NuView)

Rotary Ruling with C-Axis



Processing times are several orders of magnitude faster than raster machining

- Slow Slide Servo (S³) is inexpensive
- Does not have sag limitations
- Is very accurate, and easy to set-up
- Surface finish & form accuracy results are comparable to axisymmetric diamond turning results.
- Slow Slide Servo (S³) on the Nanotech 350UPL Ultra-precision lathe is a very viable method for producing freeform surfaces

RSP High Stiffness Alloy RSA-905

Datasheet

Meltspinning process

Markets & Applications

RSP Properties

RSA-905 is a very robust and universal alloy. No heat treatment is needed to realise its properties. Typical features are:

- Superior specific stiffness
- High fatigue
- High strength
- Corrosion resistant

Properties

	RSA-905	6082 T6
Ultimate Tensile Strength (MPa)	525	290
Yield Strength (MPa)	400	250
Elongation (%)	7	10
Hardness Brinell	150	95
E-modulus (GPa)	91	71
Thermal Expansion ($\mu\text{m}/\text{m}^\circ\text{C}$)	17	24

RSA-905 is useable in a very broad temperature bandwidth.

Room temperature:

Replacement of non aluminium alloys and 7075 as well as 6082. Strength level comparable with 7075; corrosion level comparable with 6082. Products: constructions, bicycle parts, skateframes.

Medium temperature up to 200°C:

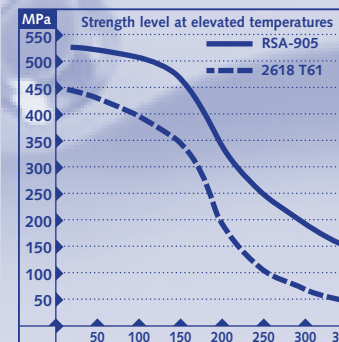
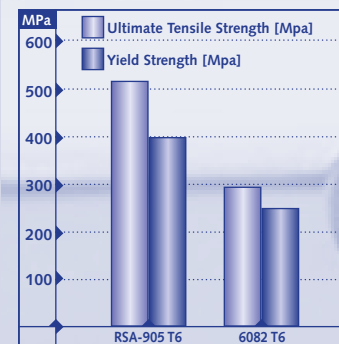
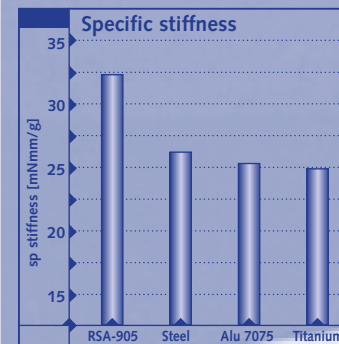
Replacement of non aluminium alloys and 2618. RSA-905 keeps its strength level very high. Products: compressor wheels, conrods and fasteners.

High temperature up to 350°C:

Replacement of 2618. Products: pistons

Typical compositions

	Zn	Si	Cu	Fe	Mg
RSA-905	-	-	2.5	2.5	0.5
Conventional 6082 T6	-	1	-	-	0,9



RSP Technology BV

Metaalpark 2

9936 BV Delfzijl

Phone: +31 (0)596 632300

Fax: +31 (0)596 632678

www.rsp-technology.com

e-mail: info@rsp-technology.com

Principles and Applications of the Slow Slide Servo

Yazid Tohme and Ralph Murray
Moore Nanotechnology Systems LLC
426A Winchester St. Keene, NH. USA



Abstract

Slow Slide Servo is a novel machining process capable of generating freeform optical surfaces or rotationally non-symmetric surfaces at high levels of accuracy. In able to achieve good results with this technology some key parameters need to be satisfied. These parameters include tool path generation, tool radius correction, machine set-up, servo system performance, and the CNC (Computer Numerical Control) computing capabilities. This paper will discuss some of the parameters that allow for good slow slide servo results and include recent experimental form and finish results on several different freeform surfaces.

Introduction/Background

With advances in optical design and the advent of advanced ultra precision machining systems freeform optical surfaces are now a practical solution to many problems. These freeform surfaces are today used in many applications including eyewear, electro-optics, defense, automotive, and others. Although these surfaces are referred to as freeform most of them in fact are mathematically determinant. These non-symmetrical surfaces include torics, biconics or bi-ashperics, phase masks, NURBS defined surfaces, F-theta lenses, progressive lenses, lens arrays, and lenses that require off-axis machining.

Several techniques exist for the manufacturing of freeform optical surfaces. These techniques include micro-milling, raster-cutting or fly-cutting, profile and form grinding and the fast tool servo. The proposed machining technique in this work is similar to the Fast Tool Servo but utilizes the existing machine Z-axis slide (Axis parallel to spindle rotation) as the oscillating axis. This method of manufacturing has proven to be as accurate and faster than most other methods. In this presentation we will discuss the steps required to manufacture parts using slow slide. This will include a machine description, the tool path generation and several examples of machined parts.

Slow Slide Servo

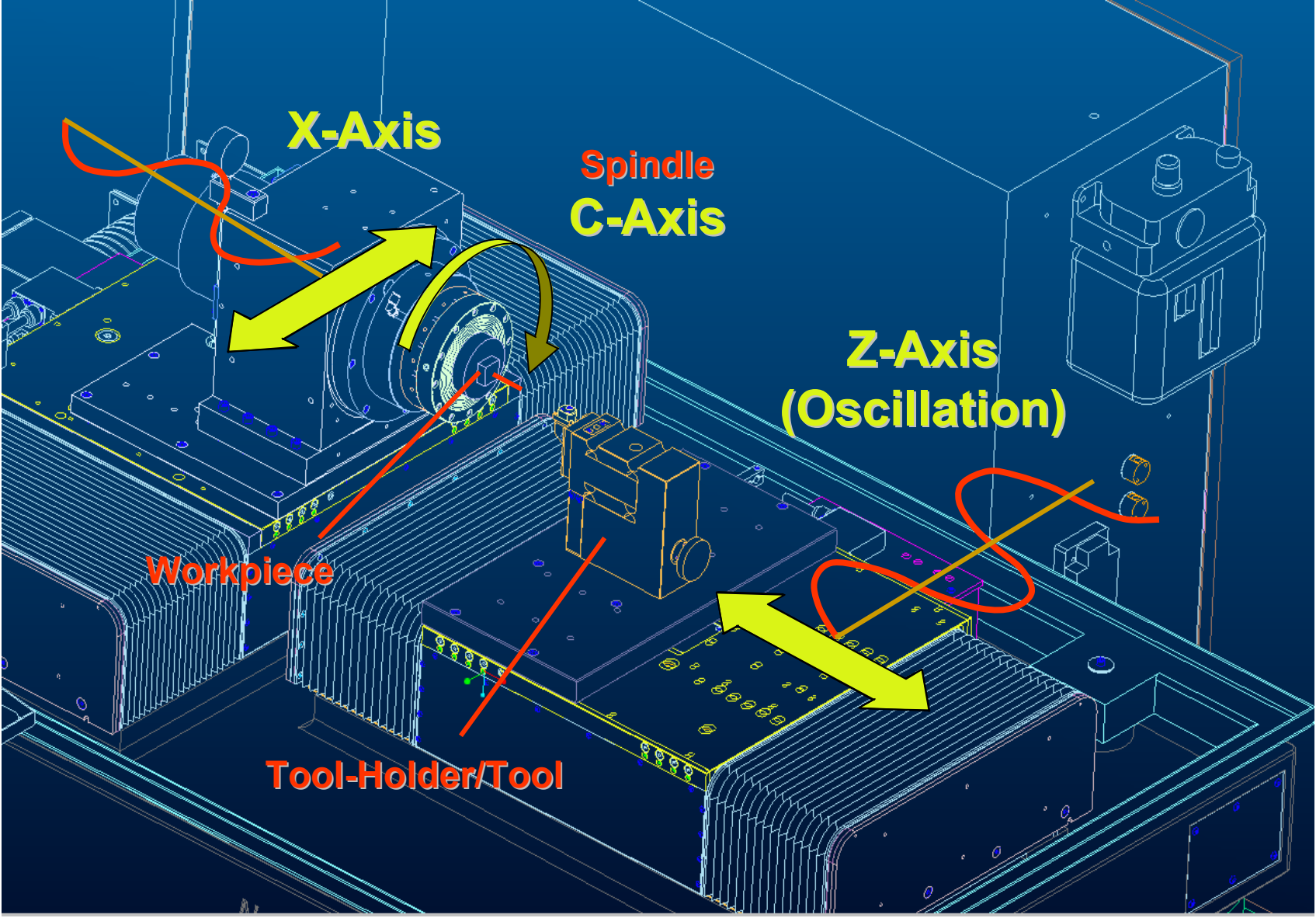
A typical diamond turning lathe consists of two linear axes and a spindle or rotary axis. Both linear axes, X and Z, are position controlled. The rotary axis is velocity controlled but in the case of the slow slide the rotary axis, or spindle axis, is position controlled. All three axes are then commanded by a CNC program to continuously contour in 3D. In typical machine tools 3D machining is performed using 3 linear axes, X, Y and Z (Cartesian Co-ordinate System). In slow slide we are performing 3D machining in Polar or Cylindrical co-ordinates. The XYZ are translated into R, Z and θ .

In slow slide servo as well as fast tool servo the z position is a function of not only x-axis but also the work spindle position or c-axis. A diamond tool is mounted along the z-axis of a lathe and the part with the freeform surface or non-symmetric surface is mounted on the work spindle. As the part rotates, the z-axis carrying the diamond tool oscillates in and out in a sinewave type motion to generate the surface. In a FTS the diamond tool is mounted on an auxiliary axis that is optimised to perform sinewave type oscillations, typically a piezo-electric stack or a voice coil motor, drives this auxiliary axis. The slow slide servo does not require any additional or auxiliary axes utilising only the existing diamond turning lathe's z-axis, as the oscillating axis. The z-axis is driven in translation by a linear motor optimised to drive the z-axis and diamond tool in a sinewave type motion varying in amplitude and frequency. Depending on the amplitude of the sinewave, frequencies up to 60 Hz can be obtained. The c-axis is simply an additional axis in the machine co-ordinate system. This axis rotates the work piece about the z-axis, and is position controlled to very high accuracy. The position loop bandwidth of the c-axis, which is a measure of system performance, is typically above 120Hz.

Machine Description

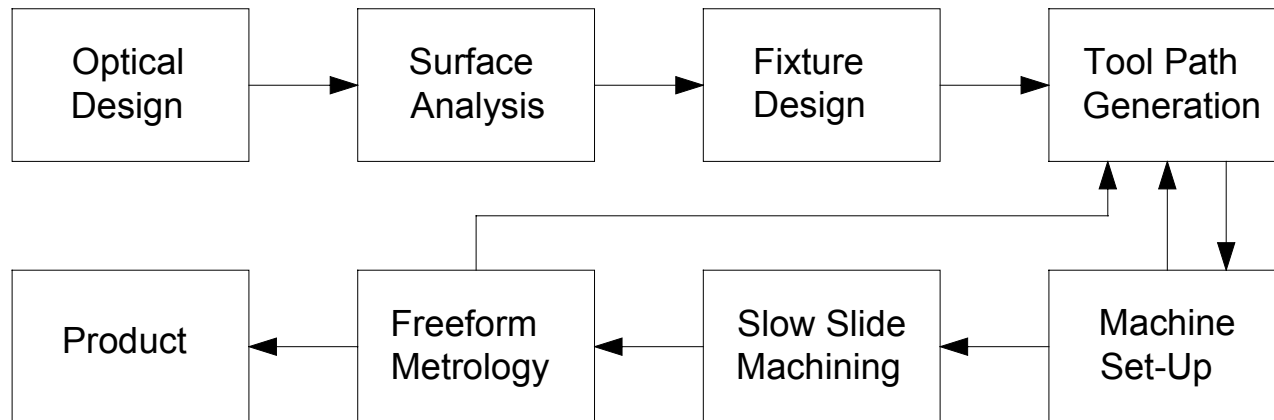


nanotech



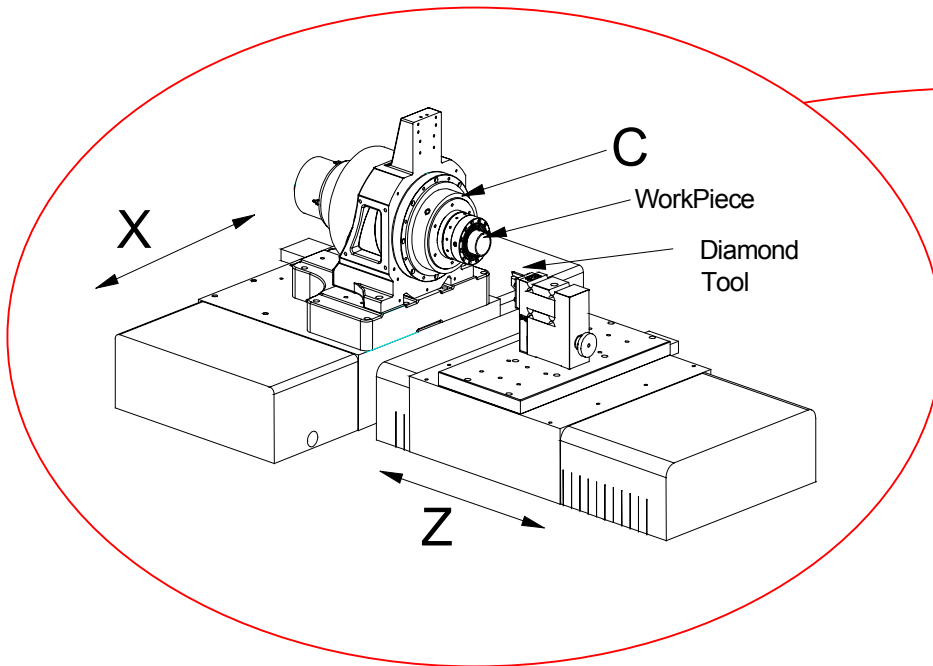
Freeform Generation

Several steps have to be completed to produce a freeform optical surface using slow slide servo. The block diagram below shows these steps. The optical design engineer usually provides a drawing of the surface along with an optical equation that describes the surface. In some cases the design is based on NURBS (Non-Uniform Rational B-Splines) so a 3D CAD model is required for these surfaces. The first step is to analyze the surface and decide whether it is possible to generate it using slow slide servo. That includes checking the surface slopes; extremely steep parts are not possible to machine due to the interface between the cutting edge of the diamond tool and the work piece surface. In addition it is important to determine the tool sweep required and the maximum allowable tool radius. The second step is to design the fixture to mount the part on the work spindle or c-axis. During fixture design it is important to keep in mind that in most cases a rotationally symmetric work piece must first be machined utilising the same fixture to establish the correct tool height, tool center and tool radius. The third step is tool path generation.



Machine Performance

The Moore Nanotechnology 350UPL was used for this work. This diamond turning lathe has a T-shape configuration with the spindle mounted on the X-axis and the diamond tool on the Z-axis. The spindle can operate in two different modes, velocity mode or position mode. The spindle is used in velocity mode for typical axisymmetric diamond turning work with a maximum speed of 10,000 RPM. In the position mode the spindle uses an optical encoder to close the position loop. The same actuator motor and amplifier is used for both configurations. The resolution of the encoder and its electronics is 0.063 arc-seconds or 20,480,000 counts/rev. The C-axis positioning accuracy is +/- 2 arc-seconds. In this mode the spindle can operate at a maximum speed of 2,000 RPM.



Axes Performance

A PID loop with feedforward compensation is used to control all the machine axes. The feedforward assists in eliminating most of the time delay between commanded and actual position. In other words it reduces the phase lag in the system.

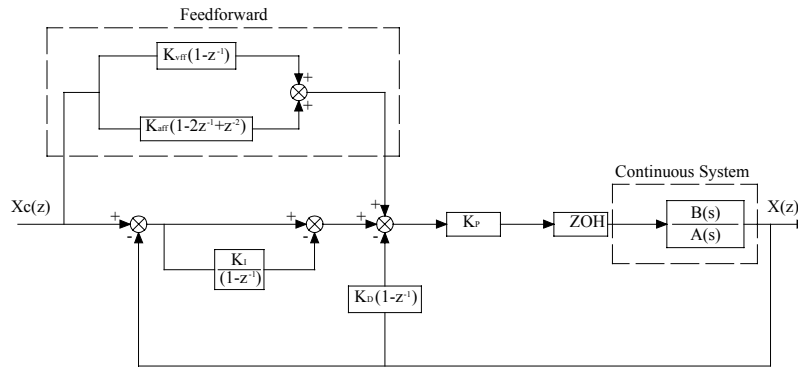
C-axis

Bearing Type: Groove compensated air bearing
 Motor: Rotary brushless DC motor
 Travel: 360 degrees
 Feedback: Rotary optical encoder
 Resolution: 0.063 arc-sec (20,480,000 cts/rev)
 Position Loop Bandwidth: > 100Hz
 Feedback Loop: P-I-D with feedforward

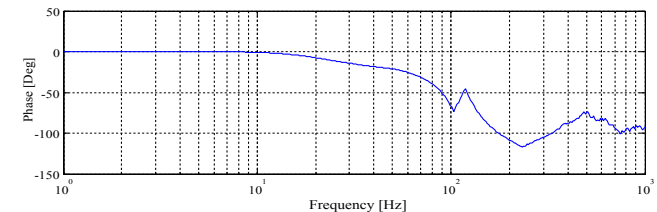
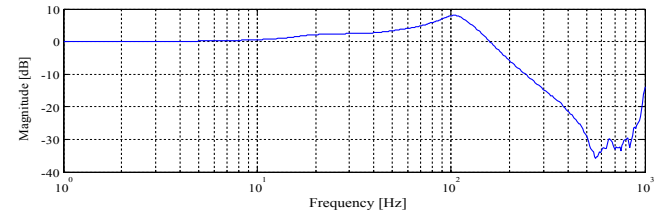
X-axis/Z-axis

Bearing Type: Fully constrained hydrostatic bearing
 Motor: Linear brushless DC motor
 Travel: 350mm/300mm
 Feedback: Holographic linear scale
 Resolution: 0.034nm (34 pico-meters)
 Position Loop Bandwidth: > 100Hz
 Feedback Loop: P-I-D with feedforward

Control Loop Strategy



Where -- K_p : Proportional Gain K_{vf} : Velocity Feedforward Gain
 K_i : Integral Gain K_{af} : Acceleration Feedforward Gain
 K_d : Derivative Gain ZOH: Zero-Order-Hold
 $B(s)/A(s)$: Open Loop Transfer Function



PID Loop with Feedforward Compensation

Rotary axis Closed position Loop Bandwidth

Tool Path Generation

Tool path generation for freeform surface is probably the most complex step in the slow slide servo process. As mentioned earlier, the surface is usually defined by an optical equation. This equation must be specified as a function in cylindrical coordinates $Z = \text{function}(r, \phi)$ where r is the radius or the machines x-axis and ϕ is the work spindle angle or c-axis position. Therefore, equations defined in Cartesian coordinates as $Z = \text{function}(X, Y)$ need to be converted to cylindrical coordinates. There are multiple ways to create the r and ϕ points before solving for z . The ϕ points or ϕ can be made from equally spaced chords or equally spaced angles. Usually equally spaced angles yield better results. After the r and ϕ points are determined they are used to solve the function for each of the z points. The next step in tool path generation is the tool radius compensation. The surface slopes of the non-rotationally symmetric surfaces are not only dependent on changes in the radius r but also on changes in the angle ϕ . Slope calculations are required at every z point. The slopes can be computed using two methods; the first method is the differentiation of the data points and the second method is the differentiation of the equation, $Z = \text{function}(r, \phi)$. The equation differentiation has been proven to be the more accurate solution, however it is the more difficult one to compute. If the optical surface is generated using NURBS the tool path is better computed using an off the shelf CAM (Computer Aided Manufacturing) software. CAM systems usually don't provide the same level of accuracy as obtained by solving an optical design equation, because they try to fit non-uniform splines to the surfaces and there are errors associated with these fitting functions.

Once the z , x , and ϕ data points are generated they are written to the NC file (The machine input file). The NC file is then executed. Unlike regular machining it is been found that to produce more accurate parts it is better to machine the part in inverse time G93 rather than mm/min G94. The reason behind this is inverse time allows the program to run with a variable velocity or axis feed rather than a fixed velocity. This variable velocity programming generates more accurate sine waves, while fixed velocity distorts the sine waves the machine is trying to perform.

Experimental Results



Several freeform surfaces are described below to illustrate the slow slide servo capabilities. The results of these surfaces are shown on the following pages.

- Surface #1: De-centred sphere.** The part is an aluminium sphere with a 75mm diameter and a 75mm concave radius it is offset from the spindle center by 7.686mm. The sphere is then cut with a 1.5mm radius diamond tool. The maximum oscillation of the Z-axis is approximately 11mm. The finish cycle on this part is about 30 minutes. A Zygo GPI laser interferometer is utilized to qualify the form accuracy of the surface
- Surface #2: Toric.** The two radii of the toric are 25mm and 75mm. A standard toric equation is used to calculate the Z points for the surface and the tool compensation was generated by differentiating the data points. The surface is machined in electroless-nickel with a 1.0mm radius tool and a spiral infeed of 2.5 microns per revolution. A Taylor Hobson Form Talysurf instrument was used to qualify the form accuracy of the surface. The surface is measured in two meridians 0 and 90 degrees, which correspond to the 25mm and the 75mm radii of the toric surface.
- Surface #3: Cubic Phase Plate.** This part was machined in Zinc Sulfide. The diamond tool radius is 0.6mm and the rake angle of the tool is negative 25 degrees. The sag of the surface is 100 μ m PV. The part was machined in about 25 minutes. The form accuracy of the part was qualified using a Panasonic UA3P profilometer.
- Surface #4: Zernike defined Surface.** This surface was designed using a Zernike equation. The same equation is then used to generate the tool path for slow slide servo. The surface was then machined in plastic (PMMA) using a 0.5mm radius diamond tool. Because the surface sag is small the form accuracy was measured using a laser interferometer with a reference flat. Although it was possible to measure this surface it was very difficult to analyze the surface for form accuracy from the laser interferometer measurement.
- Surface #5: Sinewave Surface.** This surface was generated using a mathematical equation. The same equation is then used to generate the tool path and cut the part in electroless-nickel. The form was measured using a laser interferometer, but analysis of the form was not performed.

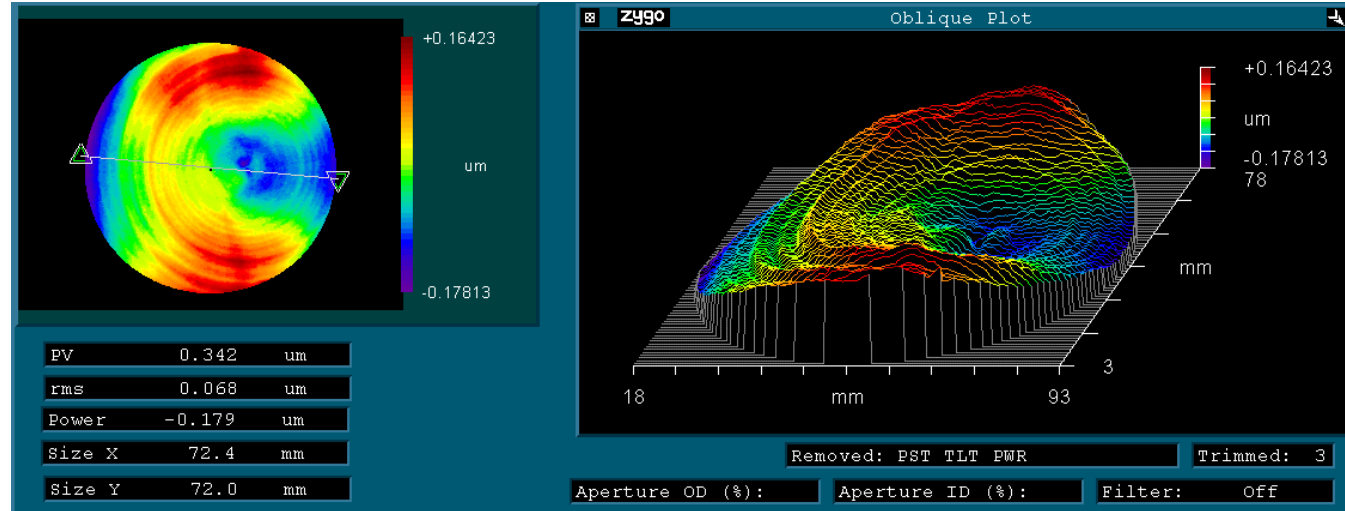
Surface #1: De-Centered Concave Sphere



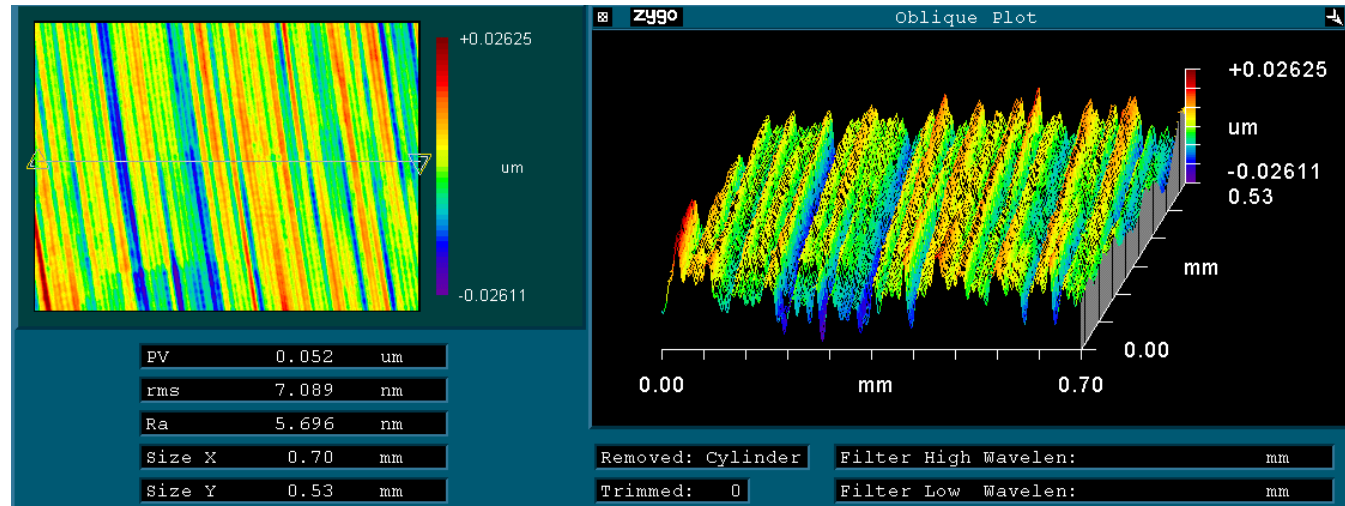
Diameter: 75mm,
Off-axis Distance: 19.4mm
Finish Machining Cycle: 30 minutes

Concave Radius: 75mm
Sag: 10mm PV

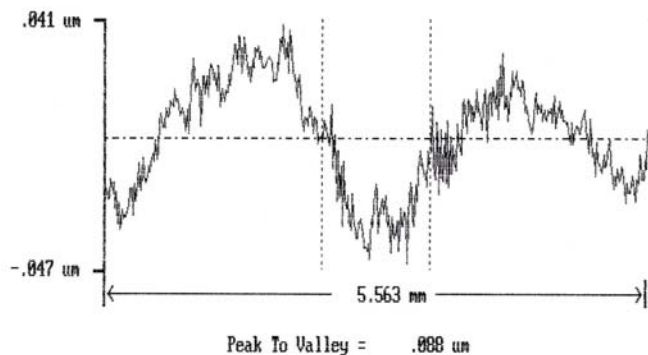
Form Accuracy:
PV-error 0.342 μm



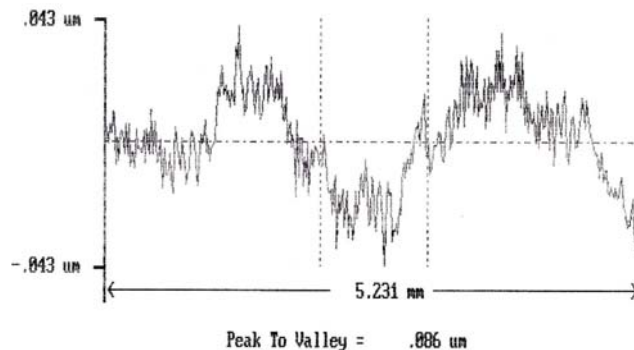
Surface Finish:
5.696nm Ra



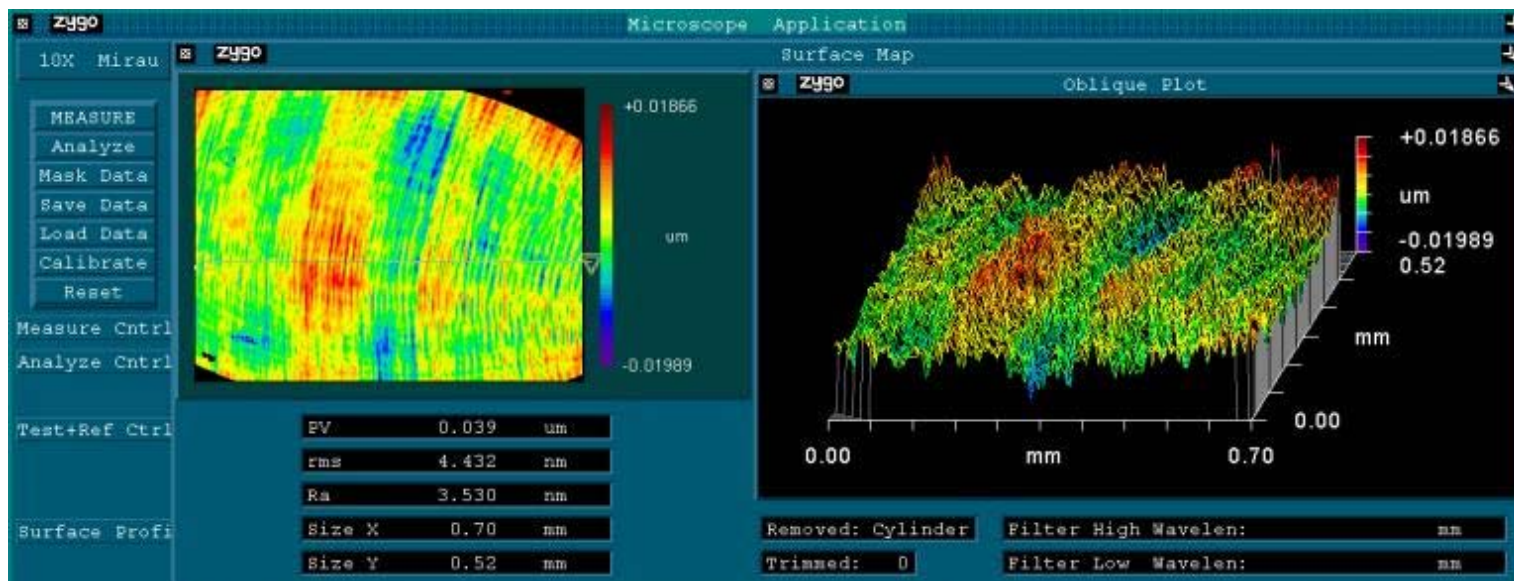
Surface #2: Toric Surface



Form Accuracy: (at 0 degrees) 0.088 μ m PV



Form Accuracy: (90 degrees) 0.086 μ m PV



Surface Finish: 3.530 nm Ra

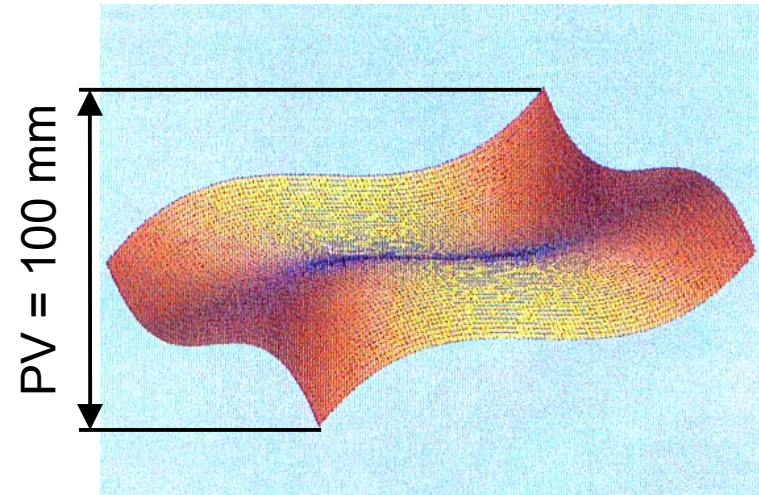
Surface #3: Cubic Phase Plate

Surface Equation: $Z=0.025 ((X/10)^3 + (Y/10)^3)$

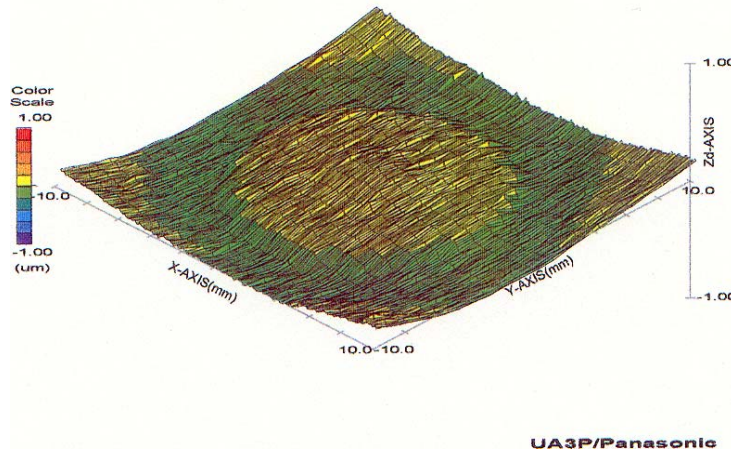
Material: ZnS (Zinc Sulfide)

- Tool:
- Material: Diamond
 - Rake Angle: -25°
 - Tool Radius: 0.6 mm

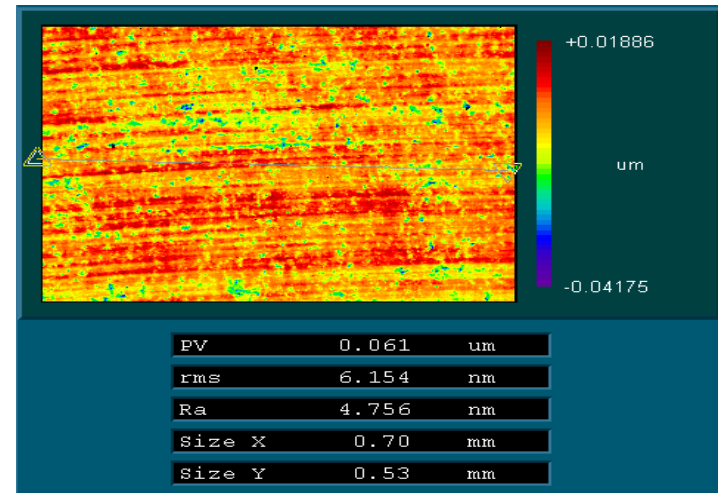
Feedrate: 7 mm/rev



Mathematical representation of the surface

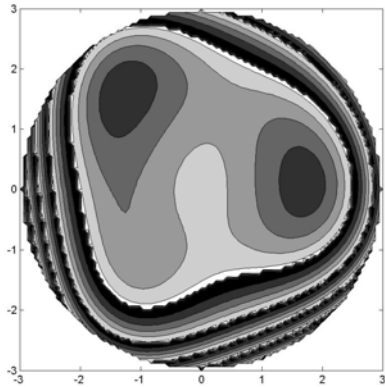


Form Accuracy: 0.263 μm PV

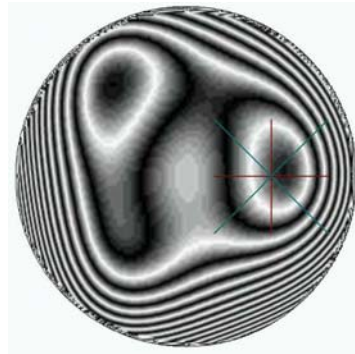


Surface Finish: 4.756 nm Ra

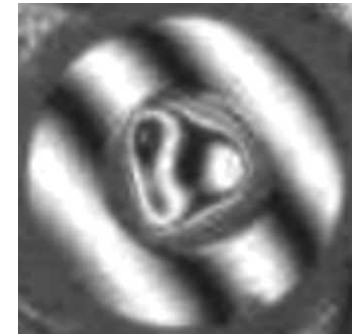
Surface #4: Zernike described Surface



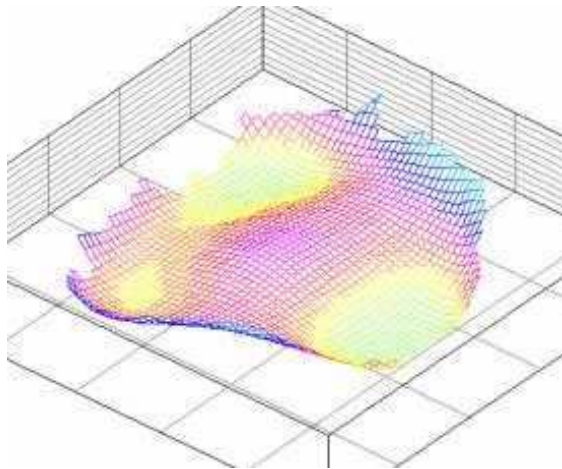
Zernike Design



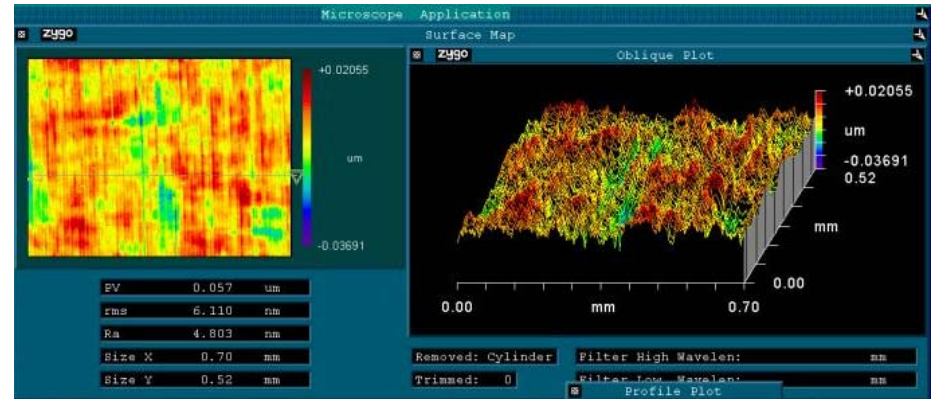
Tool Path Generator



Laser Interferometer Measurement

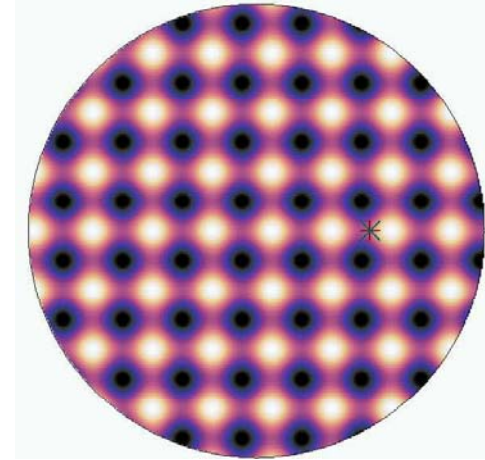
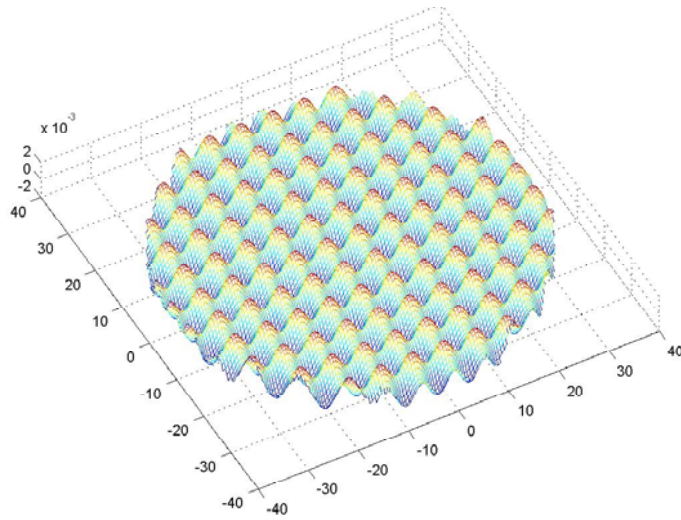


Laser Interferometer 3D map



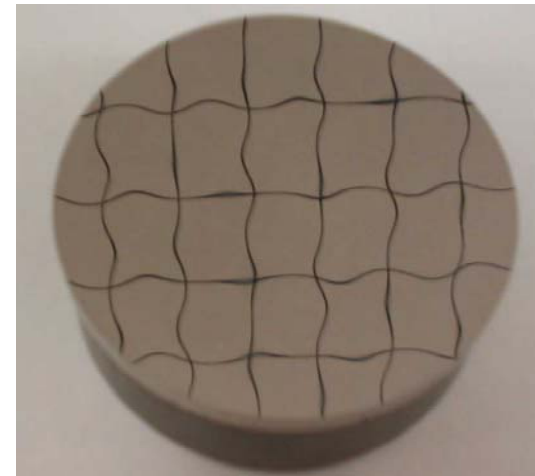
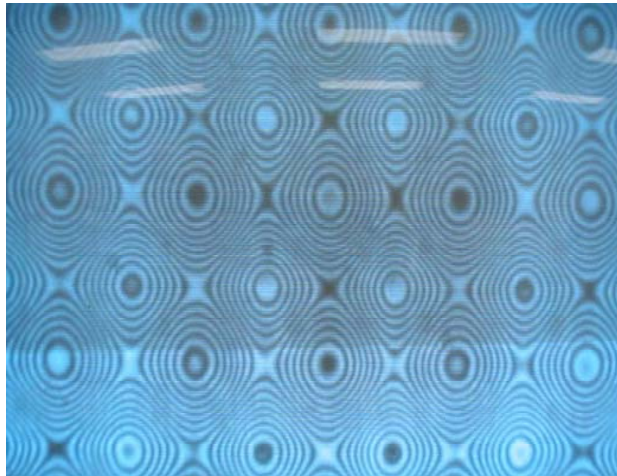
Surface Finish: 4.803 nm Ra

Surface #5: Sinewave Surface



Mathematically Generated Sinewave in the X and Y direction. The PV of waves is $8 \mu\text{m}$

The surface imported in the Tool Path Generator



Measured on a Laser Interferometer

Photograph of the Surface

Conclusion

We have briefly described the processes required to, and illustrated the capability of, the slow slide servo to produce freeform optical surfaces. In general good form accuracy can be achieved on most freeform surfaces using slow slide servo technology. Qualifying the form accuracy of freeform surfaces is a difficult task. This is primarily due to the fact that there is no cost-effective commercially available metrology equipment capable of freeform measurement.

Slow Slide Servo (S³) Machining of Freeform Optical Surfaces - Abstract

Moore Nanotechnology Systems, LLC
Keene, New Hampshire, USA

In recent years a significant amount of work has been accomplished in the area of generation of freeform optical surface. Most of this work is driven by market demand for these types of surfaces, which includes eyewear, electro-optics, defense, automotive and other industries. Presently, there are several methods of manufacturing such surfaces of which the most common are grinding and raster flycutting. Both grinding and flycutting rotate the tool and traverse either the tool and/or the workpiece in three linear axes to cut the surface. Grinding and fly cutting can produce very accurate surfaces but require long machining cycles and are difficult to set-up. Another method of fabrication is the Fast Tool Servo (FTS), which is widely applied in the contact lens industry. However, most FTS systems have a maximum travel range of less than 1mm and therefore are limited to certain part geometry with small departures.

Moore Nanotechnology Systems (Keene, NH, USA) has been applying an alternative method to generate freeform optical surfaces via "Slow Slide Servo". The Slow Slide Servo method is similar to the FTS in that, the part is mounted on the spindle and as the spindle rotates, the tool oscillates (Figure 1). Unlike the FTS method, this system does not use any additional axes for oscillating the tool; the Z-axis slide generates the oscillations. Another difference is the spindle position control (or C-axis). In an FTS set-up, the spindle has an encoder that feeds the position to the FTS unit without putting the spindle in position control. In a Slow Slide Servo all axes are under fully coordinated position control. The Slow Slide Servo can oscillate at ranges up to 25mm, is easy to set-up, inexpensive, and allows the manufacturing of highly accurate parts.

To implement the Slow Slide Servo method, several key features must be available on a diamond turning lathe. Most of these features are the same for both the linear and the rotary axes. They include friction-free bearings that generate little heat, direct drive motors with no mechanical compliance between the motor and the feedback system, high-resolution encoders, and minimal structural dynamics in the control loop. Another key feature is the control system or the CNC. The CNC must have high-speed data processing, look-ahead capability, a high-resolution data acquisition system, and high-order trajectory generation.

Several different freeform surfaces have been machined using the Slow Slide Servo method to show the viability of this type of machining. One example of these surfaces is the cubic phase plate shown in Figure 2. This part was machined in Zinc Sulfide with a negative rake-angle diamond tool. The sag of the surface was 100 μm Peak to Valley (PV). The form results shown in Figure 2 indicate that the PV error is 0.26 μm and the surface finish is 4.6 nm (Ra).

Another example of the use of this method is the machining of an off-axis sphere. A 75 mm diameter 6061 aluminum concave sphere with a 75 mm radius is offset from the spindle center by 7.686 mm. The sphere is then cut with a 1.5 mm radius diamond tool. The maximum oscillation of the Z-axis was approximately 11 mm. The form accuracy results of the sphere were 0.33 μm PV and the finish results showed a roughness average of 5.6 nm. Several other surfaces have been machined using this method including tilted flats, progressive lenses, cylinders, torics and biconics on a variety of materials. They all showed comparable form and finish results to the above samples.

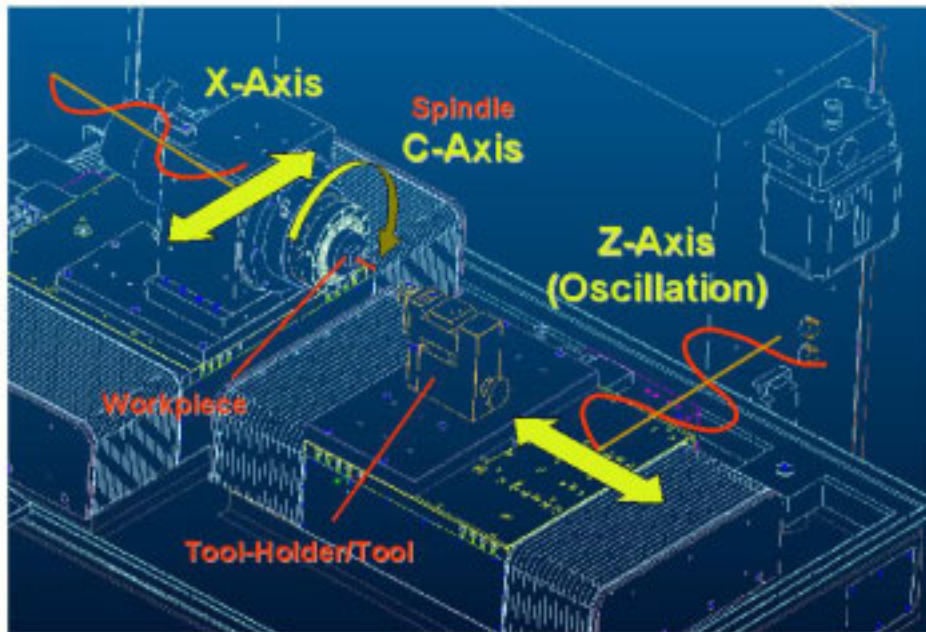


Figure 1: Setup for machining with Slow Slide Servo

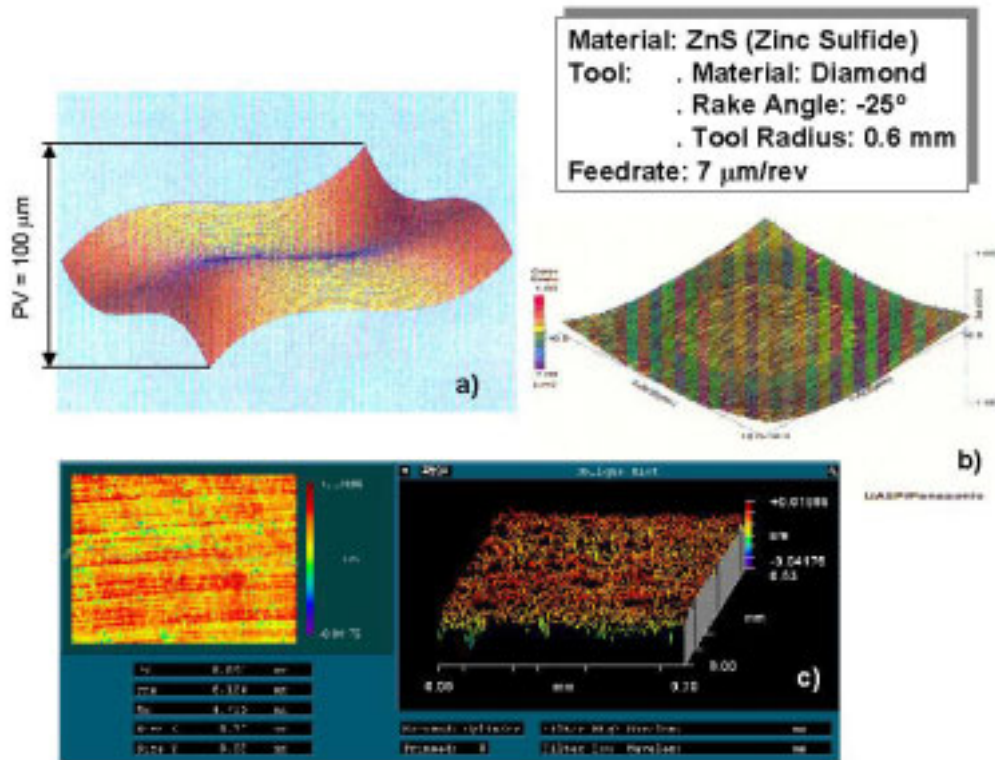


Figure 2: Cubic Phase Plate Surface. a) Mathematical representation of the cubic phase plate surface. b) Form accuracy measurement results (measured with Panasonic Profilometer UA3P). c) Surface finishing results (measured with Zygo NuView).

Ultra-precision Machining Systems; an Enabling Technology for Perfect Surfaces

Gavin Chapman

Moore Nanotechnology Systems LLC, PO Box 605, 426a Winchester Street, Keene, NH 03431, USA

A Historical Overview

The technology of ultra-precision machining, spanning almost three decades, has only in recent years experienced major advances in machine design and, subsequently, performance and productivity. In the 1970's, ultra-precision machining techniques were successfully adopted for the manufacture of computer memory discs used in hard drives, and also photoreceptor components used in many photocopier machine and printer applications. Such applications required extremely high geometrical accuracies to be achieved, in combination with super smooth surfaces. These surfaces were found to be most effectively manufactured by single point diamond turning, as opposed to multiple processes such as machining, lapping, and polishing.

The machinery developed for such applications typically required only one linear axis of motion, to generate a cylindrical or plano form. The machines often utilized an air bearing work holding spindle, and linear slide, mounted to a granite base. Machinery soon evolved into multi-axis systems, with major advances seen in CNC control, and position feedback technology. An example of one of the early multi-axis machines is shown below.



An early multi-axis single point diamond turning machine

During this era, the use of ultra-precision machining continued to revolve around the core technology of single point diamond turning. As such, the process was limited to those materials that could be machined by a diamond tool. These materials include most all Face Centered Cubic elements, fundamentally non-ferrous alloys such as

Aluminum, Copper, Nickel, Gold, Brass, & Bronze. In addition, it was found that diamond machining was well suited to cutting crystal materials such as Germanium, Silicon, Zinc Sulfide & Selenide, as well as polymers such as polymethylmethacrylate, polystyrene, and polycarbonate.

It is not surprising that applications soon developed for defense optics, in addition to commercial products. The emerging technologies of infrared night vision systems required a range of reflective components such as toroids, polygons, frame mirrors, and cold shields. These were typically machined in aluminum alloys such as 6061. In addition, lenses in Germanium were required for windows and lenses. Designers were now making use of aspheric geometries to reduce spherical aberration, minimize the number of elements thus reducing weight, and ultimately reducing the amount of costly Germanium required.

Infrared systems operating at different wavelengths utilized Silicon lens and window elements. Silicon had, and has to this day, distinct cost saving benefits, and is considerably lighter than Germanium. Silicon is however extremely difficult to diamond machine, primarily due to its hardness, and therefore did not proliferate to widespread use with aspheric geometries. With today's machine technology, incorporating stiffer axes, smoother drives, and more precise spindles, silicon aspherics can be single point diamond turned more effectively than ever. At the same time, deterministic micro-grinding developments at establishments such as the Center for Optics Manufacturing at the University of Rochester allow Silicon aspherics to be deterministically ground to a precision that often requires no further polishing.

Widespread Application

Commercial applications for single point diamond turning developed throughout the United States, Europe, and interestingly, later in the Far East. The boom in consumer electronics, and a certain dependence on optics technologies has fueled a massive growth in the use of aspherics, and other rather non-conventional geometries. Optical design software has allowed designers to optimize system performance in all respects by building in complex, yet manufactureable surface forms. In parallel to machinery being developed for general sale on a commercial basis, certain leading companies, such as Philips of The Netherlands, developed highly innovative machining technologies "in house", in order to exploit opportunities in, for example, the Compact Disc player market. Many of these applications however required optics in vast numbers and so individual diamond machining was not cost effective. Grinding processes were therefore developed that utilized basic ultra-precision machining practices, while adopting a fixed abrasive wheel in place of the single point diamond tool. This, in combination with injection molding, and hot pressing, was adopted to produce the optics required in the many consumer electronic products that we now take for granted.

The grinding process allowed mold inserts to be generated with primarily aspheric forms, but did not allow more complex diffractive geometries due to the restrictive

diameter of the grinding wheel. Mold inserts manufactured from harder, and more brittle materials are still commonly used today. Materials such as tool steels, Tungsten Carbide, and Silicon Carbide can be consistently ground to surface textures better than 10nm RMS, and figure accuracies as low as $\lambda/10$.



CD & DVD Pick-up Lenses

More Recent Developments

It is in the past 10 years however that some major advances in controls, feedback systems, servo drives, and general machine design and construction have evolved to the point where today's ultra-precision machining systems are more productive, more precise, and lower in price. This has resulted in a proliferation of their use throughout the world for a wide range of applications.

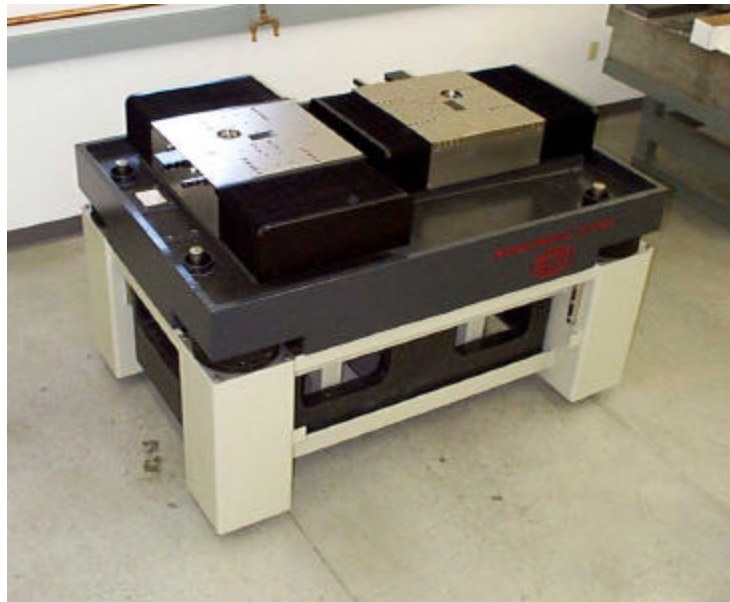
Today's single point diamond turning machines have evolved to utilize a host of new technologies. When combined in a regimented manner, these allow surfaces to be single point diamond turned in all the aforementioned materials, to a surface texture often as low as 2nm RMS, and with figure accuracies, low in absolute error, and exhibiting very low slope characteristics.

Many of these enabling machine features are listed below.

- Epoxy granite or natural granite machine bases, for thermal and mechanical stability, damping characteristics, lower center of mass, and design flexibility.
- Optimally located air isolation, for optimized servo performance, and enhanced vibration isolation.
- Hydrostatic oil bearing box-way linear axes, for enhanced damping, smoothness of motion, geometrical accuracy, and wear free operation.
- DC linear motors provide rapid feed rates, smooth, wear-free, and non-influencing motion, and superb longitudinal dynamic stiffness.
- High-speed air bearing spindles allow faster feed rates, therefore reduced cycle times, as well as smooth rotational motion, high load capacity, and stiffness.

- High speed CNC controls, utilizing PC technology, to allow networking, huge part program storage, and utilization of 3rd party programs. Also to facilitate the use of advanced drive and feedback devices to improve workpiece accuracy.
- High-resolution linear scales, providing precise axis position feedback for nanometric incremental moves, improved dimensional stability, and ultimately, consistent and precise geometrical accuracy.
- On machine workpiece measurement and error compensation systems allow residual workpiece errors to be assessed, and practically eliminated, providing they are of a repeatable nature.

A current state-of-the-art single point diamond turning machine is shown below. This has the spindle mounted on the X-axis, and would typically have the diamond turning tool mounted on the Z-axis. The Axes are mounted in a classic “T” configuration, and as such allows any rotationally symmetrical part to be machined.



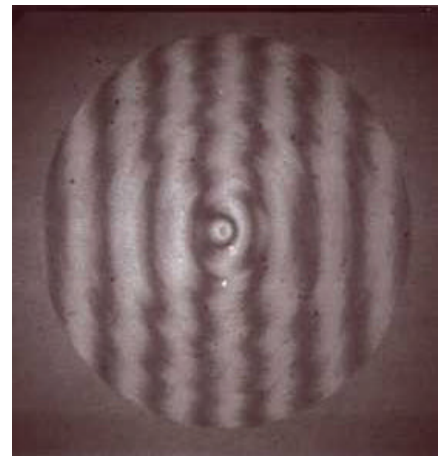
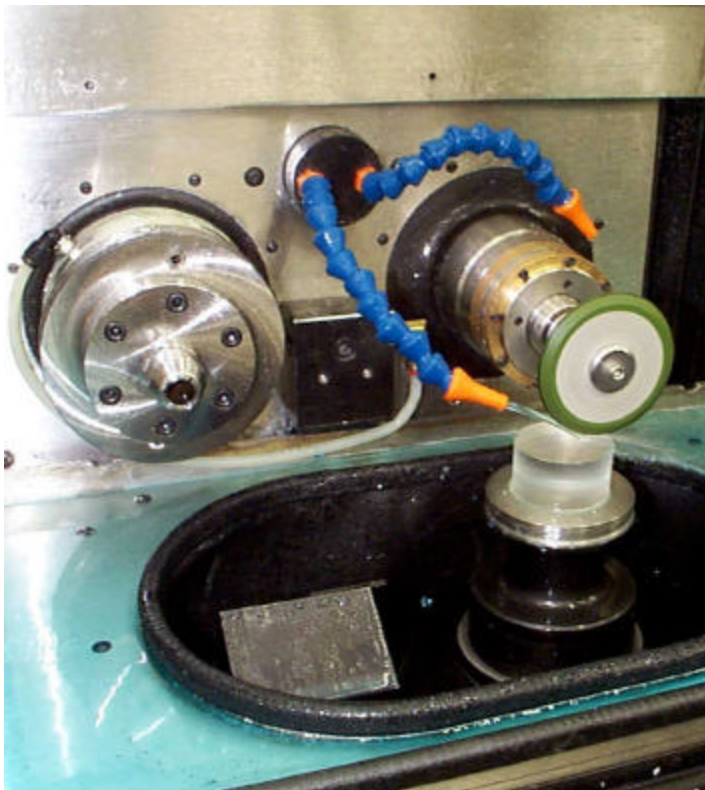
Current state-of-the-art single point diamond turning machine (base & slides)

The Need to Grind

Single point diamond turning machines are often provided with add-on grinding attachments, to extend their usage to those materials that are not diamond machineable, as described earlier. This approach provides for an extremely flexible machining system, but extreme care must be taken at the earliest design stage to ensure that the stiffness of the machine is apt to handling the increased grinding forces, and that the guarding and coolant containment measures are up to the increased demands. Due to the limited space available, the grinding attachment may also be limited to a single spindle. This might then require wheels to be changed more often than desired, for rough grinding and finish grinding operations.

If applications revolve purely around the grinding of mold inserts, or for the direct grinding of glass aspherics, then a dedicated grinding machine may be more appropriate. This type of system will be designed to handle the increased forces and coolant volumes, and will likely incorporate both a rough and finish grinding spindle for improved productivity. The workpiece might also be mounted in a vertical axis orientation that is familiar to many glass processing operatives. The ability to directly grind precision aspheric glass lenses economically has opened a floodgate of applications in both commercial and defense fields.

For example, current technology is able to take a 50mm diameter rough glass molding or pre-generated blank, and finish grind to a $\lambda/2$ figure and 3nm RMS finish, within 15-30 minutes. The specific accuracies and cycle times are of course very dependent on specific glass types, such is the process-related nature of grinding.

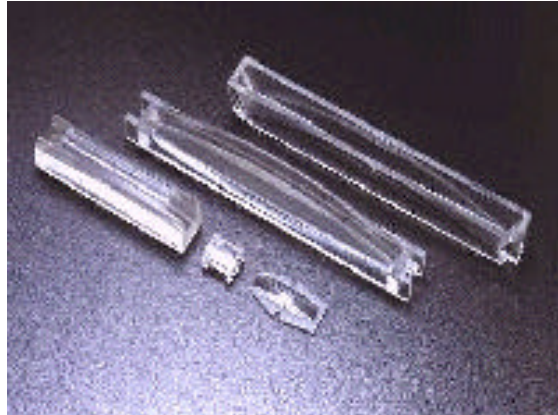


View of a typical aspheric grinding process, and resulting figure accuracy

Freeform Geometry

A common limitation of the previously mentioned single point diamond turning and grinding machines, is their inherent ability to generate only rotationally symmetrical surfaces. Although these geometries cover the majority of requirements, there is an increasing demand for optics to incorporate more random, freeform geometries. These surfaces might require raster flycutting, or grinding, depending on the material.

The raster machining process requires the part to be fixtured in a static condition, while it's relationship with the cutting tool or wheel might move simultaneously in 3, 4 or even 5 axes. This type of machining is now possible, either directly by raster flycutting on non-ferrous metals, polymers, and crystals, or by raster grinding glass or mold inserts. Examples of these "freeform" geometries might be advanced laser printer optics, as shown, or "conformal" windows that blend into the leading edge of an aircraft's wing.



Advanced freeform optics

A new breed of multi axis machines has been developed that are able to generate shapes that are no longer limited to rotational symmetry, but extend to these freeform geometries. This type of machine features three extremely stiff hydrostatic oil bearing linear axes, X, Z & Y, in addition there are air bearing B & C rotary axes, and an oil bearing grinding spindle. The machine base comprises a massive natural granite slab, mounted on optimally located air isolation mounts. An advanced CNC controller, with PC front end is utilized, while 10nm linear scales provide position feedback.



Ultra-precision 5 Axis Freeform Generator

Although it is advantageous for a machining system to be able to single point diamond turn, and also grind, and this is often accomplished by expanding a lathe platform to one of a grinding platform. This type of machine is however often compromised by inadequate guarding, coolant containment, or stiffness. It is therefore critical that the grinding requirements are considered at the point of conceptual design, to allow for all the provisions of this demanding process. The illustrations below depict a machine being used in both a single point diamond turning and grinding mode.



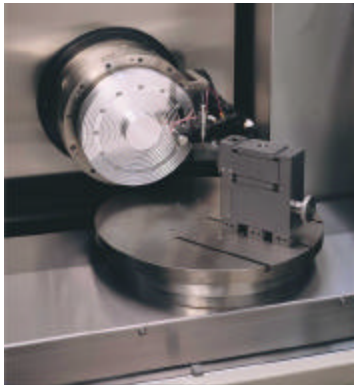
Advanced Features

Many advanced design features are built in to such a machine, an example of this is the integral axis configuration, to improve system stiffness, reduce thermal effects, and reduce geometrical errors. The view below demonstrates this technique. Note how the vertical Y-axis is buried within the Z-axis, rather than stacked one above the other. Also shown is a non-influencing, air bearing counter balance, to allow the vertical axis to be tuned to optimum performance, bi-directionally.



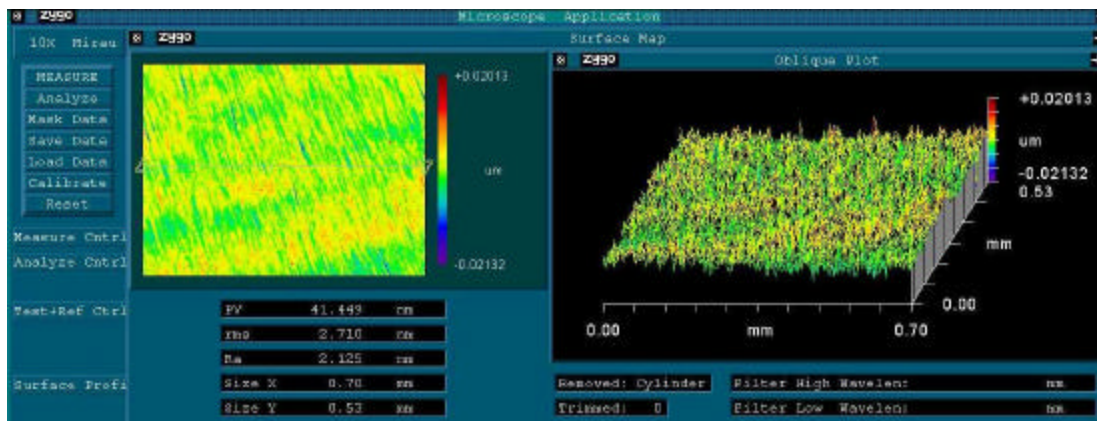
Non-influencing air bearing counter-balance

Understanding the relative position of the cutting tool or the grinding wheel on the machine is also critical to the final workpiece accuracy, and automatic systems have been developed for establishing tool/wheel radius, height, and position on the machine relative to spindle center-line. Many of these devices employ kinematic mounting techniques to ensure fast and precise location on the machine, and LVDT or optical probe technology combined with automatic setting software.



Kinematically Mounted LVDT Tool/wheel Setting System & Linear Motor Driven Hydrostatic Slide

Advanced PC based CNC motion controllers are now used in conjunction with Athermalized linear scale feedback devices and previously illustrated state-of-the-art linear motors, allowing surfaces as smooth as 2nm to be generated directly from the machine.



BK7 Glass Sphere Directly Ground – Surface Texture: 2.1nm Ra

In Conclusion

It can be seen that the technology contained within the ultra-precision machining system of today is certainly related to its earliest origins, in basic form. Time tested fundamental precision engineering principles continue to be adopted, yet at the same time these are now coupled to leading edge technologies in controls, drives, and feedback devices.

Advances in Computer Aided Design, and in particular, Finite Element Analysis, have allowed the mechanical design of machining systems to benefit from specifically selected materials and new structural configurations. This, combined with certain basic rules for oil bearing slide design, and finely tuned assembly techniques, results in machining systems that are more precise, thermally stable, flexible, more reliable, faster, and less expensive than the machines of yesteryear.

The use of ultra-precision machining techniques, originally developed for commercial applications, then fuelled by demand in defense related products, is once again being predominantly exploited by commercial industry. Everyday products such as televisions, video players and cameras, contact lenses, binoculars, security systems, compact disc players, personal computers, and many more, rely on advanced manufacturing techniques to produce high performance optics cost effectively. In the future, machine developments will continue to be driven by market requirements. Advances in computing technology, and photonics, will likely yield further advances in control and feedback technology that will allow ultra-precision machining technologies to continue to advance in line with market requirements.

Deformation analysis of a lightweight metal mirror

Jianwei Zhou*, Wumei Lin, Guoqing Liu, Tingwen Xing
State Key Laboratory of Optical Technology for Microfabrication,
Institute of Optics and Electronics, CAS, P. R. China

ABSTRACT

The weight of the optical elements of a system used in the aviation and aerospace industry must be as light as possible, on condition that the imaging performance of the system satisfies user's demand. However, optical elements will deform easily under internal or external pressure if it becomes thinner, and then influences the imaging performance of the whole optical system. In this paper, the main mirror of the Cassegrain system is studied with finite-element analysis (FEA) to predict its surface deformation through simulating its working conditions. The surface deformation is also tested and analyzed after machining and mounting. The obtained interferometric data, Zernike coefficients, is written into CODE V, an excellent software for designing optical systems, to analyze the imaging performance of the designed optical system.

Through analyzing the deformation of the metal mirror it can be found that the maxima RMS change of the whole optical system is 0.0059λ , which is only 1.52 percent of the designed value. In the full field of view, the RMS error is less than 0.07λ , that means the imaging performance of the whole optical system is close to the diffraction limit.

Keywords: lightweight, deformation analysis, Zernike coefficients.

1. INTRODUCTION

The weight of the optical elements of a system used in the aviation and aerospace industry must be as light as possible, on condition that the imaging performance of the system satisfies user's demand. Either reducing the volume or using the lightweight material can decrease the weight of the optical element parts. However, lightweight material that has excellent intensity and rigidity is rare and expensive. The most effective method is to reduce the volume of optical element.

The imaging performance of a complicated Cassegrain system is satisfactory in large field of view, at the same time the total length of the system is shortened and the total volume of the optical elements is reduced to some extent, consequently the weight of the system is reduced. In addition, the main reflective mirror will not produce chromatic aberrations and it can further lessen the total number of the optical elements needed in a Cassegrain system. The main reflector is the heaviest component of the Cassegrain, so it is especially necessary to reduce the weight of the main mirror. However, the main mirror will deform easily under internal or external pressure if it becomes thinner, and then influences the imaging performance of the whole optical system.

In this paper, the main mirror of the Cassegrain system is studied with finite-element analysis (FEA) to predict its surface deformation through simulating its working conditions. The surface deformation is also tested and analyzed after machining and mounting. The obtained interferometric data, Zernike coefficients, is written into CODE V, an excellent

software for designing optical systems, to analyze the imaging performance of the designed optical system.

2. DEFORMATION PREDICTION

The main mirror of a complicated Cassegrain system with field of view of $3^{\circ} \times 3^{\circ}$ is made up of duralumin. The density of duralumin is 2.78g/cm^3 . The schematic drawing of the lightweight metal mirror is shown in Fig. 1. Fig.1A is the front view of the mirror and Fig.1B is the rear view. The mirror surface is parabolic and its back side is flat. If the mirror is not dealt with by any special method, it will be quite heavy. In order to reduce the weight of the metal mirror, the unnecessary material of the back is removed. However, the weight-reduced mirror will deform easily because of the residual internal material stress or under the external pressure, especially, the metal mirror is mounted onto the baseplate through three handles (Fig. 1). The surface deformation of the mirror will degrade the imaging performance of the whole optical system. In order to ensure the imaging performance of the whole optical system, the surface deformation of the mirror should be predicted. Which part of the metal mirror should be removed must be simulated before the mirror is processed. Finite-element analysis provides a good tool for analyzing the surface deformation of the weight-reduced metal mirror. Two types of load including axial inertial load and radial inertial load are applied to the metal mirror to analyze its surface deformation.

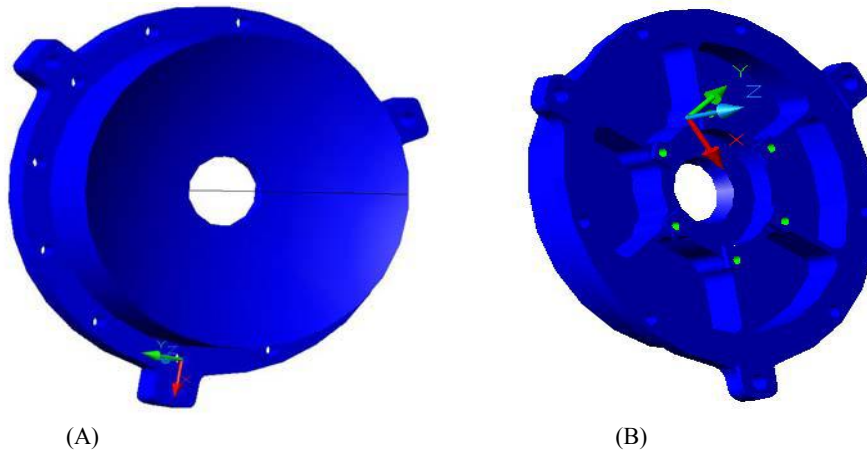


Fig. 1 Schematic drawing of the lightweight metal mirror

2.1 Axial inertial load

Assume that the joints between the metal mirror and the baseplate are rigid. The metal mirror is mounted onto the baseplate through three handles. An inertial load of 50g is added onto the metal mirror in the axial direction. Fig. 2 shows the surface deformation diagram under 50g axial inertial load. The maximum deformation occurs in the center of the metal mirror, and the value is $0.894\mu\text{m}$.



Fig. 2 Surface deformation diagram under 50g axial inertial load

2.2 Radial inertial load

Similarly, assume that the joints between the metal mirror and the baseplate are rigid. The metal mirror is mounted onto the baseplate through three handles. The model of the metal mirror is divided into 12467 cells and an inertial load of 50g is added onto the mirror in the radial direction. It results in forcing a pulling stress onto the upper handle and a compressing stress onto the other two handles. Fig3 shows the surface deformation diagram under 50g radial inertial load. The maximum deformation occurs at the bottom of the metal mirror, and the value is 0.336 μ m.

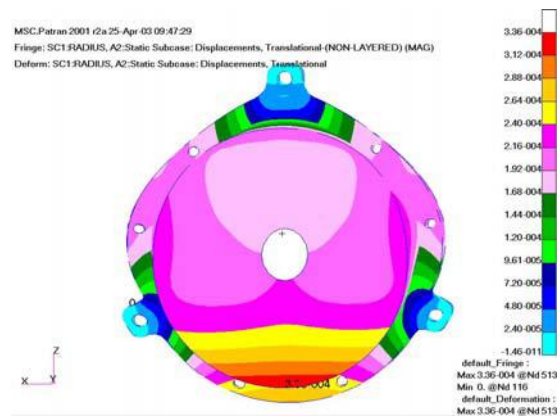


Fig. 3 Surface deformation diagram under 50g radial inertial load

3. DEFORMATION MEASURING

The metal mirror was manufactured subject to the result of finite-element analysis, to further study the deformation of the mirror after machining and mounting, the deformation of the mirror was measured with a Zygo interferometer. The results of finite element analysis show the effects of outside forces on the mirror surface deformation, while the deformation measurement carried out after the mirror is manufactured reflects the surface condition of the machined mirror. At the same time, it provides a comparison criterion for estimating the mirror surface deformation after mounting. Information of this type can provide feedback for manufacturing inspection as well as for the adjustment of fabrication and process condition to achieve optimal performance.

3.1 Methodology

Fig. 4 is the schematic of the measuring system. A He-Ne laser beam is focused by a condenser and a pinhole stop is placed at the focal plane. Then the spherical wave is collimated after propagating through in succession a splitter prism and a fixed lens. After that the collimated light passes through a standard lens. Here an optical plate is used and it is perpendicular to the optical axes. Partial of the incident light is reflected and auto-collimated by the rear surface of the optical plate. The reflected light functions as the standard reference wave front Σ_r . The remained light struck the paraboloid surface to be tested and then focused at O_t . If a standard spherical mirror is placed in the convergent light path, whose center is also at O_t , the convergent wave will be reflected by the standard spherical surface and the parabolic mirror in succession, and then is auto-collimated to form the tested wave front Σ_t . Finally, the two wavefronts superpose and the interference pattern is detected by a CCD.

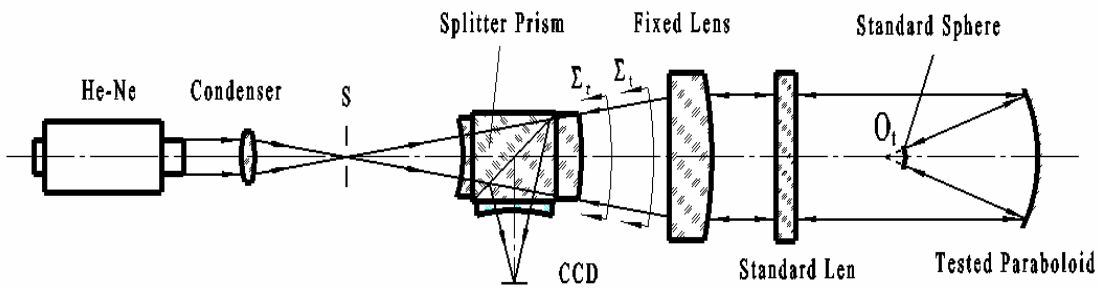


Fig. 4 Schematic of the measuring system

3.2 Measuring deformation after machining

The mirror made of duralumin was machined by a diamond lathe. During machining, the mirror was at first connected to a baseplate, and then adsorbed through the baseplate at the spindle surface of the diamond lathe. Because the baseplate is 30mm thick, the adsorption affinity from the lathe will not induce the mirror deform. When the mirror and its baseplate were moved from the lathe, the mirror surface figure would not deform. Thus, the mirror surface figure reflects the state adsorbed at the lathe. After machining, move the mirror and its baseplate from the spindle nose surface, and place them into the testing path of an interferometer to test its surface deformation. Fig5 shows the interference pattern of the mirror after machining. The testing wavelength $\lambda=0.6328\mu\text{m}$. The PV value is 0.565λ , and the RMS wavefront error is 0.069λ . As shown in Fig. 5, the RMS wavefront error of the mirror is small, while the PV value is relatively larger.

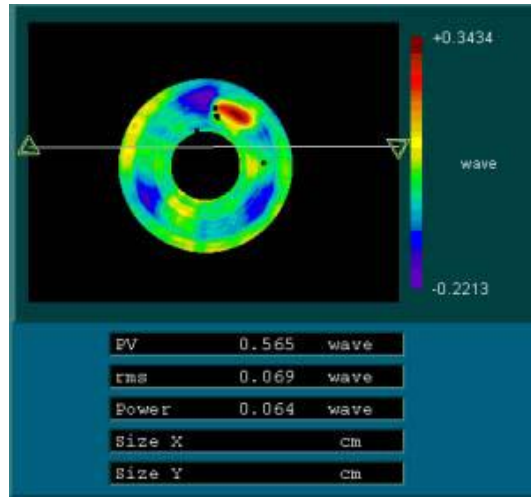


Fig. 5 the interference pattern of mirror surface after machining

3.3 Measure deformation after mounting

The metal mirror and the baseplate are fixed jointly by three screws, and the aspect ratio of the mirror is large. Thus, after loosening the three screws and moving the metal mirror from the baseplate, the mirror will deform. Then fix the mirror onto a model baseplate that simulates the actual mounting baseplate. Especially, use the same force upon the three screws which is approximate to the force used during mounting. Then put the mirror and the baseplate into the testing path of the interferometer to test the surface deformation. The tested wavelength $\lambda=0.6328\mu\text{m}$. Fig. 6 shows the interference pattern of the mirror after mounting. The PV wavefront error is 0.579λ , and the RMS value is 0.101λ .

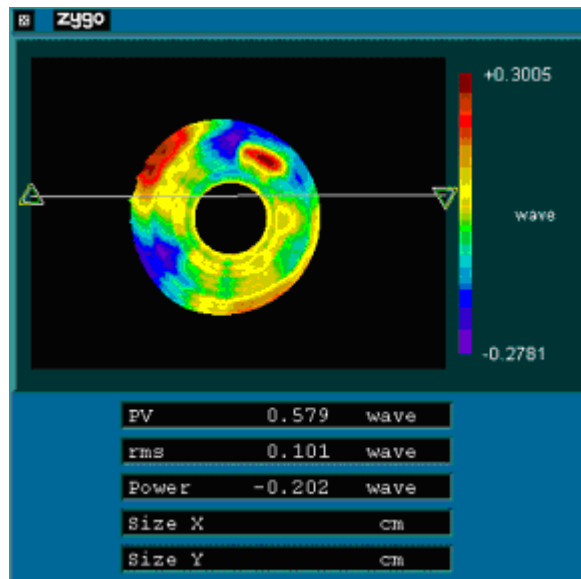


Fig. 6 the interference pattern of mirror surface after mounting

The Zernike polynomial coefficients are used to represent the surface figure obtained from the interference pattern shown in Fig. 6. Table 1 shows the first 36 Zernike polynomial coefficients of the surface figure deformation of the mounted mirror.

Table1 Zernike coefficients of the interferogram after mounting the metal mirror

Term	ZFR	Term	ZFR	Term	ZFR
0	0.751	12	-0.054	24	0.009
1	-0.248	13	0.055	25	0.007
2	-0.197	14	-0.058	26	-0.036
3	-0.143	15	-0.043	27	0.037
4	-0.001	16	-0.038	28	0.067
5	-0.146	17	-0.019	29	0.010
6	-0.012	18	0.066	30	-0.034
7	0.007	19	-0.073	31	-0.007
8	0.048	20	0.003	32	0.033
9	0.032	21	-0.010	33	0.066
10	0.109	22	0.064	34	0.029
11	-0.055	23	0.013	35	-0.035

4. SYSTEM PERFORMANCE ANALYZING

To analyze the influence of the surface deformation of the metal mirror on the image performance of the whole optical system, CODE V provides a file interface that allows the program to read or write data that is stored in a standard file format, which will be referred to as the INT file format. Here it is for representing interferometric deformation data, namely Zernike polynomial coefficients, and assigned to the corresponding surface.

The surface deformation of the metal mirror is asymmetry, so in order to evaluate the imaging performance of the optical system precisely, it is necessary to evaluate all the field points of this optical system. Different field points are obtained by rotating the Zernike polynomial coefficients about the center of INT data. Fig.7 shows the initially designed RMS wavefront error in waves of the optical system.

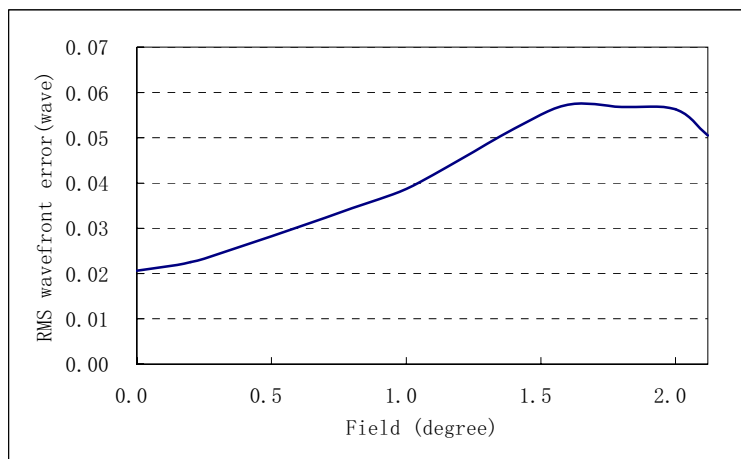


Fig. 7 RMS wavefront error of the designed optical system.

Fig. 8 shows the RMS wavefront error of the optical system calculated after assigning the deformation data to the corresponding mirror and rotating the Zernike polynomial coefficients about the center of data at 0°, 60°, 120°, 180°, 240° and 300°, respectively. The maximum variance of the RMS wavefront error of the system is 0.0059λ .

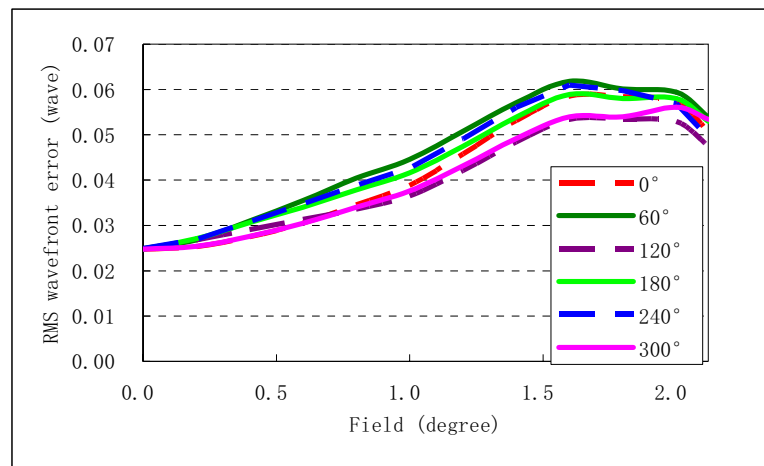


Fig. 8 RMS wavefront error of the system added the mounting deformation of the metal mirror

CONCLUSION

Through analyzing the deformation of the metal mirror it can be found that the maxima RMS change of the whole optical system is 0.0059λ , which is only 1.52 percent of the designed value. In the full field of view, the RMS error is less than 0.07λ , that means the imaging performance of the whole optical system is close to the diffraction limit.

REFERENCE

1. Lawrence D. Craig, Todd Cline, James B. Hadaway, Max E. Nein, Martin E. Smithers, John W. Keidel, H. Philip Stahl, "Structural analysis of a 50-cm-diameter open-back triangular cell beryllium mirror in a cryogenic environment", *Proc. SPIE Vol. 4444*, 78-89(2001).
2. Yoshihiro Shiode, Shuuichi Okada, Hiroki Takamori, Hideki Matsuda, Sachiko Fujiwara, "Method of Zernike coefficients extraction for optics aberration measurement", *Proc. SPIE Vol. 4691*, 1453-1464(2002).
3. Bo Qi, Hongbin Chen, Nengli Dong, "Wavefront fitting of interferograms with Zernike polynomials", *Optical Engineering 41(07)*, 1565-1569(2002).
4. John Chambers, Ronald G. Mink, Raymond G. Ohl IV, Joseph A. Connelly, John E. Mentzell, Steven M. Arnold, Matthew A. Greenhouse, Robert S. Winsor, John W. MacKenty, "Optical testing of diamond machined, aspheric mirrors for ground-based, near-IR astronomy", *Proc. SPIE Vol. 4841*, 689-701(2003).
5. Paul N. Robb, Paul B. Forney, Lynn W. Huff, "Interferometric measurements of silicon carbide and aluminum mirrors at liquid helium temperature", *Proc. SPIE Vol. 3122*, 197-202(1997).
6. Sanichiro Yoshida, Muchiar I. Muhamad, R. Widiastuti, and A. Kusnowo, Indonesian Inst. of Sciences, "Optical interferometric technique for deformation analysis", *Opt. Express 2*, 516-530 (1998).

Design of aspherical metal mirrors used to infrared thermal imaging systems

Cao Yinhua*, Li Lin, Gao guangjun, Zhang Ying
Dept. of Optoelectronic Engineering, Beijing Institute of Technology
*5 South Zhongguancun street, Haidian District, Beijing 100081 China

ABSTRACT

An important factor influencing the image quality of space or military optical systems is that the broad environmental temperature ranges. It would bring some problems on design, fabrication and mounting of the optical system. The ways of getting rid of the problems and improving the image quality of optical systems by using aspherical metal mirrors to the infrared thermal imaging system are presented in this paper. The choice of mirrors materials, the design of mirrors structure, the analysis of factors of influencing mirrors surface figure are discussed. The actual optical system designed in this paper is a Cassegrain objective, and the reflective surfaces of the primary mirror and secondary mirror are conicoid surfaces. The diameter of the primary mirror is $\Phi 240\text{mm}$, the materials of mirrors is aluminum alloys, and the mounting structure is flexible. The aspherical surface of the metal mirror are fabricated by precision diamond turning machine, and the error of the surface figure is less than $0.5\ \mu\text{m}$. The results of the battlefield test show that the infrared system with metal mirrors discussed in this paper has met the optical design specifications.

Keywords: infrared thermal imaging systems; aspherical mirrors; metal mirrors; precision diamond turning; quality of surface figure

1. INTRODUCTION

Because of the unique advantages, infrared thermal imaging technology has been widely used in the field of space or military optics in recent years. Comparing with radar, visible TV and low-light level image intensifier, infrared systems have better adaptation of poor visibility ratio condition and can operate in day and night. So it has played more and more important role in optical instruments of space or military. The infrared thermal imaging system described in this paper was designed for use of space or military. Its working wavelength band is from $3.7\ \mu\text{m}$ to $4.8\ \mu\text{m}$, and the temperature ranges from -30 to $+45^\circ\text{C}$. Since the system must be operated satisfactorily in severe environment exposing to temperatures, moisture, shock, vibration, etc., it is very relevant and important that all of the environmental requirements must be considered properly in the process of opto-mechanical design, fabrication and alignment for the system. The opto-mechanical designers' challenge is to develop an instrument that will survive and perform in all of the required environments. A successful mirror design can meet the performance criteria for the specified environment such as operating temperature range, and lifetime for reasonable cost. This requires trade-offs among materials, fabrication methods, structural considerations such as mirror design and mounting scheme, and, of course, cost. As a solving way, the technology of aspherical metal mirrors is adopted in the system discussed in this paper.

Metal mirrors are usually used in space or military instruments. To maintain optical instruments performance under severe circumstances, operating temperature range, vibrations, and shocks must be considered during design. According to the report ^[1], an aluminum mirror was designed for use in NASA's Kuiper Airborne Observatory. This

* cyh-bit@163.com

Cassegrain-type infrared telescope used a 185mm diameter oscillating secondary mirror to rapidly switch the field of view from the target of interest to the sky background for calibration purposes. Minimization of mass to be moved is vital to performance of the system. The total weight of the mirror was only 0.5 kg, representing a 70% weight reduction from a solid substrate. The optical surface figure and mounting reference surface of the hyperboloidal mirror were provided by precision diamond turning machine. Interferometric tests indicated the quality of the figure to be 0.65λ p-v at wavelength of 633nm over 90% aperture. Surface roughness was estimated as about 8nm rms.

2. MIRROR DESIGN

A mirror design criteria is that the design must meet the requirements of aberrations for mirrors surface figure under the specified environmental conditions. The main factors effected on stability for mirrors surface include: properties of mirrors materials, mirrors self-weight deflection, thermal distortion, and stress deformation resulted from mounting of mirrors.

The infrared thermal imaging system presented in this paper consists of a main optical system and image rotation system. The former is a Cassegrain-type optical configuration, and both of the primary and secondary mirrors are aspherical surfaces. The working wavelength band of the system is from $3.7 \mu\text{m}$ to $4.8 \mu\text{m}$, and the temperature ranges from -30 to $+45^\circ\text{C}$. Fig.1 shows the configuration of the infrared thermal imaging system. This optical system mainly consists of a primary mirror, secondary mirror and support structure (housing).

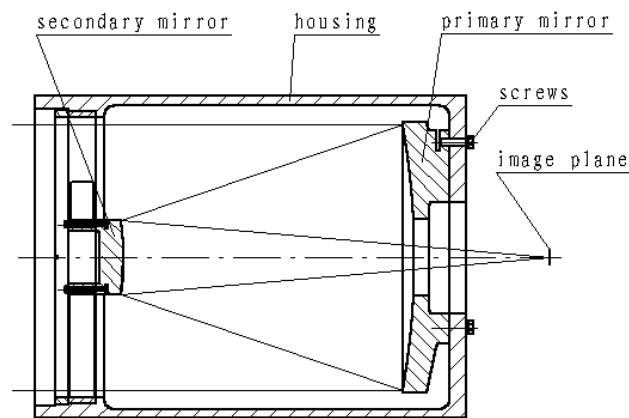


Fig.1 Configuration of the infrared thermal imaging system

2.1 Mirror materials choice

The choice of mirror materials in this system depends on two elements. The mirror materials selected should be fabricated to meet surface figure requirement, and can maintain the surface figure within specified tolerances during operation. Once an optical surface has been ground and polished into a mirror substrate, it is important for the figure not to change due to environmental exposure, temperature changes, or release of internal stress. We consider some of the most important general properties for mirror substrate materials in the following sections.^[2]

1) Smoothness

Practically all mirrors used in the optical system are polished to a high degree of smoothness. There are two categories of surface errors in mirrors, that is surface figure errors and surface irregularities. The former introduces various forms and orders of the optical aberrations (spherical, coma, and astigmatism) into the reflected wave front; the latter results in scatter of incident radiation. Although the mirror materials selected should be beneficial to machining and polishing of mirrors, not all types of optical systems require the same degree of smoothness. For example, extremely smooth surfaces can be produced on fused silica or Zerodur mirrors. Consequently, these materials are frequently used for x-ray optics where the short wavelength emphasizes scatter effects. Contrarily, mirrors made of metals such as aluminum or beryllium usually have rough surface suitable only for infrared applications.

2) Thermostability

The temperature field balance of a mirror substrate will be broken down if environmental temperature changes. It is rather complicated to explain its influence factors and results. From Claude A.Klein (1997)^[3], mirror surface deflection resulted from laser is given by

$$\delta l = \int_0^l \varepsilon_z(z) dz \quad (1)$$

where $\varepsilon_z(z)$ is differential strain.

If a reflector is elastic isotropy plate, then,

$$\varepsilon_z(z) = \alpha \delta T(z) + (1/E)[\sigma_z - \nu(\sigma_\rho - \sigma_\theta)] \quad (2)$$

where α is thermal expansion coefficient of mirror material,

$\delta T(z)$ is temperature gradient,

E is mirror material elastic modulus,

σ is stress component,

ν is Poisson's ratio of mirror material.

From the opto-mechanical engineering viewpoint, the interested basic material thermal properties include coefficient of thermal expansion, thermal conductivity, specific heat. According to Eq.(1) and (2), we obtain the following results that the thermal expansion coefficient and the thermal conductivity of mirror material have great influence on mirror surface figure. The materials which have lower thermal expansion coefficient will be better for optical system performance as it minimizes the effect of thermal gradients on dimensional changes of the components when temperature changes. Higher thermal conductivity is desirable to conduct heat quickly and to minimize temperature gradients when there is a heat source in or close to the optical system. It is advantageous to balance to mirror substrate temperature quickly, and reduction in deformation of mirror surface resulted from thermal stress. Table 1 lists thermal and mechanical properties of some mirror materials.

Table 1 Thermal and mechanical properties of some mirror materials

Material	Thermal expansion coeff. $\alpha, 10^6/^\circ\text{C}$	Specific heat Cp J/kg.K	Thermal conductivity K, W/m.K	Density P g/cm ³	Youngs modulus E, 10 ⁶ g/mm ²	Poission's ratio ν
Zerodur	0.05	821	1.64	2.53	9.24	0.24
Fused Si	0.56	741	1.37	2.2	7.47	0.167
SiC	2.4	700	146	3.21	47.55	0.21
Al	23.0	960	171	2.71	7.04	0.33

From table 1, it can be seen that the thermal expansion coefficient and thermal conductivity for metal materials are bigger compared to glass-type materials. Obviously, the metal is much more sensitive to temperature change than the nonmetals. For an opto-mechanical system to be exposed to high thermal irradiation, thermal conduction must be considered as the most important factor in the determination of gradients in design of optical and support structure. If the difference of the thermal expansion coefficients between the mirror substrate and the support structure is very large, the variation of components dimension resulted from temperature changes will be also much more different, and it will result in stress deformation of mirrors. Thus it is important to match thermal expansion coefficients of the adjacent components to minimize thermally induced strain in optical systems.

In addition to the mirror surface deformation, temperature change can also induce image shifting of optical systems.^[4] If the mirror substrate is chosen metal materials, and the thermal expansion coefficient is close to that of mounting structure, the image shifting of the optical system resulted from temperature change will be reduced.

3) Specific stiffness (E/ρ)

Under gravity field, self-weight deformation of a mirror must be considered. Williams^[5] gave the formula to calculate the effect of gravity on a mirror surface figure. The general equation for axial deflection due to self-weight is,

$$\delta_A = C \left(\frac{\rho}{E} \right) \frac{V_0}{I_0} r^4 (1 - \nu^2) \quad (3)$$

where C is support condition constant,

ρ is mirror material density,

E is mirror material elastic modulus,

r is mirror radius,

ν is Poisson's ratio of mirror material,

V_0 is unit volume of mirror,

I_0 is unit cross-sectional moment of inertia.

In Eq.(3), the material parameter determined self-weight deflection is the ratio of mirror material density to elastic modulus. This material properties ratio, ρ/E , is the inverse specific stiffness of the material. The ratio of unit volume to unit cross-sectional moment of inertia is the structural efficiency of the mirror crossing section. The ratio, V_0/I_0 , is a measure of the stiffness-to-weight independent of material properties. For a solid mirror we can get the following equation

$$\frac{V_0}{I_0} = \frac{12}{h^2} \quad (4)$$

where h is mirror thickness.

According to Eq.(3), the specific stiffness of the mirror substrate material has a significant effect on the suitability of the finished and installed mirror. A more elastic modulus of materials with low density tends to resist deformations due to polishing, mounting, gravity, and vibration during operation.

In addition, we have to consider fabrication capability and efficiency of the selected materials. With advances in the technology of precision diamond turning, the fabrication accuracy of mirrors surface figure has been greatly improved and can meet the image quality requirement of optical system in infrared band. It is feasible to use the metal mirrors in infrared optical systems. Another interesting advantage of the diamond turning is that the efficiency of fabricating aspherical surface is much higher, compared with the traditional grinding method.

Based on the above-mentioned reasons, both of the aspherical primary mirror and the secondary mirror in this system can be chosen metal materials. Because aluminum alloy is low cost, low density, high strength, and easily fabricated mirror materials, it is widely used in optical instrument. A 240mm diameter primary mirrors described in this paper for using in infrared thermal imaging system was made of wrought aluminum alloys. The primary mirror was forged from billet for better grain structure and stability. The support structure, as the housing of the optical system, is chosen cast aluminum alloys. Material properties of these metals are very close, so it can reduce thermal stress deformation, and lessen image shifting of optical system.

2.2 Mirror structural design

1) Mounting metal mirrors

The mounting forms of the metal mirrors affect directly the deformation of the mirrors' surfaces. A prior consideration is that under loading condition the stress or strain of the mirrors substrate should be uniform distribution, and the deformation should be as small as possible. The aperture of the primary mirror in this system is 240mm, and the thickness is 20mm. The size of the secondary mirror is small, so it does need to be considered.

Hall(1970)^[2] gave a rule-of-thumb criterion for the minimum number N of support points needed to prevent self-weight

deflections larger than specific peak-to-valley values during testing,

$$N = \left(\frac{1.5r^2}{h} \right) \left(\frac{\rho}{E\delta} \right)^{1/2} \quad (5)$$

where r is mirror radius,

h is mirror thickness,

ρ is mirror material density,

E is mirror material elastic modulus,

δ is allowable p-v deformation.

Put the corresponding data into Eq.5, we can obtain the minimum number of support points to meet $0.1 \mu\text{m}$ p-v deflection requirement,

$$N = \left(\frac{1.5 \times 120^2}{20} \right) \left(\frac{2.71}{7.04 \times 0.1} \right)^{1/2} \times 10^{-3} = 2.1 \approx 3$$

The usual shape of a mirror is a right circular cylinder. For the mirror in this paper, the support points lie on a circle centered about the mirror's axis, and have equal angular intervals around the circle. When the mirror is supported by three points at the 0.68 diameter, the axial deflection due to the self-weight is at a minimum for any three points support. If the mirror is supported on this optimum three-point support, the maximum deflection is,

$$\delta_A = 0.02859 \left(\frac{\rho}{E} \right) \frac{12}{h^2} r^4 (1 - \nu^2) \quad (6)$$

Put the corresponding data into Eq.6, when the optical axis is along the direction of the gravity vector, the axial deflection of primary mirror due to self-weight is,

$$\delta_A = 0.02859 \left(\frac{2.71}{7.04} \right) \frac{12}{20^2} 120^4 (1 - 0.33^2) = 6.09 \times 10^{-5} \text{ mm}$$

According to Eq. 3, 4, 6, we can see that the mirror self-weight deflection is directly proportional to r^4/h^2 and ρ/E . The effects resulted in mirror self-weight deflection include the size of the mirror's diameter, the thickness, the position and number of support points, the materials density, elastic modulus and Poisson's ratio, etc.

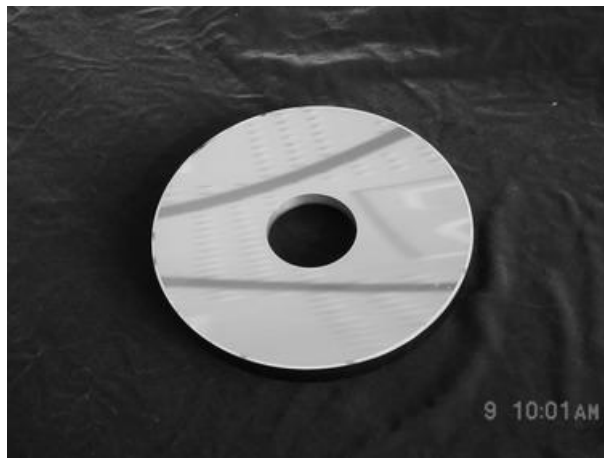
2) Flexure mountings

For the optical system discussed in this paper, the primary mirror was attached to support structure by flexible parts. Mounting stresses can be isolated from the mirror surface by flexure arms or geometric undercuts or slots that create a form of flexure mounting. The mirror should be stiffer than the interfacing mounting structure, so deformations occur in the mount rather than the mirror substrate. As a vibration isolator, flexible parts can also absorb the effects of shock and vibration on mirror surface. Besides, the thermal effects mismatched between mirrors and the support structure can induce thermal stress, and it can also be compensated by using flexible mounting structure.

The primary mirror structure is shown in Fig.2. The primary mirror is chosen three-point mounts on the mirror's back. Because the metal mirror material is a tenacity material, it can be attached directly to its housing by flexible parts to increase the interface reliability. The aspherical surface and mounting reference surface of the primary mirror are provided by precision diamond turning. The mirror should be machined in the same strained condition precisely. The mounting surfaces should be made flat and parallel to the optical surface. The quality of the surface figure fabricated by precision diamond turning instrument is better than $0.5 \mu\text{m}$ (p-v value) and surface roughness is better than 10nm. It can meet optical design requirement for the quality of the mirror surface figure.



(a)



(b)

Fig.2 Photo of the primary mirror structure

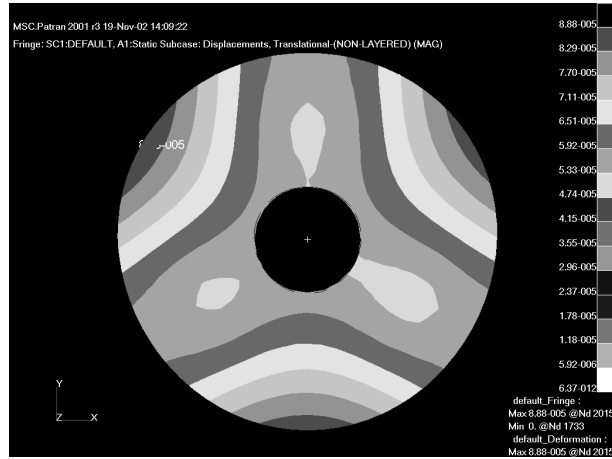
- (a) front view of the primary mirror
- (b) back view of the primary mirror

3. MIRROR ERROR ANALYSES

1) The force analysis of the primary mirror

One of the factors that should be taken into consideration during design of mirror is the deflection induced by self-weight. Self-weight deflection is very important in terrestrial systems when the direction of the gravity vector changes. The infrared thermal imaging system described in this paper changes the direction of optical axis frequently during the operation. The results of finite element analysis for the primary mirror under two types of gravity loading conditions are shown in Fig. 3(a), (b) and (c).

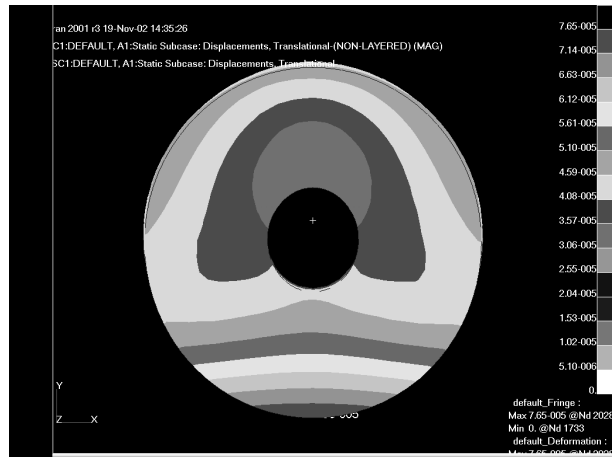
Self-weight deflection is normally calculated as normal to the mirror surface. For a coaxial mirror, in most common self-weight loading condition, the worst case is the gravity vector acting along the axis symmetrically. In this loading condition the gravity vector is normal to the surface of the mirror and parallel to the optical axis. This loading condition is called the axial deflection case (See Fig. 3(a)). Usually the worst deformation occurs at the three unsupported regions, it locates at edge of mirrors surface which made an angle of 60° with three support points. The distribution of the deformation is symmetrical, and the peak-to-valley deflection of the primary mirror surface is 8.88×10^{-5} mm.



(a)



(b)



(c)

Fig.3 Finite element analysis of the primary mirror
 (a) front view of axial deflection case
 (b) front view of radial deflection case
 (c) side view of radial deflection case

When the gravity vector acts normal to the axis symmetrically, the loading condition is called the radial deflection case (See Fig. 3(b) and (c)). In this case, gravity is acting parallel to the surface of the mirror and normal to the optical axis. Although gravity acts parallel to the mirror surface, deflection normal to the mirror surface is induced by this loading condition. The worst deformation occurs at the upper and lower edge of mirrors surface. Gravity acted on the upper support points will form pulling force and on the lower will form pressure force. The distribution of the deformation is unsymmetrical. The worst deformation occur at the lower edge of the mirror surface, and the peak-to-valley deflection of the primary mirror surface is 7.65×10^{-5} mm.

On the other hand, in the radial deflection case, the inclination of the primary mirror will also affect the image quality of the optical system.

According to the results of finite element analysis, the deformation of the primary mirror surface is less than that of the optical design requirements. It accords with the result calculated from Eq.(6).

2) Analysis of the primary mirror fabrication and mounting

The primary mirror material is wrought aluminum alloy. It is possible not to be uniform in the inner structure of the mirror substrate during forging process. In this condition it can induce internal stress, resulting in the deformation of the mirror surface and the strength of the mirror material. Besides, the fabrication stress may be induced during the mirror machining process. Therefore, in order to improve the uniformity of inner structure of the mirror substrate and reduce internal stress, the mirror substrate must be taken several times heat treatment and ageing treatment to release the internal stress, and raise strength and dimensional stability of the mirror substrate.

In addition, the force of tightening screws due to mount of the mirror may cause a greater local stress. Although it is isolated by flexible structure, the force balance of acting on three connecting points should be emphasized during mounting process.

4. CONCLUSIONS

From the above discussion it is confirmed that the use of aspherical metal mirrors in infrared thermal imaging systems is a good method to maintain their performance over broad temperature range. Mirrors substrate can be chosen as metal materials. This can not only meet thermal properties match for support structure, but also reduce fabrication period of aspherical mirrors. At the same time, the mirror can be attached easily and reliably to it's housing. The system discussed in this paper has passed test in the battlefield, and the test results show that the optical system have satisfied the system's specifications. It provides many useful experiences for the technology applications.

ACKNOWLEDGEMENTS

The authors would like to thank tutors and colleagues of Changchun Institute of Optics, Fine Mechanics & Physics, Chinese Academy of Sciences for their friendly help during the research work of infrared thermal imaging systems.

REFERENCES

1. Downey, C.H., Abbott, "The chopping secondary mirror for the Kuiper Airborne Observatory," *SPIE* 1167, pp329-335, 1989.
2. Paul R.Yoder, Jr, *Opto-mechanical Systems Design*, Second Edition, Revised and Expanded, Marcel Dekker, New York, 1992.
3. Claude A Klein, "Materials for high-power laser optics: figures of merit for thermally induced beam distortions," *Opt. Eng.* 36(6), pp1586-1595, 1997.
4. Wang Hong, Han Changyuan, "Study on the image shifting by temperature changing of the optical system in an aerospace camera," *Optical Technology*, 29(6), pp738-740, 2003.
5. Anees Ahmad, *Handbook of Opto-mechanical Engineering*, Boca Raton, CRC Press, 1997.

Lapping Metal Mirror at High Speed

Tian, Chunlin Fan, Jingfeng Wang, Weibing Zhang, Xinming Yang, Jiandong
Changchun Institute of Optics and fine Mechanics, Changchun, 130022 PRC

ABSTRACTION

This paper discusses lapping a metal mirror with solid abrasives at high speed. In this method there are three procedures. First the workpiece is ground in a grinding machine, which makes the surface roughness of the workpiece reach about $Ra1.6\mu m$. Second the workpiece is lapped roughly on a lapping machine, which makes the surface roughness of the workpiece reach about $0.1\mu m$. Last the workpiece is lapped finely, which makes the surface roughness of the workpiece reach about $Ra1nm$. Because solid abrasives are used, the machining efficiency is very high. Each lapping procedure time is only about one minute. A high speed, high efficiency and accuracy machining is realized.

Keywords: Metal mirror, high speed lapping, solid abrasives

1. INTRODUCTION

A metal mirror possesses some advantages compared with a traditional glass mirror. The strength of metal is high, the mirror made by metal is small in size and light in weight. It can be used in the case of a strong vibration and shock. The heat conductivity of metal is better. It means metal can be cooled easily, which is suitable for using in a high power strong laser. The metal resistivity against heat shock is better. It is not easy for metal to produce micro break under heat shock of strong pulse laser. The binding between metal base of metal mirror and film on its surface is stable. It is not easy for the film to drop out from metal surface. The machinability of metal is better than that of glass. It is easy for metal to be formed and machined. Because metal mirror possesses these advantages, they are developed long ago. Some achievement has been got. Many metal mirrors have been used in some optical systems.

In machining metal mirrors there are three procedures. First they are ground in a grinding machine, which make the surface roughness of the mirror reach about $Ra1.6\mu m$. It is an ordinary machining method without any problem. The rest two procedures are lapping, which is fine machining and key procedure in mirror machining. So metal mirror machining means last two procedures.

At present, traditional lapping with freedom abrasives at low speed is widely used in fine machining metal mirrors. Its machining efficiency is low, cost is high and machining accuracy is unstable. So this paper discusses machining metal mirrors using lapping method with solid abrasives at high speed.

2. HIGH SPEED LAPPING

In this paper metal mirrors are machined in a high speed lapping machine with a special lapping tool made by solid abrasives. Abrasives are artificial diamond powder. In the first place, abrasives and adhesive are mixed together, and pressed into pellets (see Fig.1). Then they are solidified and sintered. Last they are adhered to a

lapping disc to form a lapping tool (see Fig.2). Because abrasives are solidified on the lapping tool, there is no problem of abrasives splashing, the rotation speed of the lapping tool can be increased remarkably, which raises lapping efficiency obviously. The flow of coolant can be chosen according to requirement, which can improve cooling result, reduce hot distortion and wash away pieces from the workpiece in time without washing away abrasives. Since there is no relative motion among abrasives, there is no cutting action among abrasives, with saves abrasives and power.

In solid abrasives lapping by means of adhesive in pellets not only large size abrasives participate cutting, but also small size abrasives participate cutting too(In traditional lapping with freedom abrasives only large size abrasives participate cutting in most cases), which reduces groove depth on the workpiece surface produced by abrasives and improve workpiece surface quality. In lapping procedure surface of the lapping tool will wear, which makes surface accuracy of the lapping tool decrease. It means that we should often dress the lapping tool. Because the wear resistivity of abrasives is very good and they are on the lapping tool surface, dressing lapping tool is very difficult. It limit solid abrasives lapping to be used widely. In order to solve this problem, this paper designs abrasives density distribution according to the relative motion and relative motion path density between the lapping tool and workpiece by means of abrasives density controllability on the lapping tool in solid abrasives lapping, which makes abrasives density distribution suitable to relative motion path density and lapping tool wear uniformly and improves workpiece surface accuracy.

In the beginning, the workpiece is ground on a grinding machine, which makes the workpiece surface roughness reach $Ra1.6\mu m$ or so. Then the workpiece is lapped roughly on a high speed lapping machine with solid abrasives about 20 seconds, which makes workpiece surface roughness reach $Ra0.1\mu m$ or so, and flatness reach $1\mu m$ or so. Last the workpiece is lapped finely on a high speed lapping machine with solid abrasives about 40 seconds, which makes workpiece surface roughness reach $Ra0.88nm$ (see Fig.3) and flatness reach $0.07\mu m$ (RMS) (see Fig.4).

3. DISCUSSION

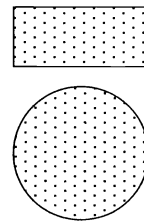


Fig.1 Sketch of pellet

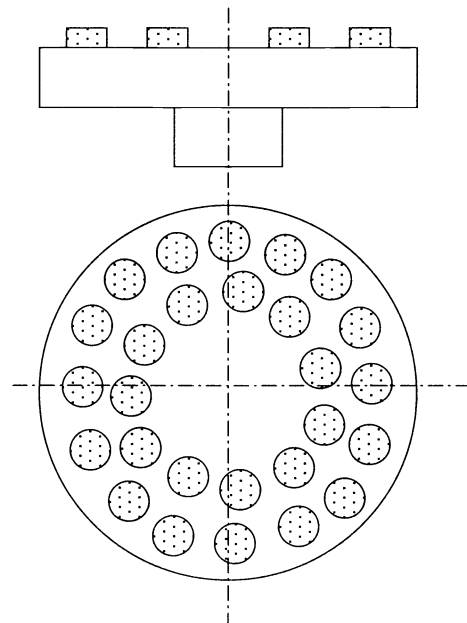


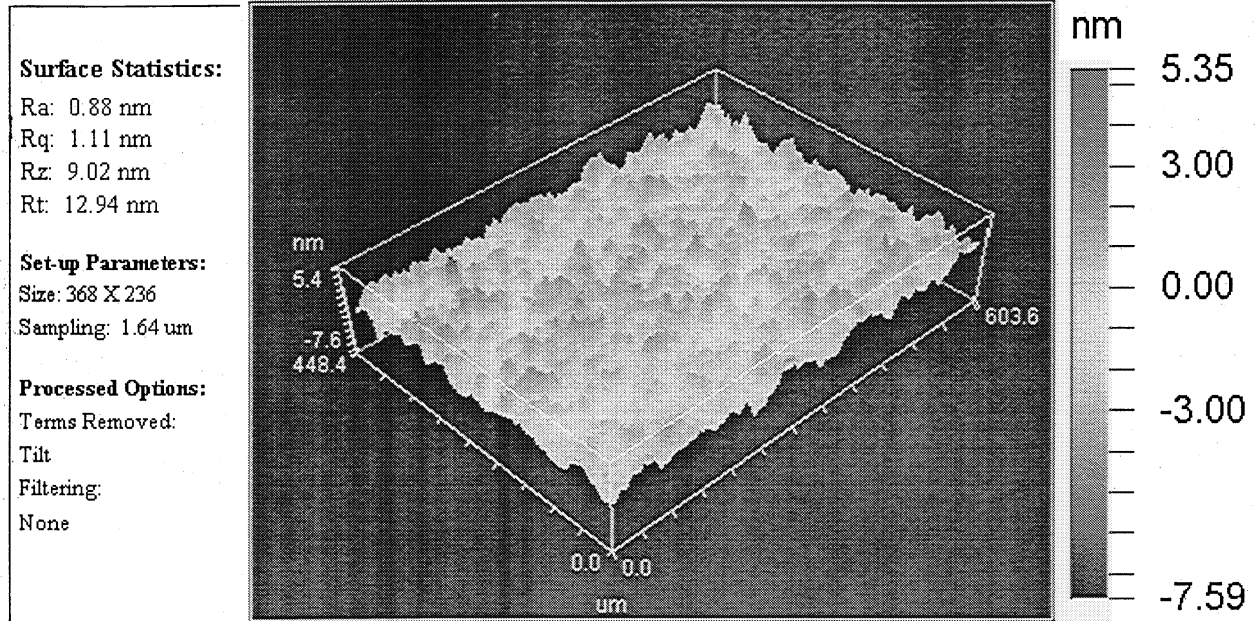
Fig.2 Sketch of lapping tool



Mag: 10.3 X
Mode: PSI

3-D Plot

Date: 04/07/00
Time: 14:49:05



Title: 03
Note:

Fig.3 Machined surface roughness
Lapping time 30s,spindle speed 460RPM

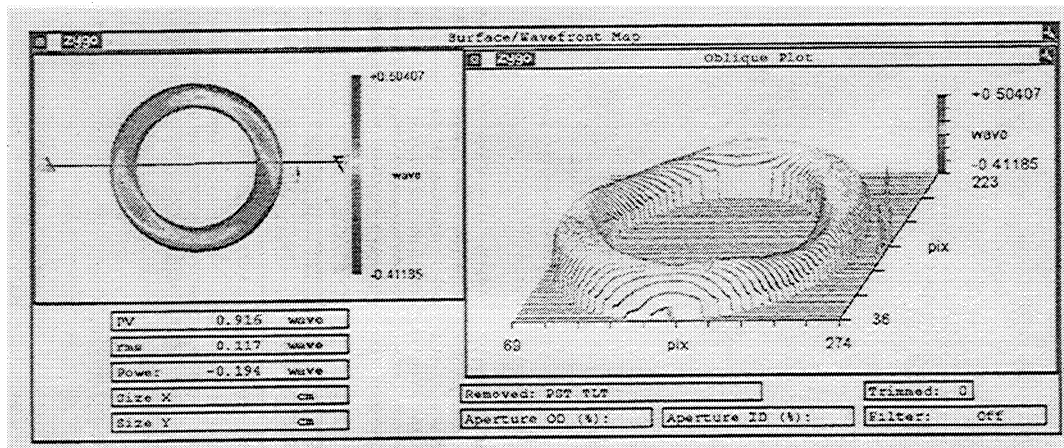


Fig.4 Machined surface flatness
Lapping time 30s,spindle speed 460RPM

Through this paper research results, it can be seen that lapping a metal mirror can improve machining efficiency, accuracy and quality with solid abrasives by a high speed lapping machine. The workpiece surface flatness can reach $0.07\mu\text{m}$ (RMS) and roughness can reach Ra0.88nm, which reaches nanometer level machining.

4.REFERENCES

1. Yang Jiandong, Wen Xueheng, Zhu Yanqiu, Wang Lijiang. "Discussing on Solid Abrasive Lapping Path". Chinese Journal of Mechanical Engineering, 10(2): 101-105,1997
2. Sun Jiashu, "Metal wear", Metallurgical Industry Press,10,1992

Metal Mirrors with Excellent Figure and Roughness

R. Steinkopf^{*a}, A. Gebhardt^a, S. Scheiding^a, M. Rohde^a, O. Stenzel^a, S. Gliech^a,
V. Giggel^b, H. Löscher^b, G. Ullrich^b, P. Rucks^c,
A. Duparre^a, S. Risse^a, R. Eberhardt^a, A. Tünnermann^a

^aFraunhofer Institute for Applied Optics and Precision Engineering; Albert-Einstein-Str. 7;
07745 Jena; Germany;

^bCarl Zeiss Jena GmbH; Carl-Zeiss-Promenade 10; 07745 Jena; Germany

^cCarl Zeiss AG, Standort Jena, Carl-Zeiss-Promenade 10, 07745 Jena, Germany

ABSTRACT

An outstanding technique in point of ultra-precision as well as economical production of mirrors is Single Point Diamond Turning (SPDT). The unique properties of the diamonds are used to get optical surfaces with roughness values down to 5 nm rms (root mean square) and very precise form accuracy down to 70 nm rms and 500 nm p.-v. (peak to valley) value over an area of 200 mm x 200 mm. This quality level is typical for applications in the Near Infrared (NIR) and Infrared (IR) range.

For applications in the VIS and UV range the turning structures must be removed with a smoothing procedure in order to minimize the scatter losses. Favorable is an aluminium base body plated with a thick-film of Nickel-Phosphorus alloy (NiP). This alloy can be polished with computer assistance. Ion Beam Figuring (IBF) is the final manufacturing step. The properties after the finishing process are better than 1 nm rms for roughness and down to 15 nm rms respectively 100 nm p.-v. regarding the surface irregularity for complex optical shapes.

The techniques SPDT, polishing and IBF ensures a high quality level for large mirrors with plan, spherical or aspherical surfaces. The manufacturing chain will be analyzed by surface characterisation based on 2D profilometry and white light interferometry to measure the roughness and 3D-profilometry and interferometry to monitor the shape irregularity. Scattering light analysis deepens these investigations.

This paper summarizes technologies and measurement results for SPDT and surface finish of metal mirrors for novel optical applications.

Keywords: metal mirror, aspherical mirror, single point diamond turning, polishing, ion beam figuring, surface characterisation

1. INTRODUCTION INTO MATERIALS AND MANUFACTURING METHODS

1.1 Materials for Metal Mirrors and Scope of Applications

Since about 6.000 years the use of metal mirrors is known in human history. Copper mirrors were probably the first metal reflectors. But after detecting that glass with a thin metal coating is high reflective and, beside other benefits, more scratch resistant, the usage off metal mirrors was decreasing.

But in the last century, metal mirrors had their comeback due to the advantages for some new and interesting applications. Used as reflectors with a high thermal conductivity in laser applications or to bend light beams in telescopes, a wide range of new application was opening up to use the specific properties of metal mirrors.

*ralf.steinkopf@iof.fraunhofer.de; phone 49 3641 807-336; fax 49 3641 807-604; www.iof.fraunhofer.de

Common materials for metal mirrors in optical applications are aluminium, copper or beryllium. Copper is often used in laser applications; the high thermal conductivity is one major benefit for this selection. Aluminium has a good reflectivity even for shorter wavelengths and is like beryllium light weight, and readily formable. But Beryllium has the negative characteristic due to its toxic behavior and is for this reason not commonly used although it is very stiff and has a light weight nature. Aluminium mirrors instead can easily be processed with the SPDT technology (SPDT). Especially novel aluminium alloys allow for surfaces with a very smooth micro roughness, even better than 3 nm rms.

A recently developed melt-spinning technology refines the grain size of the alloy 10 to 50 times compared to conventional aluminium. These results can be achieved by cooling down the metal cast with 1.000.000°C/s [1].

A lot of other non-ferrous metals can be machined too. The high affinity of iron to the carbon of the diamond leads to a high chemical wearout of the diamond tool and makes efficient cutting of ferrous metals impractical.

1.2 Single Point Diamond Turning with Different Machine Kinematics

The design of metal mirrors has almost no limits from the manufacturing side. With SPDT a very efficient and multifaceted tool is available. Rotational symmetric shapes like spheres, aspheres and off-axis aspheres are standard applications [3]. Even Off-axis aspheres are more and more common. But the potential of this technology contains the very precise manufacturing of “free form mirrors” without any rotationally symmetric shapes also.

The results, achieved with this technology are surfaces with a form irregularity less than 500 nm p.-v. and micro roughness below 10 nm rms. These are characteristically specifications for applications in the NIR or IR. To achieve these high levels of surface quality, ultra precise machines and mono-crystalline diamond tools must be deployed.

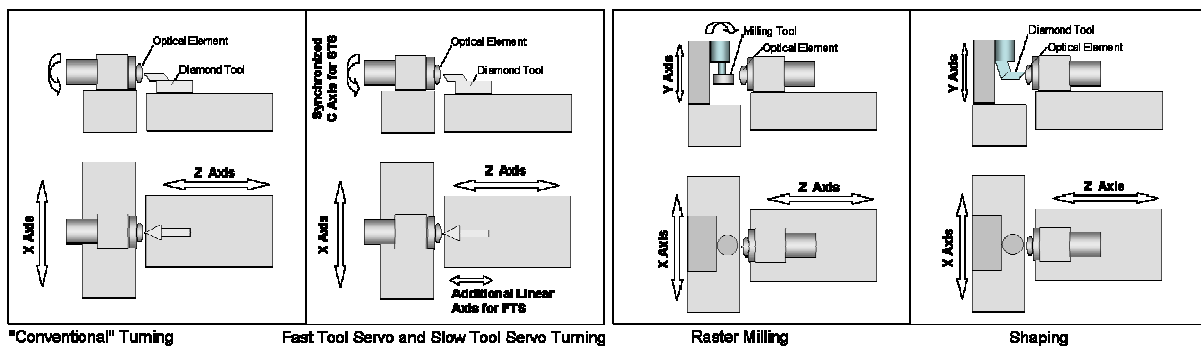


Fig. 1. Different Machine Kinematics for Different Optic Designs

Different machine kinematics are used for different shapes of optical elements. Spheres and aspheres are typically turned with two linear axes and one rotation axis. Off axis mirrors with large off-axis distances or mirrors without axial-symmetry can be machined in Slow Tool Servo technology (STS) mode. In this case, the C-axis moves synchronously with the two linear axes of the lathe (Figure 1). Free form elements with large dimensions and large asymmetries can be realized that way. For this technology heavy-weight linear axes have to be moved according to the spindle speed and the asymmetry of the part. The high inertia forces slow acceleration and so it is not possible to machine mirrors with high frequency asymmetries. Such mirrors can be manufactured with Fast Tool Servo technology (FTS). The technology consists of a tool, moved on a small linear axis on top of one of the regular linear axis. Driven by piezo or voice coil actuators, very precise movements and high accelerations are possible. To minimize the asymmetric movement of the tool, the surface has to be divided into a rotationally symmetric fraction and an asymmetric fraction. This can be done by calculating the best fit sphere or asphere. Subtracting the best fit geometry from the original design leaves the asymmetric part (Figure 2) [4].

The Fast Tool Servo unit is controlled according to the description of the asymmetric fraction of the optical element. It adds with every turn of the spindle just the high frequency asymmetries. The lathe is controlled by a separate program and moves straight conservative in an axially symmetric way. But the sum of both movements results in a free form surface with high frequency asymmetries. It is even possible to machine spheres or aspheres as base contour. The combination of slow tool servo and fast tool servo offers the opportunity to machine free form mirrors with asymmetric diffractive elements.

But there are optical elements which can't be manufactured with two linear axes. These parts have typically highly asymmetric shapes which makes it impossible to use a lathe. In this case machines with three linear axes are used and not the optical element but the tool rotates in order to remove the material. The so called raster milling is more time consuming than turning. The reason is justified in the "raster" process. The diamond tool rotates around the milling axis and takes one chip each turn. Due to the difference between the small tool tip radius and large flying wheel diameter, the resulting cavity looks more rectangular than square. This opens up the possibility to speed up the process by selecting the long side of the cavity as raster direction and the other side as feed direction. Thus valuable cutting time can be saved. And time means in case of raster milling processes often not hours but rather days. To speed up the process furthermore it is sometimes possible to combine raster milling with slow tool turning. An additional turning spindle which is synchronized with the linear axes leads to a spiral toolpath instead of the linear raster grid.

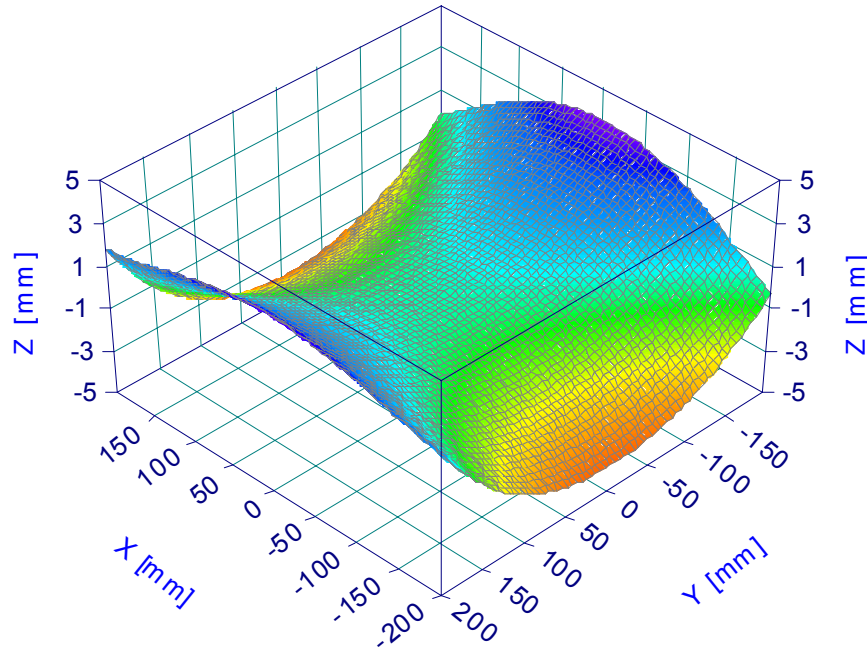


Fig. 2. Free Form Fraction of an Optical Element after Subtracting the Best Fit Sphere

Another technology for cutting free form metal mirrors is shaping. This process differs from all of the above described technologies because neither rotating tools nor rotating parts are involved. Three linear axes are moving synchronously in a raster pattern over the surface. A wide variety of geometric shapes like optical surfaces with undercuts and steep slopes are feasible because no rotating element is utilized.

2. ANALYZING THE PROCESS CHAIN FOR THE MANUFACTURING OF METAL MIRRORS

2.1 Process Chain for Metal Mirrors in Infrared Applications

After defining the optical and mechanical design of the mirror and choosing the right manufacturing technology, the process chain has to be specified. According to the wavelength of the application and its specifications the single process steps must be selected and combined to a process chain (Figure 3).

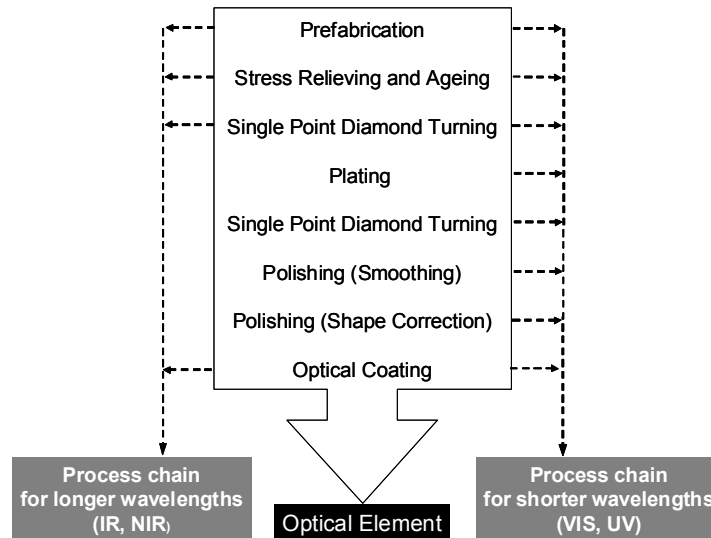


Fig. 3. Process Chain for Metal Mirrors in Different Fields of Application

Due to the longer wavelengths for infrared applications, the requirements regarding micro roughness and surface figure can be met directly with diamond turning. The process for the manufacturing of metal mirrors for infrared includes the following steps:

- Prefabrication on conventional machines
- **Stress relieving and ageing**
- **Single Point Diamond Turning**
- **Optical Coating**

While processing this manufacturing chain, a number of influences on the final optical quality of the mirror have to be accounted. The bold printed steps of the above described process chain have a huge impact on the global form error and the micro roughness. Each process step is characterized in detail in the following chapters.

2.1.1 Stress Reliving and Ageing Procedures

The most preferred material for IR applications is aluminium 6061 T6 alloy. This aluminium alloy is established for structural elements like frames and optical elements like mirrors. The major advantage of using the same material for mirrors and frame is the athermal design of the whole instrument, which is especially important for space cryogenic applications. Sound knowledge about the production process of the aluminium is a key for high quality mirrors. Using extruded bar stocks, the optical axis of the mirror should always have the same orientation as the extruder axis. In this orientation the grain structure of the material has the slightest effect on the overall micro roughness. Aluminium 6061 from the melt-spinning process allows for good results even in other orientations due to the small grain structure.

For long term stability and especially for cryogenic applications, the material has to be artificial aged. During this heat treatment the material changes its structure depending on time and temperature of the ageing cycles. This is done to reduce intrinsic stress, resulting from previous shaping and plastic deformation of the material. The prefabrication of the raw part induces stress again due to the material removal in the machining process. Hence the work piece must be relieved from stress again. Typically this procedure is done twice, first time after rough shaping and the second time after prefabrication on a conventional machine.

2.1.2 Single Point Diamond Turning

Stress induced Deformations during Diamond Turning

During the diamond turning process the mirrors get deformed by:

- Centrifugal forces
- Cutting forces and
- Mounting forces

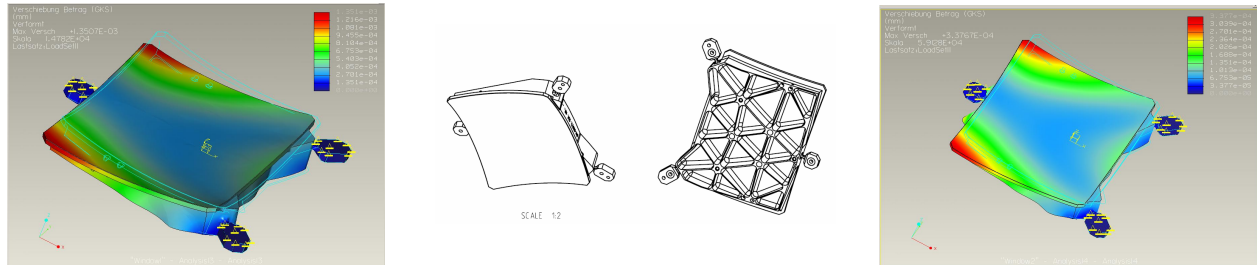


Fig. 4. Simulation of the influence of different spindle speeds on a metal mirror during diamond turning; left side: 700 rpm, max. deformation: 1.3 μm (p.-v.); right side: 350 rpm, max. deformation: 0.3 μm (p.-v.) (Mirror design: Astron, Netherlands Institute for Radio Astronomy, Spectrometer Main Optics of the Mid Infra-Red Instrument of the James Webb Space Telescope)

Deformations which are rotationally symmetric can be corrected according to the measurement in the following correction loop. Asymmetric deformations instead have to be considered during the mechanical design phase. Often it is not possible to make the design perfect to fulfill all requirements. A good compromise has to be found. Figure 4 illustrates that light-weighted mirrors tend to deformation under centrifugal forces. By reducing the spindle speed its possible to decrease the deformation from 1.3 μm to 0.3 μm , so that the remaining residuals can be placed in the tolerance budget.

Cutting forces usually have a secondary impact. Depending on the material, forces between 0.3 N and 1.5 N can be expected [2]. At the application of non-continuous cuts, which are typically for off axis mirrors, a zone with defects directly around the mirror edge has to be expected. For this reason the mirror should always be designed with a small area around the quality surface.

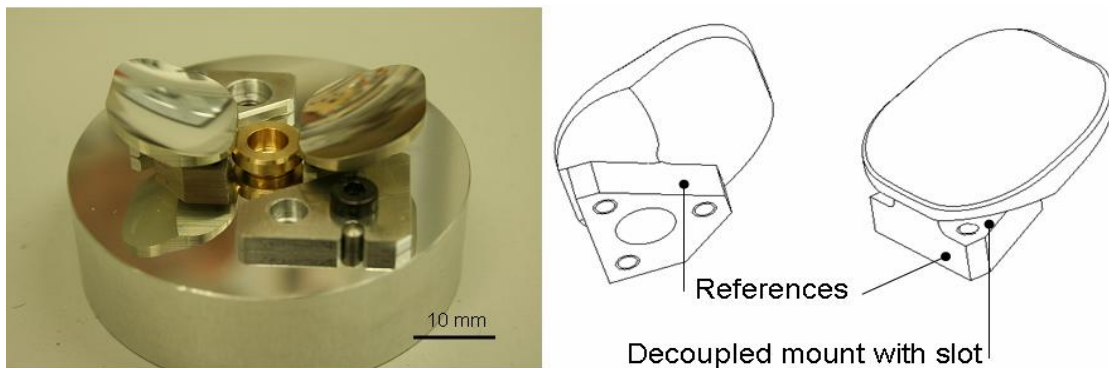


Fig. 5. left side: Two mirrors mounted on a fixture for diamond turning, right side: wire-frame view of the mirror with reference flats and mounting structure (Mirror design: DLR e.V., Mertis Spectrometoptics for BepiColombo Mission of ESA)

The optimal mirror for diamond turning with respect to mounting forces is a massive one with a perfect flat back side. But usually the mirror is designed for the application, not for the manufacturing process. Even though metal mirrors are often extremely light weighted they still have some advantages compared to conventional mirrors. A novel technology is to manufacture the mounting structure and mirror as a monolithic block and cut even the mounting structure and mirror in the same machine set up [11]. Mirror body and mounts are often designed in a decoupled arrangement (figure 5), so it is possible to manufacture and assemble almost strain free.

Influences on the Micro Roughness

The micro roughness of diamond cut metal mirrors is the sum of different influences. It is simple to figure out what the roughness should be in theory. The theoretical roughness results from a spiral with constant pitch which is described by the radius of the tool tip, the feed rate and the spindle speed [7].

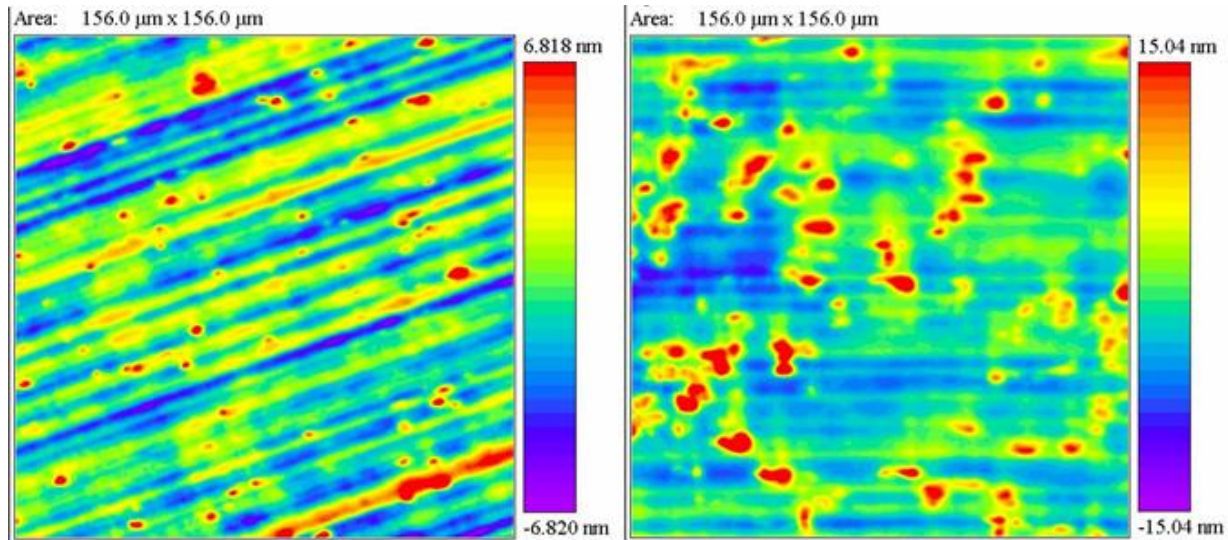


Fig. 6. White light measurement of two aluminium alloys with the same composition but different grain sizes (left side: RSA6061 [2 nm rms] with small grain sizes, right side conventional Al6061 [5 nm rms])

But there are more variables which must be accounted. The material itself is one of the influences with major impact. As shown in the white light interferometer image in figure 6 on the right side, the large grain structures results in a high surface roughness (5 nm rms). The turning structure is almost invisible. The left side of the figure shows the result of the same material composition with a much smaller grain size. This reduces the micro roughness down to 2 nm rms. The turning structure is seen as the biggest influence on the roughness in this image.

Light weight structures often make the mirror very sensitive to mechanical stimulations coming from the turning process. If the surface roughness increases too much it is possible to support the mirror at critical points with vibration damping materials like optic wax.

Shape Correction

After roughing with the diamond tool, the shape has to be measured. This can be done with a Panasonic UA3P tactile 3D-profilometer. In this contact measurement method a diamond stylus, with a typically tip radius of $2\ \mu\text{m}$, describes a raster pattern over the complete surface. This method is slower than the measurement with 2D-profilometers, but asymmetric deformations as they are common for off axis mirrors can be detected that way.

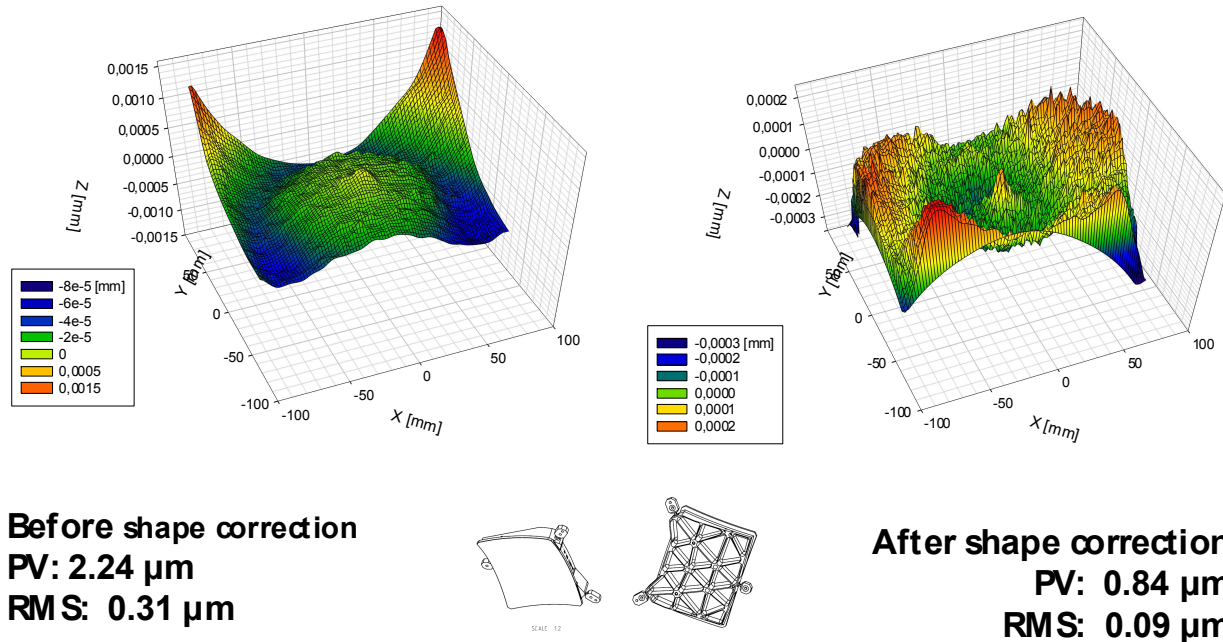


Fig. 7. Shape correction on Single Point Diamond Turned metal mirrors for the Spectrometer Main Optics of the Mid Infra-Red Instrument of the James Webb Space Telescope

The precision of this measurement depends on the slope of the mirror. With slopes smaller than 30 degree, results with almost the same accuracy as interferometric measurements can be expected. The needle causes small scratches on the surface. Hence is not a non-destructive measurement, so that the part has to be cut again. An alternative method is cutting a dummy mirror for measurement purposes.

The tool path for the final cut is calculated by subtracting the measured error from the rough cut tool path. Figure 7 illustrates that the shape deviation after the correction cycle is decreased by more than factor three, from $2.24\ \mu\text{m}$ to $0.84\ \mu\text{m}$. The residual error has still a rotational symmetric fraction, so in theory the global error could be reduced furthermore (typically values for global errors after diamond turning are between $0.1\ \mu\text{m} - 1\ \mu\text{m}$ p.-v., depending on the mirror size and geometry). Our experience shows that light weight structures and decoupled mounts often induce an irregular behavior during the turning process. From this point on, were the results are not reproducible, the shape correction should be stopped.

2.1.3 Optical Coating

Telescope mirrors, especially space-bound telescope mirrors, have high demands on long term stability against thermal and mechanical stress and strain. The optical specifications often address a broad spectral range. A good technology for coating mirrors with respect to these requirements is sputtering [8]. Looking for high reflective coating materials at IR and NIR wavelengths, gold is the material of choice.

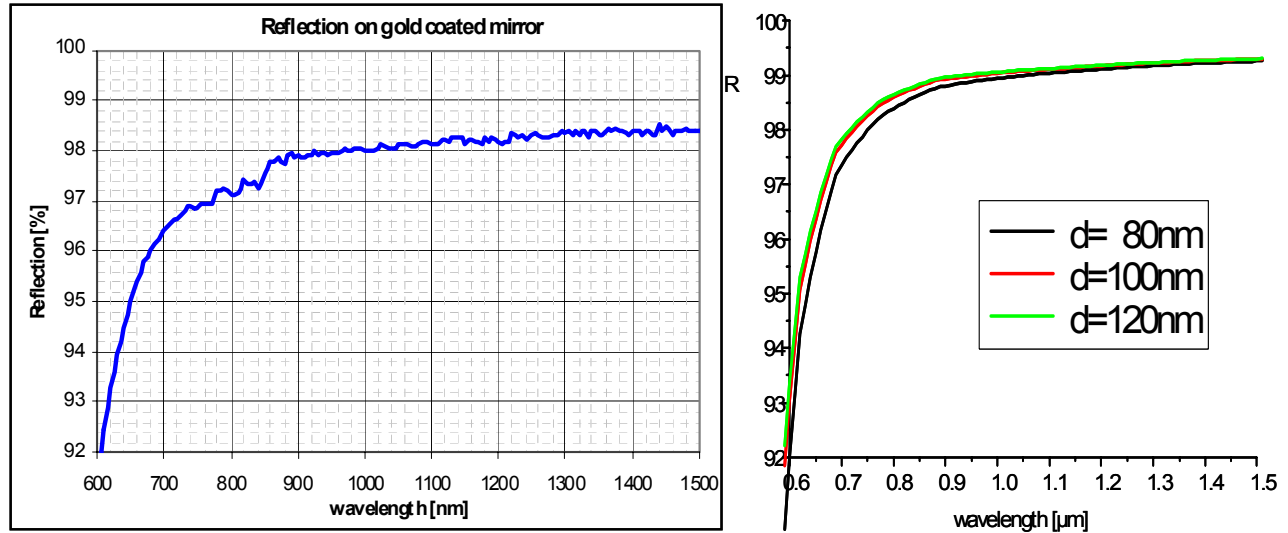


Fig. 8. Normal incidence theoretical reflection of gold coated mirrors assuming different values of the gold film thickness d (right side) versus effective achieved reflection on a gold coated mirror (left side). The theoretical reflection has been calculated assuming tabulated optical constants of gold corresponding to the database of unigit grating-solver software [9].

As shown in figure 8, the theoretical as well as the measured reflection of gold at 600 nm is already around 92% and increase fast to 98% at 900nm. The actually achieved reflection of gold coated mirrors is in a close range to the theoretical values, approximately 1% lower.

The sputtering process achieves a good adhesion and durability of the coating. The following tests have to be accomplished to proof the quality of the coated mirrors:

- Adhesion test, Procedure: Tapetest DIN 58196-6
- Humidity, Procedure: MIL-M-13508C 4.45 (49°C / 95% RH/ 24 h)
- Temperature change, Procedure: ISO 9022-2-14-04 (-50/+60 °C, 5 cycles, 30% humidity)

Going down to shorter wavelengths the optical layer has to be changed. A good reflectivity from VIS to NIR is offered by silver as coating material. Disadvantageous is the high oxidation potential, so that a protecting layer was developed to shield the optical coating. The reflectivity is better than 95% above 440nm and increase up to 97% at 600nm [11].

2.2 Process Chain for Metal Mirrors in VIS and UV Applications

The process chain for metal mirrors used for multispectral images in the range of VIS or even UV wavelengths contains a few steps more than the above described manufacturing steps for IR applications, as illustrated in figure 3. The reason is that the diamond turning process leaves structures which work as a very effective but undesirable optical grating at these wavelengths. To smooth these structures the aluminium mirror has to be plated with a material which can be polished. Nickel-Phosphorus (NiP) alloys offer a good solution for at least two reasons. First, NiP is hard enough to get polished and second, NiP is an amorphous material [5]. Hence there is no grain structure visible, like it is known from crystalline metals. The plating should be thick enough to cover at least one correction loop.

The process chain for such mirrors contains the following steps:

- Prefabrication with conventional machines
- Stress relieving and ageing
- Single Point Diamond Turning
- **Plating**
- Single Point Diamond Turning
- **Polishing (Smoothing)**
- **Polishing (Shape correction)**
- Optical Coating

Basically it is the same as for IR applications, but with plating and polishing there are new steps which are analyzed in the following.

2.2.1 Plating

Typical values for the micro roughness of diamond turned mirrors are ranging from 2 nm to 10 nm. The global form deviation is between 0.1 μm to 1 μm (p.-v.). But for VIS applications, the micro roughness should be better than 1 nm rms and the global errors, even of large mirrors, should be rather in the range of 0.1 μm than 1 μm .

Due to the intrinsic limits of the diamond turning process, an additional step like polishing must be employed to improve the surface furthermore. Unfortunately the materials which are machinable using diamond tools are difficult to polish. Plating mirrors with Nickel-Phosphorous enables the improvement of the surface quality [5].

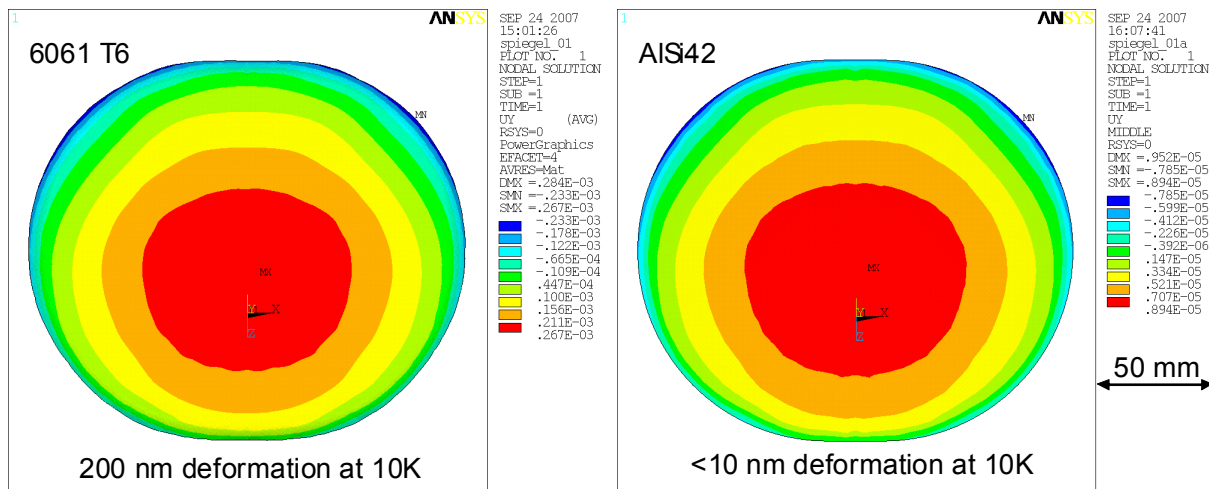


Fig. 9. The bi-metal effect is reduced dramatically by choosing different body materials, left side Al6061, right side AlSi42, both mirrors are plated with electroless Nickel

The thickness of the plating should be 20 μm , to ensure a well-closed surface. The diamond turning and polishing processes require a layer thickness of at least 50 μm . The system consisting of the NiP layer on top of the aluminium mirror body works as a bi-metal so that the mismatch of the Coefficients of Thermal Expansion (CTE) has to be considered already during the design phase [6]. The left side of figure 9 illustrates the deformation of a mirror made of standard Al6061 as bulk material with NiP plating at a temperature shift of 10 K. The deformation of the mirror reaches peak to valley values around 500 nm. After subtracting defocus, offset and tilt, 200 nm form deviation is left. Looking for diamond turnable materials with a CTE near the one of NiP (12 to $13 \times 10^{-6}/\text{K}$), aluminium alloys with high percentage of silicon come into view. AlSi42 with 42% silicon has a CTE ($12.8 \times 10^{-6}/\text{K}$) quite near to Nickel Phosphorous. The right side of figure 9 shows the deformation due to a temperature shift of 10 K using AlSi42 as bulk material and NiP as plating. The unfiltered data are 17 nm form error caused by the bi-metal effect. After filtering the data in the above mentioned way, 7 nm deformation is left. This is quiet near to the initial condition.

2.2.2 Polishing: Smoothing with Computer Aided Sub Aperture Tools

The microstructure of the optical surface after SPDT is characterized by turning grooves with a spatial wavelength in the range of 0.01 mm, overlaid by a modulation up to 1 mm (waviness). The smoothing of the waviness is a challenge, especially for aspheric surfaces. Applying computer-aided polishing with sub aperture tools, all periodical structures can be removed without any impact on the shape of the surface (Figure 10).

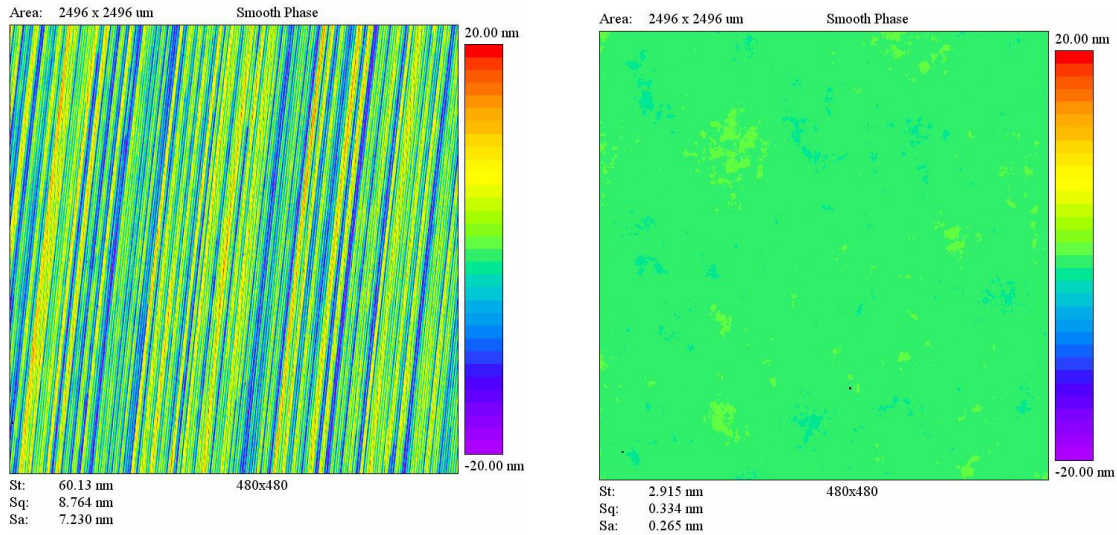


Fig. 10. Typical results of white light measurement for the smoothing of diamond turned NiP surfaces. Left hand: Result of phase shifting micro interferometry after diamond turning. Right hand: Result after smoothing operation.

It is possible to improve the surface roughness about a factor of 10. A surface roughness better than 1 nm is achievable. Irregularities between surface roughness and global error, called mid frequencies, have negative effects on the efficiency of the optical system. It has to be taken care to recognize these defects. While analyzing the micro roughness, the lower frequencies are filtered away; looking for global errors higher frequencies are too small to be seen. A good way to detect these defects is the light scattering measurement. Frequencies in a large bandwidth can be analyzed with this technology and displayed in just one single graph (figure 11).

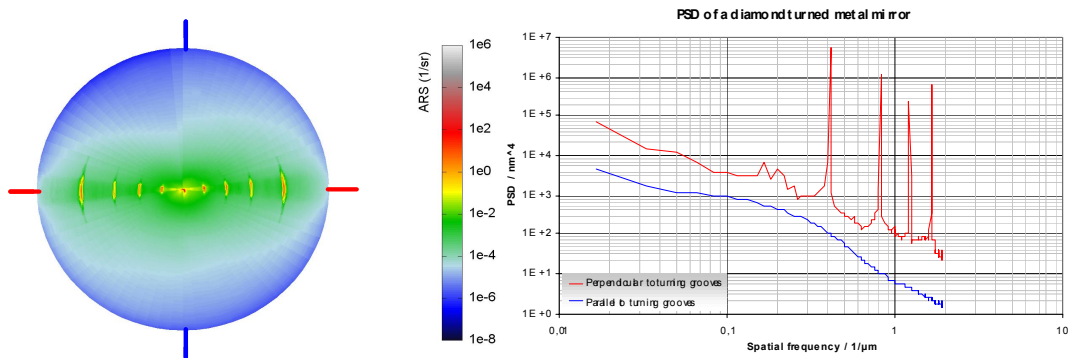


Fig. 11. Light scattering measurements shows irregularities over broad spectral range. Left side: ARS (angle resolved scattering) measurement of a metal mirror at 532 nm. Right side: PSD (Power spectral density analysis) of this measurement at two angles. The peaks are caused by turning grooves.

2.2.3 Polishing: Shape Correction with Ion Beam Figuring

To decrease the residual shape error after diamond turning, computer controlled local shape correction with small area tools (IBF) is commonly used. Shape accuracy better than $\lambda/4$ peak to valley is reached (Figure 12).

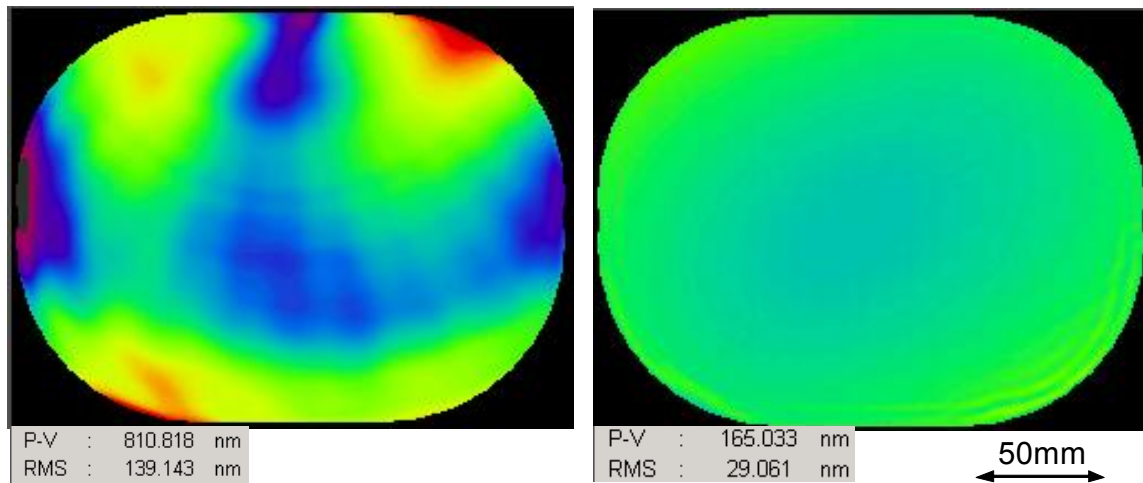


Fig. 12. Results of high-precision interferometric measurements of an off-axis aspherical element. Left hand: Shape after diamond turning. Right hand: Residual shape error after local IBF. In a deterministic process the figure error was reduced by a factor of 5.

To achieve this high quality a very precise measurement has to be employed. For aspheres and free form geometries interferometry in combination with Computer Generated Holograms (CGH) is the method of choice. These CGH's can be manufactured at the Center for Advanced Micro- and Nano-Optics at the Fraunhofer IOF. The basic principle is to use a diffractive grating to produce a certain wave front which compensates wave front differences between reference part and test part. Typically two or three measurement-polishing loops are needed to improve the optical quality by the factor of 8 [11].

3. CONCLUSION

Non ferrous metal mirrors with their specific stiffness and light body material offers great opportunities for high performance optics. SPDT is an efficient and very accurate manufacturing technology. Regarding the feasible geometries, almost no limit is in sight. Different machine kinematics are used to manufacture spheres, aspheres or even free forms. Common applications range from IR to NIR wavelengths. But leading technologies like computer assisted polishing and IBF enables the use of metal mirrors with excellent figure and roughness for VIS and UV applications. With 3D measurement technologies like the 3D profilometry and Computer Generated Hologram aided interferometry it is even possible to reduce not rotationally symmetric shape deviations. Optical coatings for superior reflectivity and high demands on long term stability against stress and strain are applied with sputtering technologies.

REFERENCES

- [1] Gubbels, G. et al, Rapidly solidified aluminium for optical applications; SPIE Proc., Marseille 2008
- [2] Oltmann Riemer; Trennmechanismen und Oberflächenfeingestalt bei der Mikrozerspannung kristalliner und amorpher Werkstoffe; Forschungsberichte aus der Stiftung Institut für Werkstofftechnik; Shaker Verlag, Aachen 2001.
- [3] K. Garrard; et al; Off-Axis Biconic Mirror Fabrication; Proc. Of the 3rd euspem international Conference, Eindhoven, The Netherlands (2002).
- [4] Christian Breche; et al; Hochgenaue optische Freiformflächen – schnell gefertigt; Photonik, 2/2005.
- [5] Risse, S.; Gebhardt, A.; Steinkopf, R.; Giggel, V.; NiP plates mirrors for astronomy and space. Proc. of the 7th EUSPEN Bremen 2007; p. 348-351
- [6] Yoder, P.R.; Opto-Mechanical Systems Design; 2nd ed. New York (Dekker), 1993
- [7] Max J. Riedl, Optical Design Fundamentals for Infrared Systems, 2nd ed., Spie Press, 2001
- [8] Norbert Kaiser, Coating development for optical instrumentation, Photonic International 2007
- [9] www.unigit.com
- [10] Parsonage, T. B.; New technologies for optical systems utilizing aluminium beryllium. SPIE Proc. 7018-23, Astronomical Instrumentation, Marseille, 2008
- [11] Risse, S. et al, Novel TMA telescope based on ultra precise metal mirrors. SPIE Proc. 7010-41, Astronomical Instrumentation, Marseille, 2008

Optical designs with large metal mirrors

Richard G. Bingham

Royal Greenwich Observatory, Madingley Road, Cambridge CB3 0EZ
and University College London, England

ABSTRACT

Metals have important advantages as mirror substrates. Existing metal mirrors exploit the bulk properties of the material for mechanical and thermal purposes, and some mounting details and useful optical features which are very difficult with glass can be more readily produced in metal. In the near future, metal substrates promise to extend the possibilities for large active optics (with control of the optical figure), on account of their mechanical properties and methods of attachment. Looking further ahead, enhanced active optics will make it possible to produce large *non-axisymmetric* or *variable* optical figures. I suggest that such optics will open new dimensions for the telescopes of the future. One potential example is a two-aperture telescope with coherent imaging. Its elements are off-axis Cassegrain telescopes. The two beams combine (if required) in an optically ideal manner and with no obstructions or further reflections. Other suggestions for further study include the reflecting Schmidt camera, beam-steering systems and systems with a non-circular field of view.

1. INTRODUCTION

1.1. Normal features of metal optical components

The metals referred to here are mainly specific aluminium alloys, as discussed at this conference and by Rozelot *et al.*¹. To prepare for optical polishing, the aluminium alloy is coated with 100–200 μm of nickel after machining. Both faces are coated to preserve symmetry in thermal expansion. The polished optical surface is normally further coated as usual with evaporated aluminium, etc., for high reflectance. Alternatively, the required optical figure may be produced directly by diamond machining.

Metals are claimed (in these proceedings and previously¹) to offer various advantages as mirror substrates. In ground-based telescopes, the basic points are the low risk of damage and excellent thermal control. (The risk of damage to brittle materials has increased with modern meniscus and other low-mass mirrors: control of temperature should result in reduced “mirror seeing”. Mirror seeing is a problem both in the telescope and in optical testing during production.) Further advantages relate to the reliability of attaching supports which are under torque or tension. The supports can be attached in threaded holes or in captive nuts or latches. (Even plain holes for attachments are unusual with glass.) Strong fixings are expected to be useful for the actuators for active optics, as discussed later. Metals also reduce the engineering effort required for safe handling and shipping, which is a significant investment with large mirrors. Thermal expansion equal to that of a telescope tube of the same alloy may be useful. The very accurate focal lengths and other dimensions produced by diamond machining may also be useful in reducing the

need for adjustments, especially if matched thermal expansion throughout the system is also achieved.

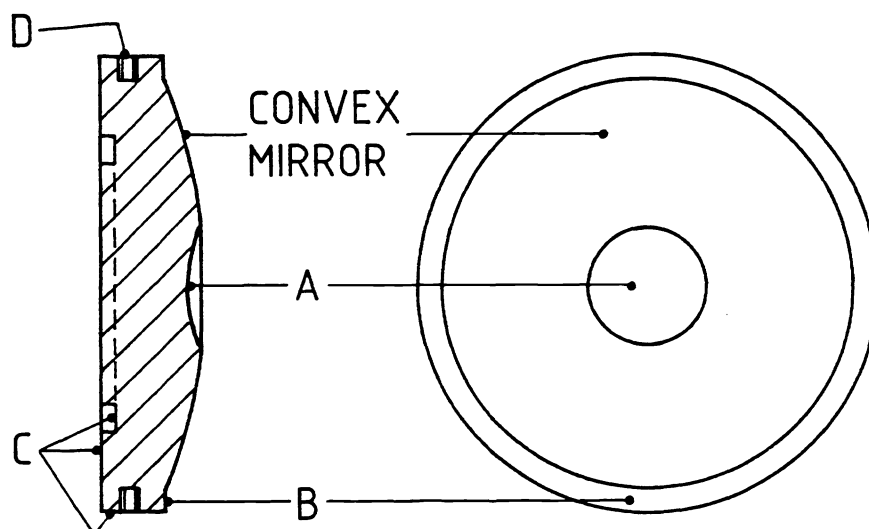


Fig. 1. A schematic metal mirror showing machined features.

Existing metal mirror substrates frequently employ some special features which can affect the design of an optical instrument. Some of these features may be produced by diamond turning, and others by conventional metalworking before the optical surface is formed. Present-day machining techniques are not advanced enough for those features to be generally practical on glass. For illustration, Fig. 1 shows a schematic convex metal mirror with the following features typical of existing applications:

A - An additional optical surface on a single element (for alignment or a second incidence) which is precisely centred by a diamond-turning machine

B - A machined optical surface (for alignment, etc) which can be produced in an internal angle

C - Mechanical locating or reference surfaces produced to optical tolerances

D - Positive fixings such as screw-threaded holes in the optical element. No cell.

1.2. Focussing a Cassegrain system

Differential thermal expansion of the primary mirror, secondary mirror and tube in a Cassegrain telescope can result in a large defocus. Correction by means of moving the secondary mirror may lead to spherical aberration but that is small in the example described below. The use of active optics has further implications.

An eight-metre, $f/1.8$ parabolic primary mirror of aluminium alloy with a zero-expansion $f/7$ Cassegrain (hyperbolic) secondary is a hypothetical example. I consider the effect of a fall in temperature of 20°C (to correspond to 40 degrees extreme range). *In this example, no active correction is considered.* The prime focus moves 6.9mm towards the primary mirror, so the Cassegrain position where spherical aberration would be zero moves 6.9mm further away from it. The mechanical structure below the primary mirror contracts, lifting the instrumentation by, say, 0.8mm, depending on the position of focus and the structural material. The total longitudinal defocus is thus 7.7mm, giving four arc seconds geometrical image spread due to defocus, when the secondary mirror is positioned such that spherical aberration is zero. Refocus is

given by positioning the secondary mirror up 0.5mm from that point. The resultant spherical aberration in wavefront terms is about $0.33\mu\text{m}$, and the geometrical circle of least confusion is about 0.03 arc seconds in diameter. The effective focal length is reduced by about 0.09 per cent. The spherical aberration is less in the case of an $f/30$ secondary mirror, for example.

Active optics will almost certainly be involved in practice, and are especially relevant in the case of metals, as discussed below. Either or both of the primary or secondary mirrors may be deformable. It is pointed out here that any type of slide mechanism for focussing may be redundant in that case. The normal up-down slide mechanism can be a problematical feature of the mount of a Cassegrain secondary mirror, which may require a complicated five-axis mount to provide for adjustments. The present suggestion is to eliminate the focussing slide. This applies when active control of the optical figure (a) is used for the normal operation of the telescope and (b) has a large enough dynamic range to focus the telescope at all temperatures and for all focal stations. Optical-design exercises on one example show that an appropriate change of the optical figure of an eight-metre primary mirror results in negligible aberrations. If this technique is used, it is not an advantage to incorporate an additional focussing mechanism in a telescope for reliability, as the telescope will not be operational in any event if the mirror support systems fail. The necessary focussing range may perhaps be minimised in the design by the choice of the optical or structural materials, with regard to their coefficients of thermal expansion.

Deformable secondary mirrors which may have substrates of aluminium alloy or silicon carbide are being considered^{2,3}. The main impetus is for adaptive optics, but the potential for focussing, other active control and chopping is clear. If one of these mirrors was retrofitted to an existing telescope, it might be a further advantage to clamp the pre-existing focussing mechanism firmly.

1.3. Extremely large telescopes

Around the 1970's, several groups proposed a variety of more or less peculiar optical design concepts for telescopes up to 25 metres aperture (e.g.⁴ a giant siderostat, az-az telescope or fixed spherical mirror). No such optical telescope was realised. One problem in some concepts was the use of mirrors whose total area was more than twice that of the telescope's aperture. Many of the concepts attempted to compensate for gravitational flexure by passive means. In contrast, modern developments aim to achieve stability and reduce mass by means of active optics applied to Cassegrain systems.

Ardeberg et al. (in these proceedings) describe a modern and probably economic concept for a 25-metre telescope, employing new technology and new optical designs. It would benefit from low cost, perhaps automated production or replication of individually passive mirror segments, probably involving metals. The structure supporting the mirror segments is actively controlled.

The 25-metre aperture is still far off, and a low-cost mirror with improved thermal control and active figure, such as metals promise, could give renewed impetus to the various concepts. Flexure under wind pressure may be the limiting factor. Developments of the "optical Arecibo" concept are possible. A principal advantage of such a dish is the elimination of flexure under wind pressure, even for very large apertures, if the mirror segments are mounted close to a concrete base or rock formation as at the Arecibo radio telescope. A distant prospect, although conceivable with metals, would be a dynamically aspherised dish. It would use active optics to deform a basically spherical dish to a paraboloid or hyperboloid lo-

cally. The local vertex and axis would thus correspond with the pointing direction. This would avoid the compromises arising from the otherwise spherical primary mirror.

2. ACTIVE OPTICS WITH METALS

2.1. Techniques of active optics

The techniques⁵ of active optics include slow adjustment of optical surface profiles and slow adjustment of tilts and centration of optical surfaces. In this paper, I concentrate on the former, referring to deformable mirrors.

Metals offer larger elastic limits than vitreous materials; an aluminium alloy mirror has a linear range around 60 times that of a glass-ceramic mirror with ground edges (private communications from L. Nöthe, ESO, and from the TELAS G.I.E. The range depends on the temperature and the nature of unpolished glass surfaces, edges etc.) Young's modulus is roughly the same for the alloys as for glass, so given larger forces of the necessary accuracy (thus with larger dynamic range) much larger strains would be available with metals. Thus subject to the performance of actuators, larger active effects are available with metals.

For the 8.2m diameter, f/1.8, 177mm thick VLT mirrors, $1.0\mu\text{m}$ of spherical aberration of the reflected wavefront corresponds to $0.005\text{N}\cdot\text{mm}^{-2}$. Thus the $20\mu\text{m}$ of spherical aberration which is required to change the back focal distance from the Nasmyth to the Cassegrain configuration produces stresses⁶ of approximately $0.12\text{N}\cdot\text{mm}^{-2}$. This is only four per cent of the critical stress in glass-ceramics. Purely to illustrate the effect of linear extrapolation, to bend an eight-metre spherical mirror of similar dimensions into a paraboloid would require about 130 times this stress — outside the range of glass ceramics in the given thickness, but within the range of aluminium alloys. In section 3.1 of this paper, I discuss an application which involves the production of large off-axis circular parts of such a paraboloid, and in that case, the necessary stress may be reduced by reducing the thickness.

Active control of optical figure can be enhanced by the additional mechanisms available with metals. Threaded fixings allow the reliable use of push-pull actuators (rather than push only), levers and torques. Those additional degrees of freedom in the control and support system may be expected to provide the opportunity for high performance, exploiting some of the increased elastic range. Lemaître's aspherising technique (this conference) is also relevant.

For active optics, the practical limit would be determined by the accuracy and distribution of the controlled forces. Accurate implementation of large deformations would probably require more actuators, though this is not the only approach: especially with metals, it should also be possible to improve the forced shape with the aid of different types of actuator and their attachments as discussed above. Such types of actuator would include levers which directly affect the local surface gradient or curvature, especially at the edge of the mirror.

For production of extreme profiles by the polish spherical, stress-and-relax technique, another suggestion is to use two-stage systems. The proposal is to use the stress-and-relax polishing process to produce an approximately correct figure, and an active system in the telescope to perform final corrections with smaller forces, subject to the proviso discussed below. Thus the necessary dynamic range of the actuators in either stage is reduced.

Corrections in the telescope would apply to those effects with the larger spatial scales. Small-scale deformations in the region of the stressing points of the figuring system must be minimised. Avoiding or correcting such small-scale deformations would generally be assisted by larger number of supports. As the types of stressing attachment used for stressed mirror figuring are much simpler than mirror supports in a telescope, so the use of many supports would be more appropriate for the figuring support than for the telescope.

Bingham et al.⁷ discussed the use of metals for segmented mirrors. They considered that a large mirror would be formed of approximately six separate sectors. The optical figures of *individual* sectors would be actively controlled. Many of the advantages suggested arise from the suggested suitability of metals for this purpose (see above). The use of segments, the use of active supports and the use of metals should all contribute to reducing the thickness and hence the mass of the mirror, with special reference to space applications. In that case the aim would be a thickness of less than one per cent of the diameter of a segment. Numerous other advantages are suggested for the segmented mirror, and many possibilities for developing optical figuring technology in the case of segments⁸.

2.2. Consequences

Wilson et al.⁵ pointed out the advantages of active optics in terms of the optical quality of telescopes, and indeed launched the technology. Of particular relevance here, the use of active optics should (a) answer any remaining uncertainty about the dimensional stability of some materials when used for large optics, and (b) lead to large reductions in mass. Thus active optics seem certain to be used in all future large telescopes.

In this paper, I discuss some applications for active optics which go beyond the capabilities of existing telescopes. The aim or hope is to identify some possibilities for optical systems which are new, or may become practical in large sizes, with the technology discussed.

A very clear application for slightly enhanced active optics is in the operation of a versatile telescope which keeps the zero-coma condition of the Ritchey-Chrétien with various secondary mirrors⁹. This is just within the range of present techniques and could easily be extended. The fact that active optics may also eliminate the normal focussing mechanism, which is often expensive or problematical, was pointed out above.

As metal substrates appear to be physically ideal for active optics, they should assist in the production of special optical figures. The suggestion is to use mechanical stress in various ways to produce the optical figure. At present, optical design concepts are strongly biased by the effectiveness of the conventional optical production processes, some of which have a history of hundreds of years. Another constraint often mentioned is the simplicity of optically testing a spherical or flat optical surface. (However, even that rapidly loses its practical simplicity with convex or flat surfaces with diameters larger than about 0.3 metre.)

A number of constraints on large optical surfaces are being relaxed:

- preferably spherical surfaces, or small asphericities
- axisymmetric optical systems

- circular apertures
- massive substrates
- invariant systems with fixed optical profiles
- one-piece (otherwise “monolithic”) substrates.

The Keck project already steps ahead from these constraints in some respects.

Especially, the production of large, non-axisymmetric optical profiles (as discussed below, with examples) and perhaps extreme aspherics should become more usual with the aid of stressed-mirror polishing, active supports, or both. (Stressed-mirror figuring may either compete with or be supplemented by local figuring, which is already carried out on glass, but which is expensive). Time-variable profiles may be considered, opening further new areas for optical design concepts. The production of new profiles demands new optical tests or other methods of measurement, but they are also expected to be within the capability of current technology.

3. EXAMPLES OF NON-AXISYMMETRIC SYSTEMS

3.1 The two-element interferometer

A Cassegrain-type telescope implemented with no obstructions by means of off-axis mirrors is sketched in Fig. 2. The mirrors are simply part of an on-axis system. It has an improved diffraction profile and reduced infrared emissivity in the absence of a central obstruction and its supports. Another advantage proposed is its use in interferometers, as discussed below. Apart from the Cassegrain system, there are other two-mirror optical systems which can be implemented in this off-centre form. Such unobstructed cameras have been implemented only as small instruments.

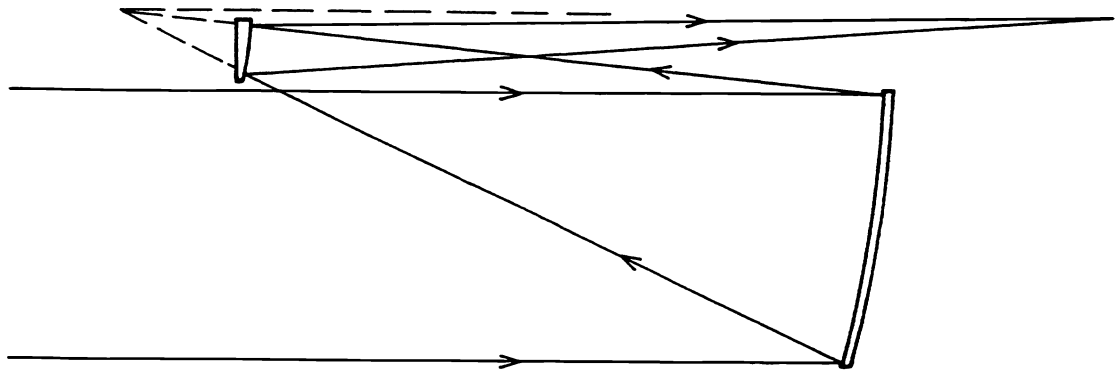


Fig. 2. The off-axis Cassegrain telescope.

A good example would be a three to six-metre telescope or interferometer element. The three-metre mirror could be (conceptually) an off-axis part of an eight-metre mirror. The theoretical eight-metre primary mirror would have an asphericity measured from the vertex sphere of about 1.3mm.

It is clearly undesirable to produce an eight to 16-metre or larger mirror and then to cut it, and so the off-axis interferometer element should be a candidate for production by the active-optics techniques outlined above. A segmented-mirror approach should also be considered.

Two off-axis telescopes can be combined as shown in Figs. 3a and 3b. The optical arrangement is as if a larger telescope had been masked down to the two apertures. It may be compared to the Columbus project¹⁰ which uses on-axis telescopes. The system is an imaging interferometer, providing angular resolution. A spectroscopic mode might use parallel but separate collimators, with the two beams illuminating a single diffraction grating in a spectrograph. The telescope could be implemented in a reasonably versatile form as discussed¹¹ previously. Some modes of operation would not combine the two beams, but use separate instruments on the two telescopes or separate detectors.

The dual off-axis arrangement provides a coherently imaging, two-aperture telescope. The problem of introducing a beam combiner can be complicated in some interferometers, but in contrast, this arrangement provides ideal, coherent recombination of the beams with no additional optical surfaces, reflections or obstructions. It is thus much simpler than the various schemes available to combine two on-axis telescopes¹¹. Similar schemes could be used for more than two primary apertures.

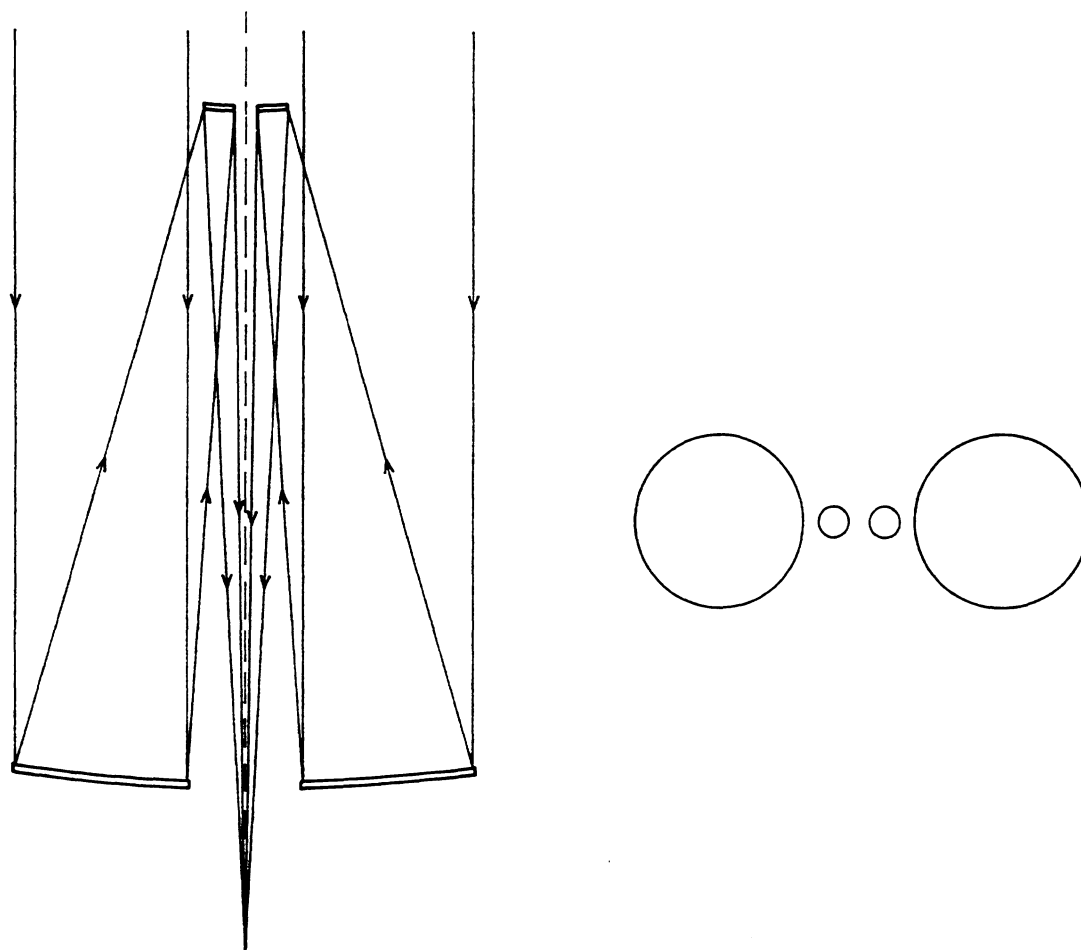


Fig. 3a (left). The two-beam interferometer with elements which are designed as off-axis sections of a single larger telescope. Fig. 3b (right). A plan view of the apertures.

With the aid of active adjustments, it should be possible to position the surfaces of two secondary mirrors near enough to a common hyperboloid without placing them on one substrate. However, the requirements of interferometry are stringent as regards vibration and this question requires specific study.

3.2. The catoptric (reflecting) Schmidt camera

The well-known Schmidt camera uses an aspheric corrector lens, but there is an analogous system in which the lens is replaced by a tilted aspheric mirror. The resultant camera is referred to here as the "catoptric Schmidt". The aberrations are not generally so small as those of the normal Schmidt but the all-reflecting property is interesting. A wide-field, 0.75-metre aperture, catoptric Schmidt camera for space use at ultraviolet wavelengths was studied¹² but not proceeded with. The Hipparcos satellite uses such a camera of 0.29 metre aperture¹⁴. The cost and advantages of a large catoptric Schmidt would need to be evaluated in comparison with other systems, principally those proposed by Willstrop¹³.

A large all-reflecting camera could be important for ground-based astronomy by virtue of its infrared capability. An aperture of up to three metres is considered here. One aim of a new manufacturing technique for the reflecting Schmidt would be to develop a deep aspheric surface for a fast camera, to reduce the length of the telescope. The problem of mounting such a telescope also obviously requires investigation.

The optical figure of the aspheric corrector mirror has elliptical contours of surface height, and is challenging to produce by conventional means. With the anticipated technology, the elliptical profile would be produced with the assistance of mechanical stress as suggested above. Wray *et al.* imply¹² a development of the method used by Schmidt for his original camera. That also used mechanical stress, applied by air pressure over a vacuum former. Another method¹⁴ for producing a nearly elliptical surface is to reposition segments from an axisymmetrical corrector, but that has not been investigated in relation to the present work.

Some preliminary optical design work has been carried out and a further discussion of the catoptric Schmidt may be given elsewhere. A small catoptric three-mirror system based on the "Cassegrain Schmidt" was described¹⁵ previously. That example is a spectrograph camera for a system requiring a finite front conjugate distance, i.e. not focussed to infinity. As a further development, the nominally spherical mirrors included in these non-axisymmetric reflecting systems may also be aspherised.

3.3. Other non-axisymmetric systems

Mirrors with controlled variable profiles could provide for some interesting beam-steering systems. They would have the effect of changing the effective pointing direction of a telescope. The required changes in mirror profiles in some cases might be obtained with either active glass mirrors or metal mirrors, depending on the size of the desired effect.

One example suggested is a Cassegrain or Ritchey-Chrétien telescope in which the central area of the optical field of view would be pointed at different parts of a focal surface. Deformable mirrors would be used to maintain a favourable and nearly symmetrical aberration pattern on the different centres. One application is to select one of a number of auxiliary instruments. This procedure would reduce the need to change instruments mechanically, and so would avoid major capital and operating costs and enhance

reliability. It would be useful where there is space to mount several instruments simultaneously.

With this instrument selector, an adaptive-optics facility might be provided by the secondary mirror. Facilities such as a field-viewing camera and wavefront sensors would be moved on a turntable, etc, to each instrument station as required, or would be provided in the individual instruments.

This capability could be obtained almost as a by-product in the presence of active optics, which might be implemented in metal or glass for the other reasons discussed. However, there are several other methods of achieving similar effects which need to be compared in practical cases, and which need not utilise deformable mirrors. A point image can be obtained off-axis from a suitably misaligned Cassegrain telescope, for example. Instrument selection is performed passively on the Hubble Space Telescope at its $f/24$ Ritchey-Chrétien focus simply by fixing the various instruments at different points in the field, and pointing the telescope accordingly. Another method is to redirect the beam with an extra flat mirror, potentially giving a large space for each instrument. However, when compared with beam-steering by means of active optics, probably none of these other methods provides as much of the capability of a typical telescope in terms of field, transmission, etc., at each instrument station. The infrared performance needs detailed evaluation of particular designs.

Another possible application of beam steering is to provide a mechanism for tracking the pointing direction of a mainly fixed telescope used for transit surveys.

A further application of large systems with non-axisymmetrical optical figures may be for two-mirror cameras which have an elongated, or one-dimensional, field of view. Such cameras would be used for survey work as "sweepers". They would carry an elongated detector system which might consist of a single row of CCD sensor chips, for example. They might again be used for astronomical transit surveys, surveys of the Earth from space or surveys of the near-space environment (including space debris) from the Earth.

4. ACKNOWLEDGEMENTS

I am grateful to Dr L. Nöthe for information on the stresses in an eight-metre mirror substrate and the stresses allowed in different materials and to Dr D. D. Walker and Dr. S. P. Worswick for comments on an earlier form of this paper.

5. REFERENCES

1. J. P. Rozelot, R. G. Bingham and D. D. Walker, "Aluminium mirrors versus glass mirrors", in *Progress in telescope and instrumentation technologies*, ed. M.-H. Ulrich, pp. 71-74, European Southern Observatory, Garching, 1992.
2. D. D. Walker, R. G. Bingham and B. C. Bigelow, "Adaptive correction at the secondary mirror", in preparation.
3. B. C. Bigelow, D. D. Walker and R. G. Bingham, "A deformable secondary mirror for adaptive optics", in preparation.
4. Various papers in *Optical telescopes of the future*, ed. F. Pacini, W. Richter and R. N. Wilson, European Southern Observatory (then at Geneva), 1977.
5. R. N. Wilson, F. Franza, L. Nöthe and G. Andreoni, "Active optics IV", *Journal of Modern Optics*, Vol. 38, No. 2, pp. 219-243, 1991, and references therein.

6. L. Nöthe, private communication.
7. R. G. Bingham, D. D. Walker and J. P. Rozelot, "Aluminium as the substrate for segmented mirrors", as ref. 1 above, pp. 339–342.
8. R. G. Bingham, D. D. Walker and F. Diego, "Technology for 8-m primary mirrors", in *Advanced technology optical telescopes IV*, ed. L. D. Barr, Proc. SPIE vol. 1236 part 2, pp. 586–597, 1990.
9. R. G. Bingham, "The reverse-hybrid Ritchey-Chrétien — and the use of active optics", as ref. 1 above, pp. 319–322.
10. P. Strittmatter, "Columbus project telescope", as ref. 8 above, part 1, pp. 71–84. Also see N. J. Woolf, J. R. P. Angel and D. W. McCarthy, Jr., "The versatile array", in *Advanced technology optical telescopes II*, Proc. SPIE vol. 444, pp. 78–84, 1983.
11. R. G. Bingham, "The two-mirror telescope (2MT)", in *Very large telescopes, their instruments and programmes*, IAU Colloquium No. 79, Garching, ed. M.-H. Ulrich and K. Kjær, pp. 347–365, 1984.
12. J. D. Wray, H. J. Smith, K. G. Henize and G. R. Carruthers, "Space Schmidt telescope", in *Advanced technology optical telescopes*, Proc. SPIE vol. 332, pp. 141–150, 1982.
13. R. V. Willstrop, "The flat-field Mersenne-Schmidt", *Mon. Not. R. astr. Soc.*, vol. 216, pp. 411–427, 1985, and references therein.
14. M. A. C. Perryman and H. Hassan (eds.), in *The Hipparcos mission*, European Space Agency, special publication SP-1111, vol. I, p. 72, Noordwijk, 1989.
15. R. G. Bingham, D. D. Walker and F. Diego, "Extending the wavelength coverage of spectrographs", in *High resolution spectroscopy with the VLT*, Garching, ed. M.-H. Ulrich, pp. 271–274, 1992.